Equatorial Pacific Variability in Climate Models

by

Christian Wengel

Dissertation

submitted to the Faculty of

Mathematics and Natural Science of the

Christian-Albrechts-Universität zu Kiel

in Fulfillment of the Requirements

for the Degree of Dr. rer. nat.

March 2018

First Examiner:	Prof. Dr. Mojib Latif
Second Examiner:	Prof. Dr. Joke Lübbecke

Day of Disputation:	17 May 2018
Approved for Publication:	17 May 2018

_____

Prof. Dr. Natascha Oppelt, Dean

Abstract

The equatorial Pacific is subject to strong variability on various timescales, which affects climate on a regional as well as on a global scale. The dominant modes of variability are the eastern equatorial Pacific (EEP) sea surface temperature (SST) annual cycle (AC) and the interannual El Niño/Southern Oscillation (ENSO). A realistic simulation of the EEP SST AC and ENSO in climate models together with a profound understanding of the underlying simulated dynamics is crucial for a robust employment of climate models in many different aspects. In this thesis, the simulation of the EEP SST AC and ENSO in climate models is investigated.

The EEP SST AC originates from complex interactions of the coupled ocean-atmosphere system and its realistic representation presents a long-standing difficulty in climate models. This thesis investigates the simulation of the EEP SST AC in a set of coupled experiments with the Kiel Climate Model (KCM) which differ in atmospheric resolution. The KCM experiment employing coarse atmospheric resolution depicts significant biases in the EEP SST AC concerning the phase as well as the amplitude of the seasonal variation of the equatorial cold tongue. A large portion of these biases is linked to an erroneous simulation of zonal surface winds, which is associated with an incorrect representation of rainfall to the north and south of the equator. An additional source for EEP SST AC biases originates from a simulated deficit in shortwave radiation related to cloud cover biases. Analyzing the analogous uncoupled atmospheric model integrations forced by observed SSTs suggests that zonal wind and cloud cover biases are inherent to the atmospheric model component. When atmospheric model resolution is enhanced, both wind and cloud cover biases are markedly reduced and the simulation of the EEP SST AC improves. The effect of enhanced atmospheric resolution is, on the one hand, to reduce convection biases over the equatorial Pacific sector and, on the other hand, to improve the simulation of surface winds near landmasses as a result of a refined representation of orography. A subset of models from the 5th phase of the Coupled Model Intercomparison Project (CMIP5) exhibits very similar biases and associated dynamics of the EEP SST AC to those identified in the KCM.

The interannual variability associated with ENSO is characterized by a distinct seasonal phase locking with strongest SST anomalies (SSTa) during boreal winter and weakest SSTa in boreal spring. This feature is here investigated in an ensemble of KCM integrations created from perturbed atmospheric physics. The KCM ensemble-mean depicts a realistic seasonal phase locking of the SST variability and of the relevant ENSO feedbacks as inferred from conducting a Bjerknes Stability index analysis. However, the amplitude of the seasonal phase locking is underestimated,

which is linked to an excessive simulation of the equatorial cold tongue that reduces the amplitude of the simulated feedbacks. The simulation of eastern equatorial SST variability, mean-state SST and ENSO feedbacks is very sensitive to perturbed atmospheric physics. KCM simulations with a more realistic mean state and ENSO feedbacks also exhibit a more realistic seasonal ENSO phase locking. A similar relationship also is obtained from a set of CMIP5 models.

A problematic feature of ENSO simulation in climate models is the large diversity in the simulated strength of ENSO variability. This thesis investigates ENSO-amplitude diversity in a CMIP5 multi-model ensemble by means of the linear recharge oscillator model, which reduces ENSO dynamics to a two-dimensional problem in terms of central and eastern equatorial SSTa (T) and equatorial heat content anomalies (h). Two major sources of the diversity are identified: One originates from stochastic forcing of T and h, the other from interactions of the dynamical processes. The latter suggests competing effects of the growth rate of T and h and the stochastic forcing. These identified sources explain more than 80% of the ENSO-amplitude diversity in the CMIP5 multi-model ensemble.

Zusammenfassung

Der äquatoriale Pazifik ist durch starke Variabilität auf verschiedenen Zeitskalen gekennzeichnet, mit regionalen und globalen Auswirkungen auf das Klima. Dabei stellen der Jahresgang der Meeresoberflächentemperatur im östlich-äquatorialen Pazifik (engl. eastern equatorial Pacific sea surface temperature annual cycle, Abk. EEP SST AC) sowie das El Niño/Southern Oscillation (ENSO)-Phänomen die dominanten Moden dar. Eine realistische Simulation dieser beiden Moden sowie ein tiefreichendes Verständnis von den zugrunde liegenden simulierten Dynamiken ist für eine verlässliche Verwendung von Klimamodellen von großer Wichtigkeit. In dieser Doktorarbeit wird die Simulation des EEP SST AC und ENSO in Klimamodellen untersucht.

Der EEP SST AC wird von einem komplexem Zusammenspiel von Ozean und Atmosphäre bestimmt und wird in den meisten Klimamodellsimulationen im Vergleich zu Beobachtungen fehlerhaft dargestellt. In dieser Doktorarbeit wird die Simulation des EEP SST AC im Kieler Klimamodell (engl. Kiel Climate Model, Abk. KCM) untersucht. Dabei bilden sechs Simulationen mit dem KCM, welche sich in der Gitterauflösung der atmosphärischen Modellkomponente unterscheiden, die Grundlage der Studie. In der KCM-Simulation mit grober atmosphärischer Auflösung lassen sich deutliche Simulationsfehler in der Phase sowie in der Amplitude des EEP SST AC identifizieren. Ein erheblicher Anteil der fehlerhaften Simulation des EEP SST AC hängt mit einer fehlerhaften Darstellung von oberflächennahen zonalen Winden zusammen. Dies wiederum geht mit einer fehlerhaften Simulation von Niederschlag und Konvektion im Sektor des tropischen Pazifiks einher. Außerdem führt eine ungenaue Simulation der Bewölkung zu einem Defizit in der simulierten kurzwelligen Strahlung an der Meeresoberfläche, welche die Darstellung der Meeresoberflächentemperatur beeinflusst. Es lässt sich zeigen, dass im KCM ein Großteil der fehlerhaften Simulation sowohl des zonalen Windes als auch der Bewölkung seinen Ursprung in der atmosphärischen Modellkomponente hat. Darüberhinaus führt eine Erhöhung der atmosphärischen Modellauflösung im KCM zu einer deutlichen Verbesserung der Simulation der zonalen Winde, der Bewölkung und des EEP SST AC im Vergleich zu Beobachtungen. Die Erhöhung der atmosphärischen Modellauflösung bewirkt eine verbesserte Darstellung des Niederschlags und der Konvektion im tropischen Pazifik, was die Simulation von zonalen Winden und Bewölkung beeinflusst. Zusätzlicher Einfluss wird einer genaueren Darstellung der Orography unter erhöhter atmosphärischer Auflösung zugeschrieben. Ein Vergleich der Ergebnisse mit Simulationsdaten von Modellen aus dem fünften Coupled Model Intercomparison Project (CMIP5) zeigt, dass diese

Mechanismen auch in anderen Klimamodellen eine wichtige Rolle für die Simulation des EEP SST AC spielen.

Die zwischenjährliche Variabilität im äquatorialen Pazifik aufgrund von ENSO ist ebenfalls durch einen Jahresgang gekennzeichnet, mit stärksten Meeresoberflächentemperaturanomalien im borealen Winter und schwächsten Anomalien im Frühling. In dieser Doktorarbeit wird die Simulation dieser Charakteristik (engl. seasonal ENSO phase locking) im KCM untersucht. Dabei stellt ein große Anzahl von KCM-Simulationen die Grundlage für die Analyse, welche sich durch Variationen physikalischer Koeffizienten in atmosphärischen Parameterisierungen unterscheiden. Der Mittelwert über alle Simulationen zeigt ein in der Phase realistisches aber in der Ausprägung zu schwaches seasonal ENSO phase locking im Vergleich zu Beobachtungen. Die Ergebnisse deuten an, dass eine im KCM zu stark ausgeprägte äquatoriale Kaltwasserzunge eine zu schwache Simulation der physikalischen Rückkopplungen bewirkt, welche wiederum das phase locking kontrollieren. Außerdem lässt sich eine hohe Empfindlichkeit der Simulation der Kaltwasserzunge, der Rückkopplungen sowie des phase locking auf die Variationen der oben-genannte physikalischen Koeffizienten im KCM feststellen. Zwischen der realistischen Darstellung der Kaltwasserzunge, den physikalischen Rückkopplungsprozessen und dem phase locking besteht im KCM ein systematischer Zusammenhang. Ein Vergleich mit Ergebnissen aus CMIP5-Modelldaten bestätigt diese Relation.

Eine weitere Problematik ist die große Diversität an ENSO-Stärke-Simulationen in Klimamodellen. In der vorliegenden Doktorarbeit wird dies mit Hilfe des linearen zwei-dimensionalen recharge oscillator-Modells in CMIP5-Klimamodellsimulationen untersucht. Zwei signifikante Faktoren für die Diversität lassen sich identifizieren: Ein Faktor ist der stochastiche Antrieb der Meeresoberflächentemperatur und des äquatorialen Wärmeinhalts, ein anderer das Zusammenspiel der unterschiedlichen dynamischen Prozesse. Letzterer bewirkt einen konkurrierenden Effekt auf die Simulation der ENSO-Stärke in Klimamodellen. Die genannten Faktoren verursachen über 80% der ENSO-Stärke-Diversität in CMIP5-Klimamodellsimulationen.

Contents

1 Introduction 13

2 Eastern equatorial Pacific sea surface temperature annual cycle in the Kiel Climate Model: Simulation benefits from enhancing atmospheric resolution 19

3 Seasonal ENSO phase locking in the Kiel Climate Model: The importance of the equatorial cold sea surface temperature bias 87

4 What controls ENSO-amplitude diversity in climate models? 111

5 Summary and Outlook 147

Bibliography 151

Own Publications 157

Acknowledgments 159

Declaration 161

1 Introduction

1.1 General introduction

The equatorial Pacific depicts the largest annual-mean equatorial zonal sea surface temperature (SST) contrast on the globe with a difference of up to 6K. Warm waters are located in the west and cold water in the east (Fig. 1a; color shading), which are referred to as the western warm pool and the equatorial cold tongue, respectively. This structure is determined by interactions of the ocean with the atmosphere. In the annual mean, the Intertropical Convergence Zone (ITCZ) is located north of the equator (Fig. 1a; indicated by mean precipitation in contours), which drives cross-equatorial southeasterly winds over the central and eastern equatorial Pacific (Fig. 1a; arrows). The winds generate equatorial and coastal upwelling of cold subsurface water, which maintains the cross-equatorial SST gradient. The zonal SST gradient in the equatorial Pacific is associated with a zonally asymmetric atmospheric circulation (Walker circulation), which is linked to a westward transport of warm surface water and maintains the zonal SST contrast. Consequently, isotherms in the upper equatorial Pacific are tilted upward from the west towards the east with a thermocline located at approximately 200m depth in the western part and at approximately 50m near the eastern boundary (Fig. 1b). The nutrient-rich cold water in the equatorial cold tongue leads to high phytoplankton concentration and to a fishery production of crucial economic importance for parts of the South American population. The western warm pool on the other hand features the largest extent of high SSTs in the global oceans and is linked to an enormous amount of precipitation (Fig. 1a; contours) and latent heat release.

The equatorial Pacific is subject to large variability on various timescales, which locally and globally affects weather, ecosystem, agriculture and human populations (Diaz and Markgraf 2000; Hsu and Moura 2001; Alexander et al. 2002; Barsugli and Sardeshmukh 2002). The dominant modes of equatorial Pacific variability are the eastern equatorial Pacific (EEP) SST annual cycle (AC) and the interannual El Niño/Southern Oscillation (ENSO). A realistic simulation of these modes of variability in coupled general circulation models (climate models hereafter) is of fundamental importance to, for example, more accurate climate predictions on various temporal and spatial scales. The aim of this thesis is to add detailed insights on the simulation of the EEP SST AC and ENSO in climate models.

The following subsections provide an introduction to the EEP SST AC and ENSO. It should be noted that there are strong indications that these two modes of variability are linked (e.g. Liu 2002), which is, however, not the subject of this thesis.

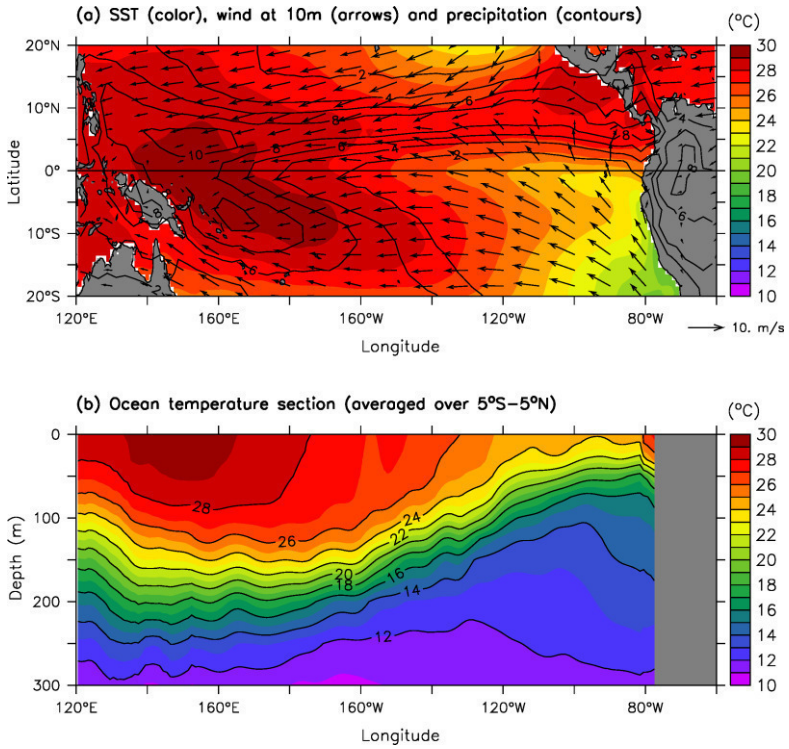

Fig. 1 Tropical Pacific long-term mean of (a) SST (color shading), precipitation (contours) and wind at 10m (black arrows) and (b) upper ocean temperature section averaged over 5°S - 5°N. For SST the HadISST 1.1 data set (Rayner et al. 2003) is used for the period 1958 – 2001, precipitation from the CMAP (Xie and Arkin 1997) for 1979 – 2014, 10m wind from CCMP V2.0 wind product (Wentz et al. 2015) for 1988 – 2014 and subsurface ocean temperature from Levitus et al. (1998) climatology. Temperature is in units of °C, precipitation in mm day^{-1} and wind in ms^{-1}.

1.2 Equatorial Pacific seasonal cycle

The equatorial Pacific features different seasonal variability patterns in the western and eastern part of the basin. Western equatorial Pacific SST varies semi-annually (Fig. 2a), following the semi-annual variation of shortwave radiation at the surface (Fig. 2d). In the EEP, SST varies annually and with much larger amplitude compared to the semi-annual cycle in the west (Fig. 2a). The EEP SST AC exhibits warm conditions during the first half and cold conditions during the second half of the calendar year, which is not determined by the equatorial semi-annual cycle of shortwave radiation as the underlying dynamics are more complex. In the review study of Xie (2005), the seasonal variation of the ITCZ is suggested as the ultimate driving factor of the EEP SST AC. The eastern part of the ITCZ is located north of the equator almost throughout the year (Xie 2005), which is because the equatorial cold tongue prevents the seasonal migration from the northern to the southern hemisphere. Annual variations in insolation drive a seasonal strengthening/weakening of the ITCZ, which determines an increase/decrease of equatorial southeasterly winds (Fig. 2b,c).

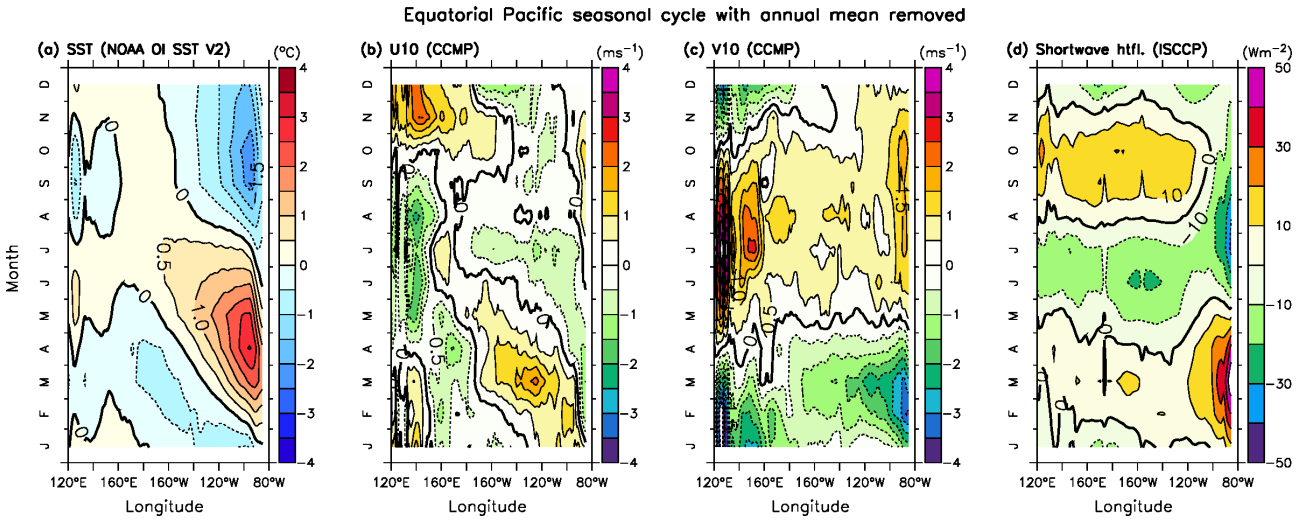

Fig. 2 Equatorial Pacific seasonal cycle with the annual mean removed of (a) SST, (b) zonal wind at 10m, (c) meridional wind at 10m and (d) shortwave radiative surface heat flux. All data is averaged over 0.5°S – 0.5°N. SST data is taken from NOAA_OI_SST_V2 (Reynolds et al. 2002) for 1981 – 2016, wind from the CCMP V2.0 product (Wentz et al. 2015) for 1988 – 2014 and shortwave heat flux from ISCCP (Rossow and Schiffer 1999) for 1984 – 2009. Temperature is in units of °C, wind in ms^{-1} and shortwave heat flux in Wm^{-2}.

This, in turn, leads to seasonal differences in evaporation and ocean upwelling at the equator. Furthermore, seasonal changes in EEP SST alter the amount of low-level clouds via modifications of atmospheric stability, which induces local changes in the shortwave radiative heat flux (Fig. 2d). These mechanisms all contribute to define the EEP SST AC.

Simulation of the eastern equatorial Pacific sea surface temperature annual cycle in climate models

A realistic simulation of the EEP SST AC in climate models can be critical for a correct simulation of climate variability on various timescales as well as for carrying out more accurate climate predictions. According to Song et al. (2014), the simulation of the EEP SST AC in climate models has improved from the Coupled Model Intercomparison Project (CMIP) phase 3 to phase 5. Nevertheless, models from CMIP5 exhibit severe errors such as a wrong timing of the seasonal onset and termination of the equatorial cold tongue by a few months. Therefore, the driving mechanisms of climate model biases in simulating the EEP SST AC and options to alleviate these biases must be identified.

The aim of the study presented in chapter 2 of this thesis is to identify driving mechanisms of climate model biases in the simulation of the EEP SST AC. A set of experiments with the Kiel Climate Model (KCM) and a subset of models from CMIP5 are investigated. The standard

model configuration of the KCM exhibits qualitatively similar biases as the CMIP5 models. Key drivers of the EEP SST AC such as winds, upper ocean dynamics and atmospheric heat fluxes are investigated. The fact that coupled ocean-atmosphere dynamics determine the EEP SST AC highly complicates the identification of sources for model biases. Therefore, both coupled and uncoupled simulations from the atmospheric model component are investigated to pin down the sources. The KCM is further used to test the potential of increased atmospheric resolution for improving the simulation of the EEP SST AC.

1.3 El Niño/Southern Oscillation

ENSO is a composite term that relates the oceanic phenomenon El Niño and the atmospheric seesaw pattern Southern Oscillation. It is the dominant interannual natural climate fluctuation and it is characterized by large SST anomalies (SSTa) primarily in the eastern and central equatorial Pacific giving rise to a basin-scale climate perturbation that has a global socioeconomic impact (Siedler et al. 2013). As an example, it was estimated that the occurrence of very large warm anomalies during 1997/1998, which were associated with ENSO, has caused 23.00 fatalities and a damage of 33 Bil. US$ worldwide (McPhaden 1999).

The warm phase of ENSO is termed El Niño, the cold phase La Niña and the events occur irregularly within the 2-7 year band. Another robust and important feature of ENSO is that El Niño and La Niña events typically peak in boreal winter, which is referred to as seasonal ENSO phase locking (e.g. Tziperman et al. 1998; Neelin et al. 2000; McGregor et al. 2012).

The different conditions during El Niño and La Niña are schematically shown in Fig. 3, the conditions referred to as “normal” are depicted in Fig. 3a. El Niño is characterized by an anomalous warming of the central and eastern equatorial Pacific (Fig. 3b), which is associated with westerly wind anomalies, an eastward shift of the western Pacific atmospheric deep-convective pattern and a reduced zonal slope of the ocean thermocline along the equator. During La Niña (Fig. 3c), central and eastern SST are anomalously low with stronger trade winds and an increased zonal thermocline slope. In this respect, Bjerknes (1969) discusses the existence of a coupled positive feedback that explains the growth of SSTa - the so-called Bjerknes feedback: An initial eastern equatorial warm sea surface anomaly induces a weakening of the wind field due to a reduced zonal SST gradient. The weakening of the wind field leads to a deepening of the thermocline in the east, which reinforces the initial warm anomaly (vice versa for La Niña). The Bjerknes feedback can explain how El Niño and La Niña reach a mature stage, but it does not provide an explanation for the

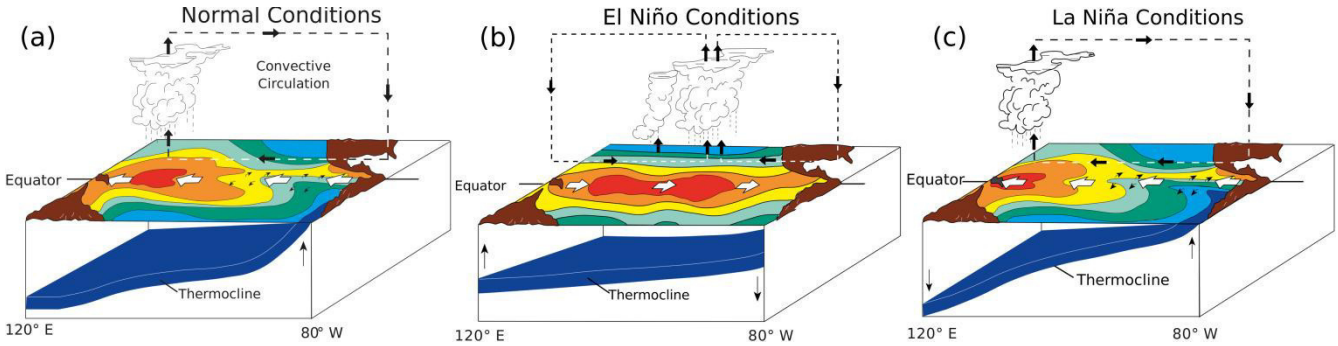

Fig. 3 Schematic of the equatorial Pacific under (a) normal conditions, (b) El Niño conditions and (c) La Niña conditions. Source: NOAA / PMEL / TAO under https://www.pmel.noaa.gov/elnino/schematic-diagrams.

transition of the two phases. In contrast to that, the conceptual recharge oscillator model (Jin 1997) offers a description of the oscillatory mode via a recharge and discharge of equatorial heat content. The oscillation is explained via the well-established Sverdrup balance between the meridional shear of zonal wind anomalies and the meridional upper-ocean mass transport. The discharge (recharge) of equatorial heat content during an El Niño (La Niña) phase eventually leads to a transition between the two phases.

A formidable challenge is to understand and predict ENSO on seasonal to multi-decadal time scales using climate models (Guilyardi et al. 2009; Wittenberg 2009; Bellenger et al. 2014). The difficulty arises from the complex interaction between ocean and atmosphere. Bellenger et al. (2014) identify large biases and great diversity in ENSO simulations among CMIP3 and CMIP5 models, introducing uncertainties in a realistic simulation of global climate variability and in predicting future climate changes.

Simulation of seasonal ENSO phase locking in climate models

Seasonal ENSO phase locking, which is the tendency of ENSO-related variability to peak in boreal winter, is poorly represented in climate models. An incorrect simulation of the peak season together with a large diversity in the simulated ENSO dynamics characterizes the models behavior (e.g. Ham et al. 2012; Bellenger et al. 2014; Ham and Kug 2014). This can have severe consequences for ENSO forecast (Jin and Kinter 2009) and for the simulation of ENSO teleconnections in climate models (e.g. Webster et al. 1998). Over the past years, progress has been made in identifying mechanisms that are responsible for an erroneous simulation of seasonal ENSO phase locking (Zheng and Yu 2007; Ham et al. 2012; Ham and Kug 2014; Rashid and Hirst 2015). However, the underlying mechanisms differ quite substantially among the models and there is only a modest amount of studies that have investigated this feature in individual climate models. Therefore, the

understanding of the controlling mechanisms of seasonal ENSO phase locking in climate models must be furthered. Advances in this regard would contribute to an improved simulation of tropical climate variability on various timescales, their teleconnections to the extratropics and to uncertainty reduction in seasonal forecasting.

The aim of the study presented in chapter 3 of this thesis is to identify the controls of seasonal ENSO phase locking in the KCM. A large ensemble of experiments generated from perturbed atmospheric physics and from the employment of different vertical atmospheric resolutions depicts a similarly large spread in the simulation of seasonal ENSO phase locking as obtained from a CMIP5 multi-model ensemble. This suggests a strong sensitivity to slightly different model configurations, which, in turn, can introduce large uncertainty in the simulation of global climate variability. A Bjerknes Stability (BJ) index analysis is employed to investigate the relevant feedbacks that control seasonal ENSO phase locking in the KCM. The final results are compared to those from models participating in CMIP5.

ENSO-amplitude diversity in climate models

A broadly discussed problematic issue is the large diversity in the strength of ENSO variability in climate models (e.g. Latif et al. 2001; Bellenger et al. 2014). This diversity in ENSO amplitude introduces uncertainties in making robust statements about long-term ENSO projections. Recent studies have presented progress in identifying controlling factors of ENSO-amplitude diversity in climate models (Kim et al. 2014; An et al. 2017). However, Kim et al. 2014 show that an analysis of the relevant feedbacks provides inconclusive results for a set of CMIP5 models. Therefore, the investigation of the controls of ENSO-amplitude diversity in climate models must be extended.

The study presented in chapter 4 of this thesis investigates ENSO-amplitude diversity in a large ensemble of models participating in CMIP5 by means of the linear recharge oscillator model (ReOsc model hereafter). The ReOsc model reduces ENSO dynamics to a two-dimensional problem in terms of eastern equatorial Pacific sea surface temperature anomalies (T) and equatorial Pacific upper ocean heat content anomalies (h). First, a proof of concept of the ReOsc model in reproducing ENSO amplitudes from the CMIP5 models is conducted. The ReOsc model is then used to identify the controlling dynamical processes of ENSO-amplitude diversity in the CMIP5 model ensemble.

2 Eastern equatorial Pacific sea surface temperature annual cycle in the Kiel Climate Model: Simulation benefits from enhancing atmospheric resolution

Citation: Wengel, C., Latif, M., Park, W., Harlaß, J., and Bayr, T. (2017): Eastern Equatorial Pacific Sea Surface Temperature Annual Cycle in the Kiel Climate Model: Simulation Benefits from Enhancing Atmospheric Resolution. Climate Dynamics, in revision.

The candidates' contributions to this publication are as follows:

1. He designed and performed the majority of the model experiments.
2. He did all the analyses.
3. He produced all the figures.
4. He authored the manuscript from the first draft to the final version.

Eastern Equatorial Pacific Sea Surface Temperature Annual Cycle in the Kiel Climate Model: Simulation Benefits from Enhancing Atmospheric Resolution

C. Wengel[1], M. Latif[1,2], W. Park[1], J. Harlaß[1], T. Bayr[1]

[1] GEOMAR Helmholtz Centre for Ocean Research Kiel

[2] University of Kiel

Email: cwengel@geomar.de

Telephone: +49 431 600-4034

Fax: +49 431 600-4052

Keywords: annual cycle, SST, equatorial Pacific, Kiel Climate Model

Abstract

A long-standing difficulty of climate models is to capture the annual cycle (AC) of eastern equatorial Pacific (EEP) sea surface temperature (SST). In this study, we first examine the EEP SST AC in a set of integrations of the coupled Kiel Climate Model (KCM) in which only atmosphere model resolution differs. When employing coarse horizontal and vertical atmospheric resolution, significant biases in the EEP SST AC are observed. These are reflected in an erroneous timing of the cold tongue's onset and termination as well as in an underestimation of the boreal spring warming amplitude. A large portion of these biases are linked to a wrong simulation of zonal surface winds, which can be traced back to precipitation biases on both sides of the equator and an erroneous low-level atmospheric circulation over land. Part of the SST biases also is related to shortwave radiation biases related to cloud cover biases. Both wind and cloud cover biases are inherent to the atmospheric component, as shown by companion uncoupled atmosphere model integrations forced by observed SSTs. Enhancing atmosphere model resolution, horizontal and vertical, markedly reduces zonal wind and cloud cover biases in coupled as well as uncoupled mode

and generally improves simulation of the EEP SST AC. Enhanced atmospheric resolution reduces convection biases and improves simulation of surface winds over land. Analysis of a subset of models from the Coupled Model Intercomparison Project phase 5 (CMIP5) reveals that in these models, very similar mechanisms are at work in driving EEP SST AC biases.

1. Introduction

Sea surface temperature (SST) in the eastern equatorial Pacific (EEP) depicts a pronounced annual cycle (AC) with warmest temperatures in March – April and coldest in August – October (Mitchell and Wallace 1992). The amplitude of the EEP SST AC is relatively large (up to 5°C in localized regions) despite relatively little seasonal change in insolation (Xie 2005). This contrasts to subtropical SST at 20° N that varies seasonally only half as much in spite of much larger annual variation in insolation. The reason for this peculiarity can be traced back to the zonal and meridional asymmetries in the tropical Pacific climatology (Xie 2005). That is a zonal SST gradient along the equator and a cross-equatorial SST gradient in the eastern equatorial regime due to the inter-tropical convergence zone (ITCZ) located to the north of the equator and cold water south of it. These asymmetries are maintained by ocean-atmosphere interaction associated with southeasterly winds across the equator, driving ocean upwelling and evaporative cooling, and by formation of stratus-clouds over cold waters (Philander et al. 1996; Xie 2005). The associated physical processes are termed upwelling-SST feedback, wind-evaporation-SST (WES) feedback and stratus cloud-SST feedback, respectively (Yu and Mechoso 1999a; Xie 2005). The strength of the ITCZ varies with the seasonal variation of insolation, but the ITCZ is located north of the equator almost throughout the year. Consequently, the strength of southeasterly winds varies seasonally, which drives seasonal variations in ocean upwelling and evaporation at the equator. Furthermore, the seasonal variation of SST alters the amount of low-level clouds via modifications of atmospheric stability. These mechanisms all contribute to define the EEP SST AC with its cold phase during August-September and warm phase during March-April (for a review see Xie 2005). An important feature of the warm phase is the westward propagation of the warming signal, which is attributed to the interaction of the SST with the zonal wind (Mitchell and Wallace 1992; Xie 2005) and can be understood within the SST mode concept (Neelin 1991).

The realistic simulation of the EEP SST AC in climate models, i.e. coupled general circulation models (CGCMs), still presents a great challenge (Mechoso et al. 1995; Covey et al. 2000; Latif et al. 2001; Xie et al. 2007; Song et al. 2014). For example, several models participating in the Coupled Model Intercomparison Project phase 3 (CMIP3) simulate a semiannual cycle (de Szoeke and Xie 2008). Improvement has been achieved towards CMIP5. Song et al. (2014) find 14 out of a set of 18 models are able to simulate a reasonable EEP SST AC. The multi-model mean captures the annual signal with a correlation coefficient of approximately 0.9 as well as the westward propagation of the warming signal. However, a large warm SST bias in boreal fall is still present in nearly all models, which the authors link to a poor representation of surface winds.

Yu and Mechoso (1999b) show that a CGCM can realistically simulate the EEP SST AC despite errors in the surface latent heat fluxes, suggesting that these heat fluxes play a secondary role. The Monsoonal circulation, on the other hand, is suggested to be an important driver of the EEP SST AC.

Chen and Jin (2017) diagnose too weak mean cross-equatorial winds as an important reason why the EEP SST AC is too weak in many CMIP5 models. In a dynamic diagnostics framework, they further attribute the large diversity in the simulations of the EEP SST AC to the spread in the internal dynamics as measured by the damping rate of the SST AC and phase speed of westward propagation. Another important source of uncertainty is the solar forcing at the surface, which is influenced by biases in the representation of stratus clouds in the EEP.

Due to the complex interactions between dynamics and physics in setting up the EEP SST AC, its simulation is a welcome test for CGCMs. Moreover, the EEP SST AC impacts tropical Pacific sector climate variability (e.g. El Niño/Southern Oscillation (ENSO), Stein et al. 2011) and predictability (Latif and Graham 1992). Here we investigate the role of the atmospheric resolution, horizontal and vertical, in determining the quality of simulating the EEP SST AC in the Kiel Climate Model (KCM) and a number of CMIP5 models. It has been shown in previous work that

enhanced atmospheric resolution strongly reduces tropical mean-state biases in the KCM. For example, enhancing atmospheric resolution improves the simulation of the surface zonal wind in the western equatorial Atlantic, which also improves eastern tropical Atlantic SST simulation via remote effects. Further, the better representation of the local coastline in the eastern tropical Atlantic improves the simulation of alongshore winds and hence local upwelling dynamics. These improvements also have a beneficial effect on the simulation of interannual SST variability in the eastern equatorial Atlantic (Harlaß et al. 2015, Harlaß et al. 2017).

This paper is structured as follows. Section 2 introduces the KCM and the experiments, the observational data used for model verification as well as the CMIP5 model data. Section 3 describes the performance of the KCM in simulating the EEP SST AC at different atmosphere model resolutions. In Section 4, we investigate a subset of CMIP5 models. Conclusions and discussion of the main findings are provided in Section 5.

2. Coupled models, observational data and methods

We analyze a series of simulations with the Kiel Climate Model (KCM, Park et al. 2009). The KCM consists of the atmospheric general circulation model (AGCM) ECHAM5 (Roeckner et al. 2003), which is coupled to the Nucleus for European Modeling of the Ocean (NEMO; Madec et al. 1998) ocean-sea ice general circulation model via the Ocean Atmosphere Sea Ice Soil version 3 (OASIS3; Valcke 2006) coupler.

A set of "present-day" control integrations of the KCM employing constant atmospheric CO_2-concentration of 348 ppm, each 100-years-long, is investigated. We skip the first 20 years of each simulation in the analyses. The horizontal ocean model resolution is identical in all experiments, based on a 2° Mercator mesh (ORCA2 grid), on average 1.3° with increased meridional resolution of 0.5° near the equator and 31 vertical levels. We conducted 6 experiments, which only differ in atmospheric horizontal and vertical resolution (Table 1). In the horizontal, we use spectral

Table 1 List of the KCM experiments, which differ in horizontal and vertical atmospheric resolution.

KCM experiment label	Atmospheric resolution	
	Horizontal resolution	Number of vertical levels
1	T42 (~ 2.8°)	19
2	T42 (~ 2.8°)	31
3	T42 (~ 2.8°)	62
4	T159 (~ 0.75°)	31
5	T159 (~ 0.75°)	62
6	T255 (~ 0.47°)	62

resolutions of T42 (~2.8°), T159 (~0.75) and T255 (~0.47°) and in the vertical 19, 31 and 62 levels with the top level at 10 hPa in all cases. The additional levels are placed in between the original levels, which effectively provides a higher amount of vertical levels in the lower atmosphere. This is the dynamical relevant part for the EEP SST AC, as discussed above, whereas vertical resolution in the upper atmosphere is expected to only have a minor influence. We note that no re-tuning of the coupled model was performed when changing the atmospheric resolution. Additionally, we performed six 30-yr long standalone experiments with the atmospheric component of the KCM, the ECHAM5 AGCM, forced by monthly climatological observed SSTs and sea ice concentrations using a combined data set consisting of GISST 2.2a (UKMO) and OISST (NCEP) for SST and ECMWF and NCEP for sea-ice concentration (Taylor et al. 2000; see below). The uncoupled experiments allow us to investigate whether errors in atmospheric circulation observed in the coupled model versions are inherent to the AGCM or due to coupling.

Data from a subset of CMIP5 models (Table 2) is additionally used. Historical simulations (1850 – 2005) with observed external forcing are taken from 12 CMIP5 models (Taylor et al. 2012)

Table 2 List of the CMIP5 models used in the analysis.

Label number	Modeling Group	CMIP5 ID	Atmosphere (1) Horizontal grid (longitude x latitude) (2) Number of vertical levels	Ocean (1) Horizontal res. (2) Number of vertical levels	Time period (year
1	CSIRO-BOM	ACCESS1.0	(1) 192 × 145 N96 (1.875°x1.25°) (2) 38	(1) 1° latitude/longitude tripolar with enhanced resolution near the equator and at high latitudes (2) 50	156
2	CSIRO-BOM	ACCESS1.3	(1) 192 x 145 N96 (1.875°x1.25°) (2) 38	(1) 1° latitude/longitude tripolar with enhanced resolution near the equator and at high latitudes (2) 50	156
3	BCC	bcc-csm1-1	(1) T42 (2.8°x2.8°) (2) 26	(1) 1° with enhanced resolution in the meridional direction in the tropics (1/3° meridional resolution at the equator) tripolar (2) 40	156
4	CMCC	CMCC-CM	(1) T159 (0.75°x0.75°) (2) 31	(1) 2° average, 0.5° at the equator (ORCA2) (2) 31	156
5	CNRM-CERFACS	CNRM-CM5	(1) TL127 (1.4°x1.4°) (2) 31	(1) 0.7° on average ORCA1 (2) 42	156
6	NOAA GFDL	GFDL-CM3	(1) ~200 km C48L48 (2.5°x2.0°)	(1) 1° tripolar 360 × 200 (2) 50	146

			(2) 48		
7	NASA GISS	GISS-E2-R	(1) 2° latitude × 2.5° longitude F (2.5°x2.0°) (2) 40	(1) 1° latitude × 1.25° longitude Russell 1 × 1Q (2) 32	156
8	IPSL	IPSL-CM5A-LR	(1) LMDZ 96 × 95 (3.75°x1.9°) (2) 39	(1) 2 × 2-0.5° ORCA2 (2) 31	156
9	IPSL	IPSL-CM5A-MR	(1) LMDZ 144 × 143 (2.5°x1.25°) (2) 39	(1) 2 × 2-0.5° ORCA2 (2) 31	156
10	MIROC	MIROC5	(1) T85 (1.4°x1.4°) (2) 40	(1) 1.4° (zonally) × 0.5–1.4° (meridionally) (2) 50	156
11	MRI	MRI-CGCM3	(1) 320 × 160 TL159 (1.125°x1.125°) (2) 48	(1) 1 × 0.5 (2) 50 + 1 Bottom Boundary Layer	156
12	NCC	NorESM1-M	(1) Finite Volume (2.5°x1.9°) (2) 26	(1) 1.125° along the equator (2) 53	156

and interpolated to a 2.5° x 2.5° regular grid. Due to technical reasons the subset had to be limited to 12 representative models. We also investigate the standalone integrations with the corresponding AGCMs, obtained from the Atmospheric Model Intercomparison Project (AMIP).

For model comparison, SST provided for the time period 1981 – 2016 from National Oceanic and Atmospheric Administration Optimum Interpolation SST version 2 (NOAA_OI_SST_V2; Reynolds et al. 2002, http://www.esrl.noaa.gov/psd/*)* is used. Furthermore, we use zonal and

meridional winds at 10 m height for 1988 – 2014 from the Cross-Calibrated Multi-Platform (CCMP) V2.0 wind product (Wentz et al. 2015). The CCMP dataset combines cross-calibrated satellite microwave winds and instrumental observations to produce high resolution (0.25°) gridded analyses. Atmospheric heat fluxes for 1984–2009 are from the Objectively Analyzed air–sea heat Fluxes (OAFlux) dataset (Yu and Weller 2007). Output from the Simple Ocean Data Assimilation (SODA) ocean reanalysis product version 2.0.2 (Carton and Giese 2008) for the period 1958-2001 is used for ocean temperatures and velocities. Precipitation for the period 1979–2014 is from CMAP (Xie and Arkin 1997) and the vertical distribution of winds for 1982–2009 on a 0.75° grid from ECMWF Re-Analysis (ERA-interim, Dee et al. 2011).

Zonal sections along the equator are calculated as averages from 2.8°S to 2.8°N, accounting for the coarsest horizontal atmosphere model resolution (T42) used here and the lack of a grid point directly at the equator in ECHAM5. Monthly deviations from the long-term annual mean are considered.

3. SST annual cycle in the KCM

The EEP SST AC simulated by the KCM at the different atmospheric resolutions is compared to observations in Fig. 1. Relative to the KCM version using the coarsest atmospheric resolution (T42L19), the obvious changes in SST when employing higher atmospheric resolution are statistically significant at the 95% level (t-test). All 6 simulations feature a warming during the first half and a cooling during the second half of the calendar year. Several biases are noticed. First, the magnitude of the boreal spring warming is underestimated by approximately 1° C in all simulations. Second, the equatorial cold tongue appears 1 – 2 months earlier in comparison to observations and third, the cold tongue disappears too early in the calendar year by up to 3 months, especially in the KCM versions with coarse atmospheric resolution. For example, the simulation with the lowest atmospheric resolution (T42L19; Fig. 1b) depicts positive SST anomalies in the very east that

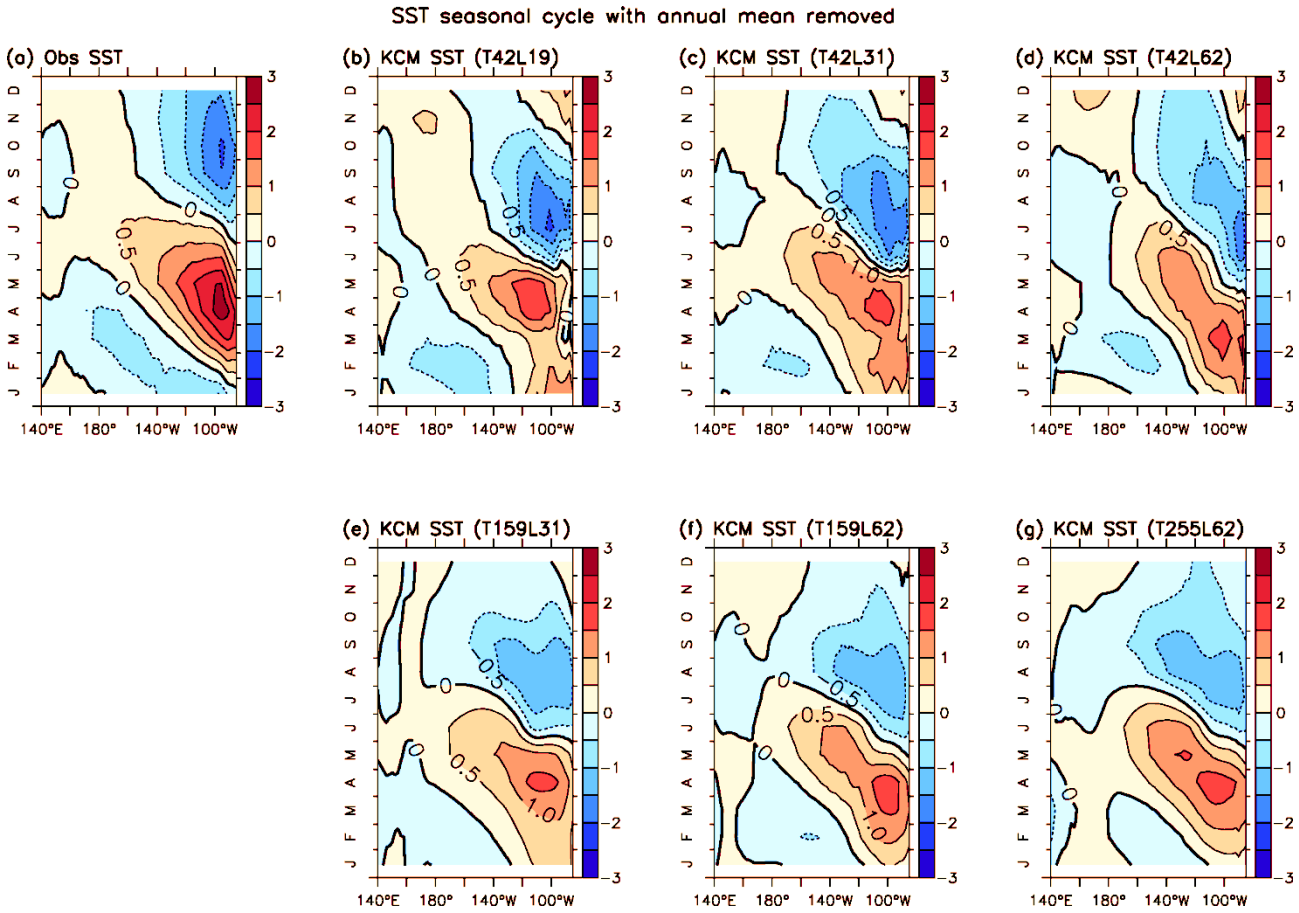

Fig. 1 Seasonal cycle of equatorial Pacific SST (°C) with the annual mean removed for (a) observations and (b) – (g) the Kiel Climate Model (KCM) with different atmospheric resolutions. All data are averaged over 2.8°S – 2.8°N.

already develop in October, whereas in the observations, positive SST anomalies in the east do not appear before January. The erroneous warm anomaly in boreal fall disappears at the highest atmospheric resolution, however, the negative SST anomaly in the east is still too small (T255L62; Fig. 1g).

We next study the processes determining the EEP SST AC in the KCM and investigate the origin of the model biases, which also are observed in other CGCMs (Song et al. 2014, see below). Figure 2 shows the bias in the SST AC along the equator. All KCM simulations depict a cold bias peaking in early boreal summer of the order of 2°C to 3°C, and a warm bias peaking in boreal fall of the order of 1.5°C to 2.5°C. The simulations employing lower atmospheric resolution (Fig. 2a,b) exhibit a second peak in the cold SST bias in boreal spring. The cold bias reflects the weaker seasonal

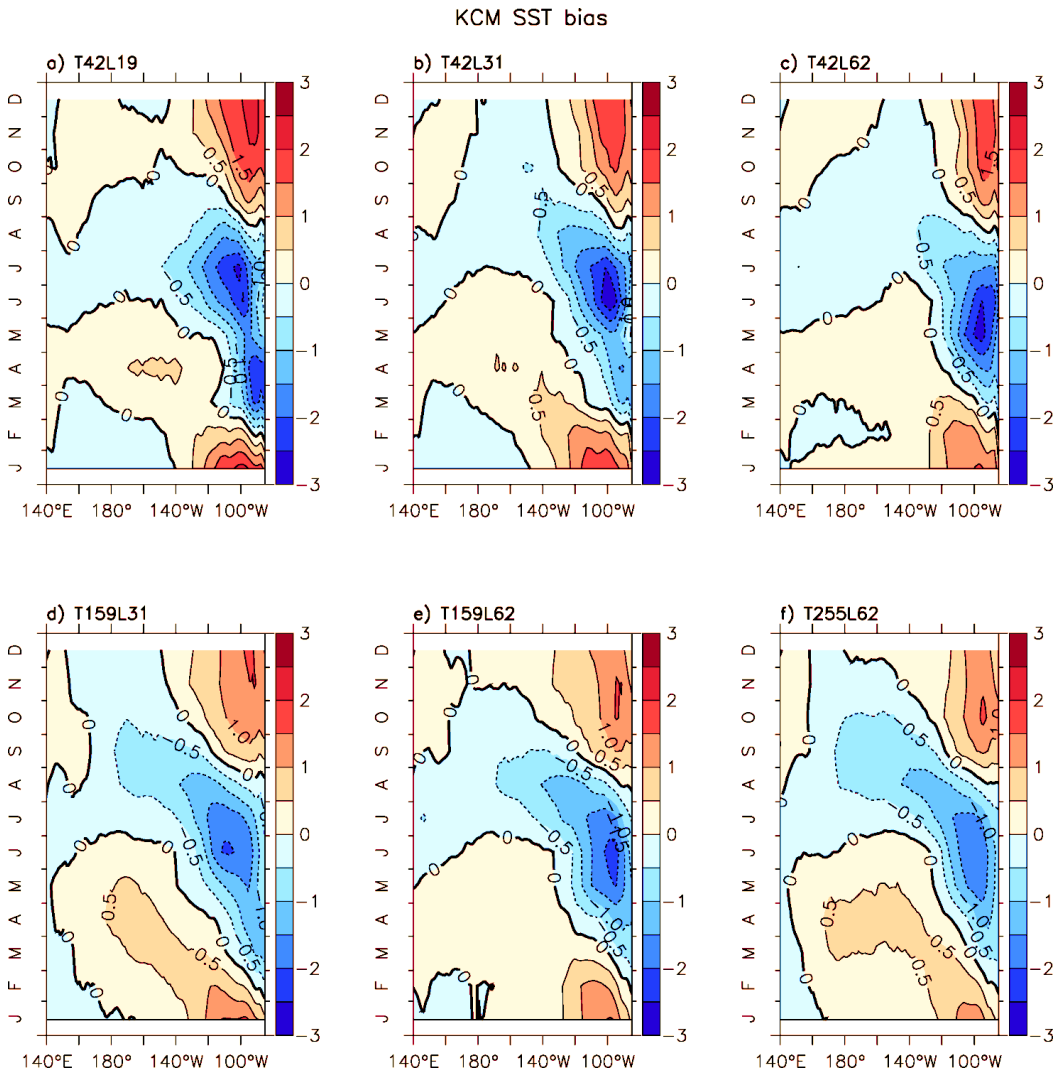

Fig. 2 Seasonal cycle of SST bias in the equatorial Pacific. The bias is calculated by subtracting observed monthly anomalies from KCM monthly anomalies. Anomalies are defined with respect to the annual mean. All data are averaged over 2.8°S – 2.8°N. SST bias is in units °C.

warming in boreal spring together with an earlier onset of the equatorial cold tongue in boreal summer (Fig. 1). The warm bias reflects the too early disappearance of the equatorial cold tongue, as discussed above. We note that the magnitude of the SST biases become smaller when atmospheric resolution is increased but remain significant even at the highest atmospheric resolution.

The analyses focus on the KCM versions with the lowest (T42L19) and highest atmospheric resolution (T255L62). Analyses from the simulations employing all atmospheric resolutions are

shown in Fig. S1 – Fig. S24. According to Yu et al. (2013) the three major driving mechanisms of the EEP SST AC are: the wind-evaporation-SST (WES) feedback, the upwelling-SST feedback and the stratus cloud-SST feedback. Figure 3 depicts equatorial near-surface (10m) zonal and meridional wind and net surface heat flux biases (color shading) together with the SST biases (contours). First, we study the role of the near-surface zonal winds in biasing the EEP SST AC. The seasonal strengthening (weakening) of the trade winds, i.e. strengthening (weakening) easterlies at the equator, forces equatorial SST to fall (rise) by increased (decreased) upwelling of cold water. In Fig. 3a and Fig. 3d, equatorial near-surface zonal wind biases (color shading) are compared to equatorial SST biases (contours). In boreal fall, the KCM version with coarse atmospheric resolution exhibits a westerly wind bias (positive values) of up to 1.5 ms^{-1} in the vicinity of the EEP warm SST bias and a westerly zonal wind bias over the western equatorial Pacific (Fig. 3a). The latter could potentially contribute to the warm SST bias in the EEP via downwelling equatorial Kelvin waves. The response timescale of SST to remote zonal wind forcing can be explained by intraseasonal equatorial Kelvin waves of the 2^{nd} baroclinic mode, which propagate eastward at a speed of about 2.4 ms^{-1} (Kessler et al. 1995) corresponding to a travel time of 1-2 months along the equator. A coupled feedback between the zonal wind and SST potentially enhances the biases. The westerly zonal wind bias in the EEP during boreal fall substantially reduces at higher atmospheric resolution in the very east (Fig. 3d) whereas near 120°W, the magnitude of the zonal wind bias is basically unchanged. Furthermore, the high atmospheric resolution version does not feature a westerly zonal wind bias in the western equatorial Pacific during boreal fall, but instead an easterly zonal wind bias with smaller magnitude. We therefore argue that on the one hand, enhancing the atmospheric resolution reduces the warm SST bias in the EEP in boreal fall due to locally reduced westerly wind biases and also potentially due to smaller zonal wind biases over the western equatorial Pacific. The remaining SST bias in the KCM version employing high atmospheric resolution (Fig. 3d) may be due to the zonal wind bias near 120°W.

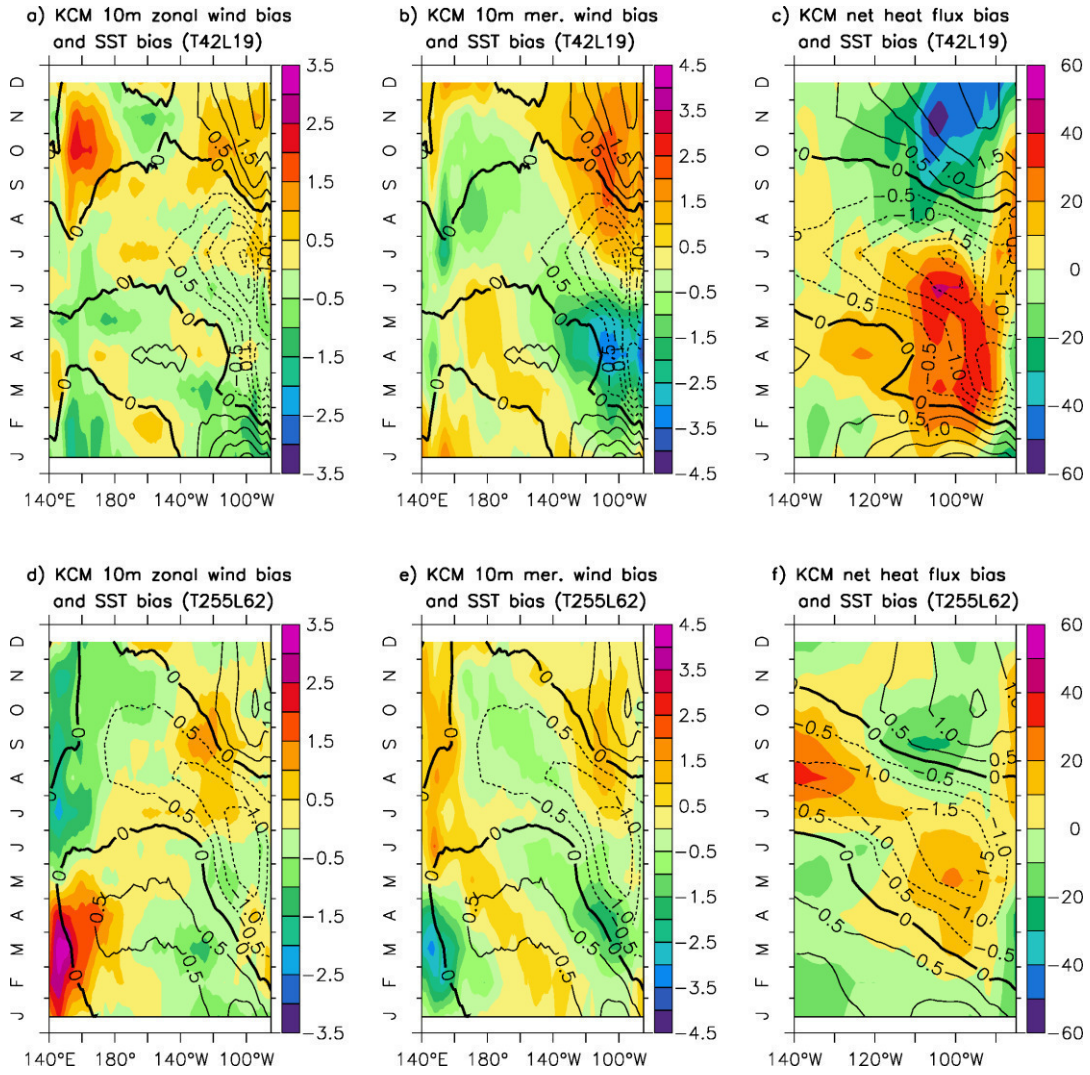

Fig. 3 Seasonal cycle of SST bias (superimposed contours) with (a) and (d) zonal (10 m) wind bias, (b) and (e) meridional (10 m) wind bias in the equatorial Pacific and (c) and (f) net surface heat flux bias in the EEP (color shading) of the KCM for (a) – (c) coarse and (d) – (f) high atmospheric resolution. The bias is calculated by subtracting observed monthly anomalies from KCM monthly anomalies. Anomalies are defined with respect to the annual mean. All data are averaged over 2.8°S – 2.8°N. SST bias is in units °C, wind in ms^{-1} and net heat fluxes in Wm^{-2}.

In boreal winter and spring, the KCM predominantly simulates easterly wind biases (negative values) in the central and eastern equatorial Pacific at coarse and high atmospheric resolution, which favors enhanced equatorial upwelling and thus would support a cold SST bias. At low atmospheric resolution (Fig. 3a), the western equatorial Pacific features easterly zonal wind biases in boreal winter, which potentially enhances the cold SST bias a couple of months later in the east

via equatorial Kelvin waves. When increasing the atmospheric resolution, the easterly wind bias in the east in boreal winter and spring is considerably reduced and partly replaced by a small westerly wind bias (Fig. 3d). Furthermore, the KCM version with high atmospheric resolution features a distinct westerly zonal wind bias in the far western equatorial Pacific during boreal winter and spring, which is not observed at low atmospheric resolution (Fig. 3a). This rather strong westerly zonal wind bias may additionally contribute to the reduction of the EEP cold SST bias via downwelling equatorial Kelvin waves. We conclude that in the KCM, biases in the near-surface zonal winds are an important factor driving biases in the EEP SST AC.

The near-surface (10 m) meridional wind biases are compared to the SST biases in Fig. 3b and Fig. 3e for the KCM versions with coarse and high atmospheric resolution, respectively. Both model versions exhibit a northerly wind bias (green-blue color shading) after the development of the warm SST bias (positive values) in boreal winter and spring and a southerly wind bias (yellow-orange color shading) after the development of the cold bias (negative values) in boreal summer and fall. The meridional wind biases, however, are much smaller in the KCM version with high atmospheric resolution in comparison the version with coarse atmospheric resolution, which is due to much better representation of the ITCZ (see below). We suggest that the meridional wind biases are a response to rather than a driver of the SST biases in the EEP, as the meridional wind biases lag the SST biases and the SST impacts the meridional SST gradient and the position of the ITCZ. Coupled feedbacks probably further enhance the biases. This conjecture is supported by the horizontal patterns of the near-surface wind biases in the tropical Pacific sector (see below). Furthermore, conditions off the equator (Fig. S3) suggest a rather instantaneous meridional-wind response to changes in the meridional SST gradient, which appears as a lagged equatorial wind response to SST change.

Next, net surface heat flux biases in the EEP are compared to SST biases at coarse (Fig. 3c) and high (Fig. 3f) atmospheric resolution. We note that these biases only are shown for the region east

of 140° W, as are the biases shown in Fig. 4. Positive heat fluxes imply ocean warming and vice versa. The largest heat flux biases with values of up to 60 Wm^{-2} are seen in the KCM version employing coarse atmospheric resolution (Fig. 3c). They decrease to about 30 Wm^{-2} at high atmospheric resolution (Fig. 3f). The heat flux and SST biases are out of phase, with positive heat flux bias over cold SST bias and vice versa, and regions of large SST bias also are regions of large heat flux bias. This suggests that the net surface heat flux damps the SST biases rather than is a source of the SST biases. We conclude that the net surface heat flux cannot explain the biases in the EEP SST AC in the KCM.

In contrast to the net surface heat flux, the shortwave radiation bias partly shows positive values over warm SST bias and vice versa (Fig. 4a,c), despite noting that the large values near the coast are less reliable in the satellite data. A flawed representation of stratus clouds in the eastern part of the tropical oceans, leading to shortwave radiation biases, is a common problem in CGCMs (Giese and Carton 1994; Stockdale et al. 1994; Ma et al. 1996). Although the shortwave radiation bias does not dominate the net surface heat flux bias over most regions (Fig. 3c,e), shortwave radiation can potentially influence the SST via an oceanic bridge. Solar radiation is allowed in climate models to penetrate through the sea surface into lower ocean layers, which can cause subsurface temperature biases and in turn SST biases mostly via vertical mixing processes. Ocean mixing in the EEP as quantified by turbulent heat fluxes in the upper 60 m is largest in boreal summer and found to be important in maintaining the annual cycle of the cold tongue (Moum et al. 2013).

Cloud cover and shortwave radiation biases are compared with the SST biases (Fig. 4). We note the following findings: first, apart from the less reliable coastal signal in the satellite data, there are large shortwave radiation biases in both KCM versions (Fig. 4a,c), typically amounting to up to 40 Wm^{-2} in limited regions. Second, at coarse atmospheric resolution a radiation surplus dominates in the region west of 90°W during the first half of the calendar year and a radiation deficit during the second half (Fig. 4a). Particularly noteworthy is the coincidence of the radiation deficit with the

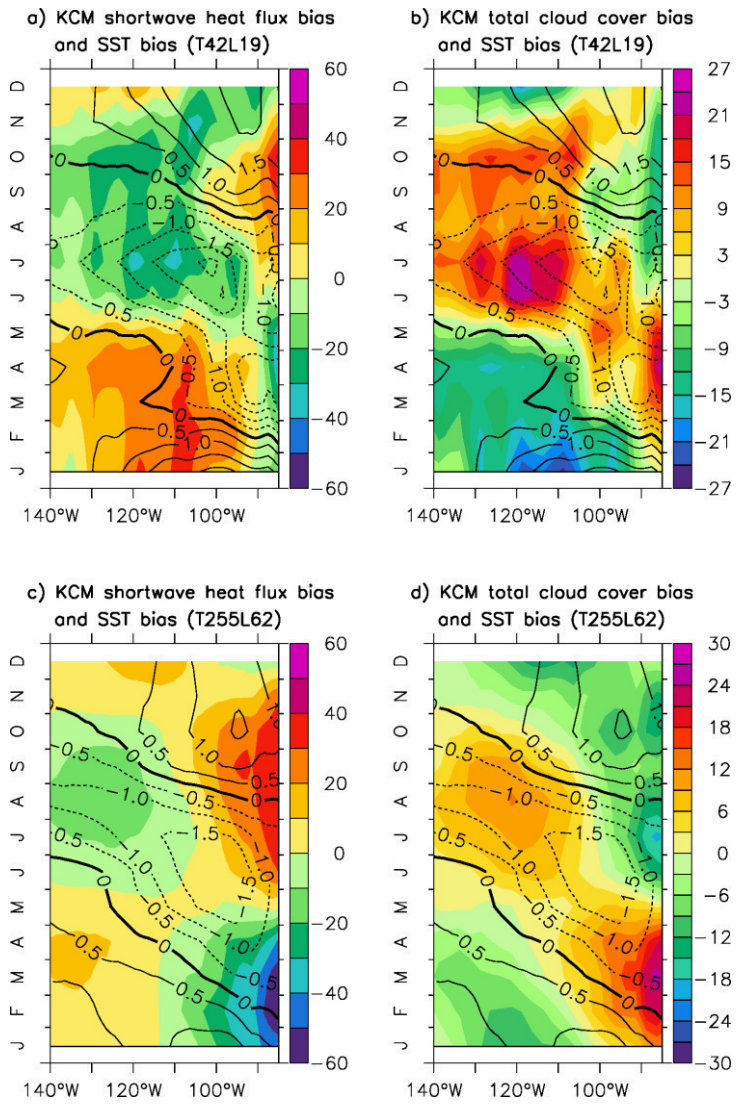

Fig. 4 Seasonal cycle of SST bias (superimposed contours) with (a) and (c) shortwave heat flux bias and (b) and (d) total cloud cover bias in the EEP (color shading) of the KCM for (a) – (b) coarse and (c) – (d) high atmospheric resolution. The bias is calculated by subtracting observed monthly anomalies from KCM monthly anomalies. Anomalies are defined with respect to the annual mean. All data are averaged over 2.8°S – 2.8°N. SST bias is in units °C, shortwave heat fluxes in Wm^{-2} and cloud cover in %.

cold SST bias maximum in boreal summer (Fig. 4a). These biases are considerably alleviated at high atmospheric resolution (Fig. 4c). Third, the shortwave radiation biases are clearly linked to cloud cover biases in both model versions (Fig. 4b,d). We therefore argue that shortwave radiation biases due to cloud cover biases could be partly responsible for the SST biases, especially during boreal summer when zonal wind biases do not provide a consistent explanation (see above).

In Fig. 5, we investigate the subsurface temperature biases in the EEP averaged over 2.8°S – 2.8°N. We note the small deviations in magnitude between the SST biases shown in Fig. 5 and those in the previous figures, which is a consequence of using SODA instead of NOAA_OI_SST_V2. In both model versions, maximum temperature biases are located in the very east and below the surface. In boreal spring (MAM), early summer (MJJ) and fall (SON), temperature biases are reduced near the sea surface when employing high atmospheric resolution (Fig. 5d – f). Interestingly, temperature biases are not reduced below 30 m in MAM and SON (Fig. 5d,f) whereas in MJJ, the bias also is reduced at deeper levels (Fig. 5e). This supports the hypothesis that in boreal summer, a shortwave radiation deficit is important in driving the large cold subsurface temperature bias at coarse atmospheric resolution, which is considerably reduced due to a smaller shortwave radiation bias at higher atmospheric resolution (Fig. 4a,c).

We also investigate EEP subsurface ocean velocity biases during MAM, MJJ and SON (Fig. 6 and Fig. 7). Both model versions show westward velocity biases in MAM (Fig. 6a,d) and to a lesser extent in MJJ (Fig. 6b,e) whereas in SON, an eastward velocity bias dominates in the EEP. This is consistent with easterly wind biases prevailing in MAM and to a lesser extent in MJJ, and with a westerly wind bias prevailing in SON (Fig. 3a,d). Zonal velocity biases are generally reduced at higher atmospheric resolution, especially near the sea surface (Fig. 6d – f). We note that biases become larger near 100 m depth.

Vertical ocean velocity biases are quite noisy but nevertheless yield spatially coherent structures in the region east of 110°W (Fig. 7). Here, both model versions exhibit an upwelling bias (positive values) in MAM (Fig. 7a,d) and to a lesser extent in MJJ (Fig. 7b,e) while in SON, a downwelling bias is observed (Fig. 7c,f). The vertical velocity biases are reduced at high atmospheric resolution, especially during MAM and SON (Fig. 7d,f). This supports our hypothesis that zonal wind biases (Fig. 3a,d) drive upwelling/downwelling biases in these two seasons. We further note that meridional currents do not provide any conclusive evidence for driving SST biases (not shown).

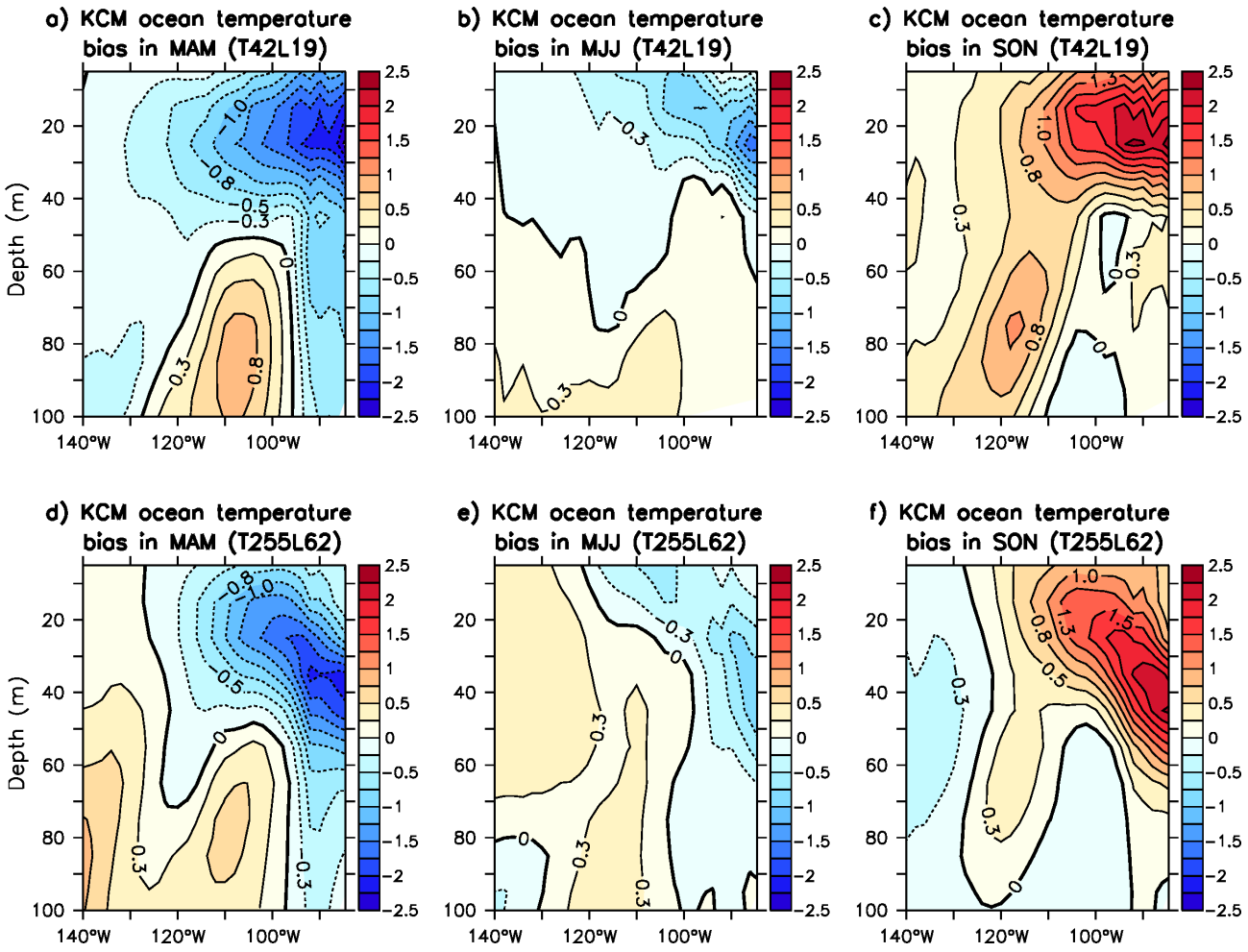

Fig. 5 Seasonal average of subsurface ocean temperature bias in the EEP during the months (a) and (d) MAM, (b) and (e) MJJ and (c) and (f) SON of the KCM for (a) - (c) coarse and (d) and (f) high atmospheric resolution. The bias is calculated by subtracting observed seasonally-averaged monthly anomalies from KCM seasonally-averaged monthly anomalies. Anomalies are defined with respect to the annual mean. All data are averaged over 2.8°S – 2.8°N. Temperature bias is in units °C.

We depict in Fig. 8 horizontal maps of near-surface wind and precipitation biases in MAM and SON. The aforementioned easterly wind bias at the equator in the east during MAM is clearly visible in both model versions (arrows and dashed contours in Fig. 8a,c) and can be related to the double-ITCZ problem (Mechoso et al. 1995; Lin 2007; de Szoeke et al. 2008), which is marked by excessive precipitation south of the equator (color shading). Further, the westerly wind bias in the east during SON can be linked in both KCM versions to an excess of precipitation north of the

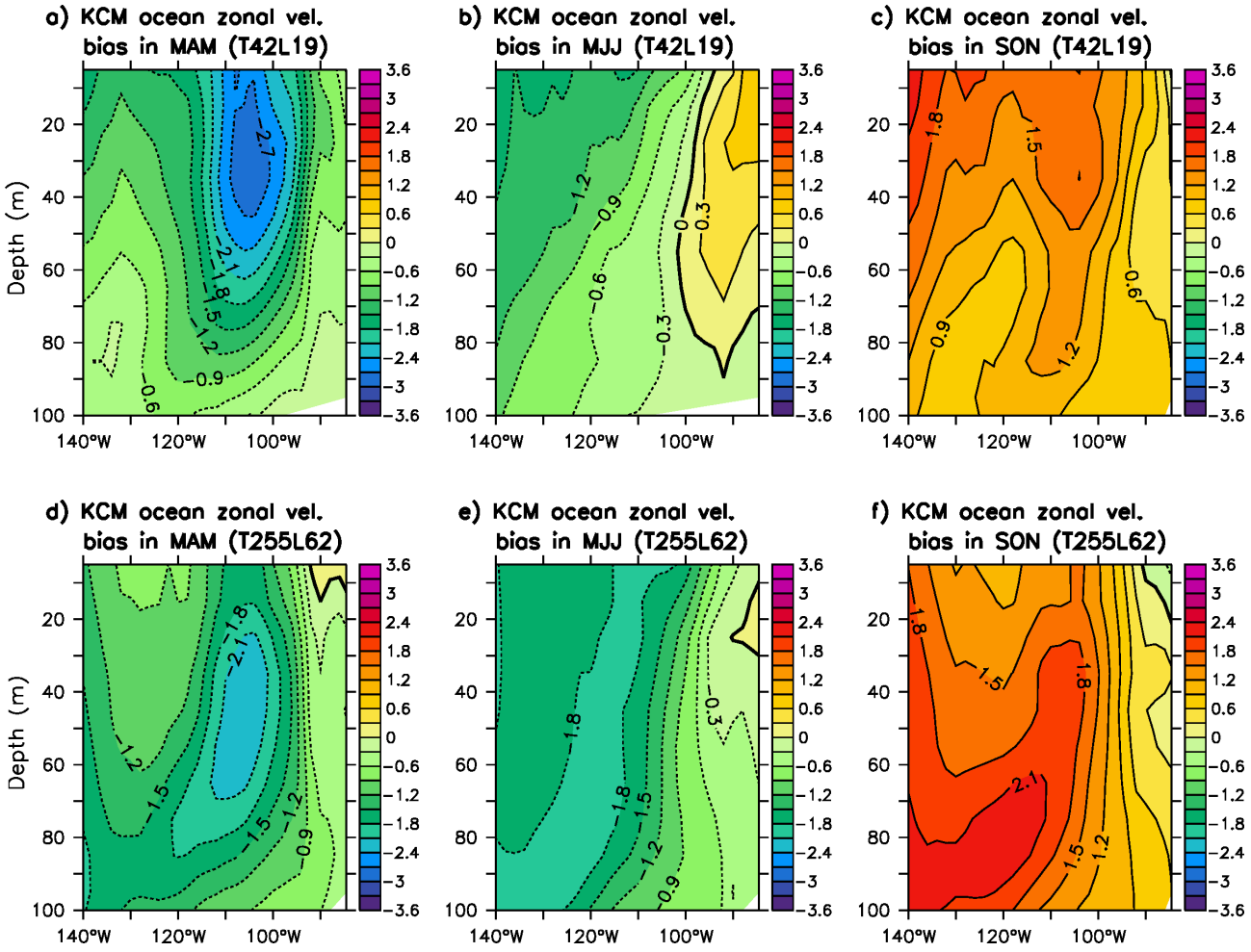

Fig. 6 Seasonal average of subsurface ocean zonal velocity bias in the EEP during the months (a) and (d) MAM, (b) and (e) MJJ and (c) and (f) SON of the KCM for (a) - (c) coarse and (d) and (f) high atmospheric resolution. The bias is calculated by subtracting observed seasonally-averaged monthly anomalies from KCM seasonally-averaged monthly anomalies. Anomalies are defined with respect to the annual mean. All data are averaged over 2.8°S – 2.8°N. Velocity bias is in units dm s^{-1}.

equator and to a too strong land-sea flow (Fig. 8b,d). Surface wind and precipitation biases in both MAM and SON are considerably reduced when atmospheric resolution is increased (Fig. 8c,d).

We next investigate the latitude-height structure of the wind biases in the eastern tropical Pacific and compare it with the precipitation biases (Fig. 9). In MAM, both model versions overestimate precipitation south and underestimate it north of the equator (Fig. 9a,c; black line), which is very pronounced in the version employing coarse atmospheric resolution (Fig. 9a). The

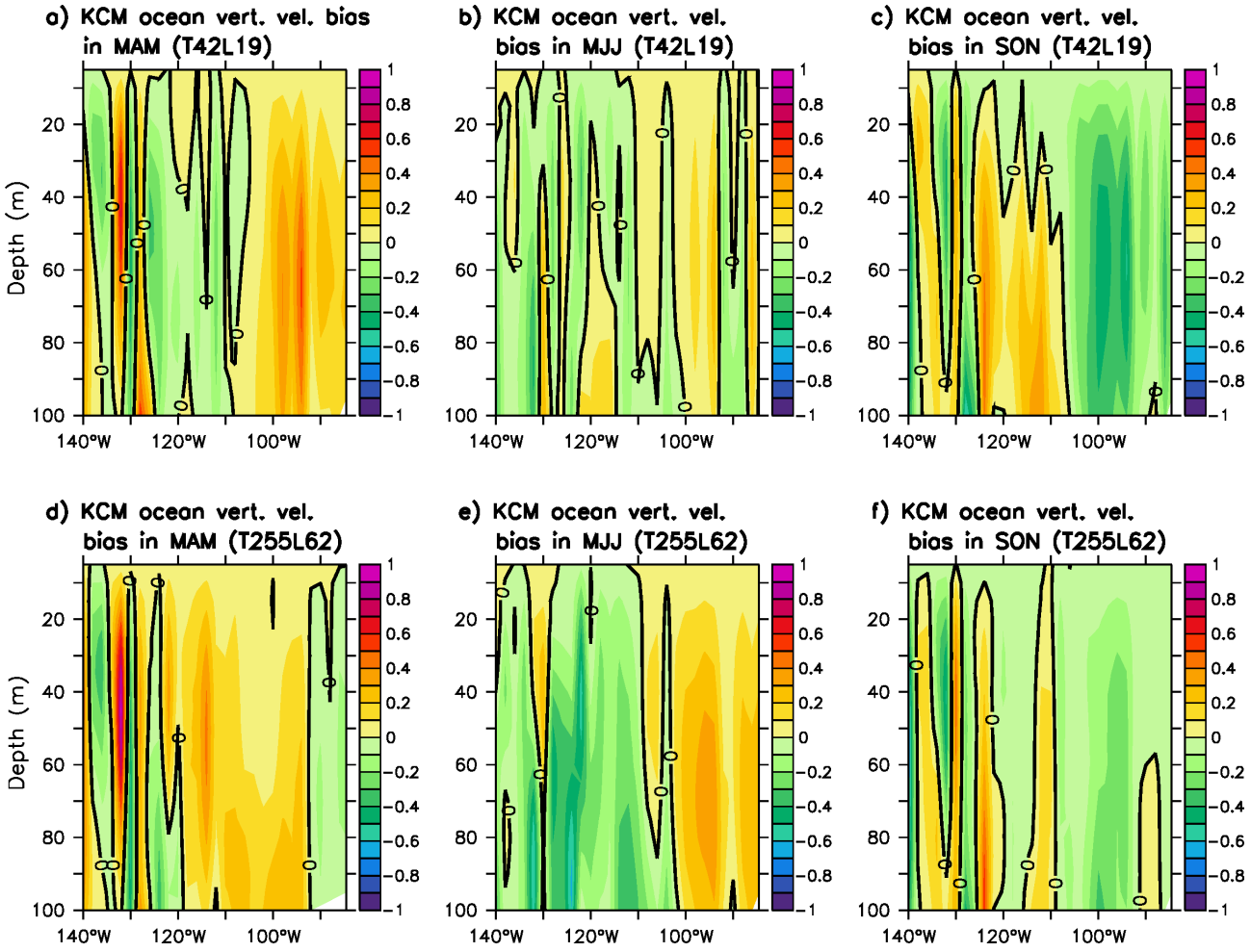

Fig. 7 Seasonal average of subsurface ocean vertical velocity bias in the EEP during the months (a) and (d) MAM, (b) and (e) MJJ and (c) and (f) SON of the KCM for (a) - (c) coarse and (d) and (f) high atmospheric resolution. The bias is calculated by subtracting observed seasonally-averaged monthly anomalies from KCM seasonally-averaged monthly anomalies. Anomalies are defined with respect to the annual mean. All data are averaged over 2.8°S – 2.8°N. Velocity bias is in units m day^{-1}.

precipitation bias south of the equator is associated with the double-ITCZ problem (Fig. 8a,c). Further, convection is overestimated south of the equator, which leads to too strong cross-equatorial surface winds (arrows) and to an easterly wind bias at the equator (green color shading). Furthermore, both KCM versions overestimate precipitation and convection north of the equator during SON (Fig. 9b,d). This is associated with a westerly zonal wind bias at the equator (yellow-red color shading) as shown above. Increasing the atmospheric resolution in the KCM reduces

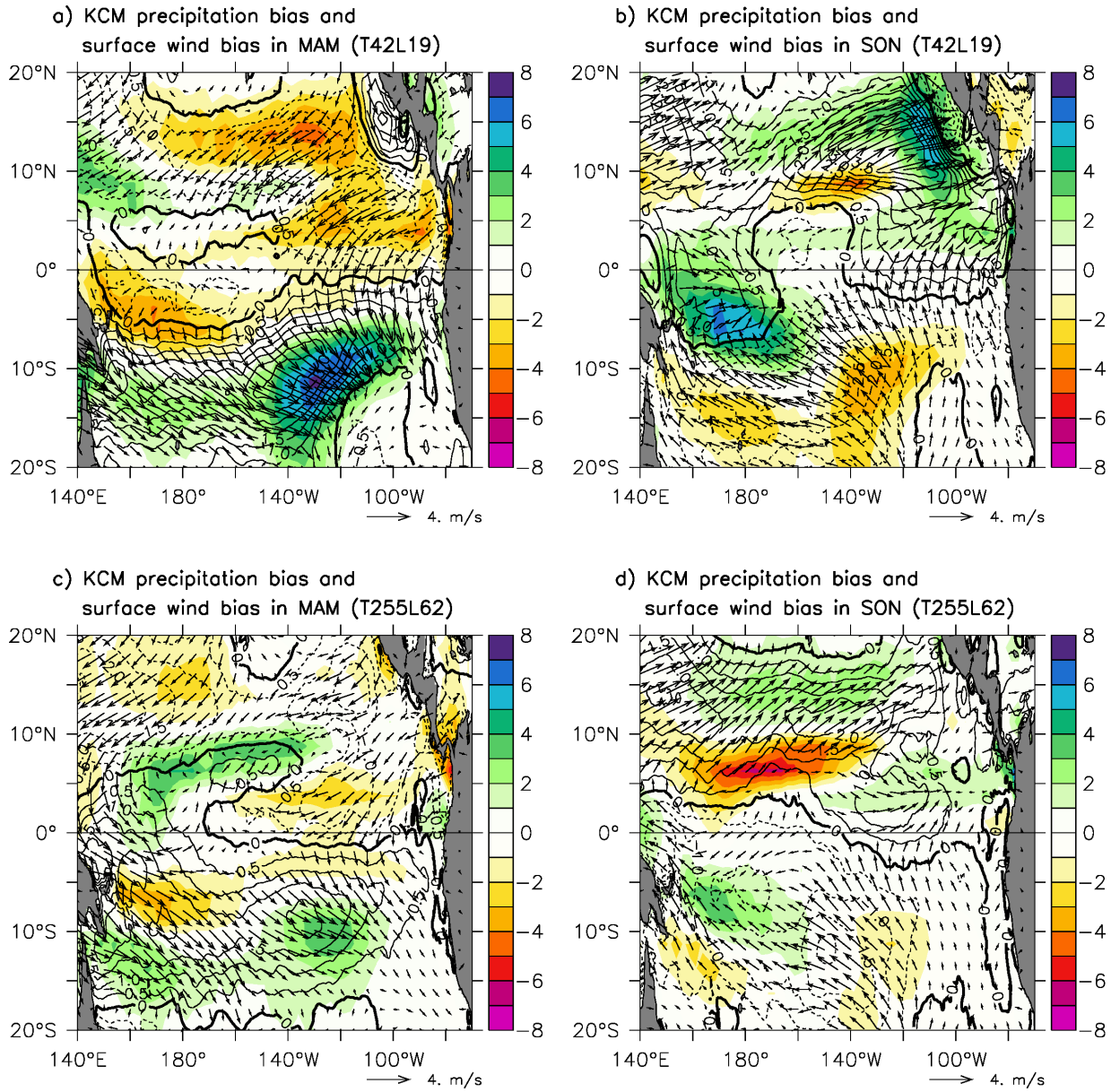

Fig. 8 Seasonal average of tropical Pacific precipitation bias (color shading), zonal wind bias (contours) and surface wind bias (arrows) during the months (a) and (c) MAM and (b) and (d) SON of the KCM for (a) and (b) coarse and (c) and (d) high atmospheric resolution. The bias is calculated by subtracting observed seasonally-averaged monthly anomalies from KCM seasonally-averaged monthly anomalies. Anomalies are defined with respect to the annual mean. Precipitation bias is in units mm day^{-1} and wind in ms^{-1}.

precipitation, convection and equatorial surface wind biases in the eastern tropical Pacific during MAM and SON (Fig. 9c,d). We argue that improved meridional and vertical transport of momentum at high atmospheric resolution accounts for reducing these biases, as discussed by

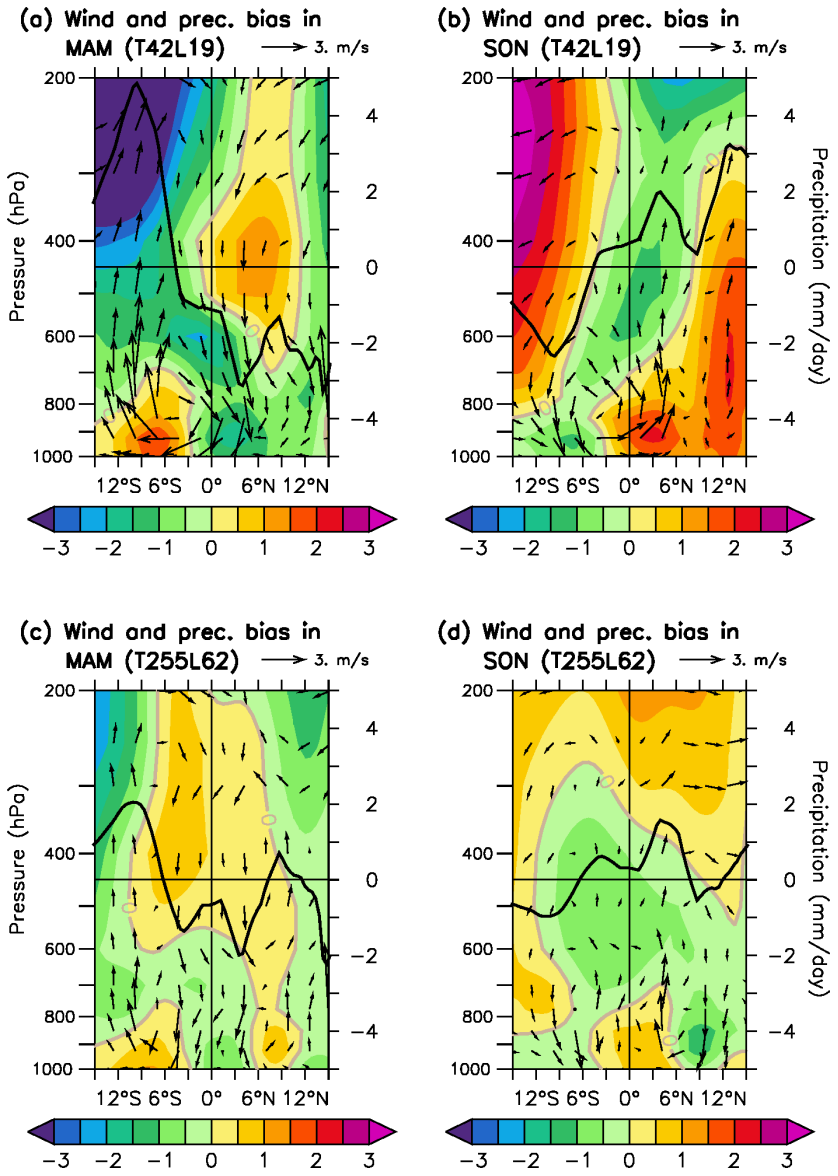

Fig. 9 Seasonal average of zonal wind bias (color shading), meridional-vertical wind bias (arrows) and precipitation bias (black line) centered about the equator in the eastern tropical Pacific during the months (a), (c) MAM and (b), (d) SON in the KCM at (a), (c) coarse and (b), (d) high atmospheric resolution. The bias is calculated by subtracting observed seasonally-averaged monthly anomalies from KCM seasonally-averaged monthly anomalies. Shown are anomalies defined with respect to the annual mean. All data are averaged over 140°W – 85°W. The horizontal black line marks zero precipitation anomalies. Precipitation bias is in units mm day^{-1} and wind in ms^{-1}. Vertical wind is scaled by 90.

Harlaß et al. (2017) analyzing the same set of KCM integrations over the Eastern Equatorial Atlantic. Another important contribution to bias reduction in the EEP may result from the enhanced

representation of orography at higher atmospheric resolution, especially during SON when a land-sea circulation influences surface winds in the EEP.

In order to further diagnose the origin of the zonal surface wind biases at the equator, we compare the equatorial zonal wind biases in the two KCM versions with those simulated in the corresponding uncoupled AGCM (ECHAM5) integrations forced by observed monthly SST climatology. The zonal wind biases in the coupled and uncoupled model versions are in qualitative agreement at both resolutions (Fig. 10a,c). For example, the westerly wind bias in the east in late boreal summer and boreal fall observed in coupled mode also is present in the corresponding uncoupled integrations. In the western equatorial Pacific, both the westerly zonal wind bias during boreal fall at coarse atmospheric resolution and that during boreal spring at high resolution also are seen in uncoupled mode. We conclude that, independent of atmospheric resolution, a large part of the equatorial zonal wind biases observed in coupled mode originates in the atmosphere model itself.

The total cloud cover in the two KCM versions also exhibits very similar biases to those in the uncoupled AGCM integrations (Fig. 10b,d). We note that in both coupled and uncoupled mode, model biases are largely reduced when atmospheric resolution is increased but not in the very east near the coast. Our findings could suggest that the origin of the cloud cover biases in this region resides in the parameterization of stratocumulus clouds and is independent of the choice of atmospheric resolution. The highest vertical resolution (L62) used here may be still inadequate to resolve the processes relevant to stratus cloud formation, e.g. the sharpness of the capping inversion layer. The reduction of cloud cover biases in the region to the west is likely linked to an improved representation of convection due to enhancing atmospheric resolution (see above). The simulation of tropical clouds strongly depends on the level of simulated precipitation as only models with much higher vertical resolution can resolve the processes relevant to stratus cloud formation.

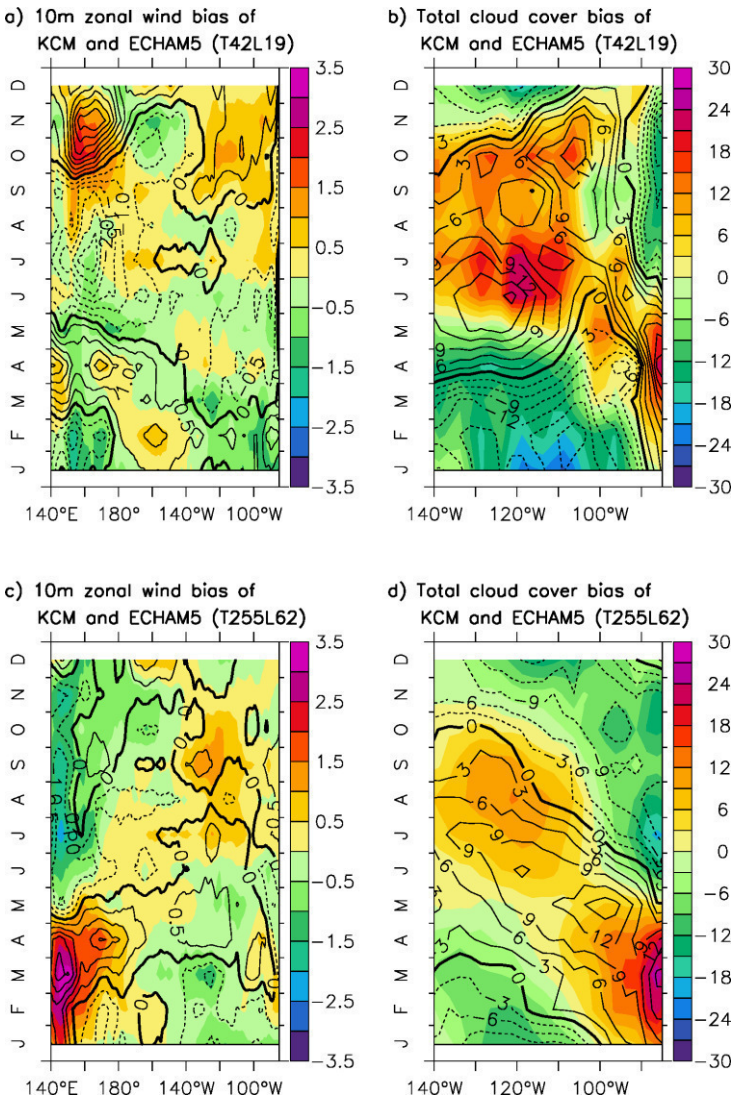

Fig. 10 Seasonal cycle of (a) and (c) 10 m zonal wind bias in the equatorial Pacific and (b) and (d) total cloud cover bias in the EEP of the KCM (color shading) and in the atmospheric model component ECHAM5 forced by observed monthly SST climatology (contours) at (a) – (b) coarse and (c) – (d) high atmospheric resolution, respectively. The bias is calculated by subtracting observed monthly anomalies from KCM and ECHAM5 monthly anomalies. Anomalies are calculated with respect to the annual mean. All data are averaged over 2.8°S – 2.8°N. Wind bias is in units ms^{-1} and cloud cover in %.

The near-surface (10 m) meridional wind biases in the KCM simulations considerably differ from those in the SST-forced atmosphere model integrations (not shown). Hence, the meridional wind biases in the EEP must be strongly influenced by coupled feedbacks, as outlined above. The same

conclusion is obtained when comparing the net surface heat flux biases in coupled and uncoupled mode (not shown).

4. SST annual cycle in CMIP5 models

A set of 12 models from the CMIP5 database is analyzed (Table 2). As in the analyses of the KCM, we consider anomalies with respect to the long-term annual-mean to highlight seasonal changes. This is different to Song et al. (2014) who analyzed the EEP SST AC in CMIP5 models in terms of the full temperatures. The CMIP5 ensemble-mean SST AC biases in the EEP are depicted by contours in Fig. 11. In agreement with the KCM simulations, there is an EEP cold SST bias peaking in boreal summer with values up to 2.5°C and a warm bias peaking in boreal winter with values up to up to 2°C. The model spread is largest when the SST bias is most distinct in July and December and amounts to 0.64°C and 0.7°C, respectively, with all models agreeing on the sign of bias in all seasons (not shown). The relationship of the near-surface (10 m) zonal wind biases (color shading) to the SST biases is analyzed by means of Fig. 11a. Also similar to the KCM, an anomalous equatorial westerly wind bias in the vicinity of the largest SST biases in the EEP is present in boreal fall with values up to 1 ms^{-1}, which likely contributes to the SST warm bias in that season. The cold bias maximum in boreal summer seen in the ensemble-mean of the subset of CMIP5 models is not associated with significant easterly wind biases anywhere at the equator, only during the onset of the cold bias in late boreal winter to early boreal spring.

Next, ensemble-means of the meridional surface wind bias and SST bias are compared (Fig. 11b). As in the KCM (Fig. 3b,e), the SST and meridional wind biases exhibit a marked phase lag, with the meridional wind bias with opposite polarity lagging the SST bias. This is consistent with the conjecture, which has been put forward above when describing the KCM results, that the meridional wind biases are a response to the SST biases and not a driver.

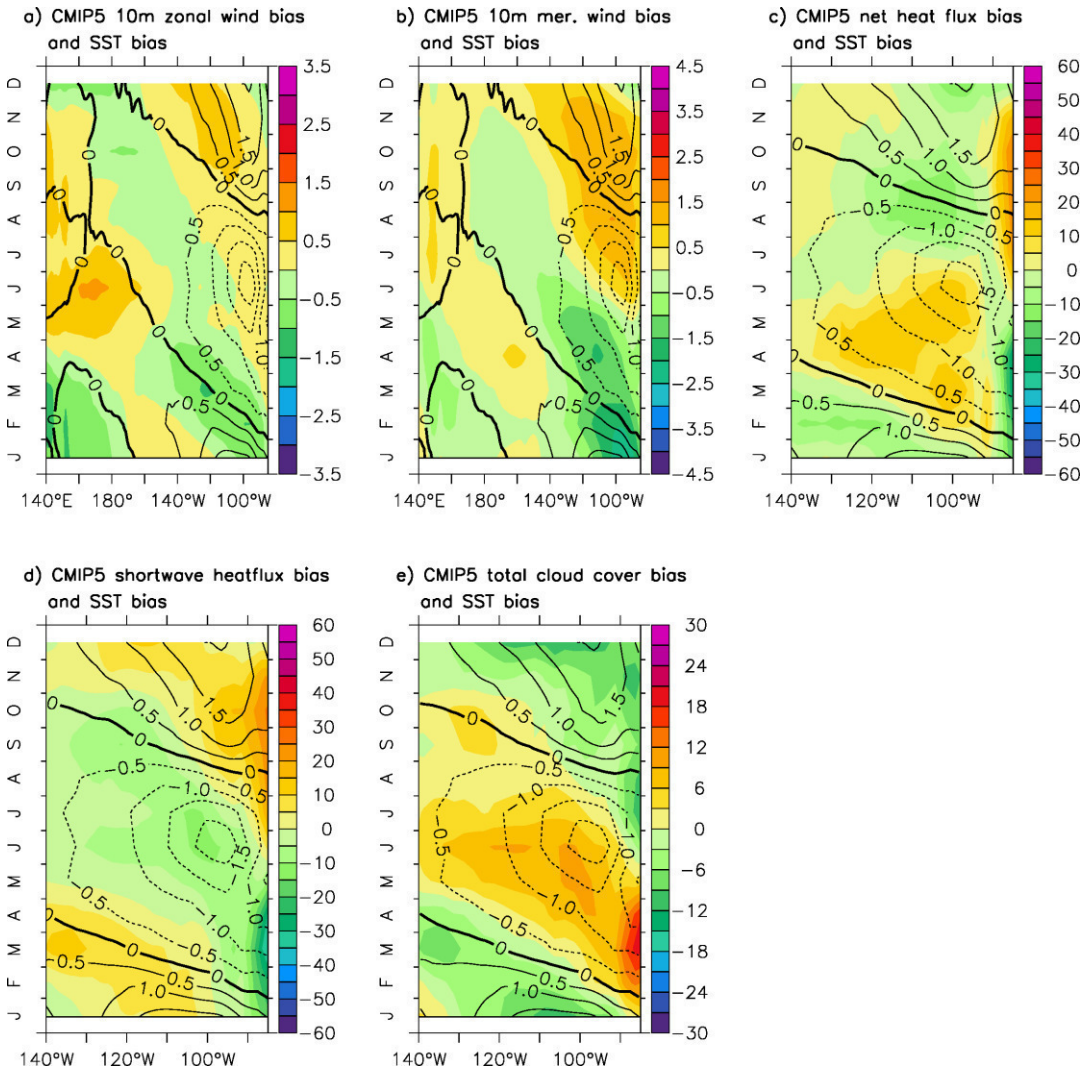

Fig. 11 Seasonal cycle of SST bias (superimposed contours) with (a) zonal (10 m) wind bias, (b) meridional (10 m) wind bias in the equatorial Pacific (c) net surface heat flux bias, (d) shortwave heat flux bias and (e) total cloud cover bias in the EEP (color shading) of the CMIP5 models (Table 2) ensemble-mean. The bias is calculated by subtracting observed monthly anomalies from ensemble-mean monthly anomalies. Anomalies are calculated with respect to the annual mean. All data are averaged over 2.8°S – 2.8°N. SST bias is in units °C, wind in ms^{-1}, net surface and shortwave heat fluxes in Wm^{-2} and cloud cover in %.

The CMIP5 ensemble-mean net surface heat flux bias is compared with the SST bias in the EEP east of 140° W in Fig. 11c. As in the KCM, the net heat flux tends to damp the SST biases rather than being a source of them. However, the opposite picture, consistent with the KCM results, is obtained when the surface shortwave radiative part alone is compared with the SST bias (Fig. 11d),

with positive values over warm SST bias and vice versa. Although the shortwave radiation bias does not dominate the net heat flux bias over large regions, it nevertheless can influence the SST via an oceanic bridge, as argued above (Section 3). Further, shortwave radiation biases are clearly linked to cloud cover biases (Fig. 11e).

The subsurface ocean temperature biases in the EEP averaged over 2.8°S – 2.8°N and over MAM, MJJ and SON are shown in Fig. 12. Deviations from the SST bias pattern shown in Fig. 11 are a consequence of using SODA instead of NOAA_OI_SST_V as noted also above. The cold subsurface temperature bias in MJJ with its maximum below the sea surface (Fig. 12b) is possibly driven by a deficit in shortwave radiation (Fig. 11d). As in the KCM, the signal is expected to return to the surface via mixing processes. In contrast, the cold bias in MAM (Fig. 12a) and the warm bias in SON (Fig. 12c) are linked probably to easterly and westerly surface wind biases, respectively (Fig. 11a).

The subsurface zonal and vertical velocity biases in the EEP averaged over MAM, MJJ and SON are depicted in Fig 13. A westward-directed zonal velocity bias dominates in the EEP in MAM (Fig. 13a) and to a lesser extent also in MJJ (Fig. 13b). An eastward-directed current bias is found SON (Fig. 13c). An upwelling bias is observed in MAM (Fig. 13d) and a downwelling bias in SON (Fig. 13f) whereas in MJJ, no robust signal in the vertical velocity is present (Fig. 13e). These findings support the hypothesis that SST biases in boreal spring and boreal fall are largely linked to zonal wind biases whereas a deficit in shortwave radiation likely is the cause of the SST biases in early boreal summer.

In Fig. 14, horizontal maps of near-surface wind and precipitation biases in MAM and SON are shown. As in the KCM, there is a pronounced double-ITCZ with excessive rainfall south of the equator during MAM (Fig. 14a; color shading). In contrast to the KCM, no easterly wind bias in the EEP during MAM (arrows and contours) is observed. An easterly wind bias, however, is present in late boreal winter and early boreal spring (Fig. 11a). In SON, the westerly wind bias in the EEP can

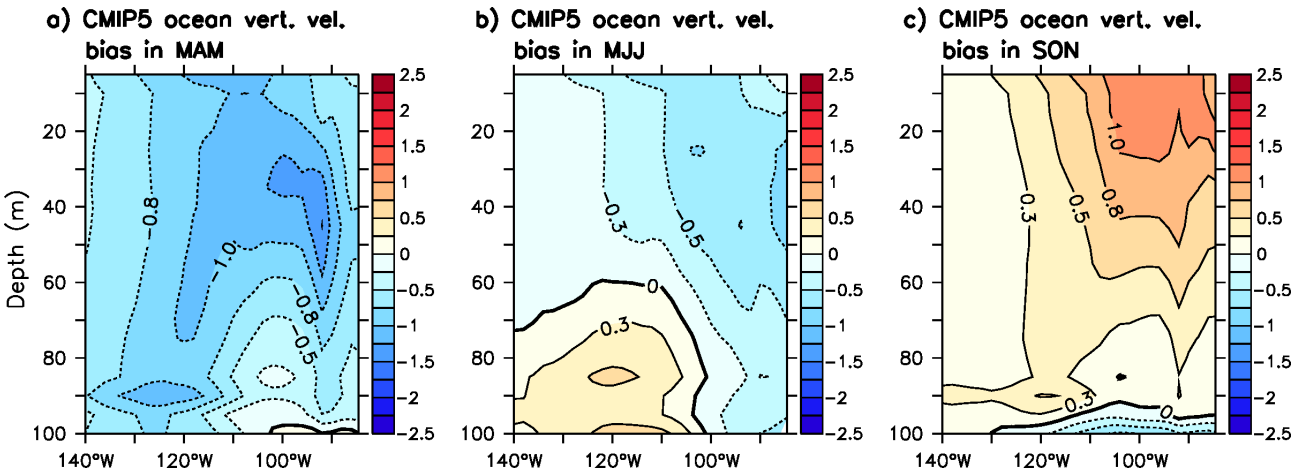

Fig. 12 Seasonal average of subsurface ocean temperature bias in the EEP during the months (a) and (d) MAM, (b) and (e) MJJ and (c) and (f) SON of the CMIP5 models (Table 2). The bias is calculated by subtracting observed seasonally-averaged monthly anomalies from ensemble-mean seasonally-averaged monthly anomalies. Anomalies are defined with respect to the annual mean. All data are averaged over 2.8°S – 2.8°N. Temperature bias is in units °C.

be linked to an excessive precipitation north of the equator and to too strong near-surface winds towards the land (Fig. 14b), as in the KCM (Fig. 8b,d). Due to the large data size of the four-dimensional atmospheric variables we could not investigate the vertical structure of equatorial winds in the subset of CMIP5 models. Based on the above results, we expect that the important biases are similar to those identified in the KCM version employing coarse atmospheric resolution (Fig. 9).

We next compare the CMIP5 ensemble-mean biases with those of the corresponding AMIP ensemble-mean (Fig. 15) to investigate whether the biases in the atmospheric circulation are systematic to the atmosphere models. The zonal wind bias in the CMIP5 ensemble-mean is in qualitative agreement with that in the AMIP ensemble-mean (Fig. 15a). As for the KCM, this finding shows that zonal wind biases observed in the set of CMIP5 models largely have their origin in the atmospheric model components. The meridional wind biases greatly differ between the coupled (CMIP5) and uncoupled atmosphere model (AMIP) simulations (not shown), which also was found in the comparison of the KCM with the forced AGCM (ECHAM5) integrations. Finally,

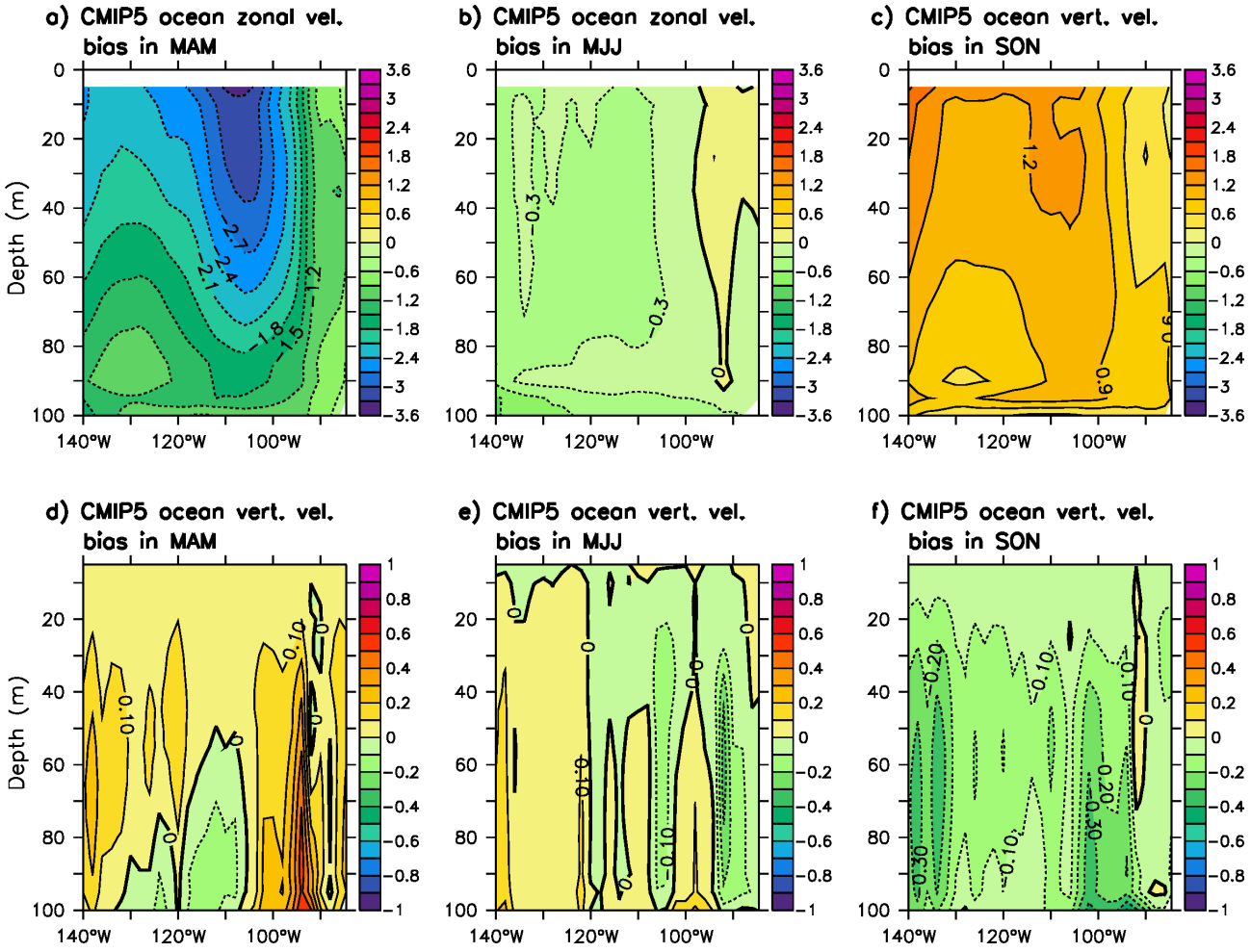

Fig. 13 Seasonal average of subsurface ocean (a) – (c) zonal and (d) – (f) vertical velocity bias in the EEP during the months (a) and (d) MAM, (b) and (e) MJJ and (c) and (f) SON of the CMIP5 models (Table 2). The bias is calculated by subtracting observed seasonally-averaged monthly anomalies from ensemble-mean seasonally-averaged monthly anomalies. Anomalies are defined with respect to the annual mean. All data are averaged over 2.8°S – 2.8°N. Zonal velocity bias is in units dm s^{-1} and vertical velocity bias in m day^{-1}.

the total cloud cover biases in the CMIP5 ensemble-mean largely agrees with that in the AMIP ensemble-mean (Fig. 15b). This implies that the erroneous cloud cover, as the zonal wind biases, also have parts of their origin in the atmospheric components. Thus both sets of coupled/uncoupled model integrations, KCM/ECHAM5 and CMIP5/AMIP, support that coupled model simulation of the EEP SST AC can significantly benefit from improvements in the atmospheric model components.

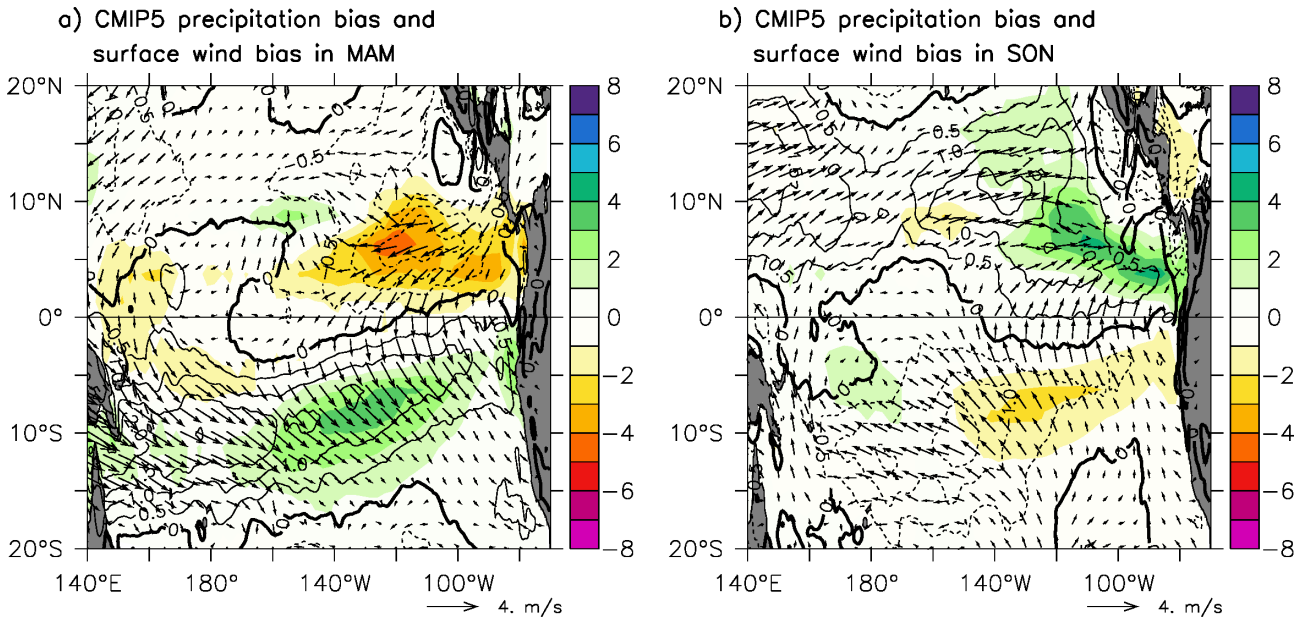

Fig. 14 Seasonal average of tropical Pacific precipitation bias (color shading), zonal wind bias (contours) and surface wind bias (arrows) during the months (a) MAM and (b) SON of the CMIP5 models (Table 2) ensemble-mean. The bias is calculated by subtracting observed seasonally-averaged monthly anomalies from ensemble-mean seasonally-averaged monthly anomalies. Anomalies are defined with respect to the annual mean. Precipitation bias is in units mm day^{-1} and wind in ms^{-1}.

A controversial issue is the relative importance of the zonal and meridional surface wind components in driving the EEP SST AC. Xie (1994) suggest that the meridional wind across the equator is the most significant driver. DeWitt and Schneider (1999) find that the wind-driven upwelling near the coast of South America is caused in approximately equal parts by the zonal and meridional component. We find that in the KCM, the zonal wind biases are most important in driving biases in the EEP SST AC during boreal fall and early boreal spring, which also appears to be the case for the subset of CMIP5 models investigated here.

In both the KCM and the CMIP5 models, the meridional near-surface wind across the equator exhibits biases of larger magnitude compared to the zonal near-surface wind. To compare the contribution of the individual wind components to the seasonal SST biases we calculate the linear regression coefficient of the wind-SST relationship in the EEP in boreal fall among the

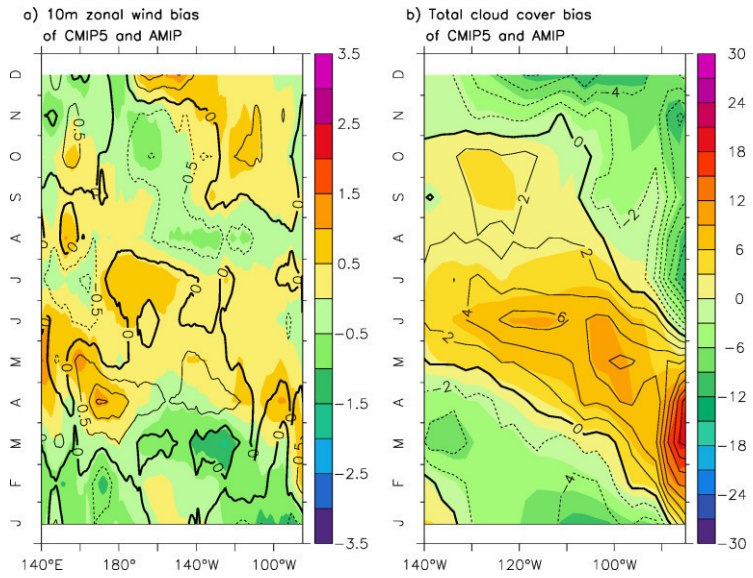

Fig. 15 Seasonal cycle of (a) 10m zonal wind bias in the equatorial Pacific and (b) total cloud cover bias in the EEP calculated from the CMIP5 model (Table 2) ensemble-mean (color shading) and the corresponding AMIP model ensemble-mean (contours) in the EEP. The bias is calculated by subtracting observed monthly anomalies from ensemble-mean monthly anomalies. Anomalies are calculated with respect to the annual mean. All data are averaged over 2.8°S – 2.8°N. Zonal wind is in unit ms^{-1} and cloud cover in %.

CMIP5 models. A reduction of the meridional wind bias of $1ms^{-1}$ during September – November is associated with a reduction of the SST bias of 0.33°C in October – December, whereas a decrease of the zonal wind bias of the same magnitude is associated with an SST bias reduction of 0.85°C. This suggests that despite weaker amplitude, biases in the zonal wind component are of larger importance compared to the meridional component.

5. Summary and discussion

We have investigated the eastern equatorial Pacific (EEP) sea surface temperature (SST) annual cycle (AC) simulated by the Kiel Climate Model (KCM) at different atmospheric but fixed oceanic resolution (2° zonally) and compared the results with those obtained from a subset of models participating in the Coupled Model Intercomparison phase 5 (CMIP5). Overall, a coarse atmospheric resolution setup of the KCM is sufficient to simulate an EEP SST AC. Biases in such a

setup, however, are rather large. For example, the warming signal of the SST in boreal spring though significant is underestimated in magnitude by about 1°C. Moreover, the equatorial cold tongue appears 1 – 2 months too early and disappears up to 3 months earlier than observed. Enhancing the atmospheric model resolution in the KCM helps to improve the simulation of the EEP SST AC with regard to the westward propagating character of the warming signal in boreal spring and the timing of the cold tongue's onset and termination. Overall, the KCM results imply that the atmosphere model resolution plays an important role in simulating the EEP SST AC, as the coarse oceanic model resolution was held fixed and atmospheric parameterizations were not re-tuned.

We diagnose the near-surface (10 m) zonal wind as a crucial factor in controlling the simulation of the EEP SST AC in the KCM. In boreal spring, an easterly wind bias contributes to a smaller warming and, to a lesser extent, to a too early onset of the cold tongue. In boreal fall, a westerly wind bias drives the too early termination of the equatorial cold tongue. Increasing the atmospheric resolution leads to a reduction of the zonal wind biases. Furthermore, the net surface heat flux and near-surface meridional wind are responding to rather than generating the SST bias. We further show that the zonal wind and the SST biases are linked via ocean upwelling/downwelling biases. This agrees with DeWitt and Schneider (1999) who show that seasonal SST variations in the EEP are primarily caused by upwelling variations. We also show that in early boreal summer, shortwave radiation biases may contribute to SST biases by penetrating through the subsurface, whereby the signal can be returned to the surface by vertical mixing. Shortwave radiation biases are associated with cloud cover biases, which are reduced in the KCM when atmospheric resolution is increased.

The subset of CMIP5 models yields very similar relationships: models with a larger warm SST bias in October – December exhibit a larger westerly wind bias in September – November (correlation of 0.67) and models with a larger cold SST bias in March – May exhibit a larger easterly wind bias in February – April (correlation of 0.50). As in the KCM, a deficit of shortwave surface radiation

also appears to be important, especially in early boreal summer. This deficit drives a subsurface cooling bias influencing the sea surface via vertical mixing. The shortwave radiation bias can be linked to excessive cloud cover, with a tendency of models with a larger SST cold bias in May – July exhibiting a larger cloud cover bias in April – June (correlation of 0.56). Chen and Jin (2017) also find that the influence of solar radiation on the EEP SST AC is overestimated in a number of CMIP5 models.

We showed that zonal wind biases are largely related to precipitation biases in both the KCM and CMIP5, in particular to the double ITCZ-problem in boreal spring and to excessive rainfall north of the equator over the EEP in boreal fall. Also, an erroneous land-surface circulation probably induced by an inaccurate representation of the adjacent orography can be linked to zonal wind biases in the EEP. For the KCM, we showed that increasing atmospheric resolution reduces precipitation biases, which improves the convection and thus surface winds in the EEP. We argue that these improvements are due to a better simulation of meridional and vertical momentum transport in the atmosphere and due to an improved land-surface circulation related to an enhanced representation of orography.

Further, we emphasize the importance of systematic errors in the atmospheric component of the KCM for the simulation of the EEP SST AC, which was shown by conducting uncoupled AGCM simulations forced by observed climatological SST. The systematic errors in zonal wind are strongly reduced in the AGCM when increasing the resolution. Consequently, a significant improvement in the simulation of the EEP SST AC is achieved in coupled mode by only increasing the atmospheric resolution while keeping coarse zonal ocean model resolution (2°). This is consistent with Harlaß et al. (2015, 2017) using the same set of coupled and uncoupled simulations and yield a substantial reduction of a warm SST bias in the southeastern Tropical Atlantic as well as realistic SST variability in that region, when especially the vertical atmosphere model resolution is

increased. For the EEP SST AC, we note that the largest improvement comes from enhancing the horizontal resolution (not shown).

Song et al. (2014) assessed the ability of a subset of CMIP5 models to simulate the EEP SST AC. Similar to our results, they find a westerly surface wind bias in boreal fall to be related with a warm SST bias in the east. In contrast to the present study stressing the importance of zonal wind biases, Song et al. (2014) find a northerly wind bias (with regard to absolute values) in boreal fall to be related with a coastal warm SST bias via weaker evaporative cooling and ocean upwelling. Furthermore, they discuss the CMIP5 models' ability to simulate the observed zonally-instant development of the cold tongue in August and September and find that models tend to produce a spurious westward propagation of the cold tongues' onset. We add that the KCM too is not able to reproduce this zonally-instant onset of the cold tongue but rather exhibits a westward propagation similar to the SST warming signal in boreal spring. Consistent with the results from the KCM, systematic errors in the atmospheric components largely explain the biases observed in the subset of CMIP5 models analyzed here. This result has been derived from the (uncoupled) AMIP-simulations and relates to surface wind and cloud cover/solar radiation biases.

We also addressed the relative importance of the zonal and meridional surface wind components in driving the EEP SST AC. Our results suggested that despite weaker amplitude, biases in the zonal wind component are of larger importance compared to the meridional component.

Acknowledgements

This work was supported by the German Ministry of Education and Research (BMBF) grant SACUS (03G0837A) and EU FP7/2007-2013 under grant agreement no. 603521, project PREFACE, and SFB 754 "Climate-Biochemistry Interactions in the tropical Ocean". We thank two anonymous reviewers for helpful comments and feedbacks on this work. The climate model integrations were performed at the Computing Centre of Kiel University. We acknowledge the

World Climate Research Programme's Working Group on Coupled Modelling, which is responsible for CMIP, and we thank the climate modeling groups (listed in Table 2 of this paper) for producing and making available their model output. For CMIP the U.S. Department of Energy's Program for Climate Model Diagnosis and Intercomparison provides coordinating support and led development of software infrastructure in partnership with the Global Organization for Earth System Science Portals.

References

Carton JA, Giese BS (2008) A Reanalysis of Ocean Climate Using Simple Ocean Data Assimilation (SODA). Mon Weather Rev 136:2999–3017.doi: 10.1175/2007MWR1978.1

Chang P, Philander SG (1994) A Coupled Ocean–Atmosphere Instability of Relevance to the Seasonal Cycle. J Atmos Sci 51:3627–3648. doi: 10.1175/1520-0469(1994)051<3627:ACOIOR>2.0.CO;2

Chen Y-Y, Jin F-F (2017) Dynamical diagnostics of the SST annual cycle in the eastern equatorial Pacific: Part II analysis of CMIP5 simulations. Clim Dyn 1–14. doi: 10.1007/s00382-017-3550-z

Covey C, Abe-Ouchi A, Boer GJ, et al (2000) The seasonal cycle in coupled ocean-atmosphere general circulation models. Clim Dyn 16:775–787. doi: 10.1007/s003820000081

Dee DP, Uppala SM, Simmons AJ et al (2011) The ERA-Interim reanalysis: configuration and performance of the data assimilation system. Q J R Meteorol Soc 137:553–597. doi:10.1002/qj.828

de Szoeke SP, Xie S-P (2008) The Tropical Eastern Pacific Seasonal Cycle: Assessment of Errors and Mechanisms in IPCC AR4 Coupled Ocean–Atmosphere General Circulation Models*. J Clim 21:2573–2590. doi: 10.1175/2007JCLI1975.1

DeWitt DG, Schneider EK (1999) The Processes Determining the Annual Cycle of Equatorial Sea Surface Temperature: A Coupled General Circulation Model Perspective. Mon Weather Rev 127:381–395. doi: 10.1175/1520-0493(1999)127<0381:TPDTAC>2.0.CO;2

Dijkstra HA, Neelin JD (1995) Ocean-Atmosphere Interaction and the Tropical Climatology. Part II: Why the Pacific Cold Tongue Is in the East. J Clim 8:1343–1359. doi: 10.1175/1520-0442(1995)008<1343:OAIATT>2.0.CO;2

Giese BS, Carton JA (1994) The seasonal cycle in a coupled ocean-atmosphere model. J Clim 7:1208–1217.

Harlaß J, Latif M, Park W (2015) Improving climate model simulation of tropical Atlantic sea surface temperature: The importance of enhanced vertical atmosphere model resolution. Geophys Res Lett 42:2401–2408. doi: 10.1002/2015GL063310

Harlaß J, Latif M, Park W (2017) Alleviating tropical Atlantic sector biases in the Kiel climate model by enhancing horizontal and vertical atmosphere model resolution: climatology and interannual variability. Clim Dyn. doi: 10.1007/s00382-017-3760-4

Kessler WS, McPhaden MJ, Weickmann KM (1995) Forcing of intraseasonal Kelvin waves in the equatorial Pacific. J Geophys Res 100:10613. doi: 10.1029/95JC00382

Latif M, Graham NE (1992) How Much Predictive Skill Is Contained in the Thermal Structure of an Oceanic GCM? J Phys Oceanogr 22: 951-962

Latif M, Sperber K, Arblaster J, et al (2001) ENSIP: the El Niño simulation intercomparison project. Clim Dyn 18:255–276. doi: 10.1007/s003820100174

Li T (1997) Air–Sea Interactions of Relevance to the ITCZ: Analysis of Coupled Instabilities and Experiments in a Hybrid Coupled GCM. J Atmos Sci 54:134–147. doi: 10.1175/1520-0469(1997)054<0134:ASIORT>2.0.CO;2

Li T, Philander S (1996) On the Annual Cycle of the Eastern Equatorial Pacific. J. Clim. 9:2986–2998.

Lin JL (2007) The Double-ITCZ Problem in IPCC AR4 Coupled GCMs: Ocean–Atmosphere Feedback Analysis. J Clim 20:4497–4525. doi: 10.1175/JCLI4272.1

Ma C-C, Mechoso CR, Robertson AW, Arakawa A (1996) Peruvian Stratus Clouds and the Tropical Pacific Circulation: A Coupled Ocean-Atmosphere GCM Study. J Clim 9:1635–1645. doi: 10.1175/1520-0442(1996)009<1635:PSCATT>2.0.CO;2

Madec G, Delecluse P, Imbard M, Lévy C (1998) OPA 8.1 Ocean General Circulation Model Reference Manual. Note du Pole de modélisation 11, Institut Pierre-Simon Laplace, 91 pp.

Mechoso CR, Robertson AW, Barth N, et al (1995) The Seasonal Cycle over the Tropical Pacific in Coupled Ocean–Atmosphere General Circulation Models. Mon. Weather Rev. 123:2825–2838.

Mitchell TP, Wallace JM (1992) The Annual Cycle in Equatorial Convection and Sea Surface Temperature. J Clim 5:1140–1156. doi: 10.1175/1520-0442(1992)005<1140:TACIEC>2.0.CO;2

Moum JN, Perlin A, Nash JD, McPhaden MJ (2013) Seasonal sea surface cooling in the equatorial Pacific cold tongue controlled by ocean mixing. Nature 500:64–7. doi: 10.1038/nature12363

Neelin JD (1991) The Slow Sea Surface Temperature Mode and the Fast-Wave Limit: Analytic Theory for Tropical Interannual Oscillations and Experiments in a Hybrid Coupled Model. J Atmos Sci 48:584–606. doi: 10.1175/1520-0469(1991)048<0584:TSSSTM>2.0.CO;2

Nigam S, Chao Y (1996) Evolution dynamics of tropical ocean-atmosphere annual cycle variability. J. Clim. 9:3187–3205.

Park W, Keenlyside N, Latif M, et al (2009) Tropical Pacific Climate and Its Response to Global Warming in the Kiel Climate Model. J Clim 22:71–92. doi: 10.1175/2008JCLI2261.1

Philander SGH, Gu D, Lambert G, et al (1996) Why the ITCZ Is Mostly North of the Equator. J Clim 9:2958–2972. doi: 10.1175/1520-0442(1996)009<2958:WTIIMN>2.0.CO;2

Reynolds RW, Rayner NA, Smith TM, et al (2002) An improved in situ and satellite SST analysis for climate. J Clim 15:1609–1625. doi: 10.1175/1520-0442(2002)015<1609:AIISAS>2.0.CO;2

Roeckner E, Baeuml G, Bonaventura L, et al (2003) The atmospheric general circulation model ECHAM 5. PART I: Model description. Max Planck Institute for Meteorology Rep. 349, 127 pp.

Song ZY, Liu HL, Wang CZ, et al (2014) Evaluation of the eastern equatorial Pacific SST seasonal cycle in CMIP5 models. Ocean Sci 10:837–843. doi: 10.5194/os-10-837-2014

Stein K, Timmermann A, Schneider N (2011) Phase Synchronization of the El Niño-Southern Oscillation with the Annual Cycle. Phys Rev Lett 107:128501. doi: 10.1103/PhysRevLett.107.128501

Stockdale T, Latif M, Burgers G, Wolff J-O (1994) Some sensitivities of a coupled ocean-atmosphere GCM. Tellus A Dyn Meteorol Oceanogr 46:367–380. doi: 10.3402/tellusa.v46i4.15486

Sun D-Z, Liu Z (1996) Dynamic Ocean-Atmosphere Coupling: A Thermostat for the Tropics.

Taylor KE, Williamson D, Zwiers F (2000) The Sea Surface Temperature and Sea-Ice Concentration Boundary Conditions for AMIP II Simulations.

Taylor KE, Stouffer RJ, Meehl GA (2012) An Overview of CMIP5 and the Experiment Design. Bull Am Meteorol Soc 93:485–498. doi: 10.1175/BAMS-D-11-00094.1

Valcke S (2006) OASIS3 user guide. PRISM Tech Rep No 3 64 pp.

Wentz, F.J., J. Scott, R. Hoffman, M. Leidner, R. Atlas, J. Ardizzone, 2015: Remote Sensing Systems Cross-Calibrated Multi-Platform (CCMP) 6-hourly ocean vector wind analysis product on 0.25 deg grid, Version 2.0. Remote Sensing Systems, Santa Rosa, CA. Available online at www.remss.com/measurements/ccmp. Accessed Feb 2016.

Xie P, Arkin PA (1997) Global precipitation: a 17-year monthly analysis based on gauge observations, satellite estimates, and numerical model outputs. Bull Am Meteorol Soc 78:2539–2558. doi:10.1175/1520-0477(1997)078<2539:GPAYMA>2.0.CO;2

Xie S-P (1994) On the genesis of the equatorial annual cycle. J. Clim. 7:2008–2013.

Xie S-P (2005) The shape of continents, air-sea interaction, and the rising branch of the Hadley circulation, in: The Hadley Circulation: Past, Present and Future, Vol. 21, Advances in Global Change Research, edited by: Diaz, H. F. and Bradley, R. S., 121–152, Springer Netherlands, 2005 doi: 10.1007/978-1-4020-2944-8_5

Xie S-P, Philander SGH (1994) A coupled ocean-atmosphere model of relevance to the ITCZ in the eastern Pacific. Tellus A 46:340–350. doi: 10.1034/j.1600-0870.1994.t01-1-00001.x

Xie S-P, Miyama T, Wang Y, et al (2007) A regional ocean-atmosphere model for eastern Pacific climate: Toward reducing tropical biases. J Clim 20:1504–1522. doi: 10.1175/JCLI4080.1

Yu, J-Y, and C R Mechoso (1999) A discussion on the errors in the surface heat fluxes simulated by a coupled GCM. J Clim 12, 416-426.

Yu, J-Y, and C R Mechoso (1999) Links between annual variations of Peruvian stratus clouds and of SST in the eastern equatorial Pacific. J Clim 23, 305-23,318

Yu L, Weller RA (2007) Objectively Analyzed Air–Sea Heat Fluxes for the Global Ice-Free Oceans (1981–2005). Bull Am Meteorol Soc 88:527–539. doi: 10.1175/BAMS-88-4-527

Yu Y, He J, Zheng W, Luan Y (2013) Annual cycle and interannual variability in the tropical pacific as simulated by three versions of FGOALS. Adv Atmos Sci 30:621–637. doi: 10.1007/s00376- 013-2184-2

Supplementary material for **chapter 2**:

Supplementary figures

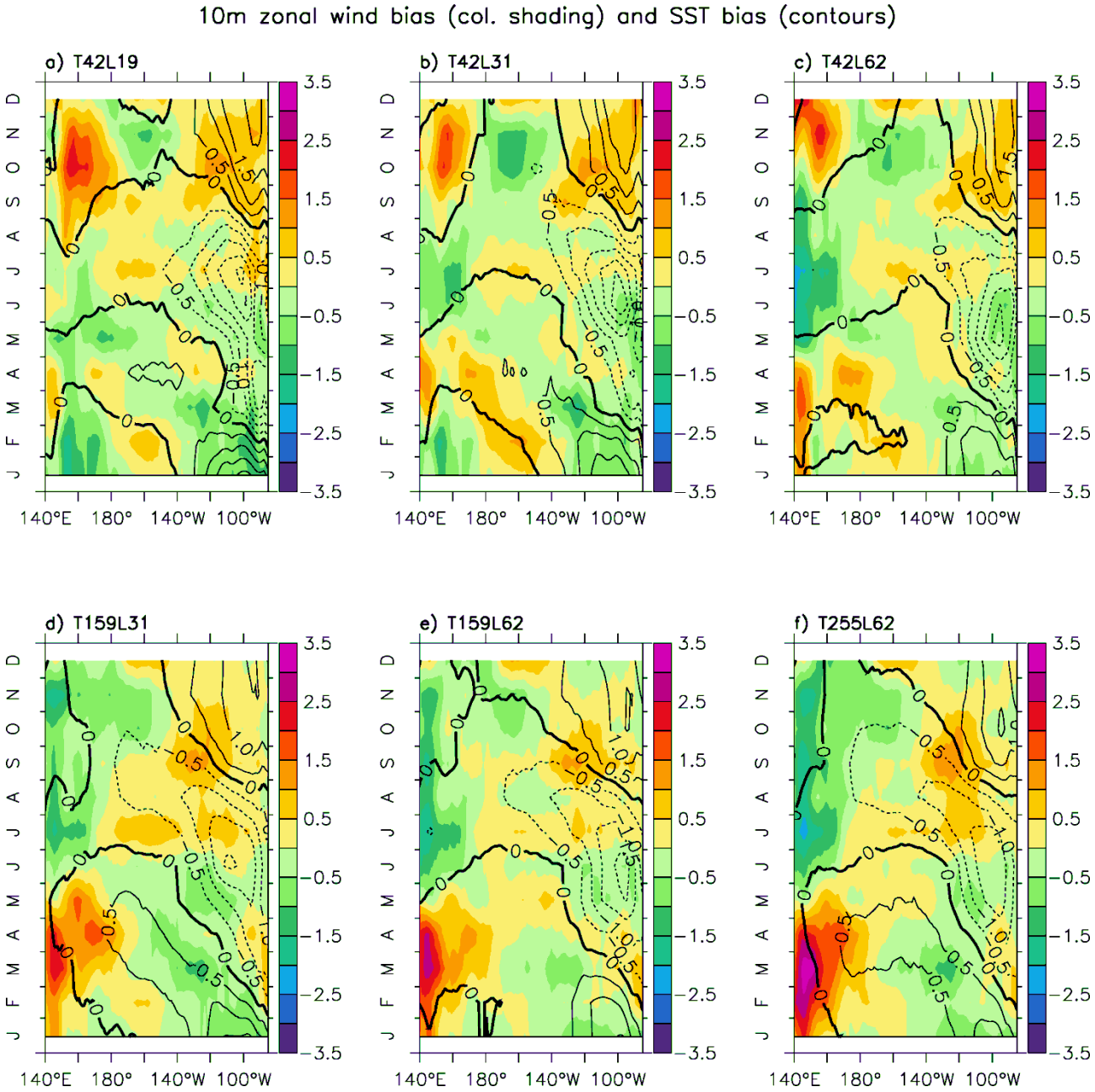

Fig. S1 Seasonal cycle of 10m zonal wind bias (color shading) and SST bias (contours) along the equator for an ensemble of six KCM integrations at different atmospheric resolutions. The bias is calculated by subtracting observed monthly anomalies from KCM monthly anomalies. Anomalies are calculated with respect to the annual mean. All data are averaged over 2.8°S – 2.8°N. SST bias is in units °C and wind bias in ms^{-1}.

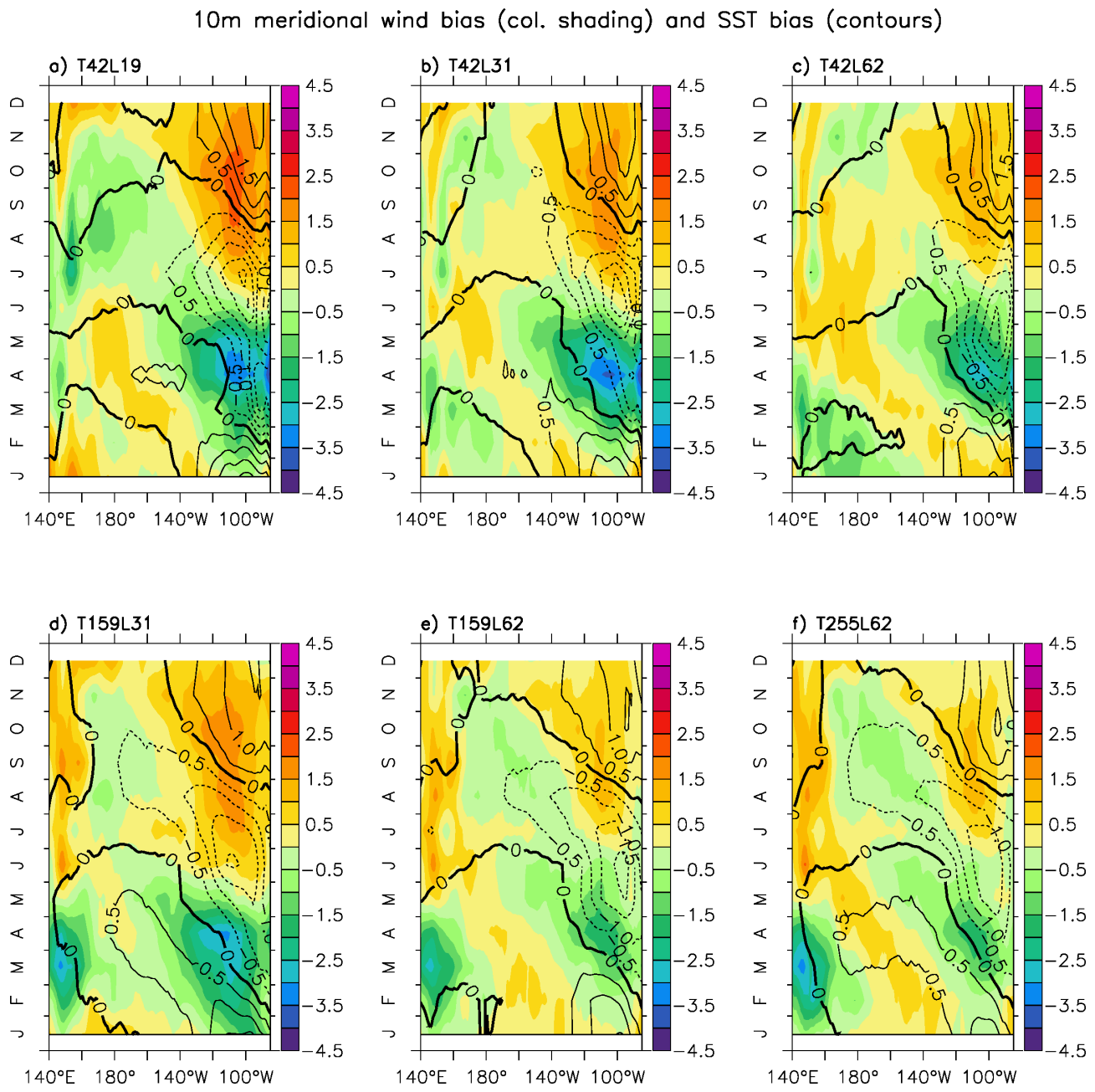

Fig. S2 Seasonal cycle of 10m meridional wind bias (color shading) and SST bias (contours) along the equator for an ensemble of six KCM integrations at different atmospheric resolutions. The bias is calculated by subtracting observed monthly anomalies from KCM monthly anomalies. Anomalies are calculated with respect to the annual mean. All data are averaged over 2.8°S – 2.8°N. SST bias is in units °C and wind bias in ms^{-1}.

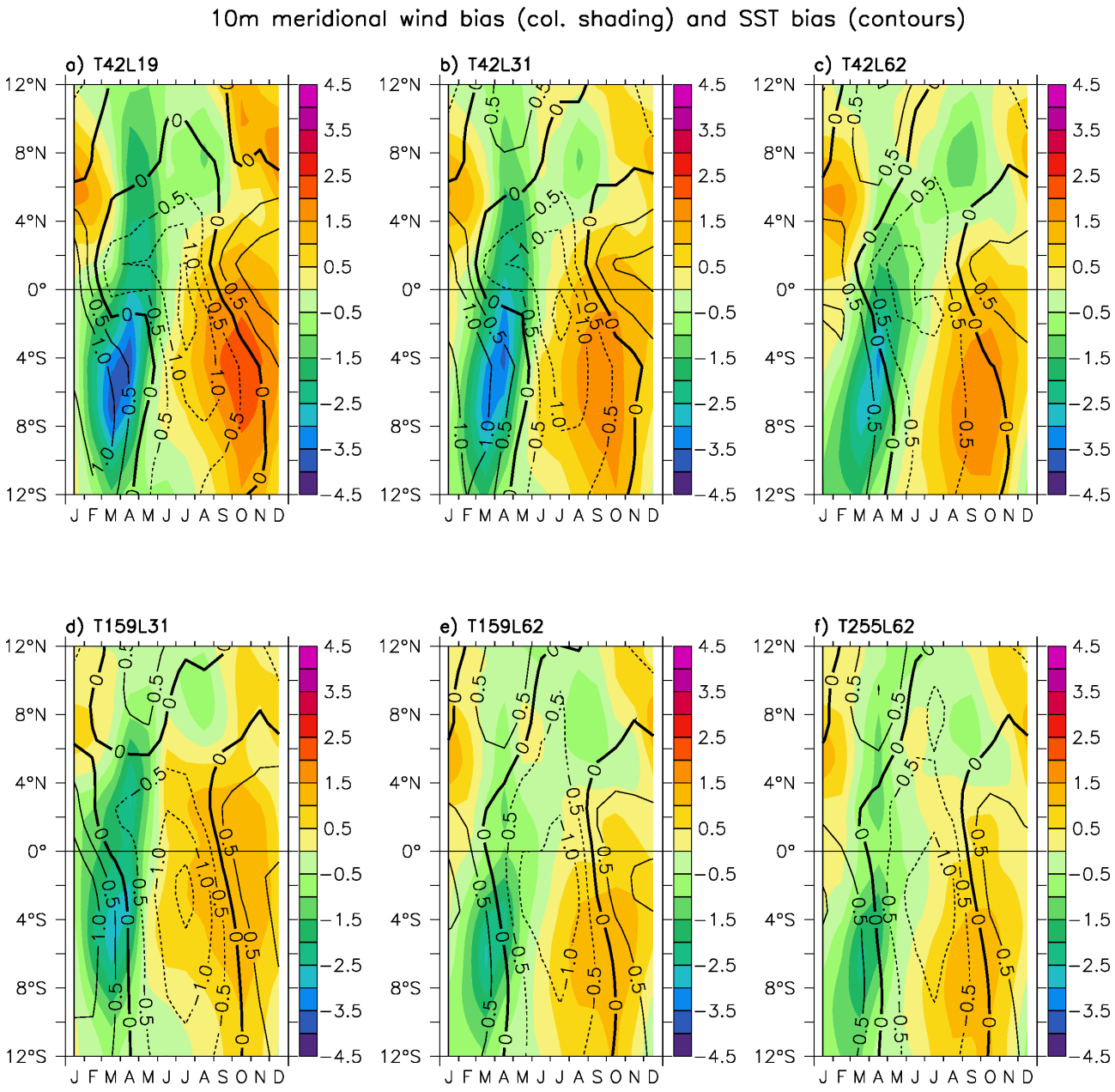

Fig. S3 Seasonal cycle of 10m meridional wind bias (color shading) and SST bias (contours) in the EEP for an ensemble of six KCM integrations at different atmospheric resolutions. The bias is calculated by subtracting observed monthly anomalies from KCM monthly anomalies. Anomalies are calculated with respect to the annual mean. All data are averaged over 140°W – 85°W. SST bias is in units °C and wind bias in ms^{-1}.

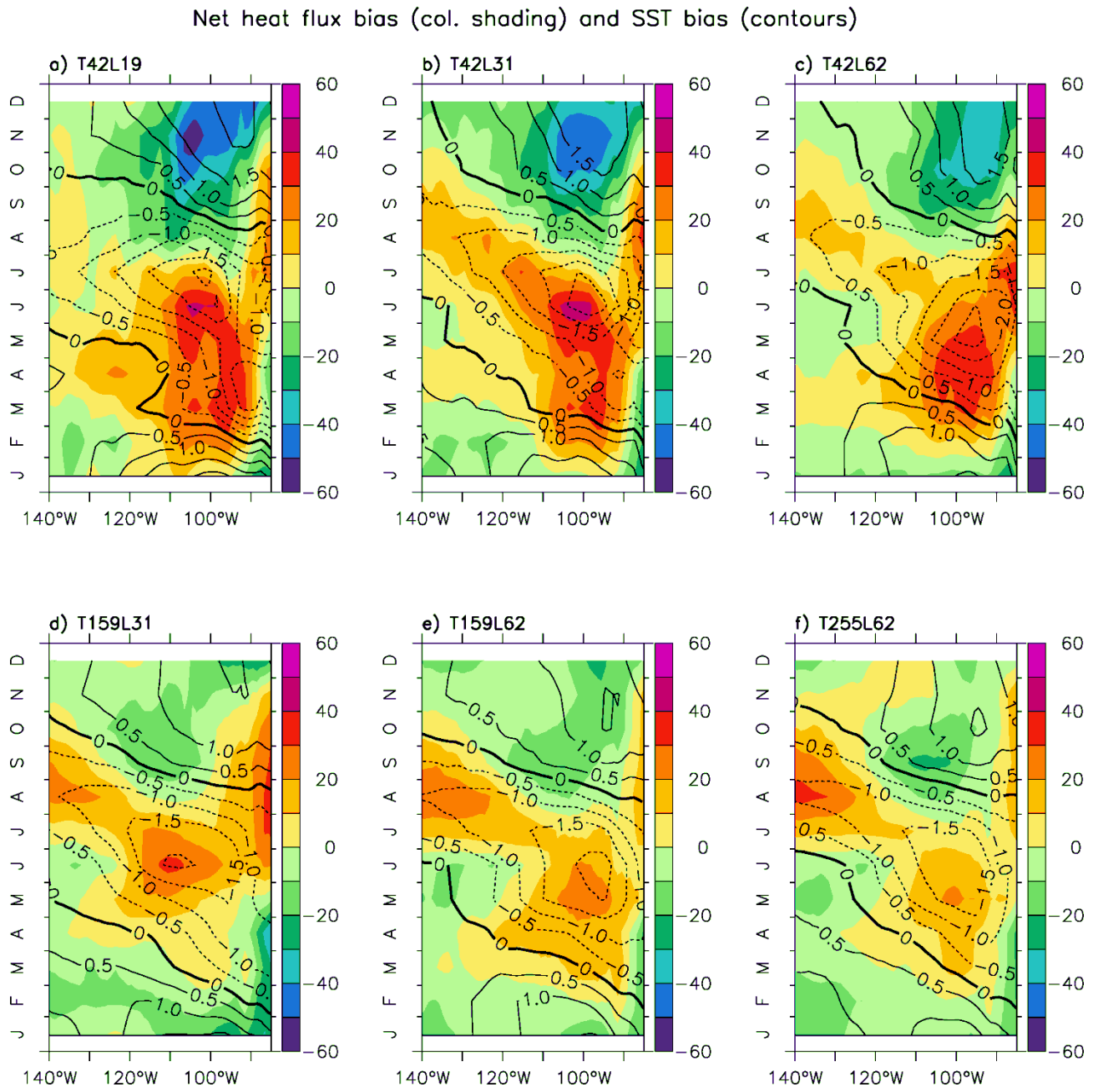

Fig. S4 Seasonal cycle of net surface heat flux (color shading; positive values of heat flux refer to a heat transfer from the atmosphere into the ocean) and SST bias (contours) in the EEP for an ensemble of six KCM integrations at different atmospheric resolutions. The bias is calculated by subtracting observed monthly anomalies from KCM monthly anomalies. Anomalies are calculated with respect to the annual mean. All data are averaged over 2.8°S – 2.8°N. SST bias is in units °C and net heat flux bias in Wm^{-2}.

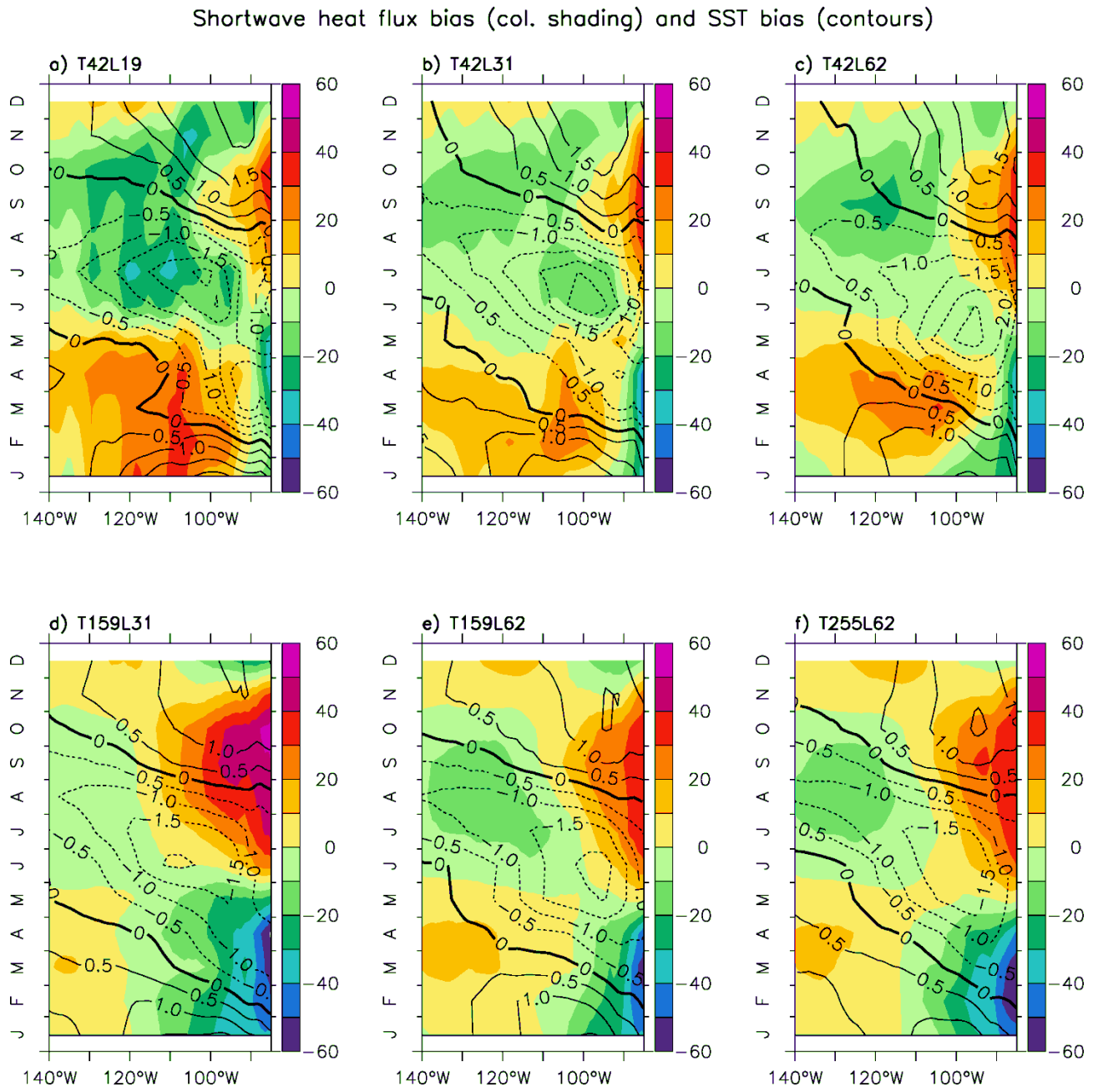

Fig. S5 Seasonal cycle of shortwave heat flux (color shading; positive values of heat flux refer to a heat transfer from the atmosphere into the ocean) and SST bias (contours) in the EEP for an ensemble of six KCM integrations at different atmospheric resolutions. The bias is calculated by subtracting observed monthly anomalies from KCM monthly anomalies. Anomalies are calculated with respect to the annual mean. All data are averaged over 2.8°S – 2.8°N. SST bias is in units °C and shortwave heat flux bias in Wm^{-2}.

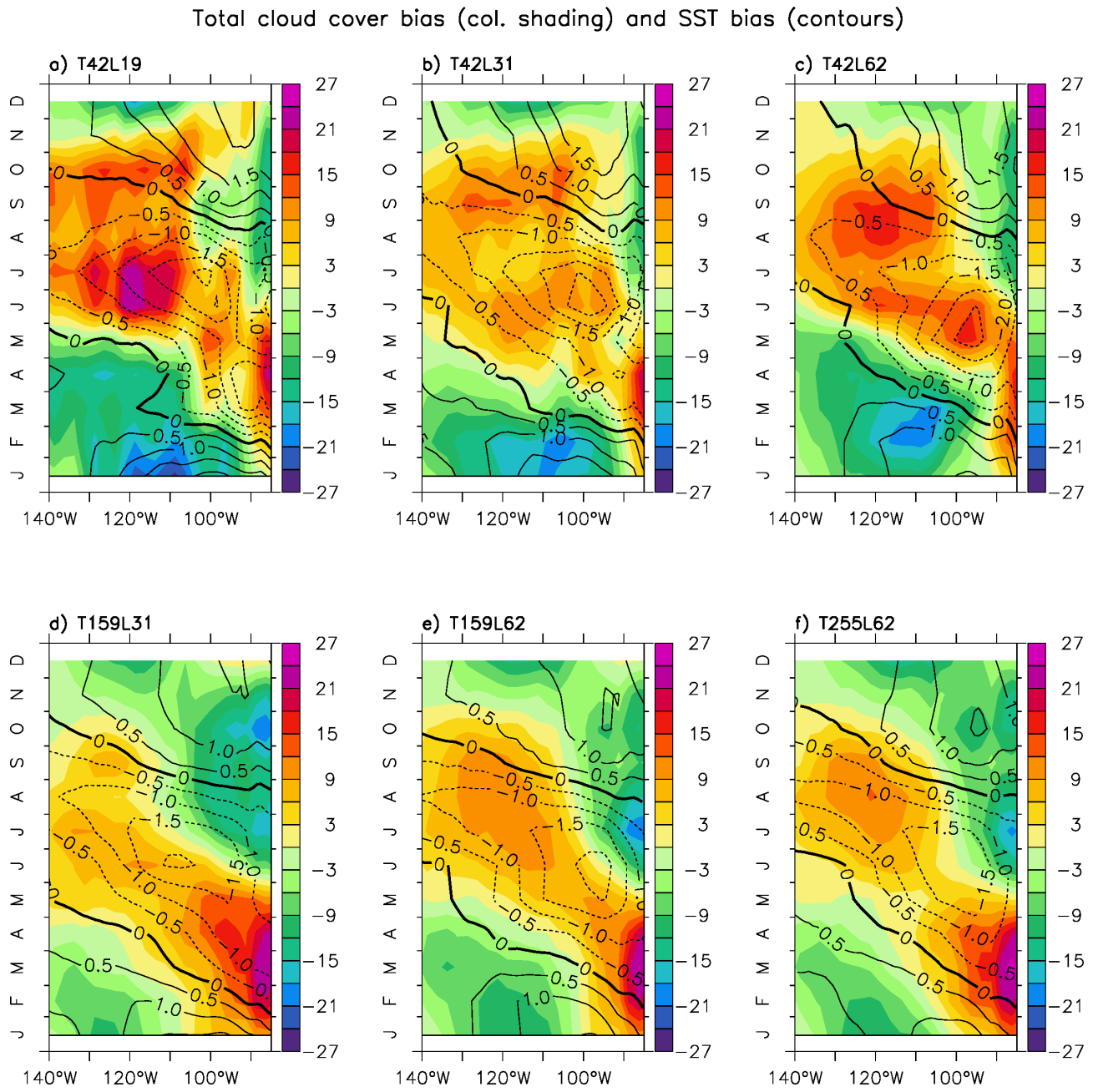

Fig. S6 Seasonal cycle of total cloud cover (color shading) and SST bias (contours) in the EEP for an ensemble of six KCM integrations at different atmospheric resolutions. The bias is calculated by subtracting observed monthly anomalies from KCM monthly anomalies. Anomalies are calculated with respect to the annual mean. All data are averaged over 2.8°S – 2.8°N. SST bias is in units °C and total cloud cover in %.

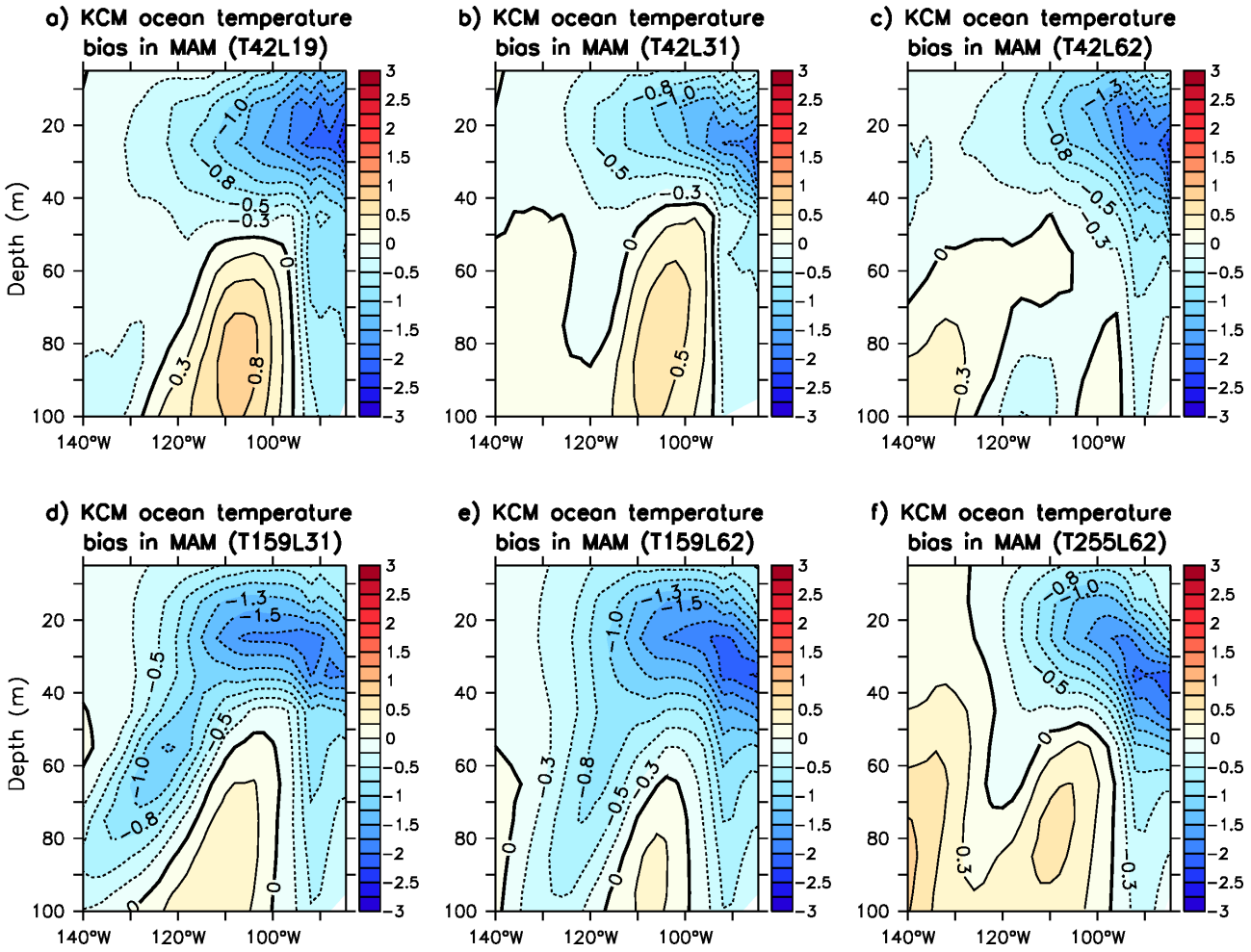

Fig. S7 Seasonal average of subsurface ocean temperature bias in the EEP during the months MAM for an ensemble of six KCM integrations at different atmospheric resolutions. The bias is calculated by subtracting observed seasonally-averaged monthly anomalies from KCM seasonally-averaged monthly anomalies. Anomalies are defined with respect to the annual mean. All data are averaged over 2.8°S – 2.8°N. Temperature bias is in units °C.

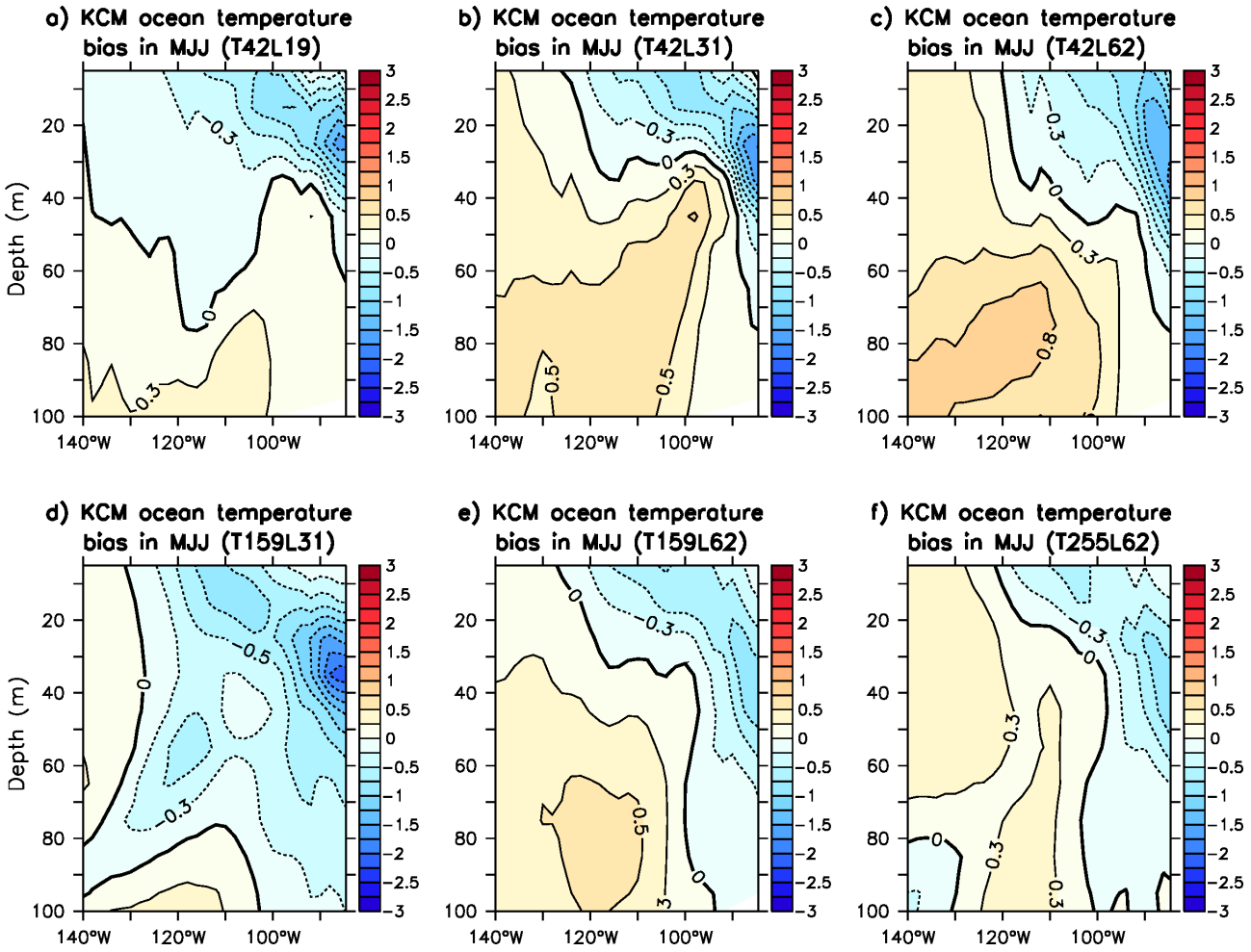

Fig. S8 Seasonal average of subsurface ocean temperature bias in the EEP during the months MJJ for an ensemble of six KCM integrations at different atmospheric resolutions. The bias is calculated by subtracting observed seasonally-averaged monthly anomalies from KCM seasonally-averaged monthly anomalies. Anomalies are defined with respect to the annual mean. All data are averaged over 2.8°S – 2.8°N. Temperature bias is in units °C.

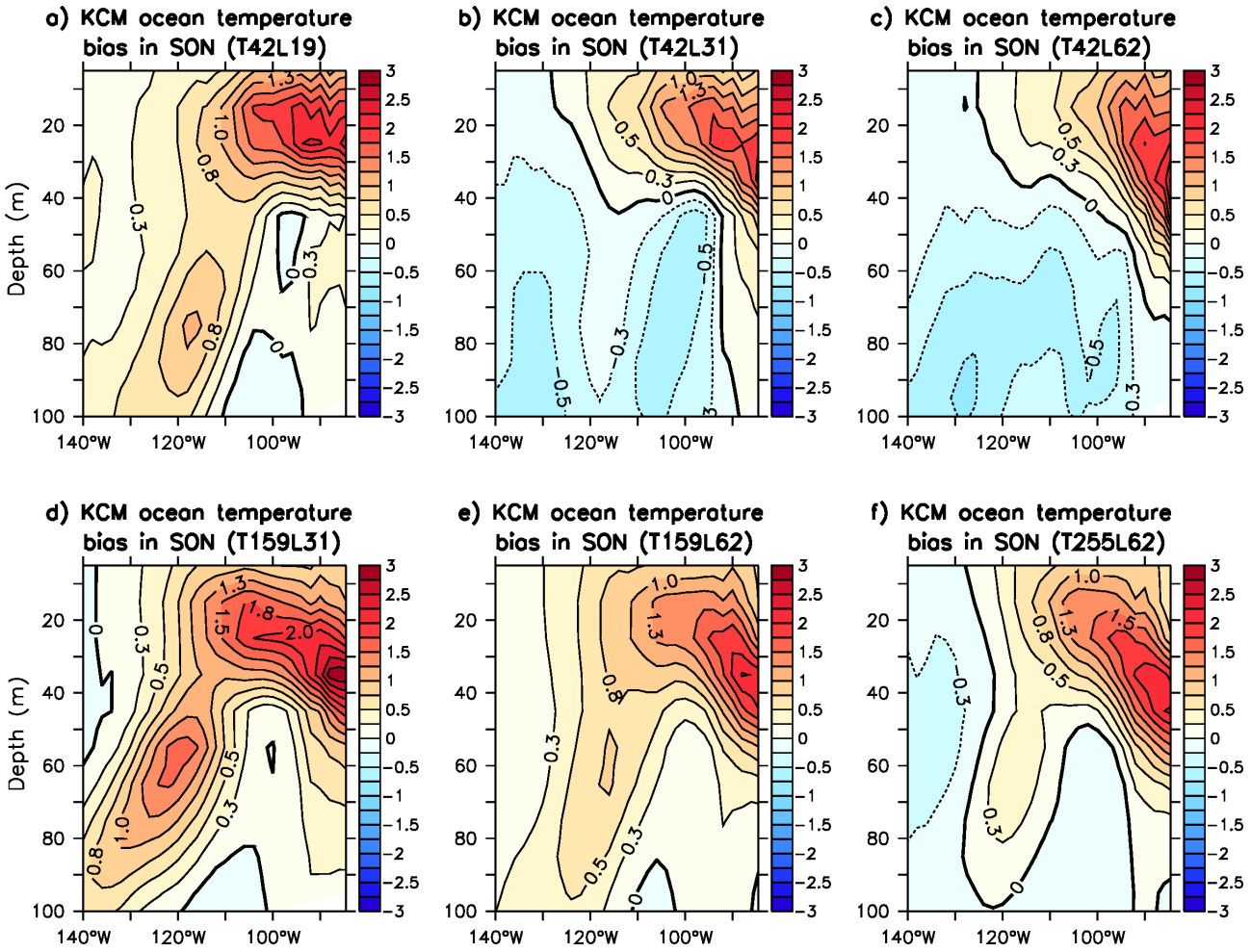

Fig. S9 Seasonal average of subsurface ocean temperature bias in the EEP during the months SON for an ensemble of six KCM integrations at different atmospheric resolutions. The bias is calculated by subtracting observed seasonally-averaged monthly anomalies from KCM seasonally-averaged monthly anomalies. Anomalies are defined with respect to the annual mean. All data are averaged over 2.8°S – 2.8°N. Temperature bias is in units °C.

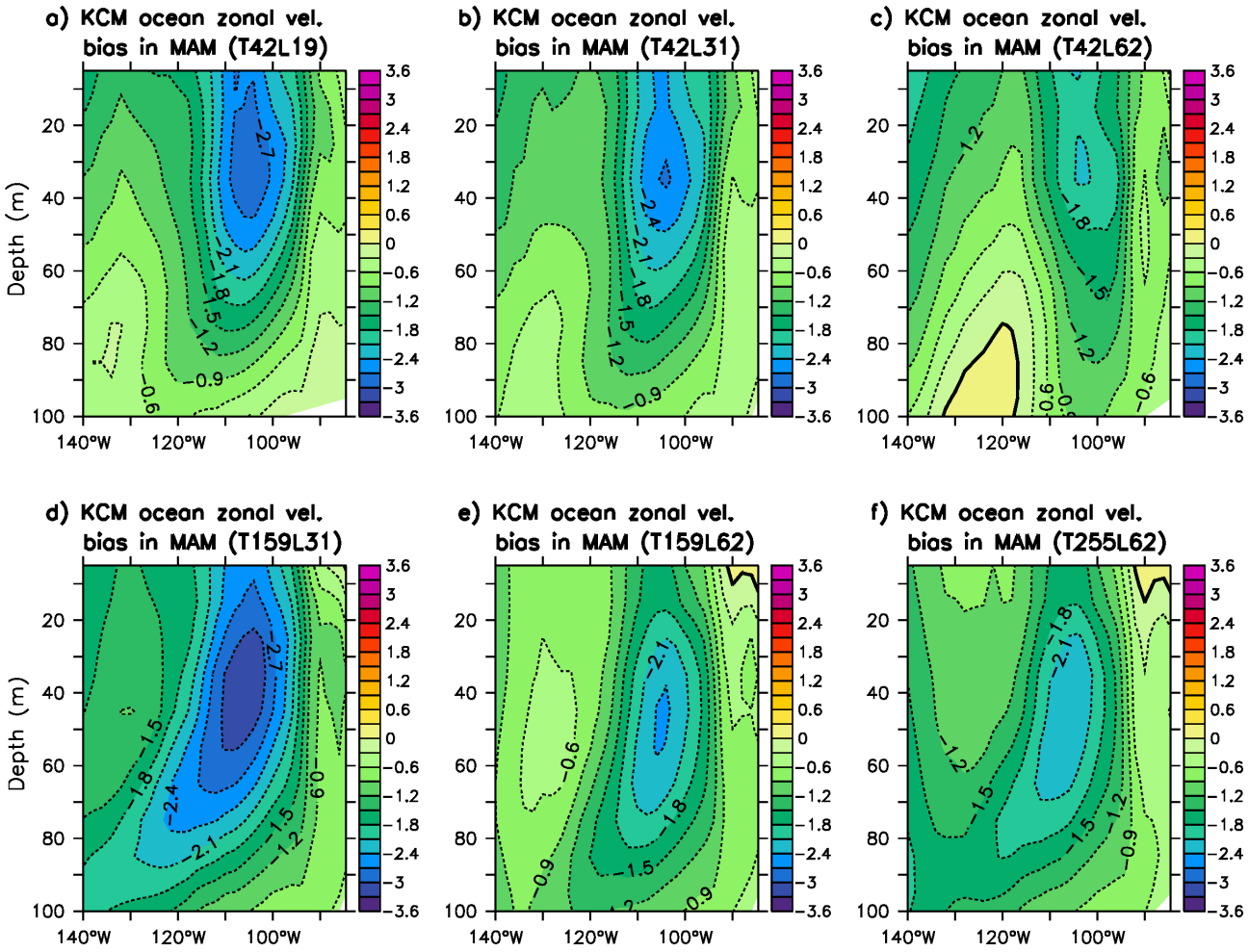

Fig. S10 Seasonal average of subsurface ocean zonal velocity bias in the EEP during the months MAM for an ensemble of six KCM integrations at different atmospheric resolutions. The bias is calculated by subtracting observed seasonally-averaged monthly anomalies from KCM seasonally-averaged monthly anomalies. Anomalies are defined with respect to the annual mean. All data are averaged over 2.8°S – 2.8°N. Velocity bias is in units dm s^{-1}.

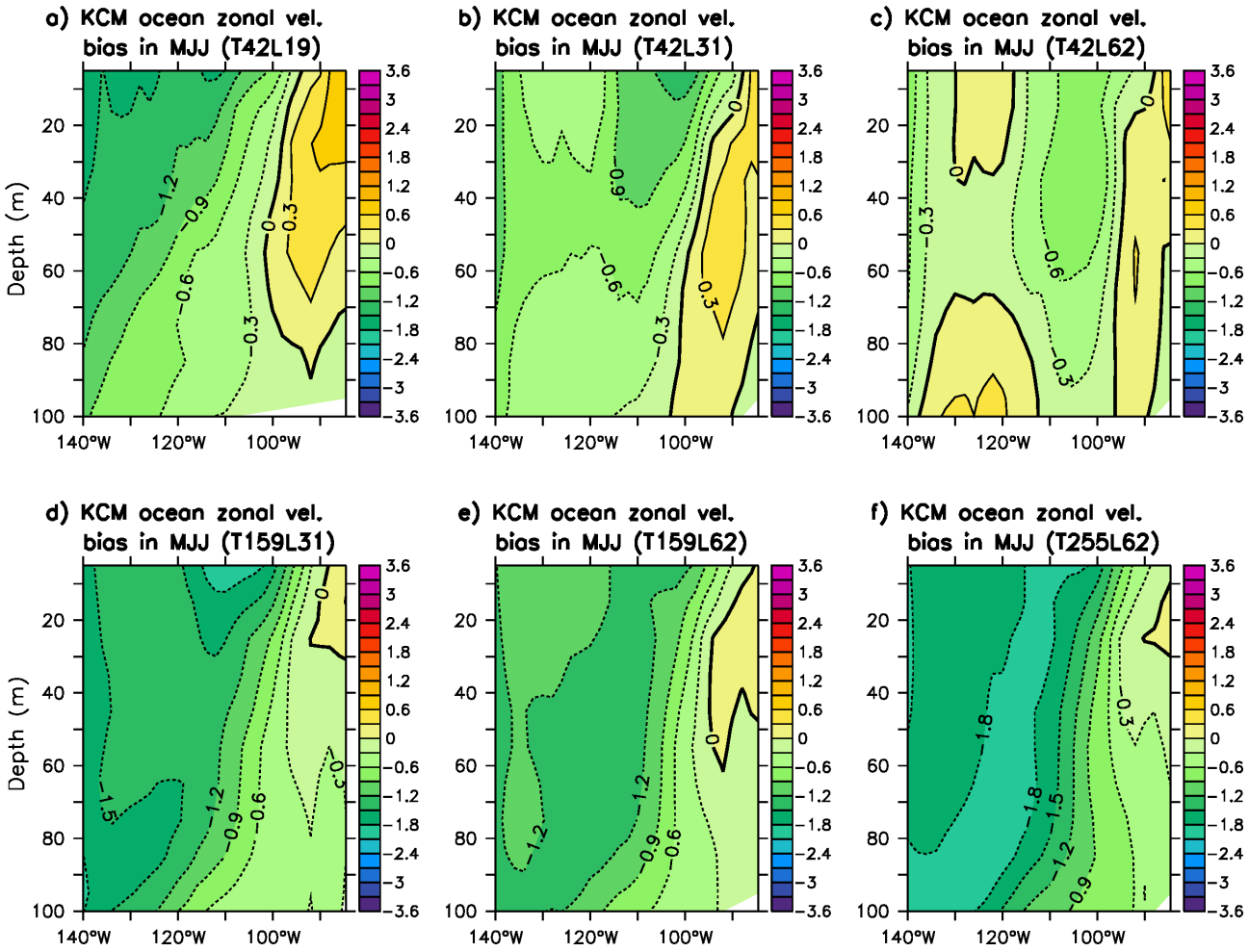

Fig. S11 Seasonal average of subsurface ocean zonal velocity bias in the EEP during the months MJJ for an ensemble of six KCM integrations at different atmospheric resolutions. The bias is calculated by subtracting observed seasonally-averaged monthly anomalies from KCM seasonally-averaged monthly anomalies. Anomalies are defined with respect to the annual mean. All data are averaged over 2.8°S – 2.8°N. Velocity bias is in units dm s^{-1}.

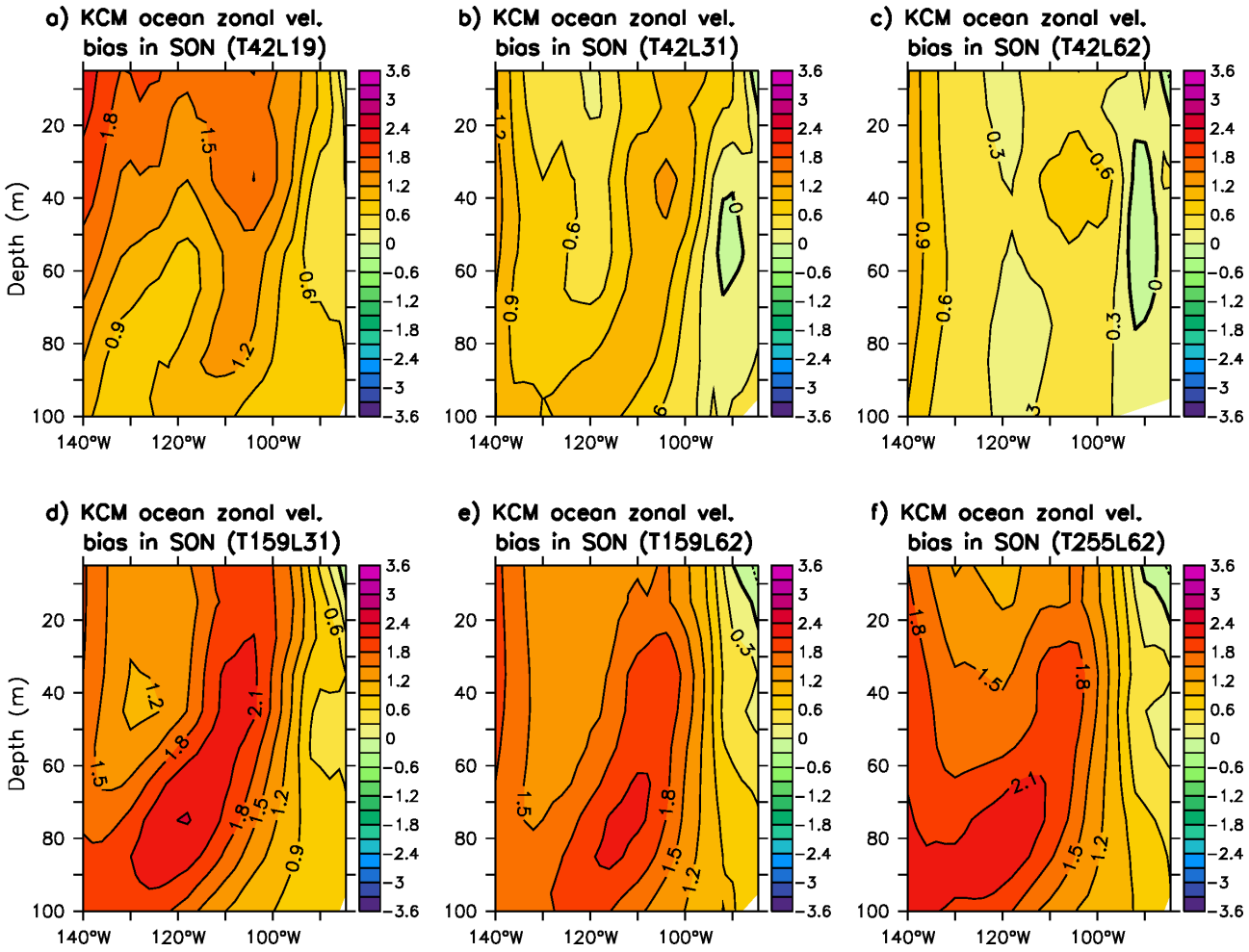

Fig. S12 Seasonal average of subsurface ocean zonal velocity bias in the EEP during the months SON for an ensemble of six KCM integrations at different atmospheric resolutions. The bias is calculated by subtracting observed seasonally-averaged monthly anomalies from KCM seasonally-averaged monthly anomalies. Anomalies are defined with respect to the annual mean. All data are averaged over 2.8°S – 2.8°N. Velocity bias is in units dm s^{-1}.

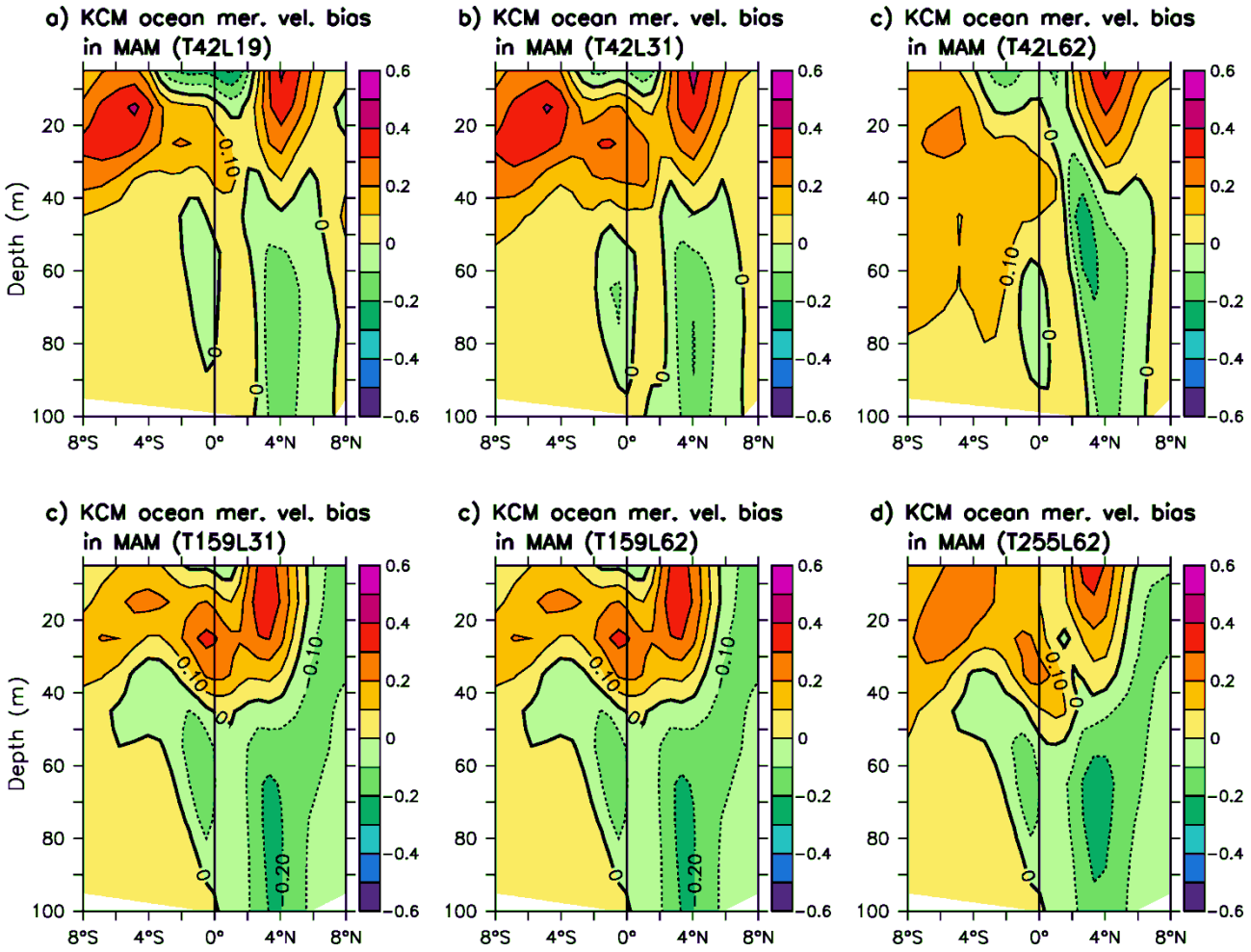

Fig. S13 Seasonal average of subsurface ocean meridional velocity bias in the EEP during the months MAM for an ensemble of six KCM integrations at different atmospheric resolutions. The bias is calculated by subtracting observed seasonally-averaged monthly anomalies from KCM seasonally-averaged monthly anomalies. Anomalies are defined with respect to the annual mean. All data are averaged over 140°W – 85°W. Velocity bias is in units dm s^{-1}.

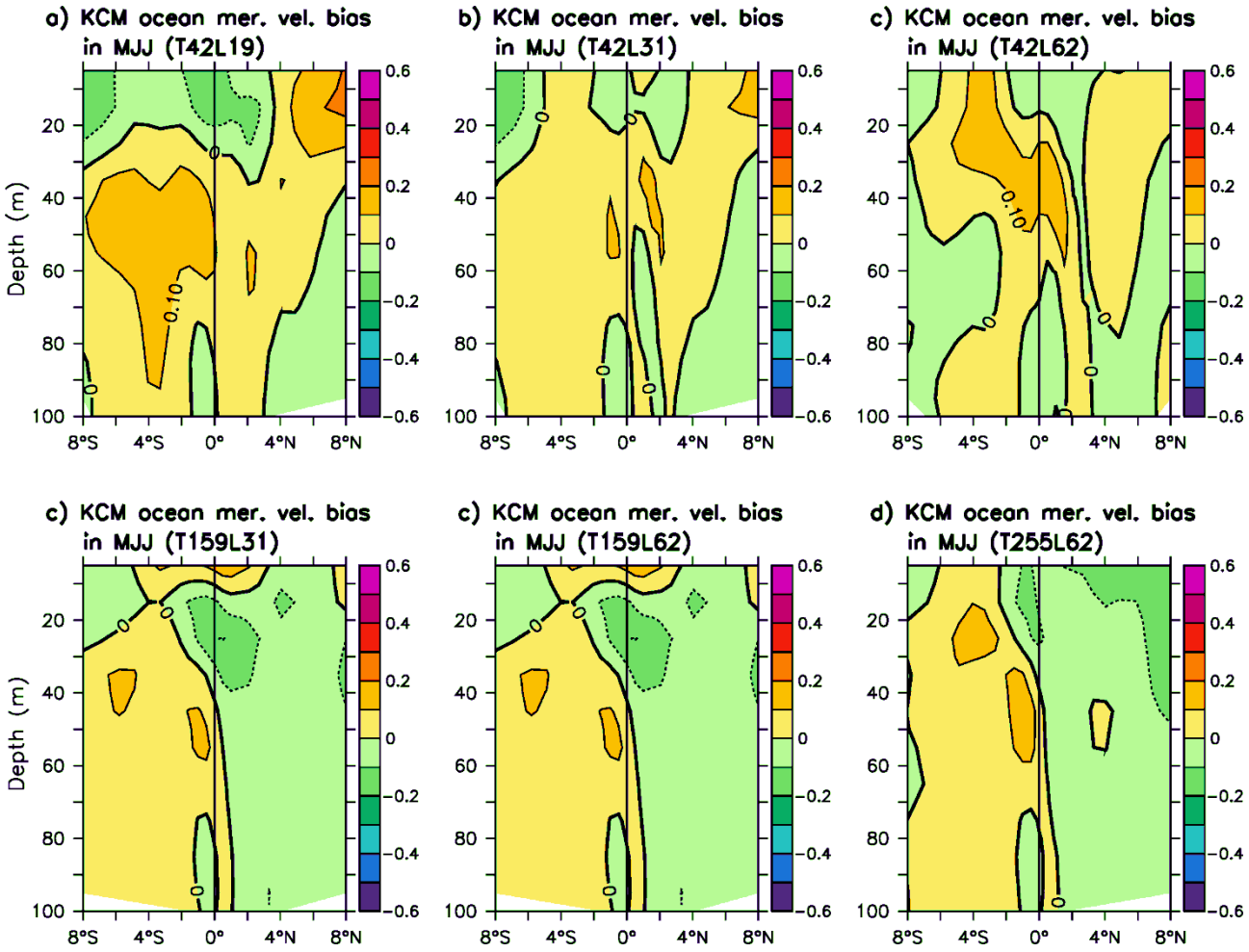

Fig. S14 Seasonal average of subsurface ocean meridional velocity bias in the EEP during the months MJJ for an ensemble of six KCM integrations at different atmospheric resolutions. The bias is calculated by subtracting observed seasonally-averaged monthly anomalies from KCM seasonally-averaged monthly anomalies. Anomalies are defined with respect to the annual mean. All data are averaged over 140°W – 85°W. Velocity bias is in units dm s^{-1}.

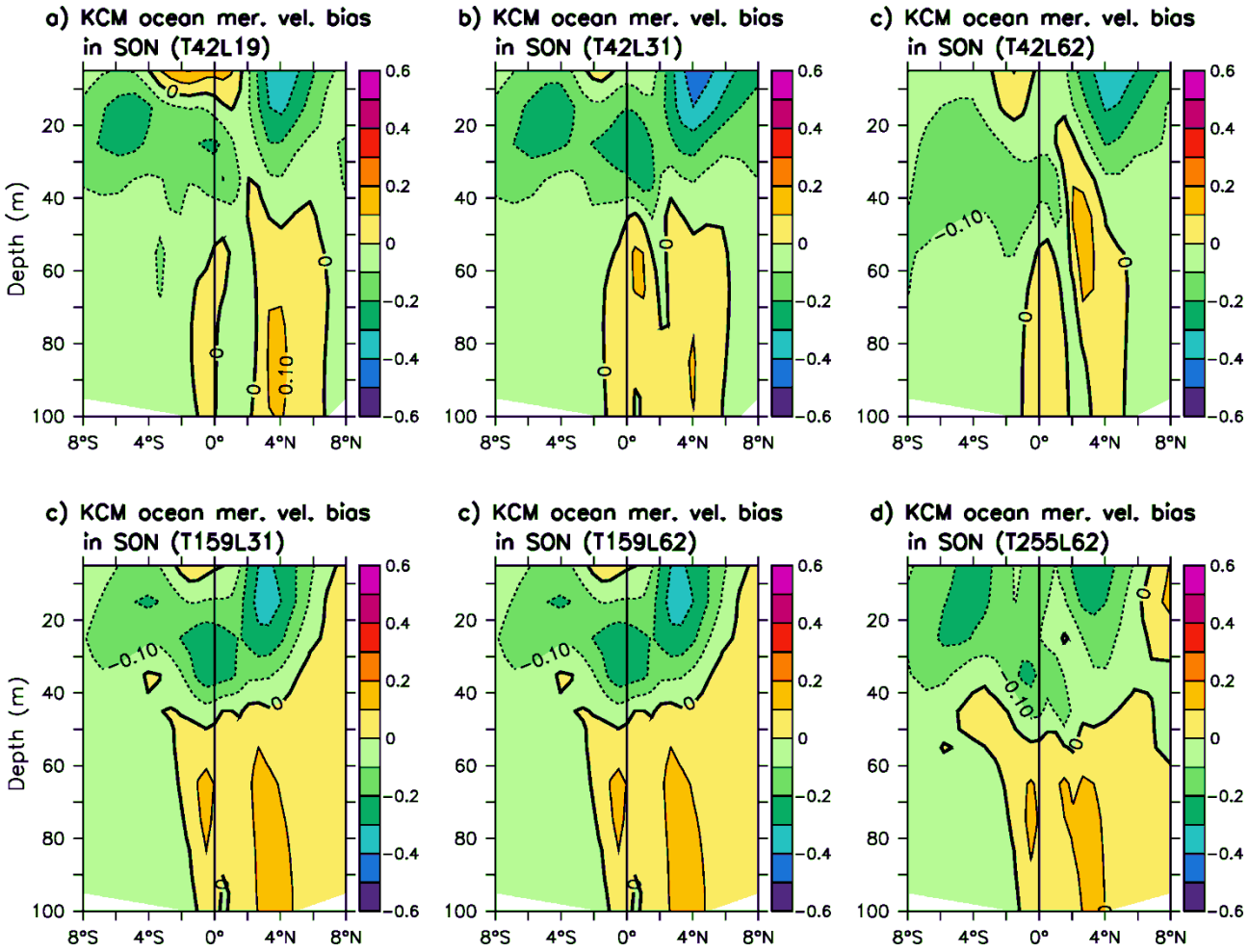

Fig. S15 Seasonal average of subsurface ocean meridional velocity bias in the EEP during the months SON for an ensemble of six KCM integrations at different atmospheric resolutions. The bias is calculated by subtracting observed seasonally-averaged monthly anomalies from KCM seasonally-averaged monthly anomalies. Anomalies are defined with respect to the annual mean. All data are averaged over 140°W – 85°W. Velocity bias is in units dm s^{-1}.

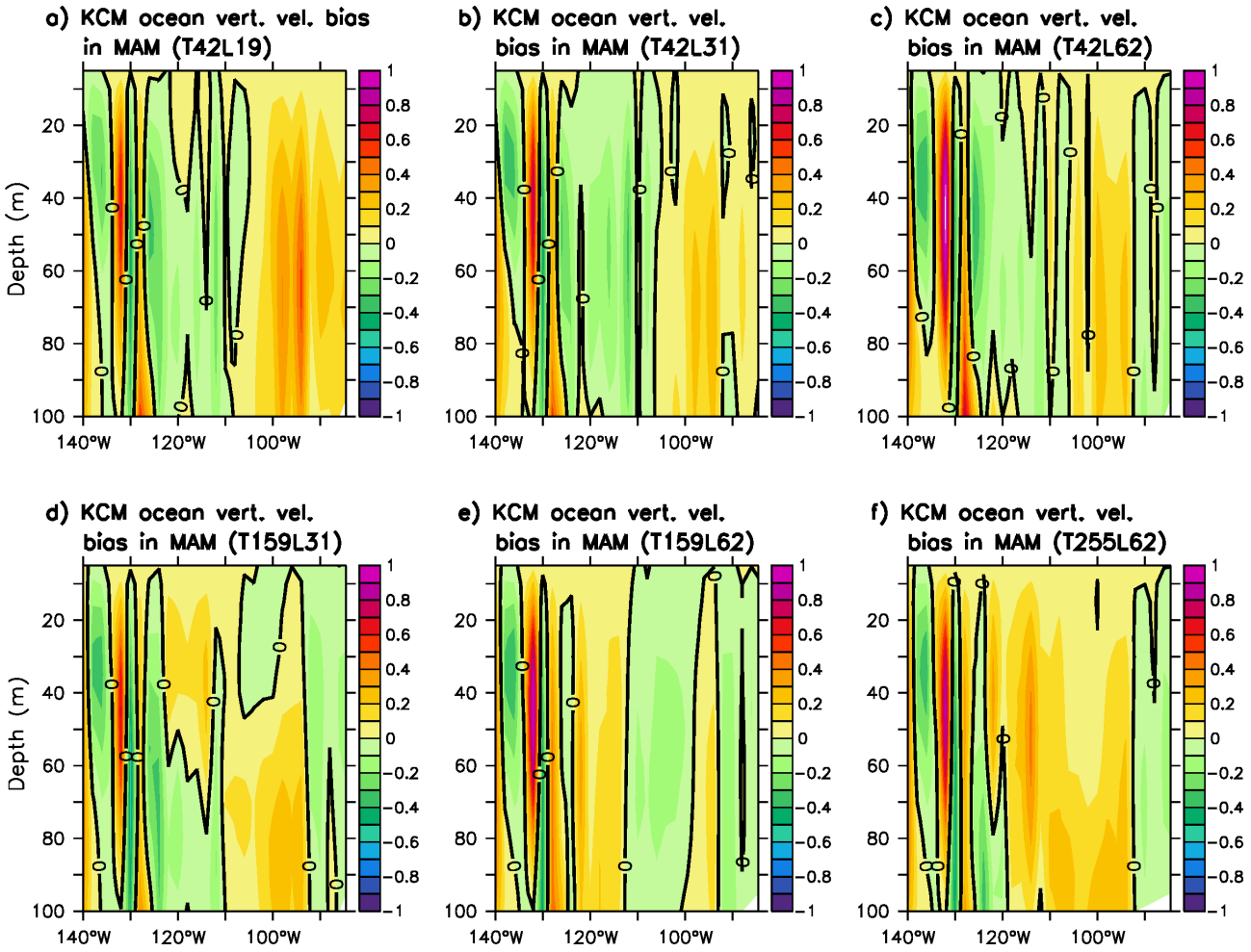

Fig. S16 Seasonal average of subsurface ocean vertical velocity bias in the EEP during the months MAM for an ensemble of six KCM integrations at different atmospheric resolutions. The bias is calculated by subtracting observed seasonally-averaged monthly anomalies from KCM seasonally-averaged monthly anomalies. Anomalies are defined with respect to the annual mean. All data are averaged over 2.8°S – 2.8°N. Velocity bias is in units m day^{-1}.

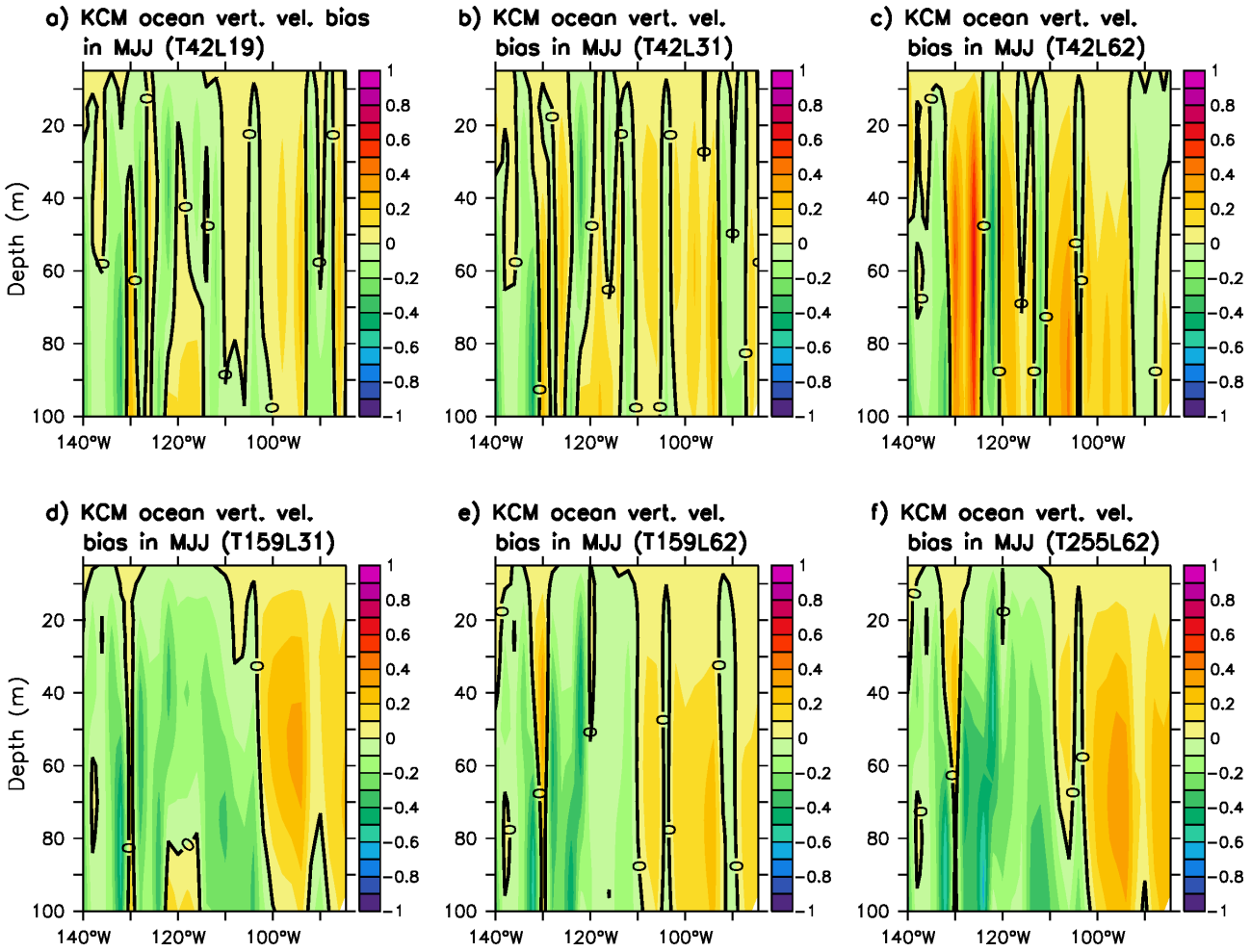

Fig. S17 Seasonal average of subsurface ocean vertical velocity bias in the EEP during the months MJJ for an ensemble of six KCM integrations at different atmospheric resolutions. The bias is calculated by subtracting observed seasonally-averaged monthly anomalies from KCM seasonally-averaged monthly anomalies. Anomalies are defined with respect to the annual mean. All data are averaged over 2.8°S – 2.8°N. Velocity bias is in units m day^{-1}.

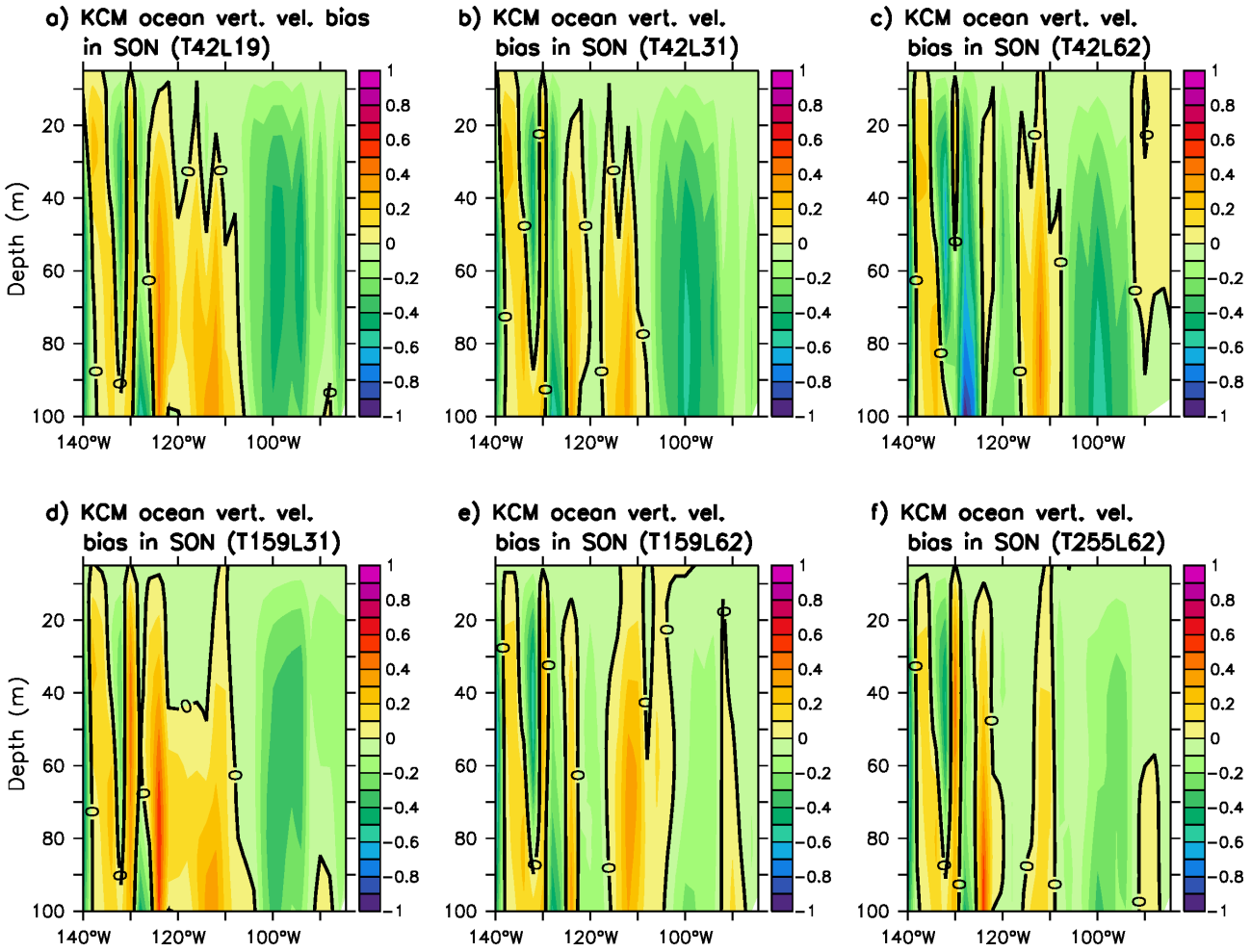

Fig. S18 Seasonal average of subsurface ocean vertical velocity bias in the EEP during the months SON for an ensemble of six KCM integrations at different atmospheric resolutions. The bias is calculated by subtracting observed seasonally-averaged monthly anomalies from KCM seasonally-averaged monthly anomalies. Anomalies are defined with respect to the annual mean. All data are averaged over 2.8°S – 2.8°N. Velocity bias is in units m day^{-1}.

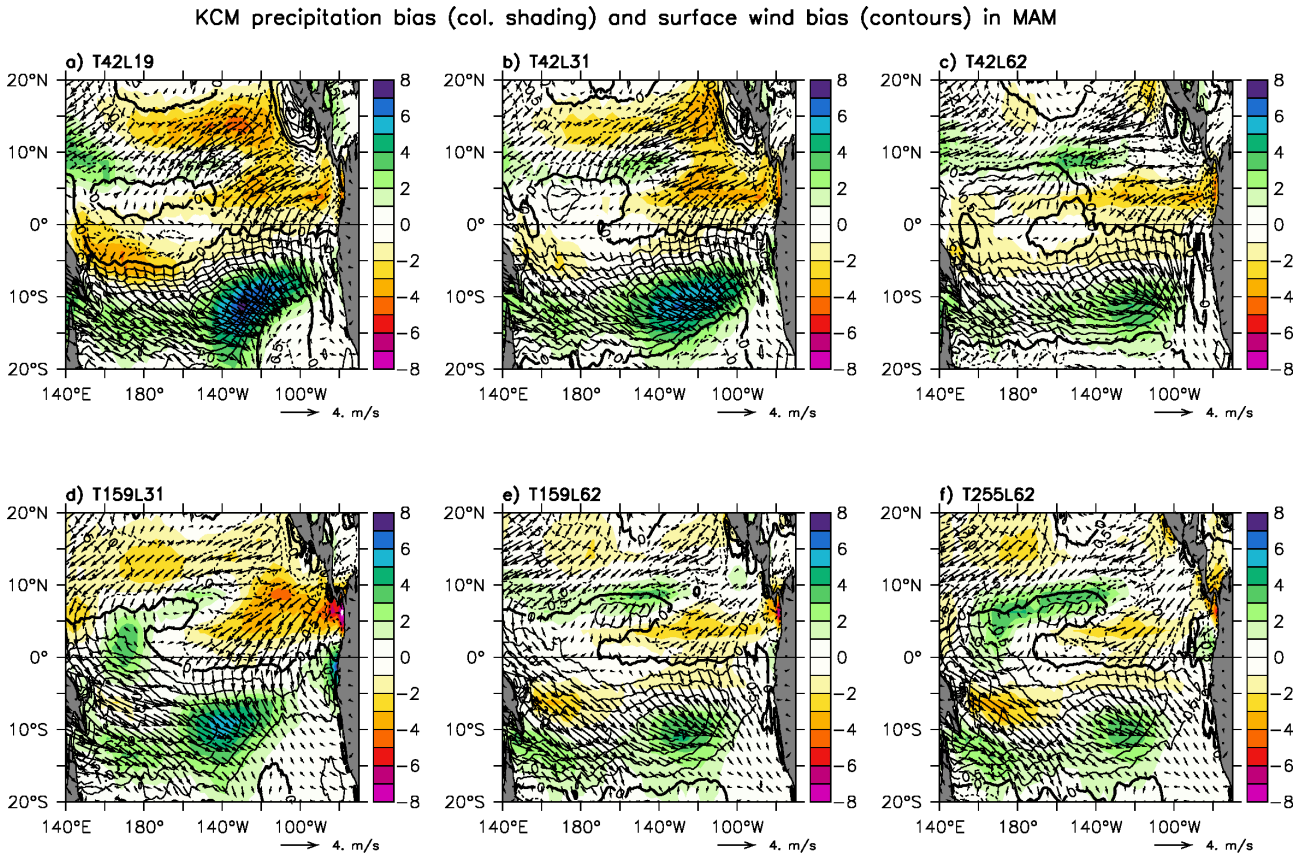

Fig. S19 Seasonal average of tropical Pacific precipitation bias (color shading), zonal wind bias (contours) and surface wind bias (arrows) during the months MAM for an ensemble of six KCM integrations at different atmospheric resolutions. The bias is calculated by subtracting observed seasonally-averaged monthly anomalies from KCM seasonally-averaged monthly anomalies. Anomalies are defined with respect to the annual mean. Precipitation bias is in units mm day^{-1} and wind in ms^{-1}.

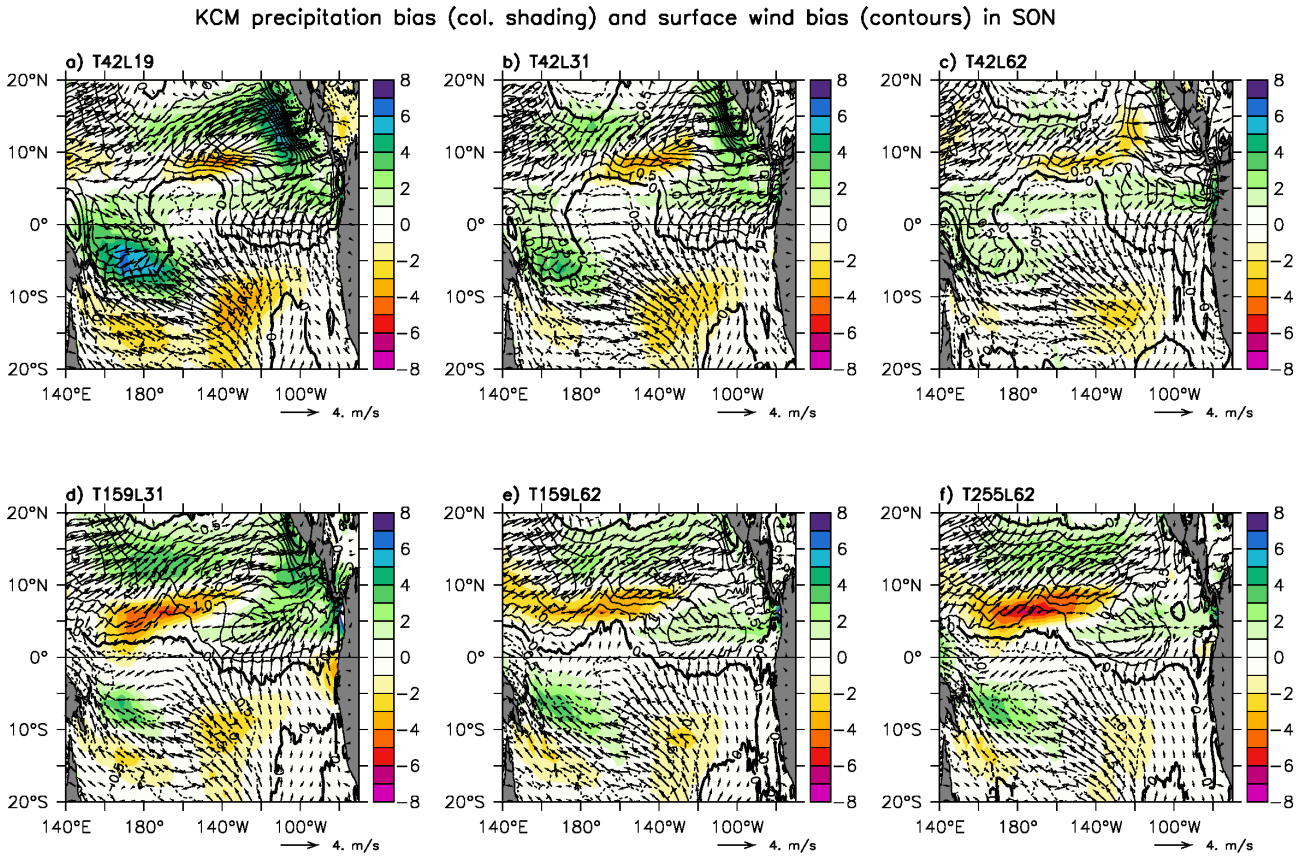

Fig. S20 Seasonal average of tropical Pacific precipitation bias (color shading), zonal wind bias (contours) and surface wind bias (arrows) during the months SON for an ensemble of six KCM integrations at different atmospheric resolutions. The bias is calculated by subtracting observed seasonally-averaged monthly anomalies from KCM seasonally-averaged monthly anomalies. Anomalies are defined with respect to the annual mean. Precipitation bias is in units mm day^{-1} and wind in ms^{-1}.

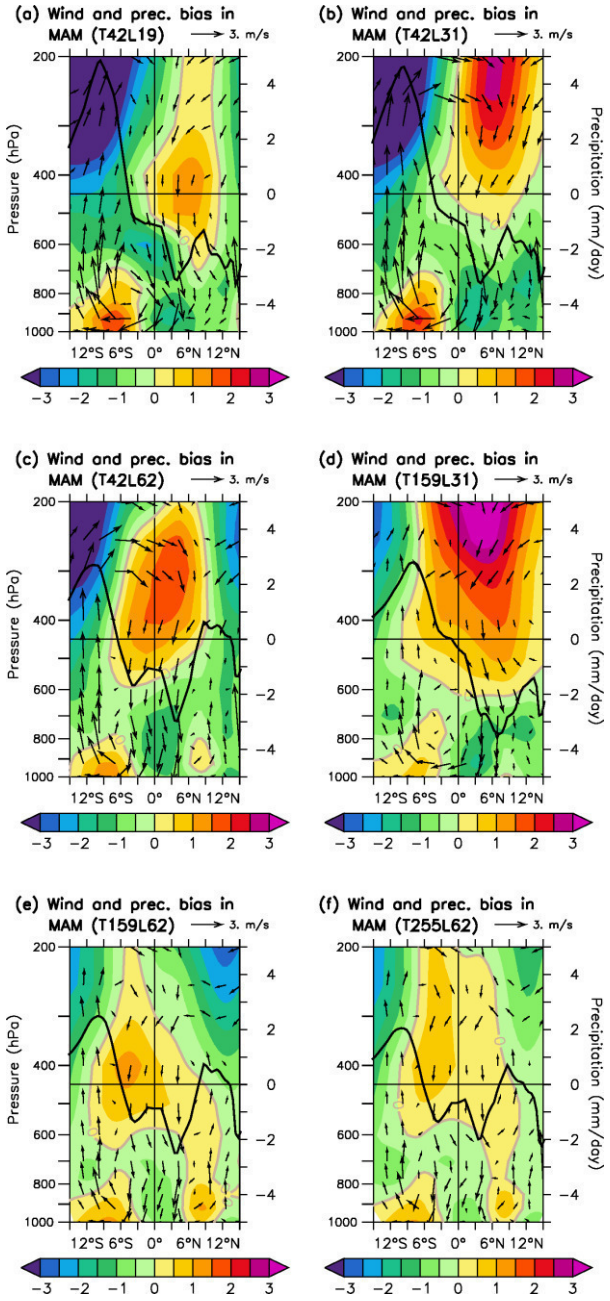

Fig. S21 Seasonal average of zonal wind bias (color shading), meridional-vertical wind bias (arrows) and precipitation bias (black line) centered about the equator in the eastern tropical Pacific during the months MAM for an ensemble of six KCM integrations at different atmospheric resolutions. The bias is calculated by subtracting observed seasonally-averaged monthly anomalies from KCM seasonally-averaged monthly anomalies. Shown are anomalies defined with respect to the annual mean. All data are averaged over 140°W – 85°W. The horizontal black line marks zero precipitation anomalies. Precipitation bias is in units mm day^{-1} and wind in ms^{-1}. Vertical wind is scaled by 90.

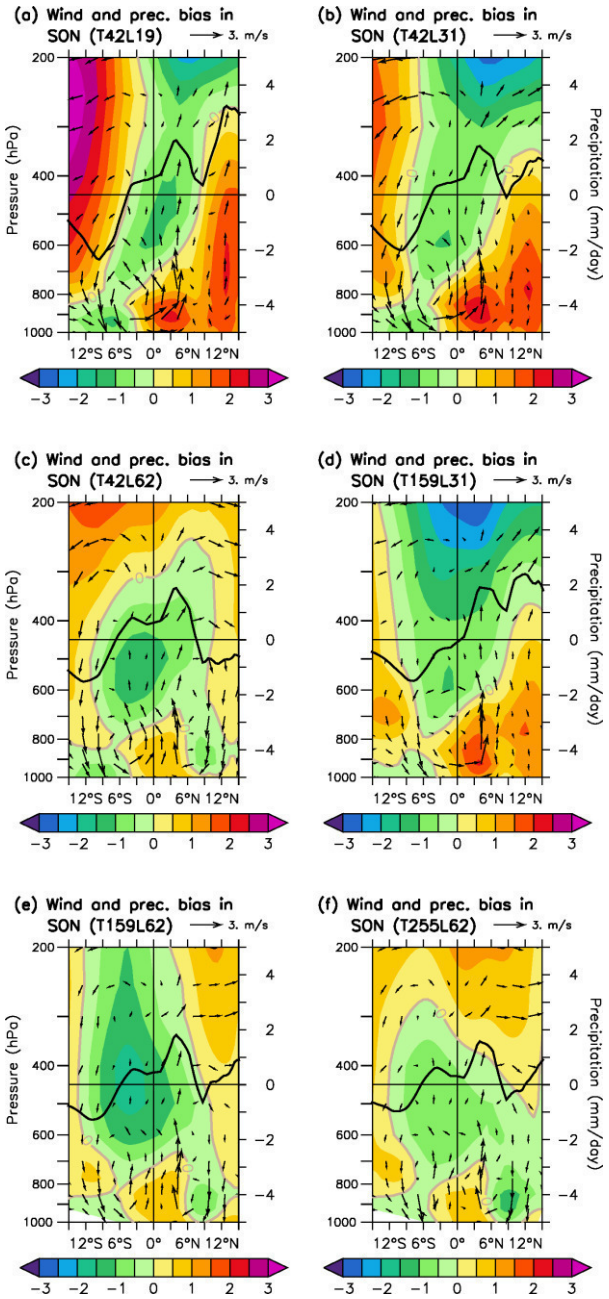

Fig. S22 Seasonal average of zonal wind bias (color shading), meridional-vertical wind bias (arrows) and precipitation bias (black line) centered about the equator in the eastern tropical Pacific during the months SON for an ensemble of six KCM integrations at different atmospheric resolutions. The bias is calculated by subtracting observed seasonally-averaged monthly anomalies from KCM seasonally-averaged monthly anomalies. Shown are anomalies defined with respect to the annual mean. All data are averaged over 140°W – 85°W. The horizontal black line marks zero precipitation anomalies. Precipitation bias is in units mm day^{-1} and wind in ms^{-1}. Vertical wind is scaled by 90.

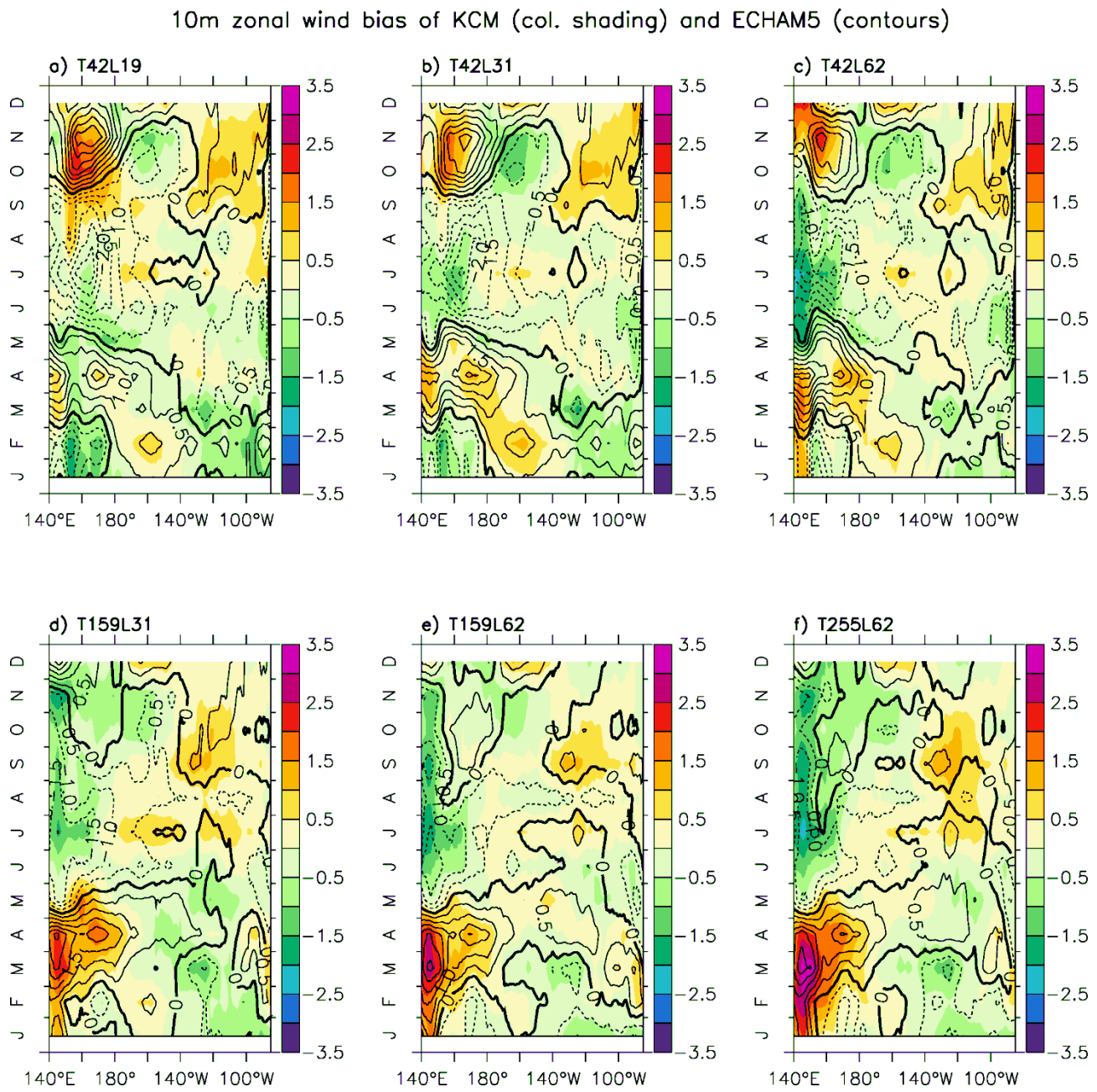

Fig. S23 Seasonal cycle of 10 m zonal wind bias in the equatorial Pacific of the KCM (color shading) and in the atmospheric model component ECHAM5 forced by observed monthly SST climatology (contours) for an ensemble of six integrations at different atmospheric resolutions. The bias is calculated by subtracting observed monthly anomalies from KCM and ECHAM5 monthly anomalies. Anomalies are calculated with respect to the annual mean. All data are averaged over 2.8°S – 2.8°N. Wind bias is in units $ms^{-1.}$

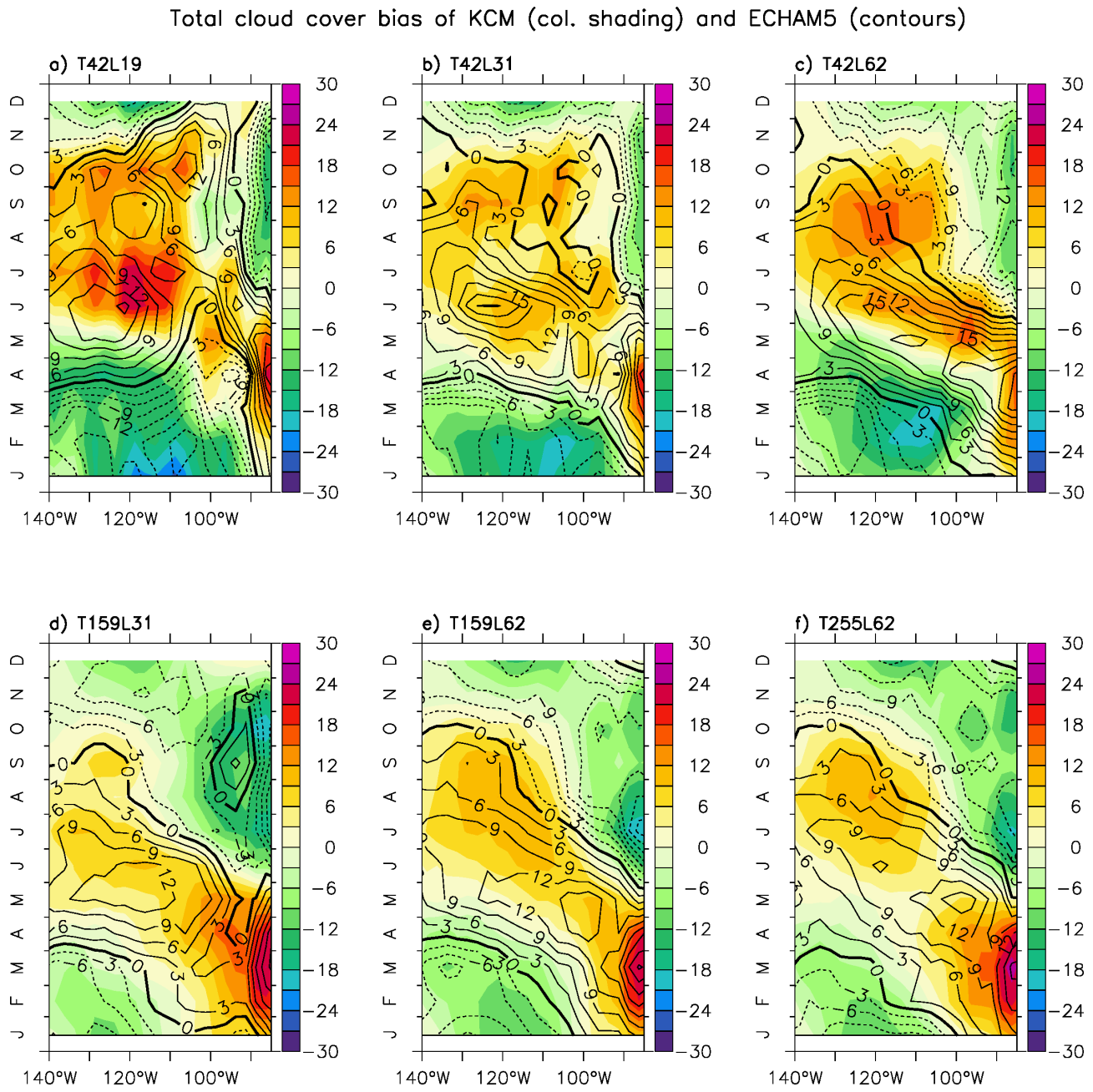

Fig. S24 Seasonal cycle of total cloud cover bias in the equatorial Pacific of the KCM (color shading) and in the atmospheric model component ECHAM5 forced by observed monthly SST climatology (contours) for an ensemble of six integrations at different atmospheric resolutions. The bias is calculated by subtracting observed monthly anomalies from KCM and ECHAM5 monthly anomalies. Anomalies are calculated with respect to the annual mean. All data are averaged over 2.8°S – 2.8°N. Cloud cover bias is in units %.

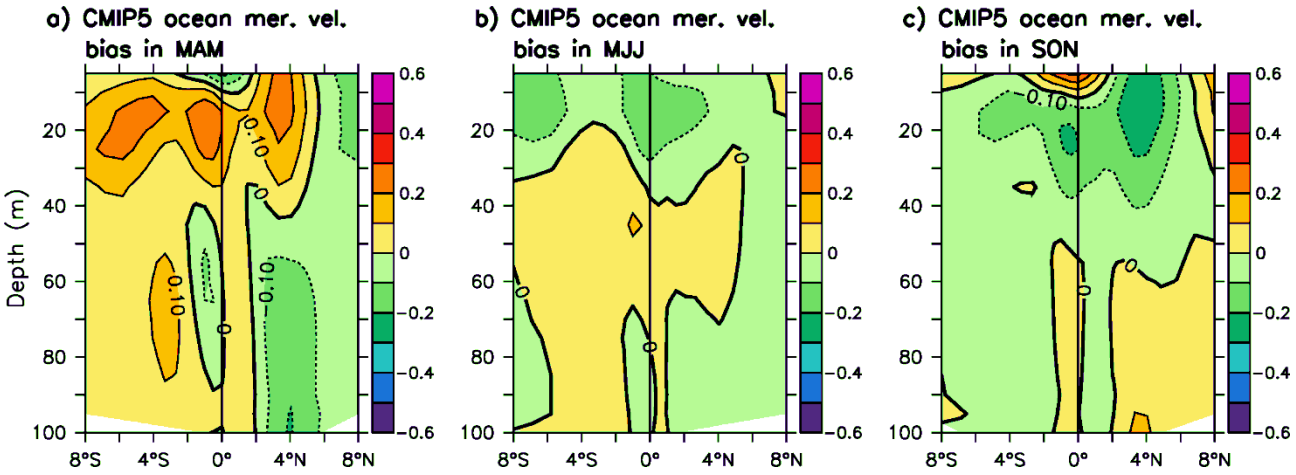

Fig. S25 Seasonal average of subsurface ocean meridional velocity bias in the EEP during the months (a) MAM, (b) MJJ and (c) SON of the CMIP5 models (Table 2). The bias is calculated by subtracting observed seasonally-averaged monthly anomalies from ensemble-mean seasonally-averaged monthly anomalies. Anomalies are defined with respect to the annual mean. All data are averaged over 140°W – 85°W.

3 Seasonal ENSO phase locking in the Kiel Climate Model: The importance of the equatorial cold sea surface temperature bias

Wengel, C., Latif, M., Park, W., Harlaß, J., and Bayr, T. (2018). Seasonal ENSO phase locking in the Kiel Climate Model: The importance of the equatorial cold sea surface temperature bias. Climate Dynamics, 50: 901. https://doi.org/10.1007/s00382-017-3648-3

The candidates' contributions to this publication are as follows:

1. He designed and performed all model experiments.
2. He did all the analyses.
3. He produced all the figures.
4. He authored the manuscript from the first draft to the final version.

Clim Dyn (2018) 50:901–919
DOI 10.1007/s00382-017-3648-3

Seasonal ENSO phase locking in the Kiel Climate Model: The importance of the equatorial cold sea surface temperature bias

C. Wengel[1] · M. Latif[1,2] · W. Park[1] · J. Harlaß[1] · T. Bayr[1]

Received: 8 July 2016 / Accepted: 16 March 2017 / Published online: 28 March 2017

Abstract The El Niño/Southern Oscillation (ENSO) is characterized by a seasonal phase locking, with strongest eastern and central equatorial Pacific sea surface temperature (SST) anomalies during boreal winter and weakest SST anomalies during boreal spring. In this study, key feedbacks controlling seasonal ENSO phase locking in the Kiel Climate Model (KCM) are identified by employing Bjerknes index stability analysis. A large ensemble of simulations with the KCM is analyzed, where the individual runs differ in either the number of vertical atmospheric levels or coefficients used in selected atmospheric parameterizations. All integrations use the identical ocean model. The ensemble-mean features realistic seasonal ENSO phase locking. ENSO phase locking is very sensitive to changes in the mean-state realized by the modifications described above. An excessive equatorial cold tongue leads to weak phase locking by reducing the Ekman feedback and thermocline feedback in late boreal fall and early boreal winter. Seasonal ENSO phase locking also is sensitive to the shortwave feedback as part of the thermal damping in early boreal spring, which strongly depends on eastern and central equatorial Pacific SST. The results obtained from the KCM are consistent with those from models participating in the Coupled Model Intercomparison Project phase 5 (CMIP5).

Keywords Seasonal ENSO phase locking · SST bias · Kiel Climate Model

1 Introduction

The El Niño/Southern Oscillation (ENSO) is the dominant mode of interannual climate variability in the tropics. ENSO is characterized by sea surface temperature (SST) anomalies of a few centigrade primarily in the eastern and central equatorial Pacific, which drive global teleconnections (e.g. Brönnimann et al. 2004). The warm phase of ENSO is termed El Niño, its cold phase La Niña. A robust feature of ENSO is its preference to exhibit peak SST anomalies in boreal winter and to depict only small anomalies in boreal spring. This behavior is referred to as seasonal ENSO phase locking (e.g. Tziperman et al. 1998; Neelin et al. 2000; McGregor et al. 2012).

Several previous studies have discussed the dynamics that cause the seasonal phase locking of ENSO (e.g. Chang et al. 1995; Tziperman et al. 1995; Jin et al. 1996; Harrison and Vecchi 1999; Neelin et al. 2000; Stuecker et al. 2013; McGregor et al. 2013; Zhu et al. 2015). Yet there are still significant gaps in our understanding of these dynamics. A majority of these studies provide an explanation in terms of stochastic forcing acting on a seasonally changing background state. Others argue in terms of feedbacks. For example, the termination of ENSO in boreal spring can be linked to the southward shift of wind anomalies (Harrison and Vecchi 1999; Stuecker et al. 2013 and; McGregor et al. 2013) or to the relatively weak linkage between SST and thermocline depth in that season (Zhu et al. 2015). Results by Stein et al. (2010) on the basis of the recharge oscillator suggest that the seasonally varying growth rate is critical to ENSO phase locking, where damping by the mean flow

Electronic supplementary material The online version of this article (doi:10.1007/s00382-017-3648-3) contains supplementary material, which is available to authorized users.

✉ C. Wengel
cwengel@geomar.de

[1] GEOMAR Helmholtz Centre for Ocean Research Kiel, Kiel, Germany

[2] University of Kiel, Kiel, Germany

field dominates the seasonally changing dynamics. Dommenget and Yu (2016) show that ENSO phase locking is strongly linked to seasonal changes in shortwave radiation due to changes in cloud cover.

In the past, significant progress has been made in understanding ENSO dynamics (see e.g. Wang and Picaut 2004 for a review) and in simulating ENSO (e.g. Bellenger et al. 2014). However, many coupled ocean–atmosphere general circulation models (CGCMs) still have difficulties in simulating seasonal ENSO phase locking as observed. Amongst others, ENSO phase locking is particularly important to ENSO forecast (Jin and Kinter 2009) and ENSO teleconnections. For example, the influence of ENSO on the Indian summer monsoon critically depends on the CGCMs' ability to realistically represent ENSO phase locking (e.g. Webster et al. 1998). Typical problems in CGCMs are that ENSO extremes either peak in the wrong season (e.g. Ham et al. 2012; Ham and Kug 2014; Rashid and Hirst 2015) or that the annual variation of SST variability is too weak (Ham and Kug 2014; Bellenger et al. 2014).

Zheng and Yu (2007) link the spurious summer peak in ENSO variability in the FGCM model to the double Intertropical Convergence Zone (ITCZ) problem. This model bias sets conditions for heat content anomalies originating erroneously south of the equator and at the wrong time of the year. Ham et al. (2012) identify an excessively large SST gradient and resultant thermocline shoaling in boreal summer to enhance zonal advection feedback and thermocline feedback as reasons for spurious boreal summer variability in the GFDL CGCM. Similar results are obtained by Ham and Kug (2014) for a set of CMIP3 and CMIP5 models. Rashid and Hirst (2015) find an incorrect simulation of the shortwave feedback and thermocline feedback to cause variability to peak in March instead December-February in the ACCESS CGCM and link the biases to errors in long-term mean SST.

A number of studies have focused on finding reasons for too weak annual variation of interannual variability in CGCMs, but with the seasonal phase being overall correct. Xiao and Mechoso (2009) show that the seasonal warming of the cold tongue in January-April favors the onset of an El Niño or La Niña event, whereas the termination of an event is connected to a southward shift of surface zonal wind anomalies. Ham and Kug (2014) also link the importance of the southward shift of surface zonal wind anomalies to a models' ability to have ENSO phase-locked to the annual cycle. Furthermore, Bellenger et al. (2014) suggest that a better simulation of the shortwave feedback helps to simulate a more pronounced annual variation of equatorial Pacific SST variability in CMIP3 and CMIP5 models.

ENSO originates from large-scale ocean–atmosphere interactions and is based on a feedback cycle, as originally proposed by Bjerknes (1969). The Bjerknes stability index (BJ index) of Jin et al. (2006) is a powerful tool to examine feedbacks, positive and negative, relevant to ENSO and the relative importance of the contributing terms on the basis of a linearized SST equation. The BJ index therefore is a measure of coupled ocean–atmosphere stability or growth rate of SST anomalies. Stein et al. (2014) argue that the seasonal modulation of the coupled stability is responsible for the ENSO being phase-locked to the annual cycle. Hence, the BJ index would form a useful and comprehensive tool for investigating ENSO phase locking, particularly because it comprises those processes in both atmosphere and ocean that are known to determine interannual variability. This also is consistent with Stein et al. (2010) who use the seasonally changing BJ index to examine ENSO phase locking in a simple recharge oscillator model.

In the equatorial Pacific, a pervasive systematic bias in CGCMs is an excessive equatorial cold tongue (e.g. Davey et al. 2002; Zhang et al. 2007; Guilyardi et al. 2009). Although relatively small in magnitude compared to other tropical SST biases (e.g. the southeastern tropical Pacific warm SST bias), the cold equatorial Pacific SST bias has far reaching implications. Too cold sea surface conditions in the cold tongue region suppress precipitation at the equator (Li and Xie 2014), among others one reason for the double ITCZ problem, and thus reduce ocean–atmosphere coupling. Therefore it is not surprising that the cold SST bias influences a CGCM's ability to simulate ENSO (e.g. Kim et al. 2013) and in particular ENSO phase locking (Battisti and Hirst 1989; Ham and Kug 2014).

In this study, the controls of seasonal ENSO phase locking in the Kiel Climate Model (KCM) are investigated. A novel approach applied here is the usage of the BJ index to identify the processes that determine ENSO phase locking in a CGCM. The BJ index is calculated for each calendar month separately to investigate its seasonal variation. Analysis of the individual feedbacks contributing to the BJ index reveals the importance of specific physical processes that control ENSO phase locking in the KCM. Moreover, the feedbacks are linked to the long-term mean-state. Thus possible reasons for ENSO phase locking biases in the KCM are discussed in terms of both the feedbacks and mean-state. A set of 40 KCM experiments provides the basis for this study. The experiments differ in atmospheric parameters used in selected physical parameterizations and vertical atmospheric model resolution, whereas the ocean configuration is held fixed. In previous studies, similar changes to the atmospheric component were shown to have large influence on both climatology and interannual variability of the tropical regions (Kim et al. 2011; Ham et al. 2012; Harlaß et al. 2015). The results from the KCM are compared to those obtained from climate models participating in the CMIP5.

First results based on the ensemble-mean calculated over all experiments conducted with the KCM are discussed. Furthermore, all sensitivity experiments are compared with each other and thus factors critical to ENSO phase locking in the KCM are identified. This paper is structured as follows. Section 2 introduces the KCM, experiment setup, observational datasets and the methodology applied in the stability analysis. Section 3 briefly describes the performance of the KCM in simulating tropical Pacific mean-state. In Sect. 4, the main results about factors controlling the ENSO phase locking in the KCM are presented. Major conclusions, comparison with CMIP5 models and discussion of the main findings follow in Sect. 5 and conclude the paper.

2 Coupled model, data and method

We employ a version of the Kiel Climate Model (KCM; Park et al. 2009). The atmospheric component of the KCM is the European Centre for Medium Range Weather Forecasts (ECMWF) Hamburg atmospheric general circulation model version 5 (ECHAM5; Roeckner et al. 2003). The ECHAM5 model used in this study, differently from Park et al. (2009) where a prognostic cloud scheme (Tompkins 2002) is used, predicts cloud fraction on the basis of relative humidity (Sundqvist 1978) and uses a cumulus mass flux scheme that includes vertical transport by shallow and deep convective clouds (Nordeng 1994). ECHAM5 is coupled to the Nucleus for European Modeling of the Ocean (NEMO; Madec et al. 1998; Madec 2008) ocean-sea ice general circulation model via the Ocean Atmosphere Sea Ice Soil version 3 (OASIS3; Valcke 2006) coupler.

A set of 40 "present-day" integrations of the KCM (each 100 years long) is analyzed (see Table 1 for a list of all experiments), in which the atmospheric CO_2-concentration is constant at 348 ppm. The atmospheric horizontal resolution is T42 (~2.8°) in all experiments. The horizontal ocean resolution also is the same throughout the experiments and based on a 2° Mercator mesh (ORCA2 grid) and is on average 1.3° with increased meridional resolution of 0.5° near the equator and 31 levels in the vertical. The experiments differ in two respects. First, in atmospheric vertical resolution: experiments 1–28 use a model version with 19 vertical levels, experiments 29–34 a model version with 31 vertical levels, and experiments 35–40 a model version with 62 vertical levels. Second, the experiments differ in atmospheric parameters.

Cloud and radiation processes cannot be resolved in current climate models and are thus parameterized. A variation of the parameters in the corresponding schemes can produce rather different mean-states, as indicated by Kim et al. (2011) and Ham et al. (2012) by investigating model sensitivity to the Tokiaka parameter—a minimum entrainment rate threshold in the cumulus convection parameterization. Ham et al. (2012) further show how a variation of this parameter can lead to a dramatic change in ENSO phase locking. The three parameters changed in this study represent convective cloud conversion rate from cloud water to rain, entrainment rate for shallow convection and convective mass-flux above level of non-buoyancy (see Mauritsen et al. 2012 for a detailed discussion). The chosen parameter range corresponds to the suggested values by Mauritsen et al. (2012). The primary quantity to determine ENSO phase locking is SST.

CMIP5 model SST data is used for comparison with the KCM results. Historical simulations (1850–2005) are taken from 43 CMIP5 models (Taylor et al. 2012) and are interpolated to a 2.5° × 2.5° regular grid (see Table 2 for a list).

Additionally, we performed an atmosphere standalone experiment with the same atmospheric component as used in the KCM, ECHAM5 (T42, 31 levels), forced by observed daily SST and sea ice concentration (Reynolds et al. 2007; Reynolds 2009). The time period of the simulation is 1982–2009.

Several observational and reanalysis datasets are used to evaluate the model results. For SST, the HadISST 1.1 dataset from the Met Office Hadley Centre (Rayner et al. 2003) is used for 1958–2001. For the BJ index calculation, output from the Simple Ocean Data Assimilation (SODA) ocean reanalysis product version 2.0.2 (Carton and Giese 2008) is used for ocean temperatures and velocities (1958–2001). SST and zonal wind stress are taken from SODA as well to provide consistency among the datasets for the BJ index calculation. Surface heat fluxes are taken from ERA40 (Simmons and Gibson 2000) that spans the same time period as SODA 2.0.2.

The BJ index calculation is based on the original formulation from Jin et al. (2006) with some modifications made by Lübbecke and McPhaden (2013) and references therein. The BJ index includes the zonal advection feedback (ZAF), Ekman feedback (EF), thermocline feedback (TF), dynamical damping (DD) and thermal damping (TD). The formulation of the positive feedbacks (ZAF, EF and TF) is based on mean-state variables and a series of coefficients that measure the sensitivity of the atmosphere (i.e. zonal wind stress) to SST changes, and the ocean (i.e. zonal currents, upwelling and thermocline tilt) to changes in the zonal wind stress. The negative feedbacks (DD and TD) describe the damping effects on SST anomalies (SSTa) from mean ocean currents and changes in atmospheric heat fluxes (see Table 3 for an overview of the contributing feedback terms to the BJ index). The sum of all feedbacks is defined as the BJ index which is therefore a measure of coupled ocean–atmosphere stability or growth rate of SSTa.

Table 1 List of all KCM experiments which differ in three atmospheric parameters (column 2–4) and vertical atmospheric resolution (column 5)

KCM experiment label	Convective mass-flux above level of non-buoyancy	Entrainment rate for shallow convection (10^{-4})	Convective cloud conversion rate from cloud water to rain (10^{-4})	Amount of atmospheric vertical levels
1	0.15	3	1	19
2	0.175	3	1	19
3	0.20	3	1	19
4	0.225	3	1	19
5	0.25	3	1	19
6	0.275	3	1	19
7	0.30	3	1	19
8	0.325	3	1	19
9	0.35	3	1	19
10	0.2	1	1	19
11	0.2	2	1	19
12	0.2	4	1	19
13	0.2	5	1	19
14	0.2	6	1	19
15	0.2	7	1	19
16	0.2	8	1	19
17	0.2	9	1	19
18	0.2	3	2.1	19
19	0.2	3	2.5	19
20	0.2	3	3	19
21	0.2	3	4	19
22	0.2	5	4	19
23	0.30	1	4	19
24	0.13	10	4	19
25	0.3	1	1.5	19
26	0.3	10	1.5	19
27	0.2	1	4	19
28	0.35	10	1	19
29	0.3	10	1.5	31
30	0.35	3	1	31
31	0.2	3	1	31
32	0.2	5	1	31
33	0.2	1	4	31
34	0.35	10	1	31
35	0.3	10	1.5	62
36	0.35	3	1	62
37	0.2	3	1	62
38	0.2	5	1	62
39	0.2	1	4	62
40	0.35	10	1	62

The region selection for computing area averages is adapted from Kim and Jin (2011a). The latitudinal range is 5°S–5°N. In the zonal direction, 120°E–180°E for western equatorial thermocline depth, 180°E–80°W for SST, subsurface ocean temperature, eastern equatorial thermocline depth, upper ocean currents and atmospheric heatfluxes and 120°E–80°W for zonal wind stress is taken. 90%-confidence intervals for the BJ index calculated from reanalysis data are estimated from linear regression via the standard error of the regression slope. For the analysis of interannual variability, the linear trend and the mean seasonal cycle were removed from all datasets.

Table 2 List of all CMIP5 models used in the analysis

Label number	Modeling group	CMIP5 ID	Atmosphere (1) Horizontal grid (2) Number of vertical levels	Ocean (1) Horizontal res. (2) Number of vertical levels	Time period (year)
1	CSIRO-BOM	ACCESS1.0	(1) 192 × 145 N96 (2) 38	(1) 1° Latitude/longitude tripolar with enhanced resolution near the equator and at high latitudes (2) 50	156
2	CSIRO-BOM	ACCESS1.3	(1) 192×145 N96 (2) 38	(1) 1° Latitude/longitude tripolar with enhanced resolution near the equator and at high latitudes (2) 50	156
3	BCC	bcc-csm1-1-m	(1) T106 (2) 26	(1) 1° With enhanced resolution in the meridional direction in the tropics (1/3° meridional resolution at the equator) tripolar (2) 40	156
4	BCC	bcc-csm1-1	(1) T42 (2) 26	(1) 1° With enhanced resolution in the meridional direction in the tropics (1/3° meridional resolution at the equator) tripolar (2) 40	156
5	GCESS	BNU-ESM	(1) T42 (2) 26	(1) 200(lat)×360(lon) (2) 50	156
6	CCCMA	CanCM4	(1) T63 (2) 26	(1) 256×192 (2) 40	45
7	CCCMA	CanESM2	(1) T63 (2) 35	(1) 256×192 (2) 40	156
8	NCAR	CCSM4	(1) 0.9° ×1.25° (2) 27	(1) Nominal 1° (1.125° in longitude, 0.27–0.64° variable in latitude) (2) 60	156
9	NSF-DOE-NCAR	CESM1-BGC	(1) 0.9° ×1.25° (2) 27	(1) Nominal 1° (1.125° in longitude, 0.27–0.64° variable in latitude) (2) 60	156
10	NSF-DOE-NCAR	CESM1-CAM5	(1) 0.9° × 1.25° (2) 27	(1) Nominal 1° (1.125° in longitude, 0.27–0.64° variable in latitude) (2) 60	156
11	NSF-DOE-NCAR	CESM1-FASTCHEM	(1) 0.9° × 1.25° (2) 27	(1) Nominal 1° (1.125° in longitude, 0.27–0.64° variable in latitude) (2) 60	156
12	NSF-DOE-NCAR	CESM1-WACCM	(1) 1.9° × 2.5° (2) 66	(1) Nominal 1° (1.125° in longitude, 0.27–0.64° variable in latitude) (2) 60	156
13	CMCC	CMCC-CESM	(1) T31 (2) 39	(1) 2° average, 0.5° at the equator (ORCA2) (2) 31	156
14	CMCC	CMCC-CM	(1) T159 (2) 31	(1) 2° Average, 0.5° at the equator (ORCA2) (2) 31	156
15	CMCC	CMCC-CMS	(1) T63 (2) 95	(1) 2° Average, 0.5° at the equator (ORCA2) (2) 31	156
16	CNRM-CERFACS	CNRM-CM5	(1) TL127 (2) 31	(1) 0.7° On average ORCA1 (2) 42	156

Table 2 (continued)

Label number	Modeling group	CMIP5 ID	Atmosphere (1) Horizontal grid (2) Number of vertical levels	Ocean (1) Horizontal res. (2) Number of vertical levels	Time period (year)
17	CSIRO-QCCCE	CSIRO-Mk3-6-0	(1) T63 (2) 18	(1) ~0.9×1.875 (2) 31	156
18	LASG-CESS	FGOALS-g2	(1) 2.8125° × 2.8125° (2) 26	(1) 1×1° with 0.5 meridional degree in the tropical region (2) 30	156
19	LASG-IAP	FGOALS-s2	(1) R42 (2.81° × 1.66°) (2) 26	(1) LICOM (2) The zonal resolution is 1°. The meridional resolution is 0.5° between 10°S and 10°N and increases from 0.5° to 1° from 10° (2) 30	156
20	FIO	FIO-ESM	(1) T42 (2) 26	(1) 1.125° In longitude, 0.27–0.64° variable in latitude (2) 40	156
21	NOAA GFDL	GFDL-CM3	(1) ~ 200 km C48L48 (2) 48	(1) 1° Tripolar 360×200 (2) 50	146
22	NOAA GFDL	GFDL-ESM2G	(1) 2.5° longitude, 2° latitude M45 (2) 24	(1) 1° Tripolar 360×210 (2) 63	145
23	NOAA GFDL	GFDL-ESM2M	(1) 2.5° longitude, 2° latitude M45 (2) 24	(1) 1° Tripolar 360×200 (2) 50	145
24	NASA GISS	GISS-E2-H-CC	(1) Nominally 1° (2) 40	(1) 0.2 To 1° latitude×1° longitude HYCOM (2) 26	156
25	NASA GISS	GISS-E2-R-CC	(1) Nominally 1° (2) 40	(1) 1° Latitude×1.25° longitude Russell 1×1Q (2) 32	156
26	NASA GISS	GISS-E2-R	(1) 2° latitude×2.5° longitude F (2) 40	(1) 1° Latitude×1.25° longitude Russell 1×1Q (2) 32	156
27	MOHC	HadCM3	(1) N48 3.75×2.5° (2) 19	(1) 1.25° In longitude by 1.25° in latitude N144 (2) 20	146
28	MOHC	HadGEM2-AO	(1) 1.875° in longitude by 1.25° in latitude N96 (2) 60	(1) 1.875° In longitude by 1.25° in latitude N96 (2) 40	146
29	MOHC	HadGEM2-CC	(1) 1.875° in longitude by 1.25°in latitude N96 (2) 60	(1) 1.875° In longitude by 1.25° in latitude N96 (2) 40	146
30	MOHC	HadGEM2-ES	(1) 1.875° in longitude by 1.25° in latitude N96 (2) 38	(1)1° By 1° between 30 N/S and the poles; meridional resolution increases to 1/3° at the equator (2) 40	146
31	INM	INM-CM4	(1) 2×1.5° in longitude and latitude latitude- longitude (2) 21	(1) 1×0.5° In longitude and latitude generalized spherical coordinates with poles displaced outside ocean (2) 40	156
32	IPSL	IPSL-CM5A-LR	(1) 96×95 equivalent to 1.9° × 3.75° LMDZ96×95 (2) 39	(1) 2×2-0.5° ORCA2 (2) 31	156
33	IPSL	IPSL-CM5A-MR	(1) 144×143 equivalent to 1.25° × 2.5° LMDZ144×143 (2) 39	(1) 2×2-0.5° ORCA2 (2) 31	156

Table 2 (continued)

Label number	Modeling group	CMIP5 ID	Atmosphere (1) Horizontal grid (2) Number of vertical levels	Ocean (1) Horizontal res. (2) Number of vertical levels	Time period (year)
34	MIROC	MIROC4h	(1) T213 (2) 56	(1) 1/4° By 1/6° (average grid spacing is 0.28° and 0.19° for zonal and meridional directions) (2) 48	56
35	MIROC	MIROC5	(1) T85 (2) 40	(1) 1.4° (zonally) × 0.5–1.4° (meridionally) (2) 50	156
36	MIROC	MIROC-ESM-CHEM	(1) T42 (2) 80	(1) 1.4° (zonally) × 0.5–1.4° (meridionally) (2) 44	156
37	MIROC	MIROC-ESM	(1) T42 (2) 80	(1) 1.4° (zonally) × 0.5–1.4° (meridionally) (2) 44	156
38	MPI-M	MPI-ESM-LR	(1) T63 (2) 47	(1) Average 1.5° GR15 (2) 40	156
39	MPI-M	MPI-ESM-MR	(1) T63 (2) 95	(1) Approx. 0.4° TP04 (2) 40	156
40	MPI-M	MPI-ESM-P	(1) T63 (2) 47	(1) Average 1.5° GR15 (2) 40	156
41	MRI	MRI-CGCM3	(1) 320 × 160 TL159 (2) 48	(1) 1 × 0.5 (2) 50 + 1 Bottom Boundary Layer	156
42	NCC	NorESM1-ME	(1) Finite volume 1.9° latitude, 2.5° longitude (2) 26	(1) 1.125° Along the equator (2) 53	156
43	NCC	NorESM1-M	(1) Finite volume 1.9° latitude, 2.5° longitude (2) 26	(1) 1.125° Along the equator (2) 53	156

Table 3 Contributing feedbacks in the Bjerknes stability index and their formulation

Contributing feedbacks	Formulation
Zonal advection feedback (ZAF)	$\mu_a \beta_u \left\langle \frac{-\partial \bar{T}}{\partial x} \right\rangle_E$
Ekman feedback (EF)	$\mu_a \beta_w \left\langle \frac{-\partial \bar{T}}{\partial z} \right\rangle_E$
Thermocline feedback (TF)	$\mu_a \beta_h \left\langle \frac{H(\bar{w})\bar{w}}{H_m} a_h \right\rangle_E$
Dynamical damping (DD)	$-\left(\frac{\bar{u}_E}{L_x} + \frac{-2y\bar{v}_E}{L_y{}^2} + \frac{\bar{w}_E}{H_m} \right)$
Thermal damping (TD)	$-\alpha$

μ_a denotes equatorial zonal wind stress response to eastern equatorial SSTa, β_u zonal ocean velocity response, β_w ocean upwelling response and β_h thermocline slope response to equatorial zonal wind stress anomalies. a_h is the ocean subsurface temperature response to thermocline depth anomalies and α the net surface heat flux response to SSTa. $\bar{u}, \bar{v}, \bar{w}$ denote mean zonal, meridional and vertical ocean velocities, $\bar{T}$ mean SST and H_m mean mixed layer depth. $\langle \cdot \rangle_E$ denotes volume-averaged quantities over the eastern equatorial regime with L_x and L_y as zonal and meridional extent. $H(\bar{w})$ is a step function to account only for upstream vertical advection. The responses are estimated via linear regressions. The methodology is adapted from Lübbecke and McPhaden (2013), region selection after Kim and Jin (2011a)

When analyzing ENSO phase locking, the Niño3.4 index region (170°W–120°W; 5°S–5°N) is chosen, because it captures both a large part of the main region of SST variability as well as the area where coupling processes between ocean and atmosphere associated with ENSO are assumed to take place. A phase locking index (PLI) is defined after Bellenger et al. (2014):

$$\mathrm{PLI} = \frac{\mathrm{STD\ DEV}\left(\mathrm{SSTa}_{\mathrm{Nino3.4}}\right)_{\mathrm{DJF}}}{\mathrm{STD\ DEV}\left(\mathrm{SSTa}_{\mathrm{Nino3.4}}\right)_{\mathrm{AMJ}}}$$

With SSTa denoting interannual SST anomalies and STD the corresponding standard deviation. A larger PLI is either determined by stronger variability in DJF or weaker variability in AMJ or both and therefore reflects stronger phase locking.

3 Mean-state SST

The long-term annual-mean SST in the tropical Pacific from observations is shown in Fig. 1a and the ensemble-mean SST derived from all KCM simulations in Fig. 1b.

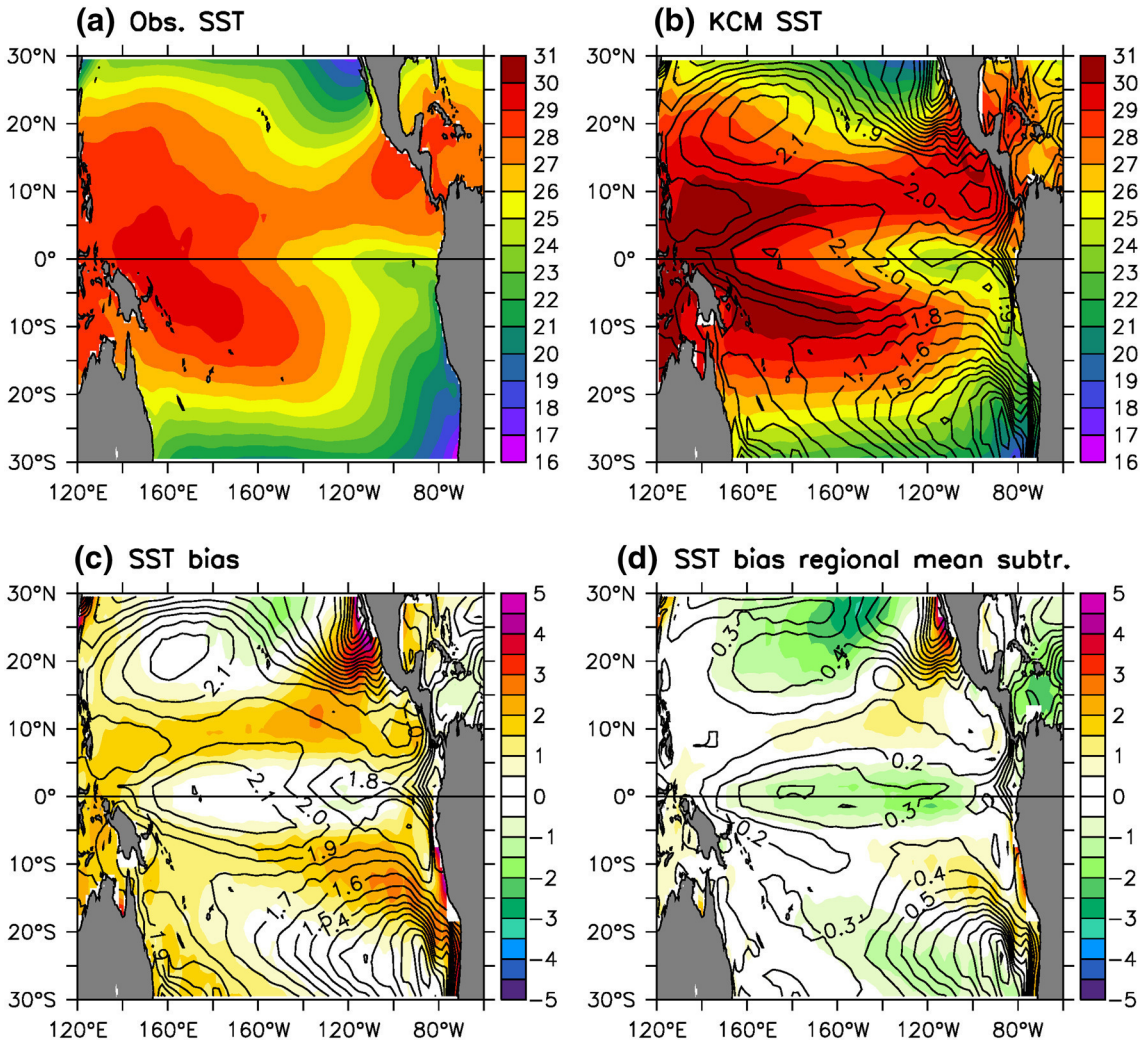

Fig. 1 **a** Long-term annual-mean SSTs from observations and **b** as given by the ensemble-mean calculated over all experiments with the KCM. **c** Total SST bias, **d** with regional mean SSTs (120°E–60°W; 15°S–15°N) subtracted. Contour *lines* depict the standard deviation over all model realizations. Unit is °C

The model captures the western Pacific warm pool, the zonal band of relatively high SST north of the equator as well as the equatorial cold tongue. Large spread among the model realizations exists, as indicated by the standard deviation among the individual ensemble members (contour lines). Ensemble-mean SSTs are too warm in several regions (Fig. 1c). Largest warm SST biases are observed in the coastal upwelling regions in the eastern Pacific, a problem that is seen in most climate models (Latif et al. 2001). The model spread is rather small in the coastal upwelling regions, indicating the changes applied to the KCM do not significantly influence the SST in these regions. SST biases in the equatorial region are considerably smaller, with the exception of the very eastern part. However, model spread is large, especially west of 140°W. This indicates that SST in this region is sensitive to the changes applied to the KCM. When the areal-mean SST is subtracted from the map (Fig. 1d) to obtain the relative SST biases, the equatorial cold bias becomes obvious (as indicated by the green color in Fig. 1d). Using relative temperatures has the advantage that it resembles the corresponding atmospheric circulation more accurately (Bayr and Dommenget 2013). The double-ITCZ problem is also seen in the SSTs, as bands of warm SST biases stretching from the western equatorial Pacific eastward in both hemispheres and merging with the warm SST biases in the subtropical coastal upwelling areas (Fig. 1c). We note that the model spread is strongly reduced when subtracting the areal-mean SST from the individual ensemble members.

Perturbing the physics (Sect. 2) has implications for the equatorial cold bias (Fig. 2). This is because the region of the equatorial cold tongue is characterized by boundary

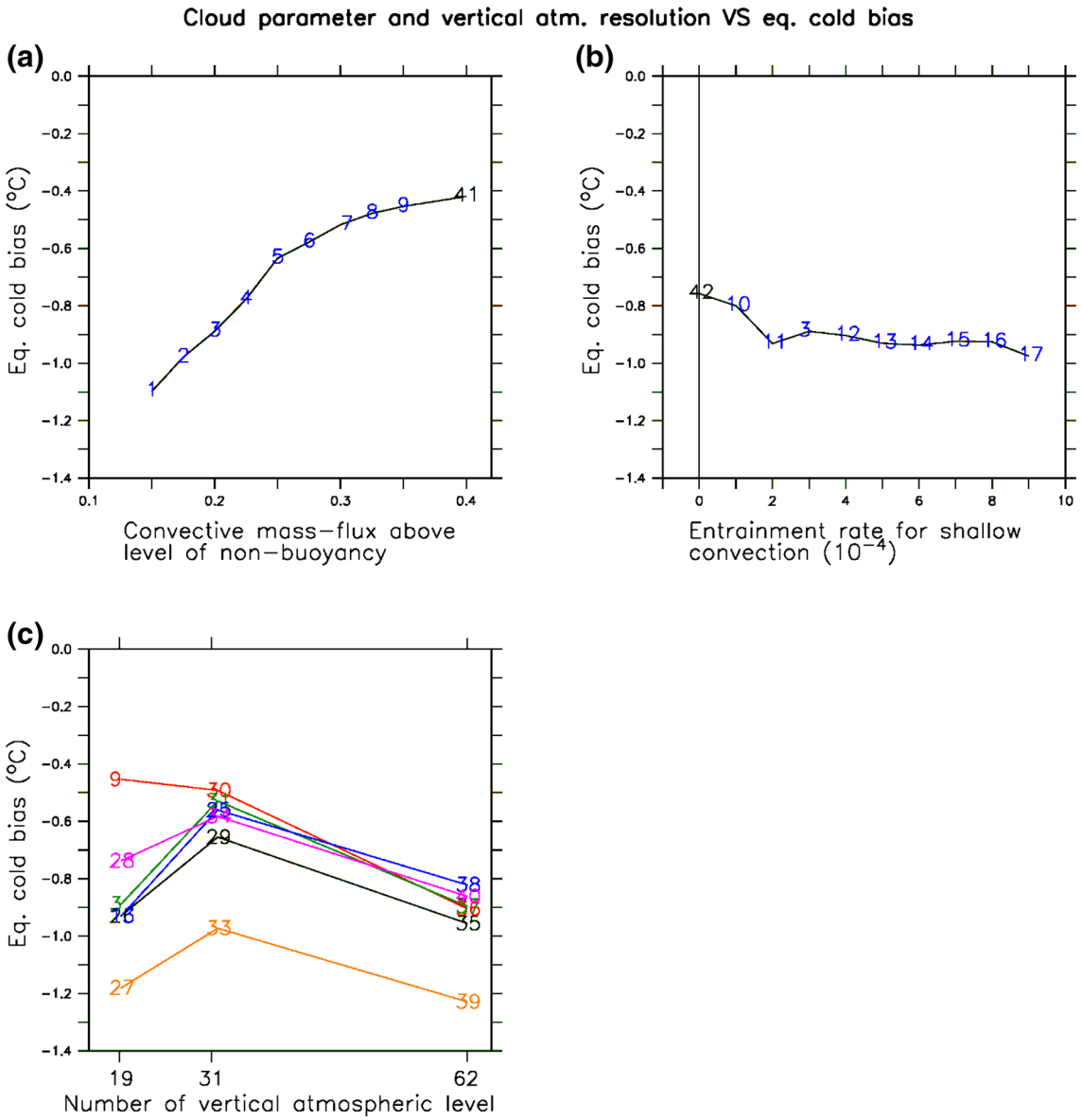

Fig. 2 Scatter plot of the cold equatorial SST bias (160°E–80°W; 5°S–5°N) with areal-mean (120°E–60°W; 15°S–15°N) subtracted versus different parameter values in the cloud parameterization of **a** the convective mass-flux above level of non-buoyancy and **b** the entrainment rate for shallow convection for a selection of KCM experiments. Model experiments 41 and 42 are not included in the set of experiments used in the previous part of the analysis due to their extreme parameter values. **c** Scatter plot of the cold equatorial SST bias versus atmospheric vertical resolution with color denoting same cloud parameters

layer cloud cover (e.g. Klein and Hartmann 1993; Lacagnina and Selten 2013) and this is affected by our perturbations. First, we need to clarify the role of the perturbed parameters, which is explained in detail in Mauritsen et al. (2012). The perturbed atmospheric parameters of interest are the convective mass-flux above the level of non-buoyancy and the entrainment rate for shallow convection. They both control the updraft in shallow convective processes and thus the amount and thickness of boundary layer clouds. Increasing the first parameter increases the strength of the updraft and thus leads to a reduction of boundary layer cloud cover. This is because a stronger updraft is associated with more evaporation of cloud water in the boundary layer. Increasing the second parameter has the opposite effect, because a larger entrainment rate weakens the updraft and therefore increases boundary layer cloud cover. The effect of modifications in the cloud cover is to change the amount of solar radiation reaching the sea surface. Therefore, the cold SST bias could in principle be reduced by decreasing shallow cloud cover over the

cold tongue region by increasing insolation at the surface. A considerably reduced cold SST bias can be achieved by increasing the convective mass-flux above the level of non-buoyancy (Fig. 2a) or with a less consistent but still visible effect by decreasing the entrainment rate for shallow convection (Fig. 2b). Changing the convective cloud conversion rate from cloud water to rain has no significant impact on the cold SST bias (not shown).

We also investigate the influence of changing the vertical atmospheric resolution, as motivated by Harlaß et al. (2015) who achieved a considerable reduction of SST biases in the tropical Atlantic by enhancing the vertical resolution. We find that varying the number of vertical levels in the atmosphere has no systematic effect on the strength of the cold bias in the equatorial Pacific (Fig. 2c). This may be partly due to the relative small number of sensitivity experiments (6 sets of KCM-experiments; each set differs in the cloud parameters). A reduction of the cold SST bias is achieved by increasing the resolution from 19 to 31 levels in 5 out of the 6 sets of sensitivity experiments, but at 62 levels the bias again increases. It should be mentioned in this context that horizontal and vertical atmosphere model resolution should be consistent with each other (Harlaß et al. 2015).

Figure 3 depicts the seasonal cycle of equatorial SST directly at the equator relative to the annual-mean SST calculated from observations (Fig. 3a) and the KCM (Fig. 3b). The ensemble-mean SST annual cycle is shown from the KCM (color shading in Fig. 3b). It captures the warming during the first half and the cooling during the second half of the year in the eastern equatorial Pacific as well as the westward propagation of the signal. However, the amplitude of the SST seasonal cycle is underestimated, and the cold phase terminates 3 months too early compared to the observations. The model spread is shown by contours in Fig. 3b. Largest spread is found in the very eastern equatorial Pacific during the first half of the year.

4 Seasonal ENSO phase locking and feedback analysis

In the ensemble-mean, the KCM produces a seasonal ENSO phase locking comparable to observations (Fig. 4a), with largest variability in December to February and smallest in April to June. There are, however, several noticeable differences. First, the interannual variability is too strong in the model during all calendar months. In the KCM, ENSO is sensitive to the mean temperature of the tropical Pacific, with a warmer mean-state leading to stronger interannual variability. This has been shown by Park et al. (2009) and Latif et al. (2015),

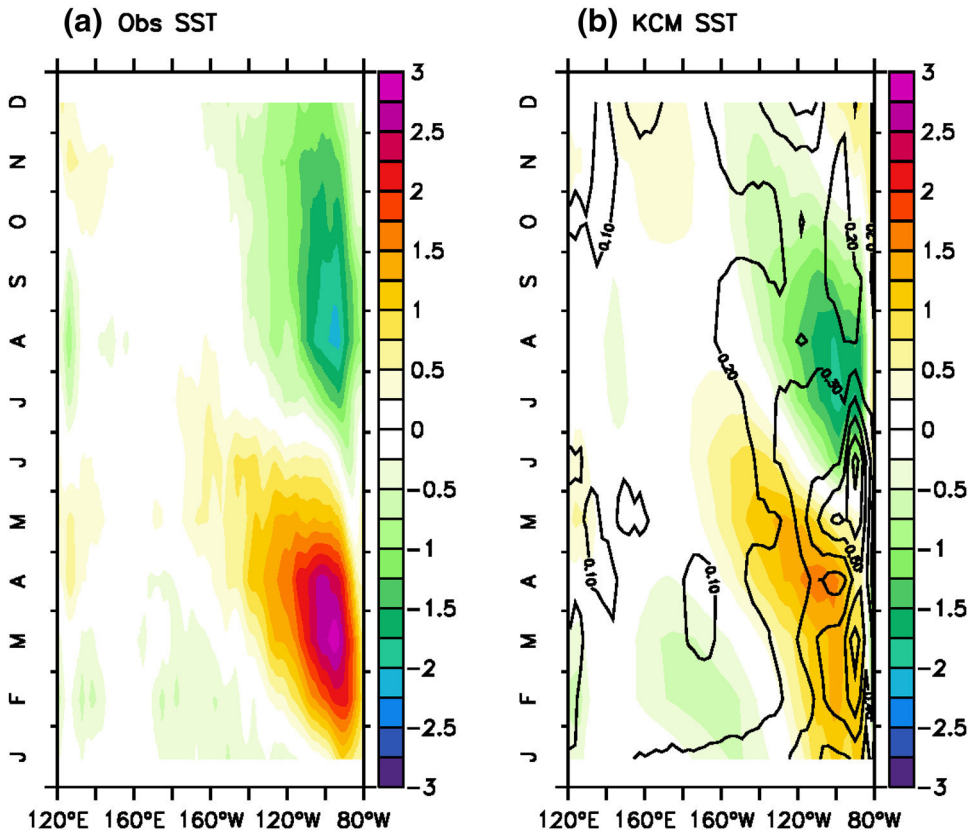

Fig. 3 Seasonal cycle of equatorial SST at the equator with the annual mean removed for **a** observations and **b** the ensemble-mean calculated over all experiments with the KCM. Contour *lines* depict the standard deviation over all model realizations. Unit is °C

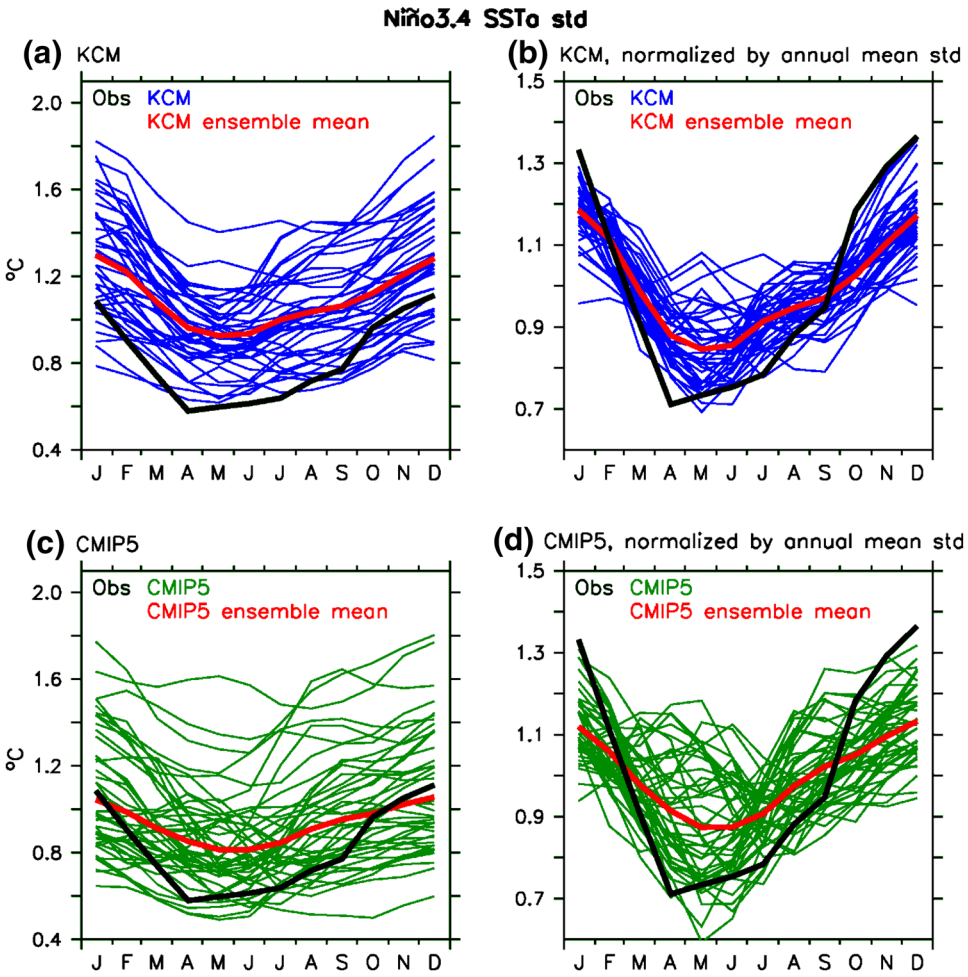

Fig. 4 Monthly standard deviation of Niño3.4 SSTa for (**a**) all 40 KCM experiments (*blue*) together with its ensemble-mean (*red*) and (**b**) normalized by the annual mean. The same for a set of (**c**) 43 CMIP5 models with (**d**) normalized by the annual mean. Observations are added in *black*

both describing the ENSO response to global warming in a T31-version of the KCM. Regarding this relationship, Fig. 5 shows tropical Pacific mean (25°N–25°S) SST for each ensemble member of the T42-version of the KCM analyzed here together with annual mean ENSO amplitude as assessed by Niño3.4-averaged SSTa standard deviation. The correlation amounts to 0.59, consistent with the T31-version. Compared to observations (black cross), the KCM ensemble-mean shows higher tropical Pacific mean SST along with a stronger ENSO (red cross). Second, the seasonal variation of monthly SSTa is smaller than that in observations, as indicated by the much less accentuated minimum in boreal spring and by the less distinct maximum in boreal winter (Fig. 4a). This becomes especially clear when normalizing the seasonal cycle of SST variability by its annual mean (Fig. 4b). And third, there is significant spread about the ensemble-mean as shown by the individual realizations. This indicates that the seasonal cycle of interannual SST variability is rather sensitive to changes in vertical atmosphere model resolution and changes in cloud and convective parameters, as shown below.

A similar analysis has been carried out for the CMIP5 models (Fig. 4c, d). In the ensemble mean, the CMIP5 models exhibit similar biases as the KCM. Most noteworthy is the weak variability minimum in boreal spring. The spread is larger than that obtained from the KCM ensemble. This is expected, since the CMIP5 ensemble covers a wider range of resolutions and physical parameterizations.

In the following, the controls of seasonal ENSO phase locking in the KCM are investigated. Biases in seasonal ENSO phase locking may be linked to a flawed simulation of the mean-state SST seasonal cycle. We calculate from each member of the KCM ensemble the correlation (on the basis of the monthly values) of the simulated mean-state SST seasonal cycle in the Niño3.4 box with the observed seasonal cycle in this region. The PLI, which was introduced above, quantifies the strength of the annual variation of interannual SST variability. Figure 6 shows the PLI against the models' ability to capture the mean-state SST seasonal cycle in the eastern equatorial Pacific. There is no significant relationship (correlation of 0.02). This agrees with Stein et al. (2014), in which it is found that the seasonal modulation of the coupled stability is responsible for

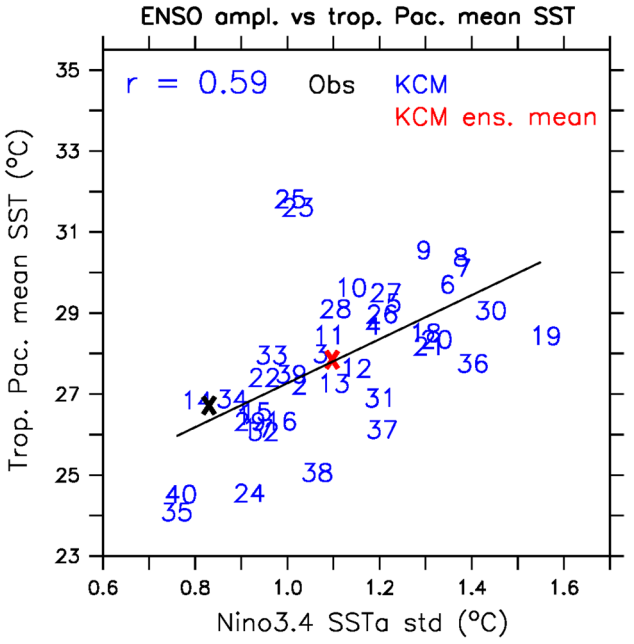

Fig. 5 Scatter plot of Niño3.4-averaged SSTa standard deviation versus tropical Pacific mean SST (120°E–60°W; 25°S–25°N) for the set of 40 KCM experiments (*blue*) together with the annual-mean SST (*red* cross) and observations (*black cross*). The correlation over all KCM experiments is given and it is significant at the 90% level. A regression *line* is also added

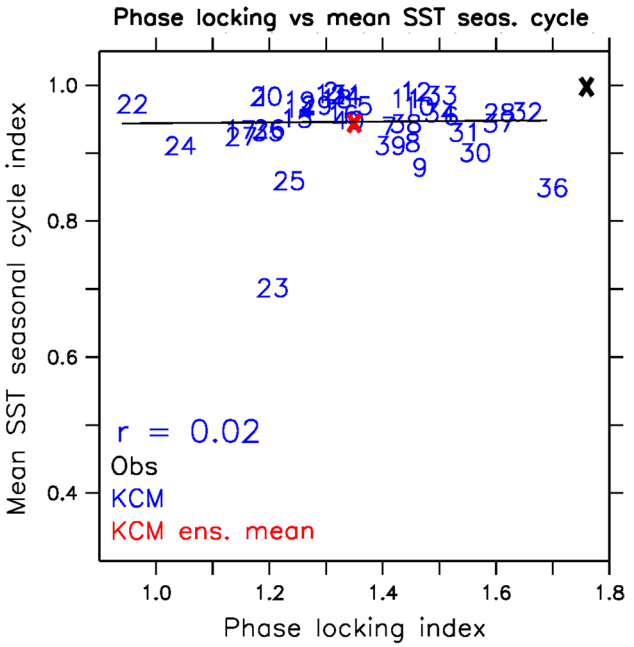

Fig. 6 Scatter plot of the phase locking index PLI versus the correlation of the mean SST seasonal cycle in the Niño3.4 between observations and the set of 40 KCM experiment (*blue*) together with the ensemble-mean (*red cross*) and observations (*black cross*). The correlation over all KCM experiments is given but not significant and a regression line also is added

the ENSO being phase-locked to the annual cycle rather than a periodic forcing by the annual cycle.

Next, we make use of the BJ index which measures the linear stability of the coupled atmosphere–ocean system and is hence a measure of SSTa growth rate. Figure 7 shows the BJ index and the individual feedbacks as a function of calendar month calculated from observations and the set of experiments with the KCM. Figure 7a–c displays the positive feedbacks, Fig. 7d, e the damping terms, and Fig. 7f the BJ index which is calculated as the sum of all feedbacks. Again, both the ensemble-mean and the individual experiments are shown from the KCM. Confidence intervals in the observations, as estimated from the standard error of the contributing terms (see Sect. 2 for more details), are quite large for the TF term, which is mainly attributed to the short time period of 44 years and the lack of subsurface data prior the TAO-array. First, we note that the annual-mean BJ index is negative in SODA (-0.18 year^{-1}; close to the value calculated in Kim et al. 2013) and in the KCM ensemble mean (-1.24 year^{-1}), which is expected since the coupled system should be overall stable. According to the BJ index calculated from observations, the coupled system is unstable from July through November, allowing SSTa to grow, and most strongly damped at the beginning of the year (Fig. 7f). This finding agrees with Stein et al. (2010) who assess the seasonal growth rate of ENSO via the BJ index and show that the coupled system is unstable around boreal fall and stable during the rest of the year. The seasonal cycle of the BJ index matches the seasonal cycle of interannual SST variability (Fig. 4) with a phase shift of a few months. This is reasonable, because SSTa, owing to the inertia of linear perturbations, may still grow after SSTa growth rate has reached its annual maximum. The BJ index can thus explain the seasonal ENSO phase locking.

The positive feedback terms derived from observations, namely EF and TF and to a lesser extent ZAF, tend to destabilize the system in late boreal summer and boreal fall. DD and TF on the other hand are strongest in early boreal spring. Together with the small positive feedbacks during that time, this contributes to stable conditions, giving rise to the so-called spring predictability barrier (Latif and Graham 1992; Torrence and Webster 1998; Levine and McPhaden 2015). The ensemble-mean of the KCM runs reproduces the seasonal cycle of the BJ index quite well. All individual feedbacks peak approximately at the right time of the year. In boreal fall, however, the SSTa growth rate is not as strong as in observations, which results from too weak positive feedbacks at that time of the year. Furthermore, in the annual mean the system is too strongly damped compared to observations. This is mostly a result of too strong DD and overall too weak positive feedbacks. We note that the relatively small ensemble-mean BJ index

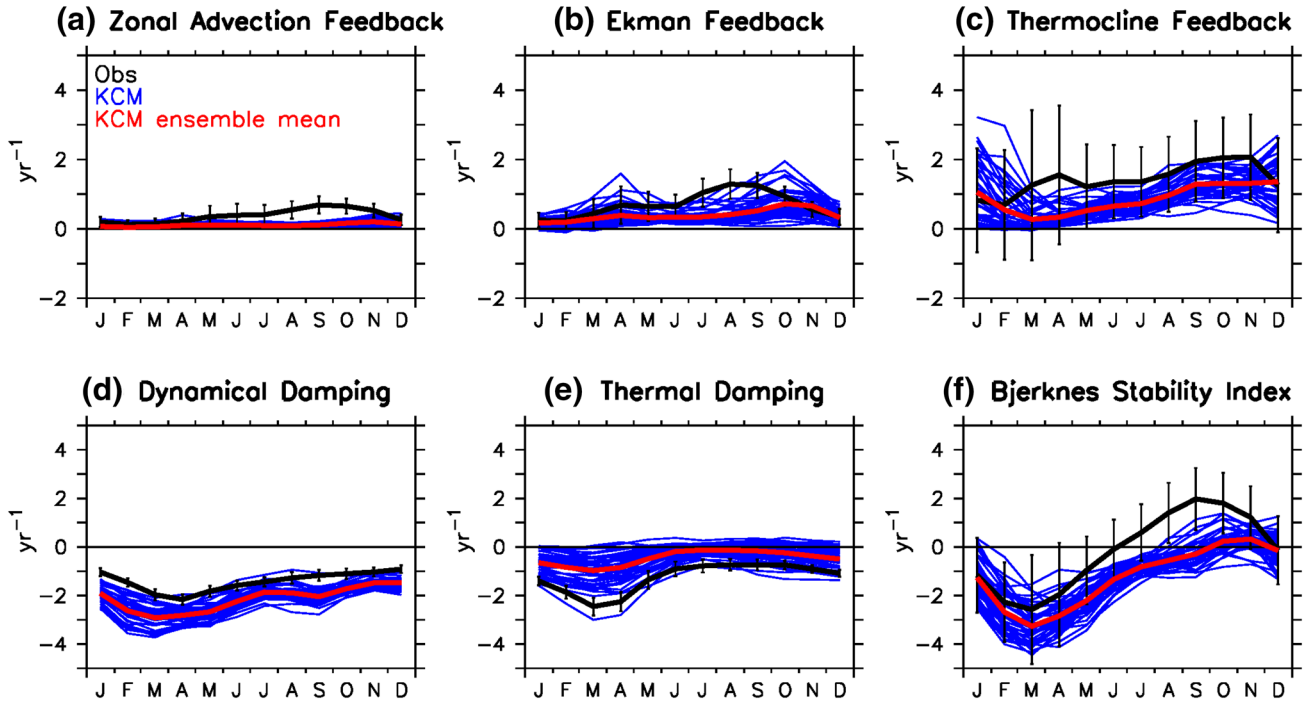

Fig. 7 Monthly **a** zonal advection feedback, **b** Ekman feedback, **c** thermocline feedback, **d** dynamical damping, **e** thermal damping and **f** the Bjerknes stability index for the set of 40 KCM experiments (*blue*) together with the ensemble-mean (*red*) and observations (*black*). *Error bars* for observations show 90% confidence intervals

cannot explain the too strong SST variability in the KCM (Fig. 4a), since low values of the BJ index would favor weak variability (Kim and Jin 2011b; Kim et al. 2013). Furthermore, it is noteworthy that TD is underestimated, especially at the beginning of the year.

Some of the feedback biases can explain why ENSO phase locking is overall too weak in the KCM:

1. The too weak positive feedbacks (ZAF, EF and TF) explain why the annual maximum of SSTa growth rate is underestimated in boreal fall. This results in a too weak SST variability maximum in boreal winter.
2. The too weak negative feedback TD at the beginning of the calendar year (February-March-April, FMA) can explain why SST variability in boreal spring does not decay as strongly as in observations.

Regarding the second point, it can be argued that too weak TD may be compensated by too strong DD. When adding TD and DD it becomes clear that in FMA, the total damping rate is underestimated with respect to observations, whereas during the remainder of the year there is compensation. Therefore the bias in TD is here considered as a potential cause for biasing ENSO phase locking.

To better assess the role of the feedbacks in controlling ENSO phase locking in the KCM, the feedbacks are computed for each single model experiment and plotted against the phase locking index, PLI. Figure 8 shows scatter diagrams of ZAF, EF, TF, TD, DD and the BJ index at their peak season with respect to the PLI. The results indicate that a stronger EF, TF and TD during September-December (SOND) and January-April (JFMA) is associated with stronger ENSO phase locking (Fig. 8b, c, e), and with significant correlations of 0.69, 0.54 and −0.67, respectively. ZAF is of less relevance for ENSO phase locking, being small in magnitude and exhibiting a correlation with PLI of only 0.21 (Fig. 8a). Also the DD is not correlated with PLI (−0.1; Fig. 8d). The highest correlation is found for the EF term. However, TF and TD are of greater magnitude and therefore may have an equivalent impact. This can be quantified by the slope of the fitted linear regression lines between PLI and EF, TF and TD in Fig. 8b, c, e, amounting to 1.18, 1.21, and −2.35 year^{-1}, respectively. We also compare the PLI with the total BJ index by taking the difference of the simulated BJ index maximum and minimum season, i.e. in SOND and JFMA, respectively (Fig. 8f). This is because the BJ index measures both the instability towards the end of the calendar year as well as the stability at the beginning of the calendar year. The results show that the BJ index is in close relation to the PLI (correlation of 0.76), which supports our hypothesis that it can to a large extent explain seasonal ENSO phase locking.

We conclude that the major controls of seasonal ENSO phase locking in the KCM is mostly due to EF and TF

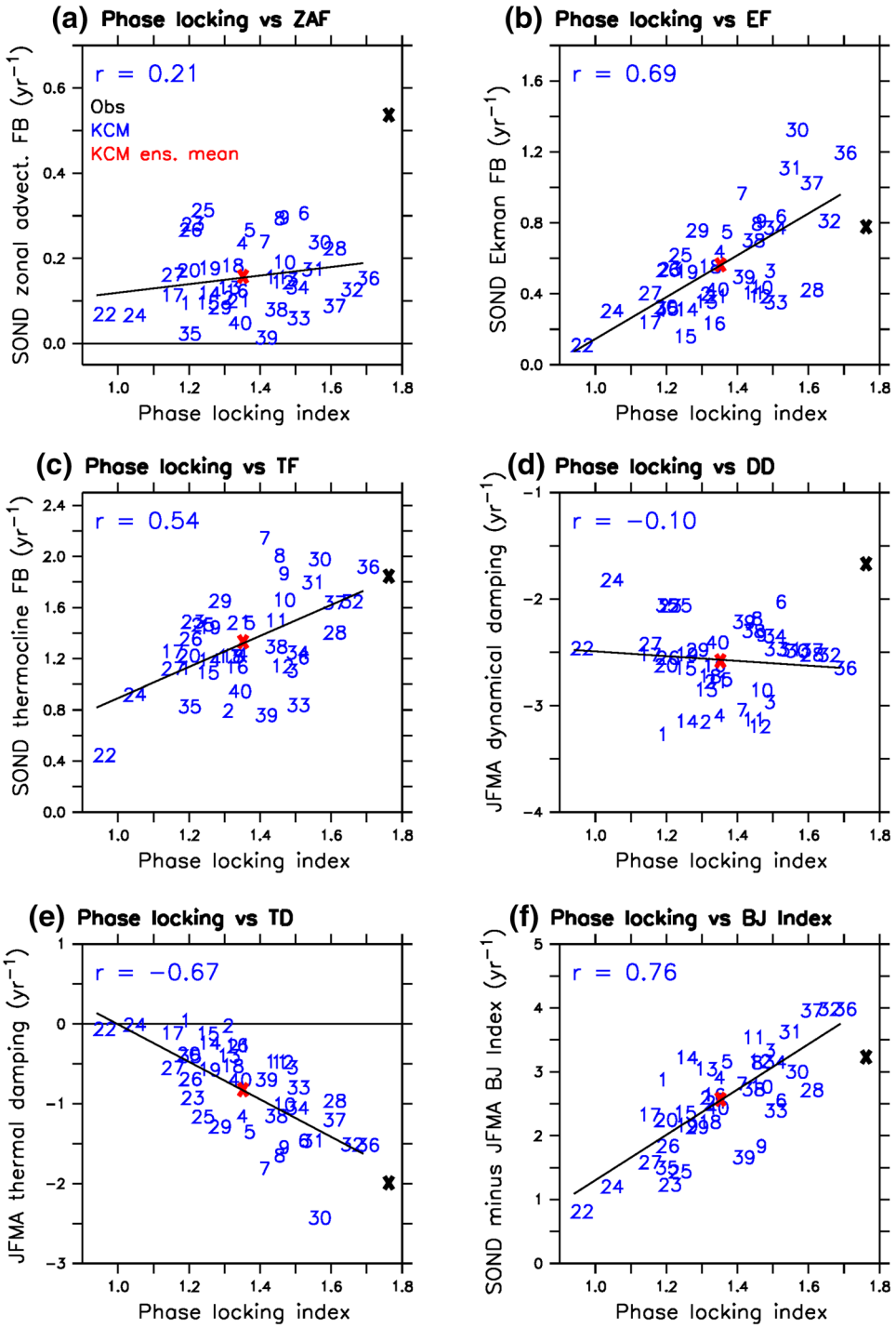

Fig. 8 Scatter plots of the phase locking index PLI versus **a** the zonal advection feedback in September-December, **b** the Ekman feedback in September–December, **c** the thermocline feedback in September–December, **d** the dynamical damping in January–April, **e** the thermal damping in January–April and **f** for the BJ index difference between September–December and January–April for the set of 40 KCM experiments (*blue*) together with the ensemble-mean (*red cross*) and observations (*black cross*). The correlation over all KCM experiments is given and it is significant at the 90% level. A regression *line* is also added

around boreal fall and TD in late boreal winter/early boreal spring. A stronger EF and TF in boreal fall increases the growth rate of the SST anomalies, which leads to larger SST variability in boreal winter. A stronger TD from the atmospheric heat fluxes in late boreal winter/early boreal spring on the other hand stabilizes the coupled system, which keeps SST variability low in boreal spring.

ENSO stability is tightly linked to the mean-state (e.g., Battisti and Hirst 1989; Neelin et al. 1998; An and Jin 2000; Fedorov and Philander 2001; Guilyardi 2006; Bejarano and Jin 2008; Kim et al. 2013). Therefore, as the next step we connect the feedback biases outlined above with the mean-state. The KCM exhibits a cold SST bias in the equatorial Pacific (Fig. 1d), which is common to many CGCMs (e.g.

Zheng et al. 2012) and has previously been linked to feedback biases in terms of the BJ index (Kim et al. 2013).

Figure 9 displays the equatorial cold bias calculated over the region 160°E–80W; 5°S–5°N against the feedbacks which we identified to be important for controlling ENSO phase locking in the KCM, i.e. EF, TF and TD. The cold bias is computed for SOND and compared to EF and TF in SOND, and to TD in JFMA. A smaller cold bias in SOND goes along with an enhanced EF (correlation of 0.69; Fig. 9a) and TF (correlation of 0.70; Fig. 9b) in SOND, and an increased TD in JFMA (correlation of −0.87; Fig. 9c). Xiang et al. (2011) and Kim et al. (2013) discuss in detail what implications the equatorial cold SST bias can have for the feedbacks. For example, an equatorial cold tongue extending too far west places the deep convection too far west, thereby reducing the response of low-level winds to SST changes over the central equatorial Pacific. A weaker low-level wind response to SST forcing contributes to the underestimation of both the EF and TF (see Table 3 for the definition of the feedbacks). Furthermore, the cold SST bias reduces the thermal stratification in the upper ocean. This too affects EF which is proportional to the strength of the mean vertical temperature gradient. Kim et al. (2013) argue that in a weaker stratified upper ocean, wind stress-forced momentum is less confined towards the sea surface. This would result in a lower ocean-upwelling response sensitivity to wind stress forcing as part of the EF. Consistent with this, we find that in the KCM a smaller cold SST bias is associated with a stronger upwelling response to wind stress forcing in SOND (correlation of 0.64; not shown). Further, the weaker stratification can lead to an underestimation of the thermocline-subsurface temperature feedback (Xiang et al. 2011) and influences the thermocline slope response to wind forcing (Kim et al. 2013). The influences on TD likely result from biases in the shortwave feedback. Lloyd et al. (2012) and Dommenget et al. (2014) show that the cold SST bias weakens the shortwave damping and can even reverse it to a positive feedback. We find in the KCM that a smaller cold bias is strongly related to a larger shortwave feedback in JFMA (correlation of −0.87; not shown). Finally, we analyze the results from an uncoupled ECHAM5 simulation forced by observed daily SSTs during 1982–2009. Here the shortwave feedback is stronger than that in any of the coupled simulations (not shown). This

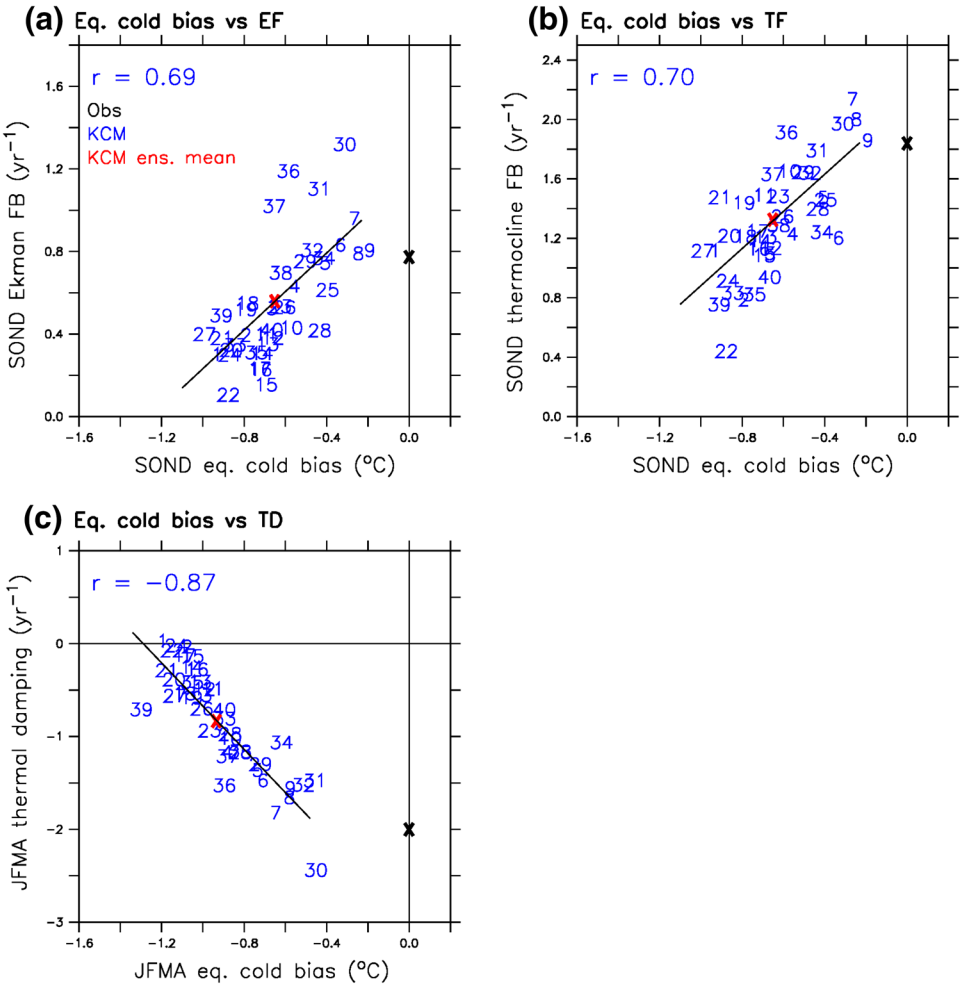

Fig. 9 Scatter plots of **a** the cold equatorial Pacific SST bias (160°E–80°W; 5°S–5°N) with areal-mean (120°E–60°W; 15°S–5°N) subtracted in September–December versus the Ekman feedback in September–December, **b** the equatorial cold SST bias in September–December versus the thermocline feedback in September–December and **c** the equatorial cold SST bias in January–April versus the thermal damping January–April for the set of 40 KCM experiments (*blue*) together with its ensemble-mean (*red cross*) and observations (*black cross*). The correlation over all KCM experiments is given and it is significant at the 90% level. A regression *line* is also added

corroborates our hypothesis that the shortwave feedback is strongly controlled by the SST bias. Based on these results, we conclude that an excessive equatorial cold tongue is the main cause for too weak seasonal ENSO phase locking in the KCM.

5 Summary and discussion

In this study, processes controlling seasonal ENSO phase locking are identified in the Kiel Climate Model (KCM) and compared to observations. A large ensemble of simulations with the KCM has been conducted, which differ in vertical atmospheric resolution and physical parameterizations. ENSO phase locking in observations is explained by the seasonal variation of the coupled system's stability and the associated feedbacks, here measured by the Bjerknes (BJ) index. Positive feedbacks are strongest towards the end of the calendar year, leading to a maximum in SST anomaly growth rate, whereas negative feedbacks are strongest at the beginning of the year, thereby setting relatively stable conditions. The ensemble-mean of the KCM simulations depicts ENSO phase locking and seasonal variation of the BJ index consistent with observations. The model spread, however, is rather large, as discussed below. A major result of this study is that the ability of a coupled model to realistically simulate seasonal ENSO phase locking is closely linked to the strength of the cold equatorial Pacific SST bias, with less biased models exhibiting more realistic phase locking owing to more realistic coupled feedbacks.

The KCM in the ensemble-mean features too weak seasonal ENSO phase locking compared to observations, that is a less accentuated SST variability maximum and SST variability minimum in December to February and April to June, respectively. This bias is induced by a too weak Ekman feedback (EF) and thermocline feedback (TF) towards the end of the year and too weak thermal damping (TD) at the beginning of the year. When comparing the individual KCM experiments from the ensemble with each other, we find that stronger EF and TF in SOND and TD in JFMA are associated with stronger seasonal ENSO phase locking. Improving these feedbacks holds great potential to enhance seasonal ENSO phase locking in the KCM.

It is suggested that an excessive equatorial cold tongue significantly affects the simulation of these feedbacks and thus seasonal ENSO phase locking not only in the KCM but also in the CMIP5 models. Figure 10 depicts results from all KCM runs and from the CMIP5 models. The scatter diagram shows for each simulation the seasonal ENSO phase locking index (PLI) and the strength of the cold equatorial Pacific SST bias. In both ensembles, a smaller cold SST bias corresponds to stronger seasonal ENSO phase locking, with significant correlations of 0.61 (KCM) and 0.48 (CMIP5). We note that the CMIP5 models tend to simulated overall warmer conditions.

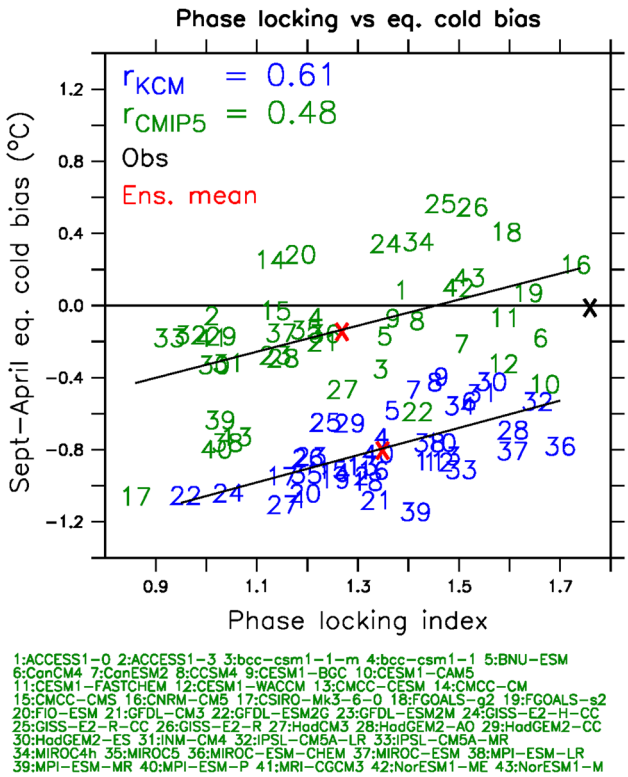

Fig. 10 Scatter plot of the phase locking index PLI versus the cold equatorial SST bias (160°E–80°W; 5°S–5°N) with areal-mean (120°E–60°W; 15°S–15°N) subtracted in September–April for the set of 40 KCM experiments (*blue*) and the set of 43 CMIP5 models together with their ensemble-means (*red crosses*) and observations (*black cross*). The correlations over all KCM experiments and CMIP5 models are given and they are significant at the 90% level. A regression line is also added

We hypothesize that the link between seasonal ENSO phase locking and cold equatorial Pacific SST bias can be explained as follows: An excessive equatorial cold tongue weakens the low-level wind response to SST forcing (Xiang et al. 2011) and thus reduces the strength of both EF and TF. Furthermore, the cold SST bias weakens the thermal stratification in the upper ocean (Xiang et al. 2011; Kim et al. 2013). This also reduces the strength of EF, because subsurface temperature influence on SST and ocean upwelling response to wind forcing are reduced. Furthermore, a weaker stratification can reduce the thermocline-subsurface temperature feedback (Xiang et al. 2011) and the thermocline slope response to wind stress anomalies (Kim et al. 2013). Consequently, the total TF is reduced. Since these feedbacks are strongest in boreal fall, this lowers SST anomaly growth and eventually interannual SST variability in boreal winter. Further, the cold SST bias weakens the shortwave damping and can even cause it to

be amplifying (Lloyd et al. 2012; Dommenget et al. 2014). This reduces TD and thus increases interannual SST variability in boreal spring. To summarize, the cold SST bias weakens seasonal ENSO phase locking by reducing SST variability in boreal winter and increasing SST variability in boreal spring.

We relate the strength of the equatorial cold SST bias to the perturbed physics in our set of experiments with the KCM. We show that changing specific parameters in the cloud scheme has an effect on the cold SST bias by altering the amount of low-level clouds over the cold tongue region, allowing realistic seasonal ENSO phase locking for specific parameter choices. We note that the applied changes to the convection scheme are specific to our atmospheric model, ECHAM5, and it is of interest whether this can be valid to other models. We also show that the vertical resolution in the atmosphere model has no systematic effect on the strength of the cold Pacific SST bias. However, it has to be kept in mind that atmospheric horizontal resolution has been kept fixed and consistency between horizontal and vertical resolution may be required. We note that a realistic seasonal ENSO phase locking can be achieved at coarse vertical atmosphere model resolution (e.g. experiment 28). This situation in the tropical Pacific is different to that in the tropical Atlantic: Harlaß et al. (2015) show that a reasonable seasonal phase locking of interannual SST variability in the equatorial Atlantic can only be achieved in the KCM at sufficiently high vertical and horizontal atmospheric resolution.

Previous studies have discussed the relationship between the equatorial Pacific cold SST bias, ENSO feedbacks and seasonal ENSO phase locking, which are consistent with this study. For instance, Bellenger et al. (2014) suggest that a larger shortwave feedback strengthens seasonal ENSO phase locking in CMIP3 + CMIP5 models. Furthermore, Rashid and Hirst (2015) point out the dependency of the shortwave feedback on local SST. Kim et al. (2013) also connect cold tongue biases to atmospheric and oceanic response biases, restricting the analysis, however, to annual mean conditions. Ham and Kug (2014) and Rashid and Hirst (2015) link the cold SST bias with phase locking biases via errors in the simulated feedbacks, but referring to a SST variability peak in the wrong season. We provide, with the aid of the BJ index, a comprehensive analysis of the importance of the cold equatorial Pacific SST bias for the seasonal variation of coupled feedbacks that control seasonal ENSO phase locking.

Due to its comprehensiveness, the BJ index is highly valuable for highlighting out significant processes that control ENSO-associated variability, especially in the ocean. Nevertheless, there are arguments about limitations of the BJ index in representing ENSO feedbacks. We find that the relatively small ensemble-mean BJ index cannot explain the too strong SST variability in the KCM (Fig. 4a), since low values of the BJ index would favor weak variability. Similar results are obtained by Kim et al. (2013) for a set of CMIP5 models. This suggests limitations of the BJ index in reflecting the overall strength of ENSO variability and should be the subject of further investigation. Furthermore, Graham et al. (2014) analyze the ability of the BJ index in representing ocean dynamics and point out the role of assuming linearity in the formulation, although ENSO processes can be inherently nonlinear (Lloyd et al. 2012; Bellenger et al. 2014). Duan et al. (2013) also underpin the important role of nonlinearities in seasonal ENSO phase locking. Yet the consistency between the results obtained from the KCM ensemble with those obtained from the CMIP5 ensemble is reassuring.

Acknowledgements This study is supported by the SACCUS project of the German Ministry of Education and Research (BMBF), the European Union's PREFACE project and the SFB754 "Climate-Biochemistry Interactions in the tropical Ocean". The climate model integrations were performed at the Computing Centre of Kiel University. We thank Dietmar Dommenget and an anonymous reviewer for helpful comments and feedback on this work. We thank Zhaoyang Song for his help for the Bjerknes Stability Index calculation. We acknowledge the World Climate Research Programme's Working Group on Coupled Modelling, which is responsible for CMIP, and we thank the climate modeling groups (listed in Table 2 of this paper) for producing and making available their model output. For CMIP the U.S. Department of Energy's Program for Climate Model Diagnosis and Intercomparison provides coordinating support and led development of software infrastructure in partnership with the Global Organization for Earth System Science Portals.

References

An S-I, Jin F-F (2000) An eigen analysis of the interdecadal changes in the structure and frequency of ENSO mode. Geophys Res Lett 27:2573–2576. doi:10.1029/1999GL011090

Battisti DS, Hirst AC (1989) Interannual variability in a tropical atmosphere–ocean model: influence of the basic state, ocean geometry and nonlinearity. J AtmosSci 46:1687–1712

Bayr T, Dommenget D (2013) The tropospheric land-sea warming contrast as the driver of tropical sea level pressure changes. J Climate 26:1387–1402

Bejarano L, Jin F-F (2008) Coexistence of equatorial coupled modes of ENSO. J Clim 21:3051–3067. doi:10.1175/2007JCLI1679.1

Bellenger H, Guilyardi E, Leloup J, et al (2014) ENSO representation in climate models: From CMIP3 to CMIP5. ClimDyn 42:1999–2018. doi:10.1007/s00382-013-1783-z

Bjerknes J (1969) Atmospheric teleconnections from the equatorial Pacific 1. Mon Weather Rev 97:163–172. doi:10.1175/1520-0493(1969)097<0163:ATFTEP>2.3.CO;2

Brönnimann S, Luterbacher J, Staehelin J et al (2004) Extreme climate of the global troposphere and stratosphere in 1940–42 related to El Niño. Nature 431:971–974. doi:10.1038/nature02982

Carton JA, Giese BS (2008) A Reanalysis of Ocean Climate Using Simple Ocean Data Assimilation (SODA). Mon Weather Rev 136:2999–3017. doi:10.1175/2007MWR1978.1

Chang P, Wang B, Li T, Ji L (1995) Interactions between the seasonal cycle and the Southern Oscillation—frequency

entrainment and chaos in a coupled ocean-atmosphere model. Geophys Res Lett 21:2817–2820. doi:10.1029/94GL02759
Davey MK, Huddleston M, Sperber KR, et al (2002) STOIC: a study of coupled model climatology and variability in tropical regions. ClimDyn 118:403–420
Dommenget D, Yu Y (2016) The seasonally changing cloud feedbacks contribution to the ENSO seasonal phase-locking. ClimDyn 47:1–12. doi:10.1007/s00382-016-3034-6
Dommenget D, Haase S, Bayr T, Frauen C (2014) Analysis of the Slab Ocean El Nino atmospheric feedbacks in observed and simulated ENSO dynamics. ClimDyn 42:3187–3205. doi:10.1007/s00382-014-2057-0
Duan WS, Zhang R, Yu YS, Tian B (2013) The role of nonlinearities associated with air-sea coupling processes in El Niño's peak-phase locking. Sci China. Earth Sci 56:1988–1996. doi:10.1007/s11430-013-4629-y
Fedorov AV, Philander SG (2001) A Stability Analysis of Tropical Ocean–Atmosphere Interactions: Bridging Measurements and Theory for El Niño. J Clim 14:3086–3101. doi:10.1175/1520-0442(2001)014<3086:ASAOTO>2.0.CO;2
Graham FS, Brown JN, Langlais C, et al (2014) Effectiveness of the Bjerknes stability index in representing ocean dynamics. ClimDyn 43:1–16. doi:10.1007/s00382-014-2062-3
Guilyardi E (2006) El Niño-mean state—Seasonal cycle interactions in a multi-model ensemble. ClimDyn 26:329–348. doi:10.1007/s00382-005-0084-6
Guilyardi E, Wittenberg A, Fedorov A, et al (2009) Understanding El Niño in Ocean–atmosphere general circulation models: progress and challenges. Bull Am MeteorolSoc 90:325–340. doi:10.1175/2008BAMS2387.1
Ham Y-G, Kug J-S (2014) ENSO phase-locking to the boreal winter in CMIP3 and CMIP5 models. ClimDyn 43:305–318. doi:10.1007/s00382-014-2064-1
Ham Y-G, Kug J-S, Kim D-H, et al (2012) What controls phase-locking of ENSO to boreal winter in coupled GCMs? ClimDyn 40:1551–1568. doi:10.1007/s00382-012-1420-2
Harlaß J, Latif M, Park W (2015) Improving climate model simulation of tropical Atlantic sea surface temperature: The importance of enhanced vertical atmosphere model resolution. Geophys Res Lett 42:2401–2408. doi:10.1002/2015GL063310
Harrison DE, Vecchi GA (1999) On the termination of El Niño. Geophys Res Lett 26:1593–1596. doi:10.1029/1999GL900316
Jin EK, Kinter JL (2009) Characteristics of tropical Pacific SST predictability in coupled GCM forecasts using the NCEP CFS. ClimDyn 32:675–691. doi:10.1007/s00382-008-0418-2
Jin F-F, Neelin JD, Ghil M (1996) El Niño/Southern Oscillation and the annual cycle: subharmonic frequency-locking and aperiodicity. Phys D Nonlinear Phenom 98:442–465. doi:10.1016/0167-2789(96)00111-X
Jin F-F, Kim ST, Bejarano L (2006) A coupled-stability index for ENSO. Geophys Res Lett 33:2–5. doi:10.1029/2006GL027221
Kim ST, Jin F-F (2011a) An ENSO stability analysis. Part I: Results from a hybrid coupled model. ClimDyn 36:1593–1607. doi:10.1007/s00382-010-0796-0
Kim ST, Jin F-F (2011b) An ENSO stability analysis. Part II: Results from the twentieth and twenty-first century simulations of the CMIP3 models. ClimDyn 36:1609–1627. doi:10.1007/s00382-010-0872-5
Kim D, Jang Y-S, Kim D-H et al (2011) El Niño-Southern Oscillation sensitivity to cumulus entrainment in a coupled general circulation model. J Geophys Res Atmos 116:D22112. doi:10.1029/2011JD016526
Kim ST, Cai W, Jin F-F, Yu J-Y (2013) ENSO stability in coupled climate models and its association with mean state. ClimDyn 42:3313–3321. doi:10.1007/s00382-013-1833-6
Klein S, Hartmann DL (1993) The seasonal cycle of low stratiform clouds. J Clim 6:1587–1606
Lacagnina C, Selten F (2013) Changes in the cloud properties in response to El Niño: a bivariate approach. ClimDyn 40:2973–2991. doi:10.1007/s00382-012-1645-0
Latif M, Graham NE (1992) How Much Predictive Skill Is Contained in the Thermal Structure of an Oceanic GCM? J Phys Oceanogr 22:951–962
Latif M, Sperber K, Arblaster J, et al (2001) ENSIP: the El Nino simulation intercomparison project. ClimDyn 18:255–276. doi:10.1007/s003820100174
Latif M, Semenov VA, Park W (2015) Super El Niños in response to global warming in a climate model. Clim Change 132:489–500. doi:10.1007/s10584-015-1439-6
Levine AFZ, McPhaden MJ (2015) The annual cycle in ENSO growth rate as a cause of the spring predictability barrier. Geophys Res Lett 42:5034–5041. doi:10.1002/2015GL064309
Li G, Xie S-P (2014) Tropical Biases in CMIP5 Multimodel Ensemble: The Excessive Equatorial Pacific Cold Tongue and Double ITCZ Problems. J Clim 27:1765–1780
Lloyd J, Guilyardi E, Weller H (2012) The role of atmosphere feedbacks during ENSO in the CMIP3 models. Part III: The shortwave flux feedback. J Clim 25:4275–4293. doi:10.1175/JCLI-D-11-00178.1
Lübbecke JF, Mcphaden MJ (2013) A comparative stability analysis of Atlantic and Pacific Niño modes. J Clim 26:5965–5980. doi:10.1175/JCLI-D-12-00758.1
Madec G (2008) NEMO ocean engine. Note du Pole de modélisation 27, Institut Pierre-Simon Laplace
Madec G, Delecluse P, Imbard M, Lévy C (1998) OPA 8.1 Ocean General Circulation Model Reference Manual. Note du Pole de modélisation 11, Institut Pierre-Simon Laplace
Mauritsen T, Stevens B, Roeckner E et al (2012) Tuning the climate of a global model. J Adv Model Earth Syst. doi:10.1029/2012MS000154
McGregor S, Timmermann A, Schneider N et al (2012) The Effect of the South Pacific Convergence Zone on the Termination of El Niño Events and the Meridional Asymmetry of ENSO. J Clim 25:5566–5586. doi:10.1175/JCLI-D-11-00332.1
McGregor S, Ramesh N, Spence P et al (2013) Meridional movement of wind anomalies during ENSO events and their role in event termination. Geophys Res Lett 40:749–754. doi:10.1002/grl.50136
Neelin, JD, Battisti DS, Hirst AC, Jin F-F, Wakata Y, Yamagata T, Zebiak SE (1998) ENSO theory. JGR Ocean 103: 14261–14290. doi:10.1029/97JC03424
Neelin JD, Jin F-F, Syu HH (2000) Variations in ENSO phase locking. J Clim 13:2570–2590. doi:10.1175/1520-0442(2000)013<2570:VIEPL>2.0.CO;2
Nordeng TE (1994) Extended Versions of the Convective Parametrization Scheme at ECMWF and Their Impact on the Mean and Transient Activity of the Model in the Tropics. In Technical Memorandum; European Center for Medium-Range Weather Forecasts (ECMWF): Reading, UK, 1994
Park W, Keenlyside N, Latif M et al (2009) Tropical Pacific Climate and Its Response to Global Warming in the Kiel Climate Model. J Clim 22:71–92. doi:10.1175/2008JCLI2261.1
Rashid H, Hirst AC (2015) Investigating the mechanisms of seasonal ENSO phase locking bias in the ACCESS coupled model. ClimDyn. doi:10.1007/s00382-015-2633-y
Rayner N, Parker DE, Horton EB et al (2003) Global analyses of sea surface temperature, sea ice, and night marine air temperature since the late Nineteenth Century. J Geophys Res 108:4407. doi:10.1029/2002JD002670
Reynolds RW (2009) What's New in Version 2. NOAA/NCDC Rep 1–10

Reynolds RW, Smith TM, Liu C et al (2007) Daily High-Resolution-Blended Analyses for Sea Surface Temperature. J Clim 20(22):5473–5496

Roeckner E, Baeuml G, Bonaventura L, et al (2003) The atmospheric general circulation model ECHAM 5. PART I: Model description. Max Planck Institute for Meteorology Rep. 349

Simmons EAJ, Gibson JK (2000) The ERA-40 project plan. Tech Rep, ERA-40 Project Report Series 1, ECMWF, Reading, United Kingdom

Stein K, Schneider N, Timmermann A, Jin F-F (2010) Seasonal synchronization of ENSO events in a linear stochastic model. J Clim 23:5629–5643

Stein K, Timmermann A, Schneider N et al (2014) ENSO Seasonal Synchronization Theory. J Clim 27:5285–5310. doi:10.1175/JCLI-D-13-00525.1

Stuecker MF, Timmermann A, Jin F-F et al (2013) A combination mode of the annual cycle and the El Niño/Southern Oscillation. Nat Geosci 6:540–544. doi:10.1038/ngeo1826

Sundqvist H (1978) A parameterization scheme for non-convective condensation including prediction of cloud water content. Q J R MeteorolSoc 104:677–690. doi:10.1002/qj.49710444110

Taylor KE, Stouffer RJ, Meehl GA (2012) An overview of CMIP5 and the experiment design. Bull Am MeteorolSoc 93:485–498. doi:10.1175/BAMS-D-11-00094.1

Tompkins AM (2002) A prognostic parameterization for the Subgrid-scale variability of water vapor and clouds in large-scale models and its use to diagnose cloud cover. J Atmos Sci 59:1917–1942. doi:10.1175/1520-0469(2002)059<1917:APPFTS>2.0.CO;2

Torrence C, Webster PJ (1998) The annual cycle of persistence in the El Niño/Southern Oscillation. Q J R MeteorolSoc 124:1985–2004. doi:10.1002/qj.49712455010

Tziperman E, Cane MA, Zebiak SE et al (1995) Irregularity and locking to the seasonal cycle in an ENSO prediction model as explained by the Quasi-Periodicity route to chaos. J AtmosSci 52:293–306. doi:10.1175/1520-0469(1995)052<0293:IALTTS>2.0.CO;2

Tziperman E, Cane MA, Zebiak SE et al (1998) Locking of El Niño's Peak Time to the End of the Calendar Year in the Delayed Oscillator Picture of ENSO. J Clim 11:2191–2199. doi:10.1175/1520-0442(1998)011<2191:LOENOS>2.0.CO;2

Valcke S (2006) OASIS3 user guide. PRISM Tech Rep No 3

Wang C, Picaut J (2004) Understanding ENSO physics: a review. GeophysMonogr AGU 147:21–48

Webster PJ, Magaña VO, Palmer TN et al (1998) Monsoons: Processes, predictability, and the prospects for prediction. J Geophys Res Ocean 103:14451–14510. doi:10.1029/97JC02719

Xiang B, Wang B, Ding Q, et al (2011) Reduction of the thermocline feedback associated with mean SST bias in ENSO simulation. ClimDyn 39:1413–1430. doi:10.1007/s00382-011-1164-4

Xiao H, Mechoso CR (2009) Seasonal cycle–El Niño relationship: validation of hypotheses. J AtmosSci 66:1633–1653

Zhang X, Lin W, Zhang M (2007) Toward understanding the double Intertropical Convergence Zone pathology in coupled ocean-atmosphere general circulation models. J Geophys Res 112:D12102. doi:10.1029/2006JD007878

Zheng W, Yu Y (2007) ENSO phase-locking in an ocean-atmosphere coupled model FGCM-1.0. AdvAtmosSci 24:833–844. doi:10.1007/s00376-007-0833-z

Zheng Y, Lin J-L, Shinoda T (2012) The equatorial Pacific cold tongue simulated by IPCC AR4 coupled GCMs: Upper ocean heat budget and feedback analysis. J Geophys Res 117(C5).doi:10.1029/2011jc007746

Zhu J, Kumar A, Huang B (2015) The relationship between thermocline depth and SST anomalies in the eastern equatorial Pacific: Seasonality and decadal variations. Geophys Res Lett 42:4507–4515. doi:10.1002/2015GL064220

Supplementary material for **chapter** 3:

Supplementary figures

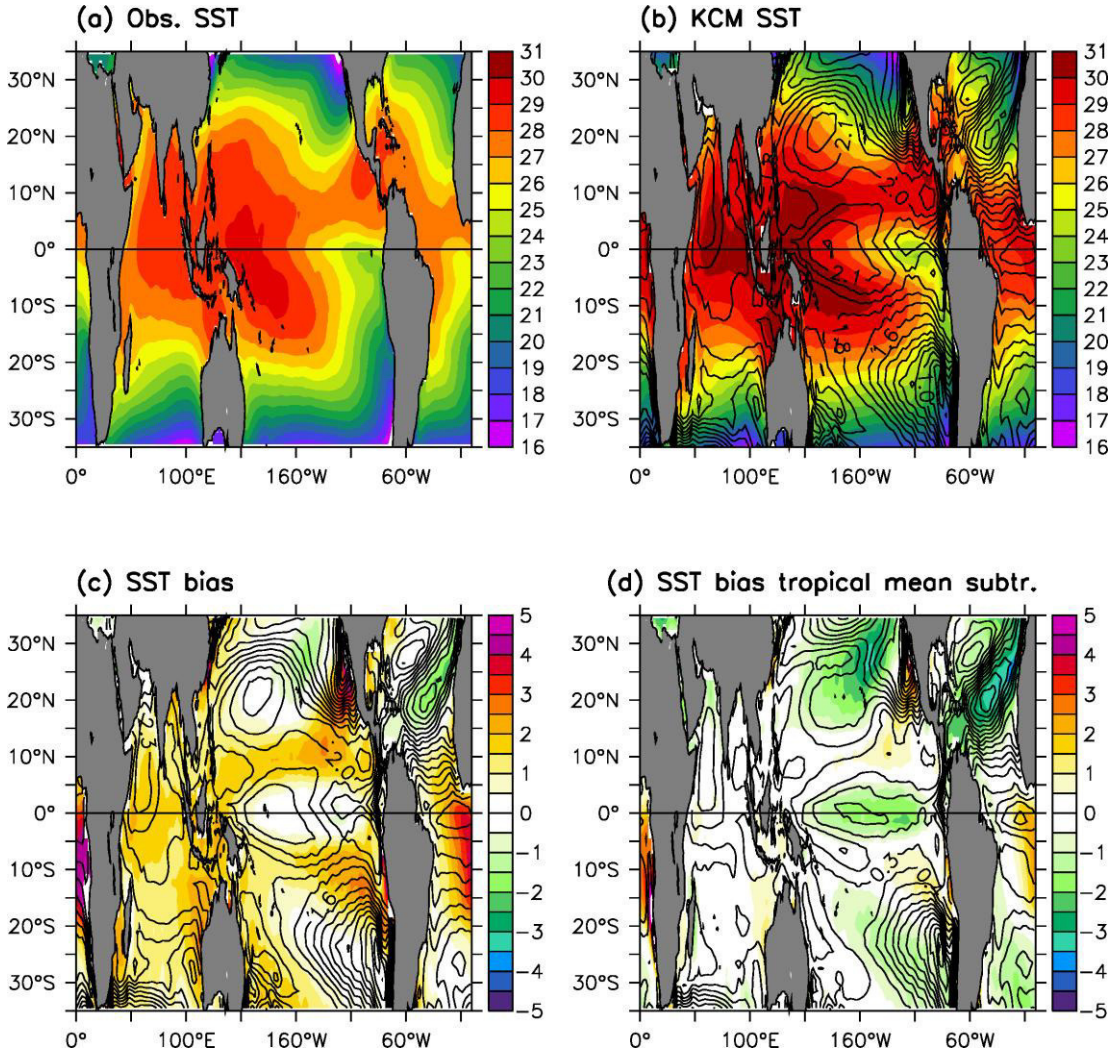

Fig. 1s (a) Long-term annual-mean SSTs from observations and (b) as given by the ensemble-mean calculated over all experiments with the KCM. (c) Total SST bias, (d) with tropical mean SSTs (15°S-15°N) subtracted. Contour lines depict the standard deviation over all model realizations. Unit is °C.

4 What controls ENSO-amplitude diversity in climate models?

Wengel, C., Dommenget, D., Latif, M., Bayr, T., and Vijayeta, A. (2018). What controls ENSO-amplitude diversity in climate models? Geophysical Research Letters, 45, 1989–1996. https://doi.org/10.1002/2017GL076849

The candidates' contributions to this publication are as follows:

1. He did all the analyses.

2. He produced all the figures.

3. He authored the manuscript from the first draft to the final version.

AGU PUBLICATIONS

Geophysical Research Letters

RESEARCH LETTER
10.1002/2017GL076849

Key Points:
- Large contribution to El Niño/Southern Oscillation (ENSO)-amplitude diversity in climate models originates from stochastic forcing
- Competing effects in the ENSO dynamics present an important source for ENSO-amplitude diversity
- Due to the importance of stochastic forcing and competing processes, the growth rate of sea surface temperature anomalies must not necessarily correlate with ENSO amplitude

Supporting Information:
- Supporting Information S1
- Data Set S1

Correspondence to:
C. Wengel,
cwengel@geomar.de

Citation:
Wengel, C., Dommenget, D., Latif, M., Bayr, T., & Vijayeta, A. (2018). What controls ENSO-amplitude diversity in climate models? *Geophysical Research Letters*, *45*, 1989–1996. https://doi.org/10.1002/2017GL076849

Received 18 DEC 2017
Accepted 10 FEB 2018
Accepted article online 16 FEB 2018
Published online 24 FEB 2018

What Controls ENSO-Amplitude Diversity in Climate Models?

C. Wengel[1], D. Dommenget[2], M. Latif[1,3], T. Bayr[1], and A. Vijayeta[2]

[1]GEOMAR Helmholtz Centre for Ocean Research Kiel, Kiel, Germany, [2]School of Earth, Atmosphere and Environment, Monash University, Clayton, Victoria, Australia, [3]Excellence Cluster "The Future Ocean", Kiel University, Kiel, Germany

Abstract Climate models depict large diversity in the strength of the El Niño/Southern Oscillation (ENSO) (ENSO amplitude). Here we investigate ENSO-amplitude diversity in the Coupled Model Intercomparison Project Phase 5 (CMIP5) by means of the linear recharge oscillator model, which reduces ENSO dynamics to a two-dimensional problem in terms of eastern equatorial Pacific sea surface temperature anomalies (T) and equatorial Pacific upper ocean heat content anomalies (h). We find that a large contribution to ENSO-amplitude diversity originates from stochastic forcing. Further, significant interactions exist between the stochastic forcing and the growth rates of T and h with competing effects on ENSO amplitude. The joint consideration of stochastic forcing and growth rates explains more than 80% of the ENSO-amplitude variance within CMIP5. Our results can readily explain the lack of correlation between the Bjerknes Stability index, a measure of the growth rate of T, and ENSO amplitude in a multimodel ensemble.

1. Introduction

The El Niño/Southern Oscillation (ENSO) is the dominant mode of interannual climate variability in the tropics. ENSO is characterized by sea surface temperature (SST) anomalies of a few centigrade primarily in the eastern and central equatorial Pacific, which drive global teleconnections (e.g., Brönnimann et al., 2004). Large diversity among coupled general circulation models (CGCMs) in ENSO statistics such as ENSO amplitude exists (Bellenger et al., 2014; Latif et al., 2001). Understanding the different ENSO dynamics among CGCMs is fundamental for making robust statements about the level of related seasonal climate predictability and uncertainty in long-term ENSO projections.

Over the past years, considerable progress has been made in understanding ENSO diversity in CGCMs by applying conceptual models that condense the dynamics of ENSO into a simple theoretical framework. One example is the Bjerknes Stability (BJ) index (Jin et al., 2006), which approximates the growth rate of SST anomalies (T) in the eastern equatorial Pacific by the recharge oscillator framework (Jin, 1997) and allows examination of the positive and negative feedbacks relevant to ENSO. The BJ index has been used to study ENSO-amplitude diversity among CGCMs (Ferrett & Collins, 2016; Kim et al., 2014; Kim & Jin, 2011). A recent study by An et al. (2017) showed that the diversity in the thermocline feedback is highly correlated to ENSO-amplitude diversity. The BJ index has also been used to study potential ENSO changes in a warmer climate (Ferrett & Collins, 2016; Kim & Jin, 2011). In theory, a larger BJ index is associated with larger ENSO amplitude. Kim et al. (2014) have shown that the BJ index is correlated to ENSO amplitude in models from the Coupled Model Intercomparison Project Phase 3 (CMIP3). However, this correlation breaks down in models participating in CMIP5 (due to a few outliers). One possible explanation is that nonlinear dynamics are not represented by the BJ index (Graham et al., 2014). Further, the potential influence from atmospheric noise has been discussed in this context (Ferrett & Collins, 2016).

Another powerful tool for investigating ENSO diversity among models is the simplest version of the recharge oscillator model of Burgers et al. (2005) (ReOsc model hereafter). The growth mechanism in this model is due to a positive coupled feedback (Bjerknes, 1969), whereas the oscillatory component is driven by the recharge-discharge of equatorial ocean heat content (Cane & Zebiak, 1985; Wyrtki, 1975, 1986). This dynamical framework can be described by a damped harmonic oscillator (Burgers et al., 2005) with SST and thermocline depth playing the roles of momentum and position, respectively. The oscillatory nature of ENSO allows the ReOsc model to capture important characteristics of ENSO dynamics. Many studies have used the ReOsc model to analyze ENSO dynamics in various approaches (Burgers et al., 2005; Frauen & Dommenget, 2010; Jansen et al., 2009; Jin et al., 2007; Levine & McPhaden, 2015; Vijayeta & Dommenget, 2017; Yu et al., 2016). In contrast to the one-dimensional framework underlying the BJ index, the ReOsc model is based on two coupled

equations in which six parameters, including stochastic noise forcing (hereafter stochastic forcing), control ENSO amplitude.

In this paper, the ReOsc model is used to investigate ENSO-amplitude diversity in CMIP5 models. We investigate the relative importance of the ReOsc model parameters for ENSO amplitude with a special focus on the role of stochastic forcing for ENSO-amplitude diversity among CMIP5 models.

2. Data and Methods

We analyze the historical experiments from 35 CMIP5 models (Taylor et al., 2012) for the time period from 1921 to 2000 (Table S1). Output from the Simple Ocean Data Assimilation (SODA) ocean reanalysis product version 2.0.2 (Carton & Giese, 2008) for the period 1958–2001 is used for comparison.

The ReOsc model describes the oscillatory behavior of ENSO by the interaction of eastern equatorial Pacific SST and equatorial Pacific zonal-mean upper ocean heat content:

$$\frac{dT}{dt} = a_{11} \cdot T + a_{12} \cdot h + \xi_T \tag{1}$$

$$\frac{dh}{dt} = a_{21} \cdot T + a_{22} \cdot h + \xi_h \tag{2}$$

where T is the monthly eastern equatorial Pacific SST anomaly; h is the monthly equatorial Pacific zonal-mean thermocline depth anomaly, which is commonly used to approximate the upper ocean heat content anomaly; a_{11} and a_{22} are the growth rate of T and h, respectively; a_{12} and a_{21} are the coupling of T to h and h to T, respectively; and ξ_T and ξ_h are stochastic forcing terms of T and h, respectively. T is averaged here over the Niño3.4-region (170°W–120°W; 5°S–5°N), and h is averaged across the equatorial Pacific (130°E–80°W; 5°S–5°N). The ReOsc model parameters a_{11}, a_{12}, a_{21}, and a_{22} are estimated via multivariate linear regression of the T and h tendencies against T and h, respectively. The stochastic forcing terms are approximated as the standard deviation (SD) of the residuals of the fit, which also may contain dynamics that cannot purely be considered as noise in the sense that they are independent of the large-scale coupled dynamics. We note that the stochastic forcing could be further separated into a state-dependent and a state-independent part (Levine et al., 2016). This, however, would be beyond the scope of this paper. Following Kim et al. (2014) we approximate ENSO amplitude by the SD of T.

The parameter a_{11} is influenced by a number of atmospheric and oceanic processes (Frauen & Dommenget, 2010; Vijayeta & Dommenget, 2017; Yu et al., 2016) such as the Bjerknes feedback and atmospheric heat fluxes as well as ocean dynamics such as mixing and advection. In general, a_{22} is assumed to be close to zero as changes in h are not determined by the thermocline depth itself but rather by the geostrophic response to wind stress (Burgers et al., 2005). On the other hand, a damping of h can be achieved via wave-friction as in the delayed action oscillator model (Suarez & Schopf, 1988). The oscillatory behavior of the ReOsc model is determined by the coupling between T and h, whereby a_{12} is the local warming effect of h on T and a_{21} is the influence of T on h via the atmospheric bridge. Parameter ξ_T is the stochastic forcing of T primarily related to westerly wind bursts, whereas ξ_h is supposed to be largely influenced by ξ_T as both terms are correlated (see below). The stochastic forcing introduces an irregularity to the harmonic oscillation.

The ReOsc model equations can be integrated with stochastic forcing terms to generate time series of T and h using fixed values for a_{11}, a_{12}, a_{21}, and a_{22}. We use a time step of 24 hr and assumed red-noise stochastic forcing terms ξ_T and ξ_h with a decorrelation time of 3 days, mimicking weather systems, which effectively results in white noise forcing when considering monthly means. Identical stochastic forcing is used in all integrations, which allows us to discuss changes of T as functions of parameter changes without any uncertainties resulting from the noise. The integration length of all experiments is 1000 years. Prior to analysis, the linear trend was subtracted from all data and anomalies of T and h were obtained by subtracting the climatological seasonal cycle.

3. Results

The relative importance of the growth rates, coupling, and stochastic forcing terms, as represented by the six ReOsc model parameters, in determining ENSO amplitude is investigated in the CMIP5 model ensemble

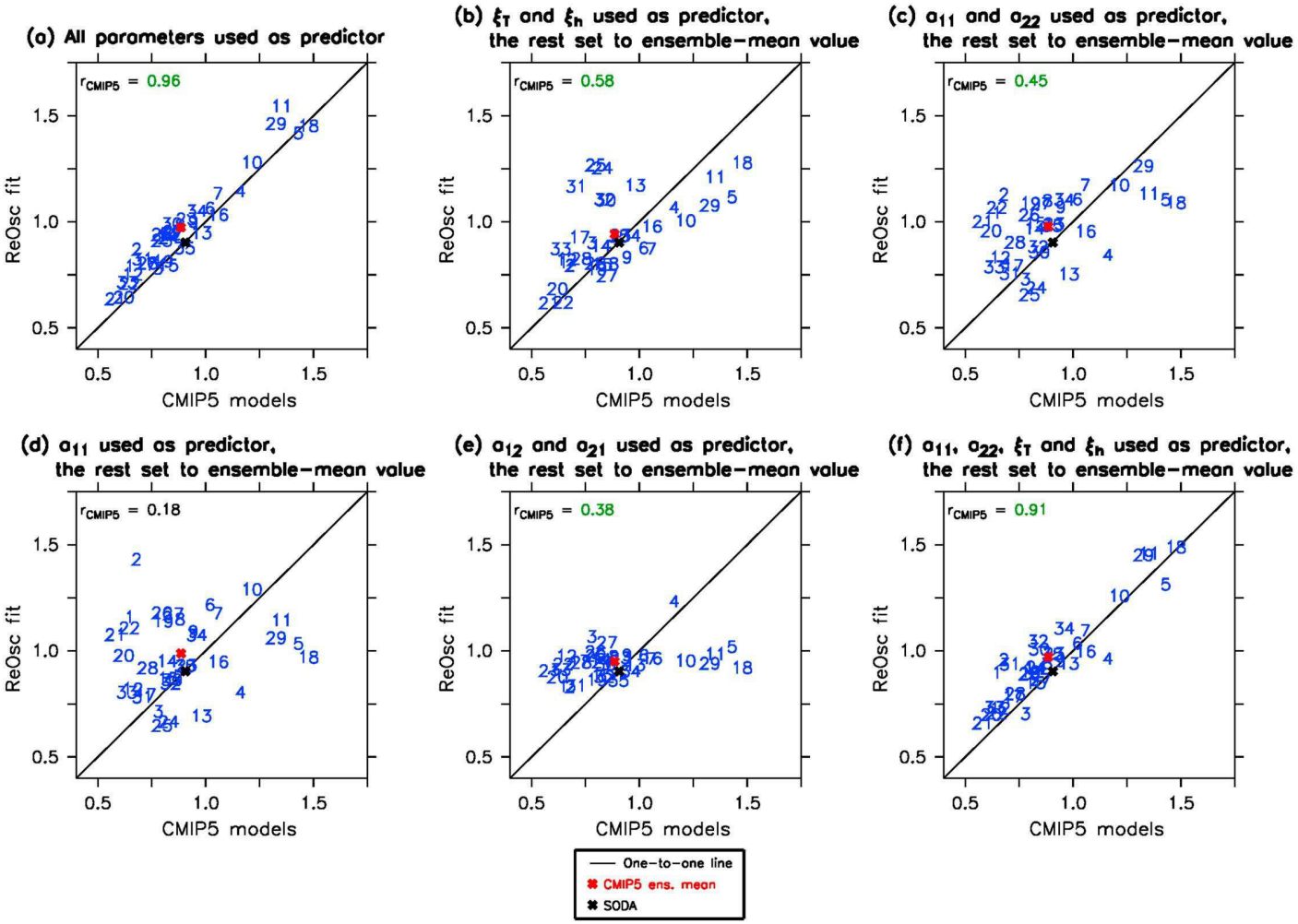

Figure 1. Scatter plots of El Niño/Southern Oscillation (ENSO) amplitude (K) as simulated by the Coupled Model Intercomparison Project Phase 5 (CMIP5) models (horizontal axes) and that obtained from integrating the recharge oscillator (ReOsc) model with parameters estimated for each CMIP5 model (vertical axis) where (a) all six ReOsc parameters are used for the integration, (b) only ξ_T and ξ_h are used, (c) only a_{11} and a_{22}, (d) only a_{11}, (e) only a_{12} and a_{21}, and (f) only a_{11}, a_{22}, ξ_T, and ξ_h with the other parameters set fixed at the ensemble-mean values. Shown are also the CMIP5 ensemble-mean (red cross) and Simple Ocean Data Assimilation (SODA) (black cross), the linear correlation coefficient over all CMIP5 models in the upper left corner of each figure panel (values marked in green indicate statistical significance at the 95%) and the diagonal (black line).

(Figure 1). We compare ENSO amplitude obtained from integrating the ReOsc model using the parameters estimated separately for each CMIP5 model with that directly calculated from each model (Figure 1a). All models are located near the diagonal with a correlation coefficient of 0.96, implying that the ReOsc model is capable to reproduce ENSO amplitude with the respective parameters from each model. We then repeated the integrations by only using from each model the stochastic forcing terms ξ_T and ξ_h (Figure 1b), the respective growth rates a_{11} and a_{22} (Figure 1c) and a_{11} (Figure 1d), and the coupling terms a_{12} and a_{21} (Figure 1e) while keeping the other parameters fixed at the ensemble-mean value. The results suggest that the largest influence on ENSO amplitude originates from the stochastic forcing terms of T and h with a correlation of 0.58. The stochastic forcing term exhibits a large variability among the CMIP5 models, while it is quite constant in time within each individual CMIP5 simulation. The model spread is roughly three times larger than the temporal variability within each individual CMIP5 model simulation (Table S2). Second largest influence on ENSO amplitude is due to the growth rates of T and h with a correlation of 0.45. When only varying the growth rate of T (a_{11}), the variation of ENSO amplitude is large but the correlation is very low (0.18). The integrations of the ReOsc model by only using the coupling parameters from each CMIP5 model yields very little variation in ENSO amplitude. The combined variation of the growth rates and the stochastic

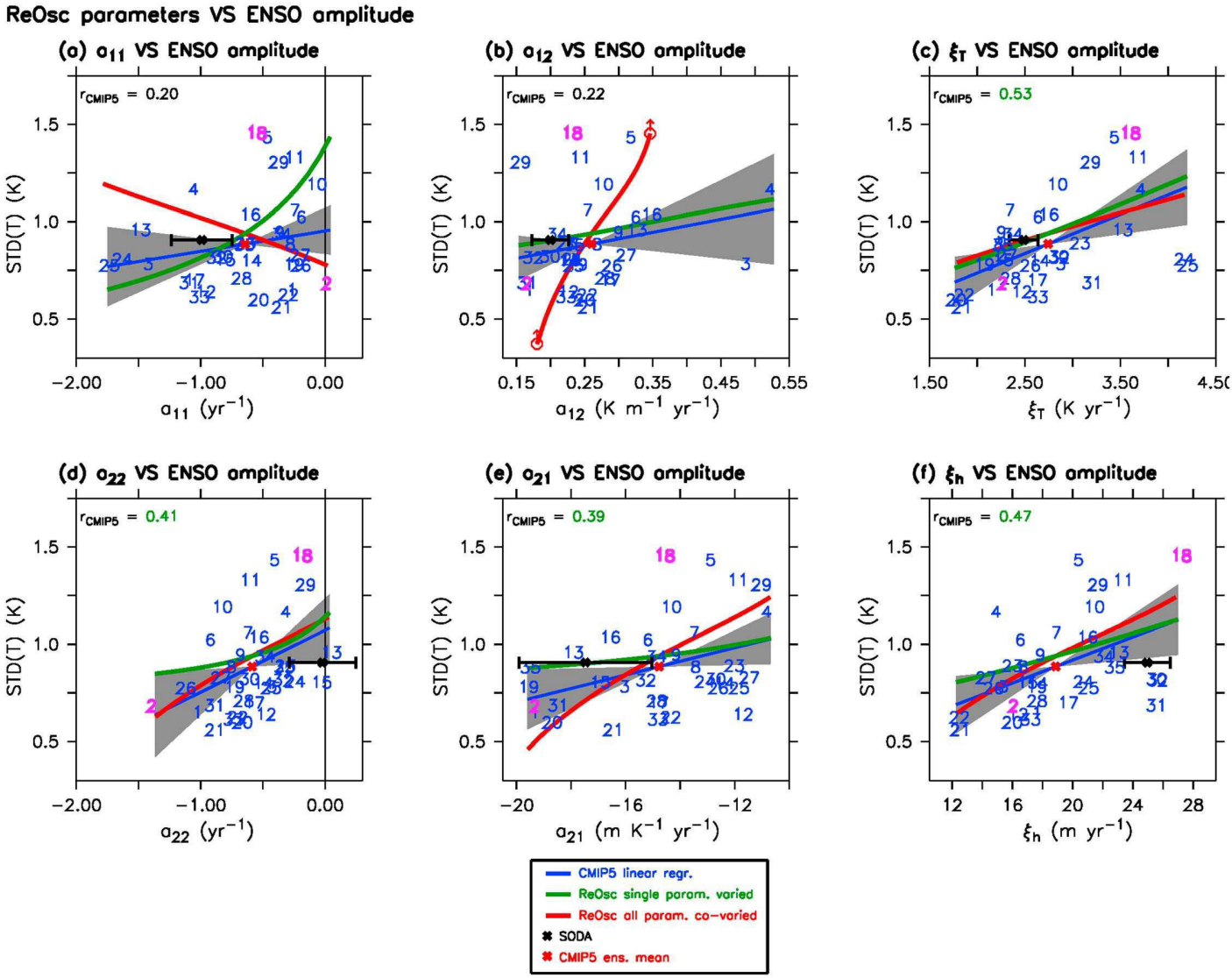

Figure 2. Scatter plot of El Niño/Southern Oscillation (ENSO) amplitude versus the (a) growth rate of T (a_{11}), (b) coupling of T to h (a_{12}), (c) stochastic forcing of T (ξ_T), (d) growth rate of h (a_{22}), (e) coupling of h to T (a_{21}), and (f) stochastic forcing of h (ξ_h) in the Coupled Model Intercomparison Project Phase 5 (CMIP5) models (blue numbers), the CMIP5 ensemble mean (red cross), and Simple Ocean Data Assimilation (SODA) (black cross with 95% confidence interval). The linear correlation coefficient over all CMIP5 models is given in the upper left corner of each figure panel (statistically significant values at the 95% level are shown in green), and a linear regression line is added (blue line) with a 95% uncertainty range (gray shading). Also shown is ENSO amplitude obtained from integrating the recharge oscillator (ReOsc) model as a function of a single parameter (green graph) and as a function of covarying parameters based on EOF-1 (red graph). The red circles with an upward arrow in (b) illustrate infinite growth of ENSO amplitude (see text for details). CMIP5 models 2 and 18 are highlighted in magenta for discussion (see text).

forcing terms (Figure 1f) yields a correlation of 0.91, which is very similar to the case in which all six parameters were varied. Thus, besides the stochastic forcing, the growth rates of T and h are important factors in controlling ENSO-amplitude diversity in CMIP5.

We next compare ENSO amplitude in the CMIP5 model ensemble and as derived from SODA (black cross) with the parameters a_{11}, a_{12}, a_{21}, a_{22}, ξ_T, and ξ_h estimated separately for each model (Figure 2, blue numbers). The uncertainty of the estimated parameters from each individual CMIP5 model (Table S3) is on average smaller than the uncertainty estimated from SODA (black horizontal error bar), which in turn is much smaller than the model spread in CMIP5. In CMIP5, the growth rate of T (a_{11}) shows no significant correlation with ENSO amplitude (Figure 2a), which is consistent with the results from Kim et al. (2014) applying the BJ index. Both a_{11} and the BJ index are estimates of the growth rate of T.

Table 1
ReOsc Parameter Cross Correlations in CMIP5

	Cross correlations					
	a_{11}	a_{12}	a_{21}	a_{22}	ξ_T	ξ_h
a_{11}		−0.18	−0.07	**−0.57**	**−0.58**	−0.26
a_{12}			0.20	0.17	0.17	**−0.34**
a_{21}				0.23	**0.44**	−0.07
a_{22}					**0.49**	**0.38**
ξ_T						**0.52**

Note. Correlation values marked in bold indicate statistical significance at the 95% level.

The relationship between each single ReOsc parameter and ENSO amplitude is modeled by a set of ReOsc model integrations. Each parameter is varied separately to cover the full range in CMIP5, while the other parameters are set to the ensemble-mean values (see section 2 for details). The results (green lines in Figures 2a–2f) are quite different from the linear relationships obtained from the CMIP5 models themselves (blue line in Figures 2a–2f), especially for the growth rates a_{11} (Figure 2a) and to a lesser extent a_{22} (Figure 2d).

The combined effect of all parameters ultimately determines the ENSO amplitude in each CMIP5 model. There are significant cross relationships between the variations of the ReOsc parameters within the CMIP5 ensemble, as shown by their cross correlations (Table 1). Largest anticorrelation is found between a_{11} and a_{22} (−0.57) as well as between a_{11} and ξ_T (−0.58) and largest positive correlation between ξ_T and ξ_h (0.52). This suggests the presence of competing ENSO processes, which previously has been discussed in terms of ENSO feedbacks (e.g., Bayr et al., 2017; Bellenger et al., 2014; Lloyd et al., 2009). These studies addressed the compensation between the too weak positive zonal wind feedback and the too weak negative heat flux feedback observed in most climate models, which possibly is reflected by the anticorrelation of a_{11} with a_{22} and ξ_T. The heat flux feedback is contributing to a_{11} (Frauen & Dommenget, 2010), and changes in h and hence in a_{22} are mainly governed by the geostrophic response to wind stress (Burgers et al., 2005). Further, ξ_T is driven by atmospheric noise primarily associated with westerly wind bursts. However, a detailed analysis of the origin of these covariations is beyond the scope of this paper.

To investigate the impact of the competing processes on ENSO amplitude, we extract modes of covariance from the ReOsc model parameters (Figure 3) by performing an empirical orthogonal function (EOF) analysis, with the six ReOsc model parameters as one dimension and the individual CMIP5 models as the other dimension. The leading mode (EOF-1) explains 42% of the parameter variability (Figure 3a). Consistent with the most significant cross correlations (Table 1), EOF-1 describes covariability between a_{11} and a_{22}, between a_{11} and ξ_T with opposite signs (Figure 3b), and between ξ_T and ξ_h with the same sign. Explained variances for each parameter are depicted in Figure 3c. EOF-1 explains largest variance in a_{11} (59%), a_{22} (63%), and ξ_T (77%), whereas it explains less variance in ξ_h (31%) and low variance in a_{12} (4%) and a_{21} (17%). EOF-2, on the other hand, accounts for the largest explained variance in a_{12} (67%), a_{21} (26%), and ξ_h (50%) but only less than 1% in the other parameters.

The sensitivity of ENSO amplitude to the covariability given by EOF-1 can be estimated by scaling the EOF-1 pattern (Figure 3b) over the range of a_{11}. Using this new set of parameters, the ReOsc model is again

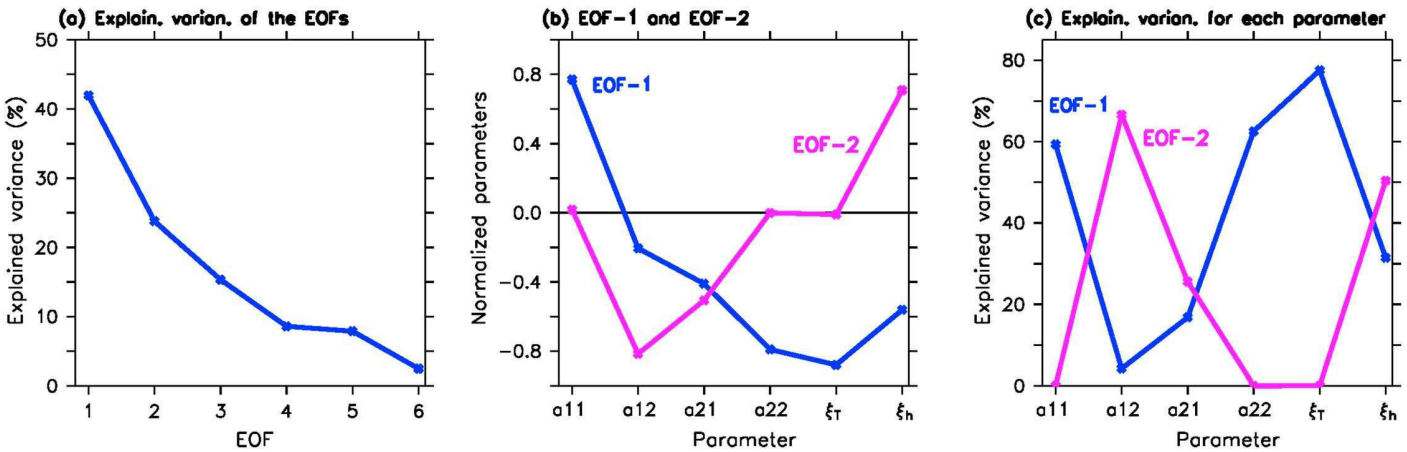

Figure 3. Results from the empirical orthogonal function (EOF) analysis of recharge oscillator parameters in the Coupled Model Intercomparison Project Phase 5. Shown are (a) the explained variances of the EOFs, (b) EOF-1 and EOF-2 (normalized by the standard deviation of the parameters), and (c) the explained variances of EOF-1 and EOF-2 for each parameter.

integrated and ENSO-amplitude dependence calculated (red line in Figures 2a–2f). The covariation among the parameters as given by EOF-1 leads to a dramatic change of ENSO-amplitude dependence on the ReOsc model parameters (red lines in Figures 2a–2f). For example, ENSO amplitude decreases with larger values of a_{11} (red line in Figure 2a), which is the opposite relationship as if only a_{11} is varied (green line). Considering the covariability among the parameters reduces the root-mean-square errors (Table S4). This demonstrates a significant influence of competing processes on ENSO amplitude, mainly between a_{11}, a_{22}, and ξ_T.

We illustrate the impact of the competing processes for specific models using the growth rate of T (a_{11}) as a first guess of ENSO amplitude. For example, the Australian Community Climate and Earth System Simulator 1.3 (ACCESS1.3) model exhibits rather small ENSO amplitude compared to the other models and SODA (black cross), although a_{11} is largest (magenta number 2 in Figure 2a).On the other hand, the growth rate of the thermocline depth perturbation h (a_{22}) is small in ACCESS1.3 (Figure 2d) as are the coupling terms (Figures 2b and 2e). Further, there are rather small stochastic forcing terms in ACCESS1.3 (Figures 2c and 2f). Altogether, this may explain why ENSO amplitude is unexpectedly small in this model. Another interesting example is the Geophysical Fluid Dynamics Laboratory Earth System Model 2M, which exhibits the largest ENSO amplitude but not exceptionally large a_{11} (magenta number 18 in Figure 2a). In this model, the growth rate of h (a_{22}) is high as are the two stochastic forcing terms. It is this combination that leads to large ENSO amplitude. Our results suggest that competing ENSO processes is a key to explain ENSO-amplitude diversity in the CMIP5 model ensemble and that the growth rate of T (a_{11}) alone cannot explain the diversity.

With respect to the coupling parameter a_{12}, the ReOsc model with the covariability of EOF-1 included becomes unstable for certain parameter values and ENSO amplitude grows to infinity, which is illustrated in Figure 2b (red circle with upward arrow). This is because EOF-1 explains only a small fraction of the total variance in a_{12}. Variations in this parameter are better modeled by EOF-2 (not shown), as suggested by Figure 3c.

We also repeated the analysis for those CMIP5 models that were selected by Kim et al. (2014), for a set of perturbed physics simulations with the Kiel Climate Model (Park et al., 2009; Wengel et al., 2017) and for the CMIP3 models (Figures S1–S9 and Tables S5–S13). Qualitatively, the results from the KCM and CMIP3 ensembles are very similar to the CMIP5 results presented here. The stochastic forcing, however, explains less variance in ENSO-amplitude diversity in the former two ensembles relative to CMIP5, but the combined variation of the stochastic forcing and the growth rate again explains the largest fraction of the spread as in CMIP5. Further, the growth rate of T (a_{11}) explains less variance in the parameter space in CMIP3 in comparison to CMIP5 and yields slightly different behavior with respect to the competing processes.

4. Conclusions

We have investigated ENSO-amplitude diversity in models from the CMIP5 within the framework of the linear ReOsc model. The model involves six parameters representing the growth rates of the eastern equatorial Pacific sea surface temperature anomaly (T) and equatorial Pacific upper ocean heat content anomaly (h), the mutual coupling and stochastic forcing of T and h. The ReOsc model has the form of a damped harmonic oscillator with T and h playing the roles of momentum and position, respectively. Regardless of the ReOsc models' simplicity, it can well represent ENSO statistics in reanalysis data (SODA) and climate models.

A large fraction contributing to ENSO-amplitude diversity in the CMIP5 model ensemble is due to variations in stochastic forcing (34%). This was shown by comparing ENSO amplitudes calculated from the CMIP5 models themselves with those obtained from ReOsc model integrations when only taking into account the effect of stochastic forcing. This finding relates to the limited predictability of El Niño and La Niña events due to the chaotic nature of high-frequency variability (Eckert & Latif, 1997). Relatively large influence on ENSO-amplitude diversity also originates from the growth rates of T and h (20%), whereas their coupling strength is of minor influence. The combined effect of stochastic forcing and the growth rates explains more than 80% of the variance in ENSO amplitude.

Further analysis revealed competing effects in the ENSO dynamics of the CMIP5 models, primarily between the growth rates of T and h, and the stochastic forcing of T. The competing processes present an important source for ENSO-amplitude modulations in climate models. This was shown by integrating the ReOsc model

for a range of parameters, with and without taking into account the effects of the competing processes, and comparing the results with those directly obtained from the CMIP5 models. The effect of changes in the growth rate of T on ENSO amplitude is largely offset by that of the growth rate of h and by the stochastic forcing of T. The cause of these dynamic cross relations is unclear at this point but presents an interesting aspect of ENSO dynamics and requires further investigation. The possible relation to ENSO feedback compensation has been noted (Bayr et al., 2017; Bellenger et al., 2014; Lloyd et al., 2009).

We find that the growth rate of T from the ReOsc model only explains a very little fraction of ENSO-amplitude variance. Further, the growth rate does not significantly correlate with ENSO amplitude in CMIP5. This is consistent with the finding by Kim et al. (2014), who applied the BJ index, which approximates the growth rate of T in terms of positive and negative ENSO feedbacks. We show that the effects of stochastic forcing and competing processes are important factors contributing to ENSO-amplitude diversity. Since the BJ index does not account for these effects, it must not necessarily correlate with ENSO amplitude.

Acknowledgments
This work was supported by the Integrated School of Ocean Sciences (ISOS) at the Excellence Cluster "The Future Ocean" at Kiel University, the German Ministry of Education and Research (BMBF) grant SACUS (03G0837A) and EU FP7/2007–2013 under grant agreement 603521, project PREFACE, the ARC Centre of Excellence for Climate System Science, Australian Research Council (grant CE110001028), and SFB 754 "Climate-Biochemistry Interactions in the tropical Ocean." We thank two anonymous reviewers for helpful comments and feedback on this work. We acknowledge the World Climate Research Programme's Working Group on Coupled Modeling, which is responsible for CMIP, and we thank the climate modeling groups (listed in Table S1 in the supporting information of this paper) for producing and making available their model output. The CMIP5 data output is available at http://www.ipcc-data.org/sim/gcm_monthly/AR5/Reference-Archive.html. For CMIP the U.S. Department of Energy's Program for Climate Model Diagnosis and Intercomparison provides coordinating support and led development of software infrastructure in partnership with the Global Organization for Earth System Science Portals. The processed CMIP5 data used for this paper are available in the supporting information. Data presented in the supporting information can be provided upon request. The supplementary climate model integrations with the Kiel Climate Model were performed at the Computing Centre of Kiel University. This study is a contribution to the Cluster of Excellence "The Future Ocean."

References

An, S.-I., Heo, E. S., & Kim, S. T. (2017). Feedback process responsible for intermodel diversity of ENSO variability. *Geophysical Research Letters*, *44*, 4272–4279. https://doi.org/10.1002/2017GL073203

Bayr, T., Latif, M., Dommenget, D., Wengel, C., Harlaß, J., & Park, W. (2017). Mean-state dependence of ENSO atmospheric feedbacks in climate models. *Climate Dynamics*. https://doi.org/10.1007/s00382-017-3799-2

Bellenger, H., Guilyardi, E., Leloup, J., Lengaigne, M., & Vialard, J. (2014). ENSO representation in climate models: From CMIP3 to CMIP5. *Climate Dynamics*, *42*(7-8), 1999–2018. https://doi.org/10.1007/s00382-013-1783-z

Bjerknes, J. (1969). Atmospheric teleconnections from the equatorial Pacific. *Monthly Weather Review*, *97*(3), 163–172. https://doi.org/10.1175/1520-0493(1969)097%3C0163:ATFTEP%3E2.3.CO;2

Brönnimann, S., Luterbacher, J., Staehelin, J., Svendby, T. M., Hansen, G., & Svenøe, T. (2004). Extreme climate of the global troposphere and stratosphere in 1940–42 related to El Niño. *Nature*, *431*(7011), 971–974. https://doi.org/10.1038/nature02982

Burgers, G., Jin, F. F., & van Oldenborgh, G. J. (2005). The simplest ENSO recharge oscillator. *Geophysical Research Letters*, *32*, L13706. https://doi.org/10.1029/2005GL022951

Cane, M. A., & Zebiak, S. E. (1985). A theory for El Niño and the southern oscillation. *Science*, *228*, 1084–1087.

Carton, J. A., & Giese, B. S. (2008). A reanalysis of ocean climate using simple ocean data assimilation (SODA). *Monthly Weather Review*, *136*(8), 2999–3017. https://doi.org/10.1175/2007MWR1978.1

Eckert, C., & Latif, M. (1997). Predictability of a stochastically forced hybrid coupled model of El Niño. *Journal of Climate*, *10*(7), 1488–1504. https://doi.org/10.1175/1520-0442(1997)010%3C1488:POASFH%3E2.0.CO;2

Ferrett, S., & Collins, M. (2016). ENSO feedbacks and their relationships with the mean state in a flux adjusted ensemble. *Climate Dynamics*, 1–20. https://doi.org/10.1007/s00382-016-3270-9

Frauen, C., & Dommenget, D. (2010). El Niño and la Niña amplitude asymmetry caused by atmospheric feedbacks. *Geophysical Research Letters*, *37*, L18801. https://doi.org/10.1029/2010GL044444

Graham, F. S., Brown, J. N., Langlais, C., Marsland, S. J., Wittenberg, A. T., & Holbrook, N. J. (2014). Effectiveness of the Bjerknes stability index in representing ocean dynamics. *Climate Dynamics*, *43*(9-10), 2399–2414. https://doi.org/10.1007/s00382-014-2062-3

Jansen, M. F., Dommenget, D., & Keenlyside, N. (2009). Tropical atmosphere-ocean interactions in a conceptual framework. *Journal of Climate*, *22*(3), 550–567. https://doi.org/10.1175/2008JCLI2243.1

Jin, F.-F. (1997). An equatorial ocean recharge paradigm for ENSO. Part I: Conceptual model. *Journal of the Atmospheric Sciences*, *54*(7), 811–829. https://doi.org/10.1175/1520-0469(1997)054%3C0811:AEORPF%3E2.0.CO;2

Jin, F.-F., Kim, S. T., & Bejarano, L. (2006). A coupled-stability index for ENSO. *Geophysical Research Letters*, *33*, L23708. https://doi.org/10.1029/2006GL027221

Jin, F.-F., Lin, L., Timmermann, A., & Zhao, J. (2007). Ensemble-mean dynamics of the ENSO recharge oscillator under state-dependent stochastic forcing. *Geophysical Research Letters*, *34*, L03807. https://doi.org/10.1029/2006GL027372

Kim, S. T., Cai, W., Jin, F.-F., & Yu, J.-Y. (2014). ENSO stability in coupled climate models and its association with mean state. *Climate Dynamics*, *42*(11-12), 3313–3321. https://doi.org/10.1007/s00382-013-1833-6

Kim, S. T., & Jin, F. F. (2011). An ENSO stability analysis. Part II: Results from the twentieth and twenty-first century simulations of the CMIP3 models. *Climate Dynamics*, *36*(7-8), 1609–1627. https://doi.org/10.1007/s00382-010-0872-5

Latif, M., Sperber, K., Arblaster, J., Braconnot, P., Chen, D., Colman, A., et al. (2001). ENSIP: The El Niño simulation intercomparison project. *Climate Dynamics*, *18*(3-4), 255–276. https://doi.org/10.1007/s003820100174

Levine, A., Jin, F.-F., & McPhaden, M. J. (2016). Extreme noise–extreme El Niño: How state-dependent noise forcing creates El Niño–La Niña asymmetry. *Journal of Climate*, *29*(15), 5483–5499. https://doi.org/10.1175/JCLI-D-16-0091.1

Levine, A. F. Z., & McPhaden, M. J. (2015). The annual cycle in ENSO growth rate as a cause of the spring predictability barrier. *Geophysical Research Letters*, *42*, 5034–5041. https://doi.org/10.1002/2015GL064309

Lloyd, J., Guilyardi, E., Weller, H., & Slingo, J. (2009). The role of atmosphere feedbacks during ENSO in the CMIP3 models. *Atmospheric Science Letters*, *10*(3), 170–176. https://doi.org/10.1002/asl.227

Park, W., Keenlyside, N., Latif, M., Ströh, A., Redler, R., Roeckner, E., & Madec, G. (2009). Tropical Pacific climate and its response to global warming in the Kiel climate model. *Journal of Climate*, *22*(1), 71–92. https://doi.org/10.1175/2008JCLI2261.1

Suarez, M. J., & Schopf, P. S. (1988). A delayed action oscillator for ENSO. *Journal of the Atmospheric Sciences*, *45*(21), 3283–3287. https://doi.org/10.1175/1520-0469(1988)045%3C3283:ADAOFE%3E2.0.CO;2

Taylor, K. E., Stouffer, R. J., & Meehl, G. A. (2012). An overview of CMIP5 and the experiment design. *Bulletin of the American Meteorological Society*, *93*(4), 485–498. https://doi.org/10.1175/BAMS-D-11-00094.1

Vijayeta, A., & Dommenget, D. (2017). An evaluation of ENSO dynamics in CMIP simulations in the framework of the recharge oscillator model. *Climate Dynamics*. https://doi.org/10.1007/s00382-017-3981-6

Wengel, C., Latif, M., Park, W., Harlaß, J., & Bayr, T. (2017). Seasonal ENSO phase locking in the Kiel climate model: The importance of the equatorial cold sea surface temperature bias. *Climate Dynamics*. https://doi.org/10.1007/s00382-017-3648-3

Wyrtki, K. (1975). El Niño - the dynamic response of the equatorial Pacific Ocean to atmospheric forcing. *Journal of Physical Oceanography*, *5*(4), 572–584. https://doi.org/10.1175/1520-0485(1975)005%3C0572:ENTDRO%3E2.0.CO;2

Wyrtki, K. (1986). Water displacements in the Pacific and the genesis of El Niño cycles. *Journal of Geophysical Research*, *91*, 7129–7132.

Yu, Y., Dommenget, D., Frauen, C., Wang, G., & Wales, S. (2016). ENSO dynamics and diversity resulting from the recharge oscillator interacting with the slab ocean. *Climate Dynamics*, *46*(5-6), 1665–1682. https://doi.org/10.1007/s00382-015-2667-1

Supplementary material for **chapter 4**:

Geophysical Research Letters

Supporting Information for

What controls ENSO-amplitude diversity in climate models?

C. Wengel[1], D. Dommenget[2], M. Latif[1,3], T. Bayr[1], Asha Vijayeta[2]

[1] GEOMAR Helmholtz Centre for Ocean Research Kiel
[2] School of Earth, Atmosphere and Environment, Monash University, Clayton, Victoria, Australia
[3] University of Kiel

Corresponding author: Christian Wengel (cwengel@geomar.de)

Contents of this file

Figures A1 to A9 and Tables A1 to A13.

Additional Supporting Information (Files uploaded separately)

Captions for Data sets A1 to A10.

Introduction

In the following we list the CMIP5 models used in the main analysis (Table A1). We further show the temporal parameter variability within each CMIP5 model and compare it to the intermodel parameter spread across all CMIP5 models (Table A2). We further show the uncertainty of the ReOsc model parameter estimated for SODA and CMIP5 (Table A3). We also show the root-mean-square (RMS) errors between ENSO amplitude as simulated by CMIP5 and that obtained from the ReOsc model integrations with single parameter variation and with co-varying parameters from EOF-1 (Table A4). Furthermore, we show the results obtained for a Kiel Climate Model (KCM) perturbed physics ensemble (Figure A1-A3 and Table A5-A7), of the CMIP5 model selection from *Kim et al.* [2014] (Figure A4-A6 and Table A8-A10) and for the CMIP3 models (Figure A7-A9 and Table A11-A13). At last, the captions of the data sets describe the uploaded data files (Data sets A1 – A10).

CMIP5 model list

Label number	Model
1	ACCESS1-0
2	ACCESS1-3
3	bcc-csm1-1
4	bcc-csm1-1-m
5	BNU-ESM
6	CanESM2
7	CCSM4
8	CESM1-BGC
9	CESM1-FASTCHEM
10	CESM1-WACCM
11	CMCC-CESM
12	CMCC-CM
13	CNRM-CM5
14	CSIRO-Mk3-6-0
15	FGOALS-g2
16	GFDL-CM3
17	GFDL-ESM2G
18	GFDL-ESM2M
19	GISS-E2-H-CC
20	GISS-E2-H
21	GISS-E2-R-CC
22	GISS-E2-R
23	HadCM3
24	HadGEM2-CC
25	HadGEM2-ES
26	IPSL-CM5A-LR
27	IPSL-CM5A-MR
28	IPSL-CM5B-LR
29	MIROC5
30	MPI-ESM-LR
31	MPI-ESM-MR
32	MPI-ESM-P
33	MRI-CGCM3
34	NorESM1-ME
35	NorESM1-M

Table A1 List of CMIP5 models used in the analysis.

CMIP5 model	STD(a_{11})	STD(a_{12})	STD(a_{21})	STD(a_{22})	STD(ξ_T)	STD(ξ_h)
1	0.181	0.016	1.695	0.238	0.135	1.449
2	0.286	0.013	1.415	0.225	0.105	1.109
3	0.206	0.027	1.023	0.189	0.242	1.034
4	0.079	0.051	0.957	0.176	0.235	1.688
5	0.208	0.036	1.420	0.122	0.293	0.792
6	0.197	0.032	1.484	0.189	0.177	0.680
7	0.190	0.026	2.290	0.119	0.149	1.295
8	0.080	0.035	1.054	0.109	0.105	1.145
9	0.116	0.013	0.869	0.111	0.129	1.051
10	0.172	0.029	1.493	0.080	0.275	1.982
11	0.121	0.035	0.962	0.232	0.265	1.811
12	0.128	0.042	2.603	0.185	0.183	0.588
13	0.166	0.033	1.326	0.225	0.179	2.568
14	0.132	0.037	1.189	0.232	0.231	0.893
15	0.307	0.039	2.377	0.180	0.169	1.609
16	0.113	0.017	2.467	0.266	0.181	2.050
17	0.405	0.028	2.855	0.224	0.096	0.539
18	0.145	0.024	1.728	0.090	0.198	2.450
19	0.173	0.026	1.429	0.245	0.172	0.858
20	0.121	0.014	2.126	0.225	0.170	0.346
21	0.304	0.012	1.024	0.237	0.090	0.687
22	0.152	0.044	0.623	0.170	0.101	0.845
23	0.205	0.041	1.425	0.150	0.077	0.740
24	0.432	0.020	2.168	0.124	0.218	1.629
25	0.354	0.065	1.807	0.216	0.318	0.618
26	0.100	0.021	2.370	0.126	0.218	0.524
27	0.222	0.038	1.210	0.294	0.165	1.134
28	0.171	0.027	1.503	0.175	0.145	1.186
29	0.162	0.013	0.983	0.103	0.270	1.200
30	0.159	0.038	2.437	0.142	0.325	1.488
31	0.283	0.021	3.798	0.275	0.141	1.369
32	0.222	0.017	0.980	0.372	0.162	2.348
33	0.300	0.016	1.368	0.113	0.115	0.598

34	0.167	0.023	1.392	0.167	0.227	0.697
35	0.202	0.020	2.777	0.197	0.178	1.518
Ensemble-mean	0.199	0.028	1.675	0.186	0.184	1.215
Intermodel STD	0.457	0.079	2.646	0.302	0.634	3.786
Fraction of mean and intermodel STD	43,55 %	35,44 %	63,30 %	61,59 %	29,02 %	32,09 %

Table A2 Temporal ReOsc parameter variability for each CMIP5 model calculated as the standard deviation over a set of parameters estimated from a moving window with 30 years length and 10 year interval (row 1 – 35), the ensemble-mean over all 35 rows (row 36), the intermodel parameter spread as the standard deviation over all CMIP5 models (entire time period used; row 37) and the fraction of the ensemble-mean temporal variability of the intermodel spread for each parameter (row 38). Units are yr^{-1} for a_{11} and a_{22}, K m^{-1} yr^{-1} for a_{12}, m K^{-1} yr^{-1} for a_{21}, K yr^{-1} for $\boldsymbol{\xi_T}$ and m yr^{-1} for $\boldsymbol{\xi_h}$.

	a_{11}	a_{12}	a_{21}	a_{22}	ξ_T	ξ_h
SODA	0.24	0.026	2.44	0.27	0.15	1.51
1	0.22	0.024	1.77	0.19	0.10	0.80
2	0.24	0.026	1.66	0.18	0.10	0.73
3	0.24	0.044	1.28	0.23	0.13	0.70
4	0.21	0.046	0.83	0.19	0.17	0.68
5	0.15	0.026	0.91	0.15	0.16	0.92
6	0.17	0.027	1.04	0.17	0.12	0.75
7	0.14	0.021	1.14	0.17	0.11	0.85
8	0.16	0.025	1.21	0.19	0.10	0.76
9	0.15	0.024	1.20	0.19	0.10	0.81
10	0.15	0.023	1.14	0.17	0.13	0.95
11	0.18	0.027	1.11	0.17	0.16	1.04
12	0.25	0.037	1.62	0.24	0.11	0.72
13	0.24	0.033	1.58	0.22	0.16	1.02
14	0.21	0.029	1.38	0.19	0.12	0.78
15	0.18	0.022	1.35	0.16	0.10	0.75
16	0.17	0.025	1.27	0.19	0.12	0.93
17	0.24	0.036	1.79	0.27	0.12	0.87
18	0.16	0.020	1.18	0.15	0.16	1.21
19	0.17	0.020	1.42	0.17	0.09	0.78
20	0.19	0.023	1.67	0.21	0.08	0.71
21	0.21	0.029	1.41	0.19	0.08	0.55
22	0.19	0.027	1.25	0.18	0.08	0.55
23	0.22	0.033	1.12	0.17	0.14	0.71
24	0.34	0.048	1.65	0.24	0.19	0.92
25	0.35	0.056	1.76	0.28	0.19	0.93
26	0.21	0.037	1.22	0.21	0.11	0.65
27	0.18	0.032	1.08	0.19	0.10	0.63
28	0.21	0.032	1.56	0.24	0.10	0.78
29	0.15	0.019	1.04	0.13	0.14	0.96
30	0.22	0.031	1.98	0.27	0.13	1.14
31	0.30	0.036	2.35	0.29	0.14	1.14
32	0.22	0.026	2.01	0.23	0.13	1.14
33	0.27	0.039	1.76	0.26	0.12	0.76
34	0.16	0.020	1.48	0.18	0.11	0.98
35	0.16	0.018	1.63	0.18	0.10	1.01
Ensemble-mean	0.21	0.030	1.42	0.20	0.12	0.85

Table A3 95% confidence interval of all six ReOsc model parameters estimated for SODA, all CMIP5 models and of the CMIP5 ensemble-mean. Units are yr^{-1} for a_{11} and a_{22}, K m^{-1} yr^{-1} for a_{12}, m K^{-1} yr^{-1} for a_{21}, K yr^{-1} for $\boldsymbol{\xi_T}$ and m yr^{-1} for $\boldsymbol{\xi_h}$.

RMS error	$\mathbf{a_{11}}$	$\mathbf{a_{12}}$	$\mathbf{a_{21}}$	$\mathbf{a_{22}}$	ξ_T	ξ_h
Single parameter variation	1.72	1.39	1.36	1.36	1.23	1.28
All parameter variation (EOF-1)	1.65	-	1.51	1.31	1.23	1.27

Table A4 Root-mean-square (RMS) error of ENSO amplitude as obtained from the ReOsc model integrations with (first row) single parameter variation and (lower row) with co-varying parameters from EOF-1 with respect to the ENSO amplitudes directly derived from the CMIP5 models. No RMS error is given for a_{12} for the co-varying parameters due to infinite ENSO amplitude within the ensembles parameter-range (see main text).

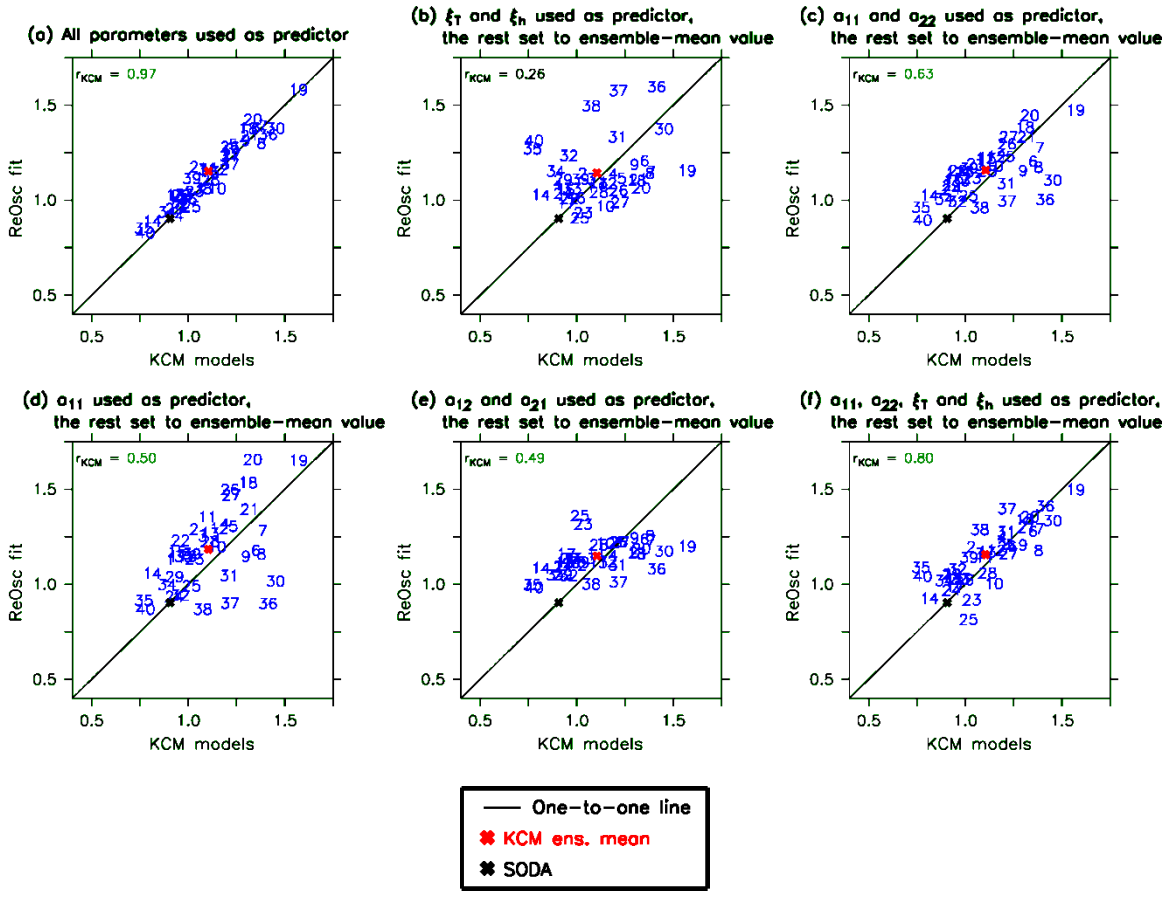

Figure A1 Same as Figure 1 but for the KCM perturbed physics ensemble.

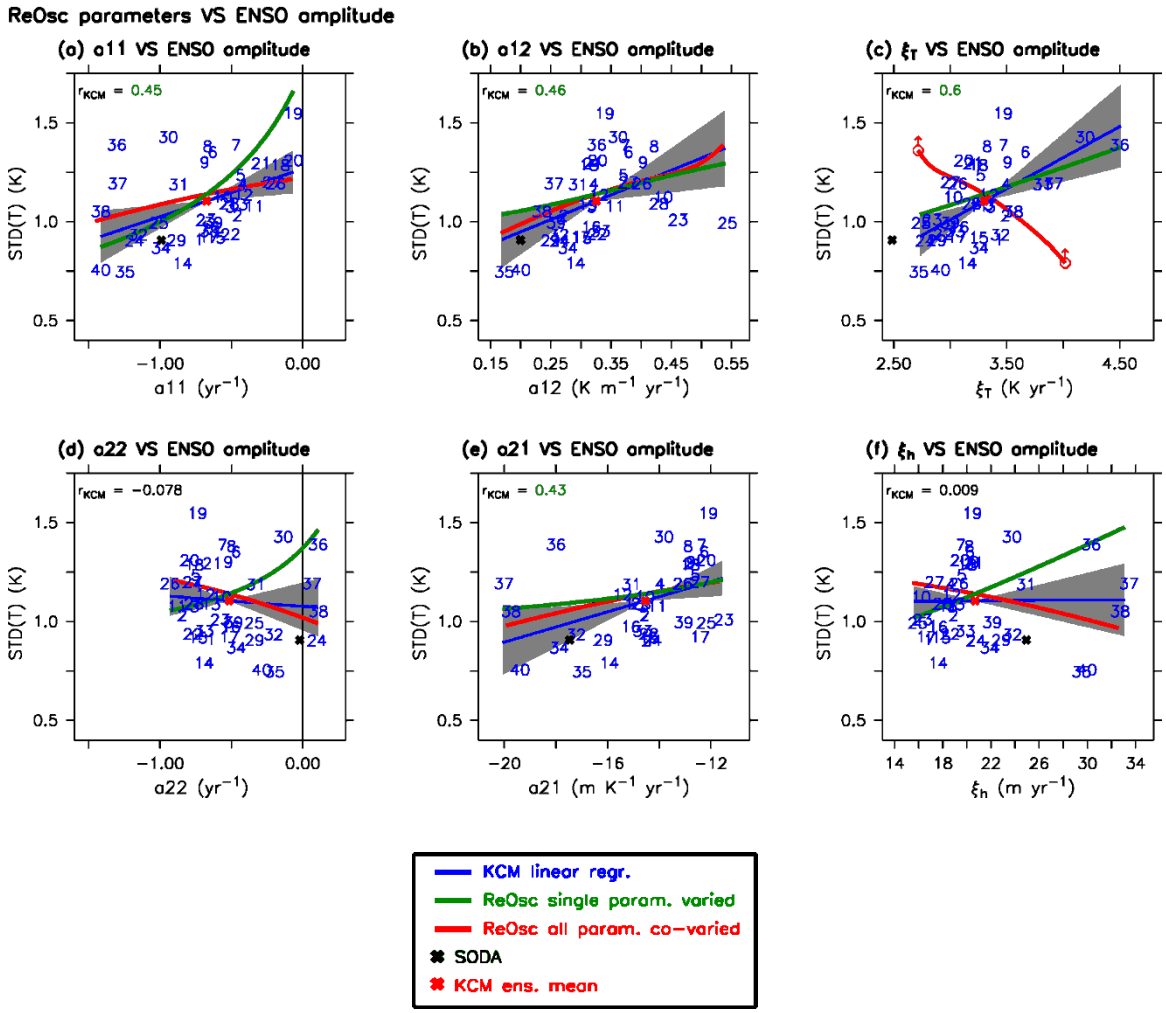

Figure A2 Same as Figure 2 but for the KCM perturbed physics ensemble. Note the different axis scales.

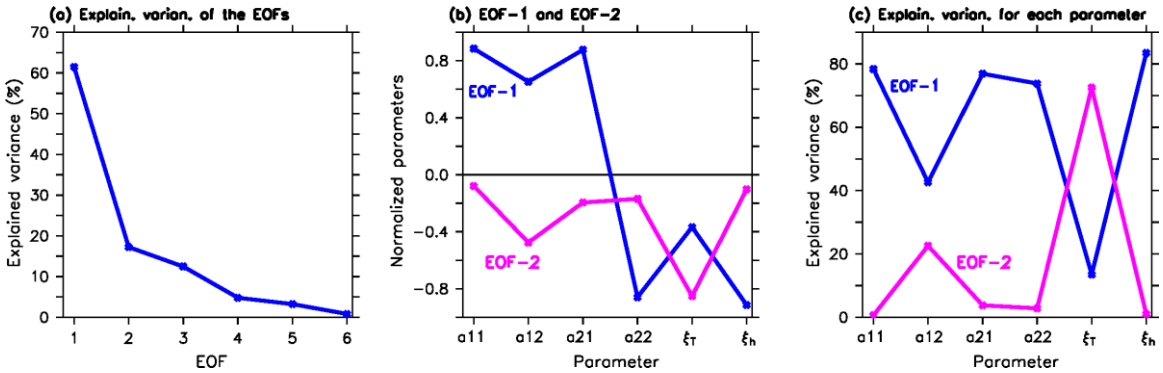

Figure A3 Same as Figure 3 but for the KCM perturbed physics ensemble. Note the different axis scales.

KCM experiment label	Convective mass-flux above level of non-buoyancy	Entrainment rate for shallow convection [10^{-4}]	Convective cloud conversion rate from cloud water to rain [10^{-4}]	Amount of atmospheric vertical levels
1	0.15	3	1	19
2	0.175	3	1	19
3	0.20	3	1	19
4	0.225	3	1	19
5	0.25	3	1	19
6	0.275	3	1	19
7	0.30	3	1	19
8	0.325	3	1	19
9	0.35	3	1	19
10	0.2	1	1	19
11	0.2	2	1	19
12	0.2	4	1	19
13	0.2	5	1	19
14	0.2	6	1	19
15	0.2	7	1	19
16	0.2	8	1	19
17	0.2	9	1	19
18	0.2	3	2.1	19
19	0.2	3	2.5	19
20	0.2	3	3	19
21	0.2	3	4	19
22	0.2	5	4	19
23	0.30	1	4	19
24	0.13	10	4	19
25	0.3	1	1.5	19
26	0.3	10	1.5	19
27	0.2	1	4	19
28	0.35	10	1	19
29	0.3	10	1.5	31
30	0.35	3	1	31
31	0.2	3	1	31
32	0.2	5	1	31
33	0.2	1	4	31
34	0.35	10	1	31
35	0.3	10	1.5	62
36	0.35	3	1	62
37	0.2	3	1	62
38	0.2	5	1	62
39	0.2	1	4	62
40	0.35	10	1	62

Table A5 List of KCM experiments which differ in three atmospheric parameters (column 2-4) and vertical atmospheric resolution (column 5). See *Wengel et al.* [2017] for details.

	$\mathbf{a_{11}}$	$\mathbf{a_{12}}$	$\mathbf{a_{21}}$	$\mathbf{a_{22}}$	ξ_T	ξ_h
$\mathbf{a_{11}}$		0.41	**0.75**	**-0.88**	-0.14	**-0.70**
$\mathbf{a_{12}}$			**0.64**	**-0.34**	-0.03	**-0.58**
$\mathbf{a_{21}}$				**-0.58**	-0.21	**-0.76**
$\mathbf{a_{22}}$					**0.32**	**0.75**
ξ_T						**-0.70**

Table A6 Same as Table 1 but for the KCM perturbed physics ensemble.

RMS error	$\mathbf{a_{11}}$	$\mathbf{a_{12}}$	$\mathbf{a_{21}}$	$\mathbf{a_{22}}$	ξ_T	ξ_h
Single parameter variation	1.35	1.15	1.17	1.49	1.06	1.46
All parameter variation (EOF-1)	1.15	1.12	1.16	1.29	-	1.31

Table A7 Same as Table A4 but for the KCM perturbed physics ensemble.

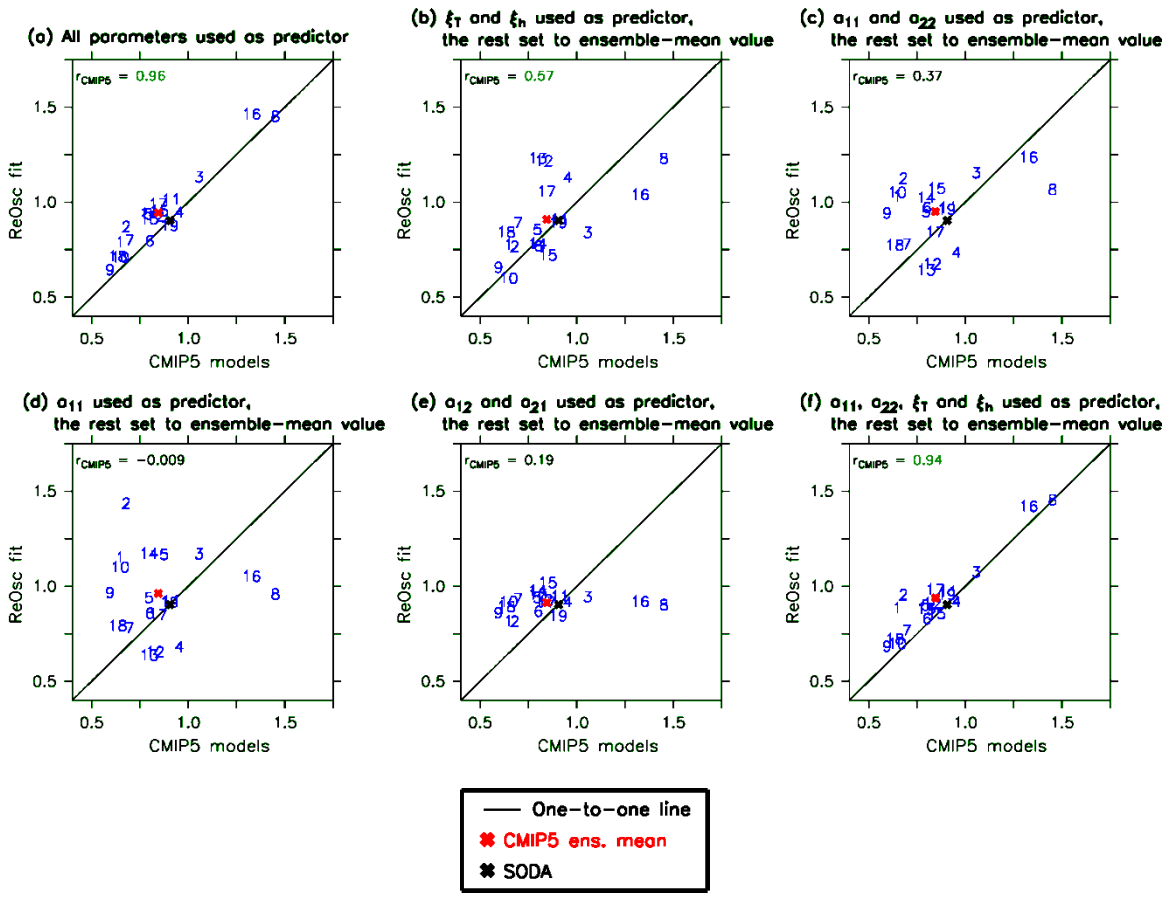

Figure A4 Same as Figure 1 but for the CMIP5 model selection of *Kim et al.* [2014].

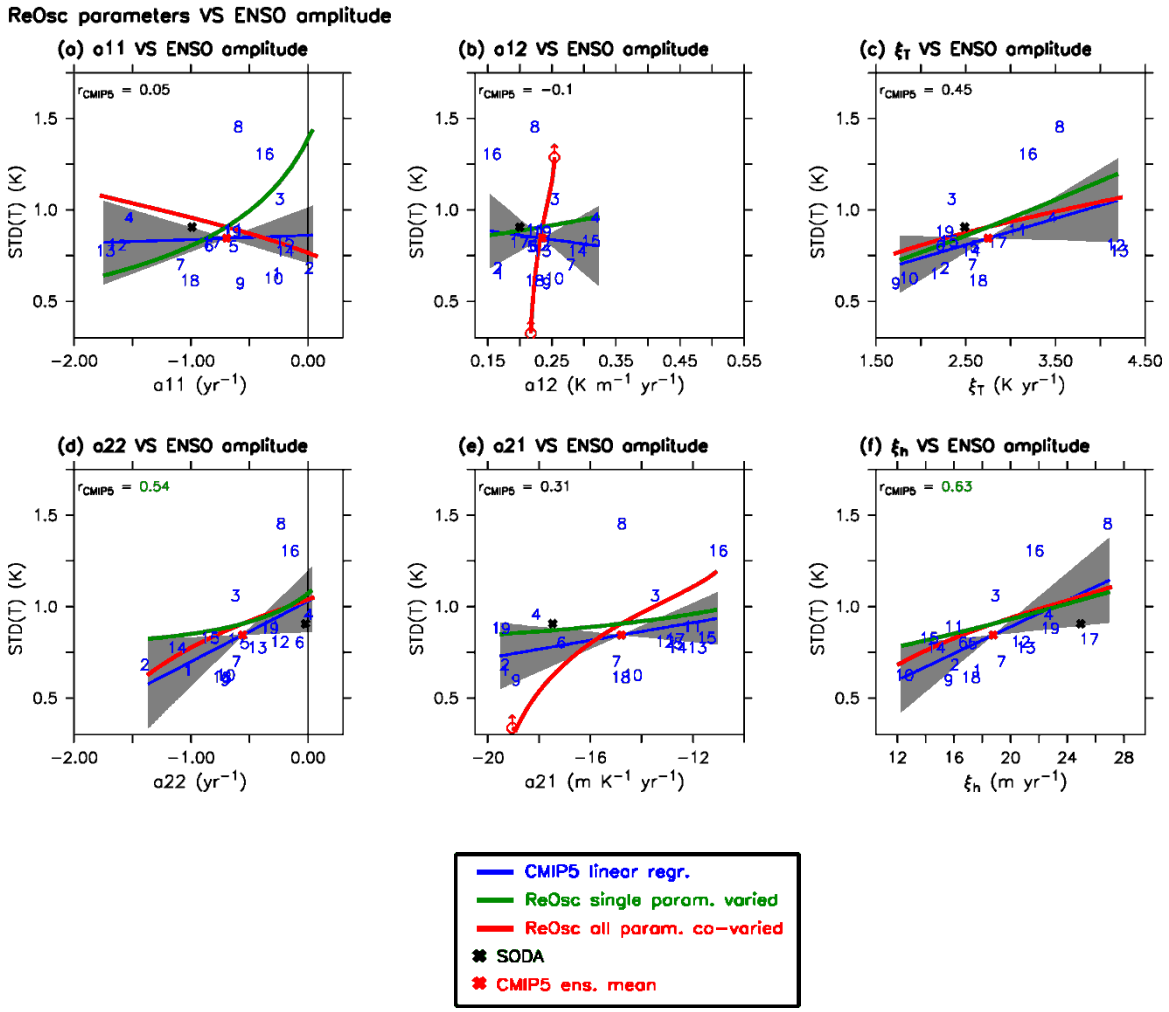

Figure A5 Same as Figure 2 but for the CMIP5 model selection of *Kim et al.* [2014].

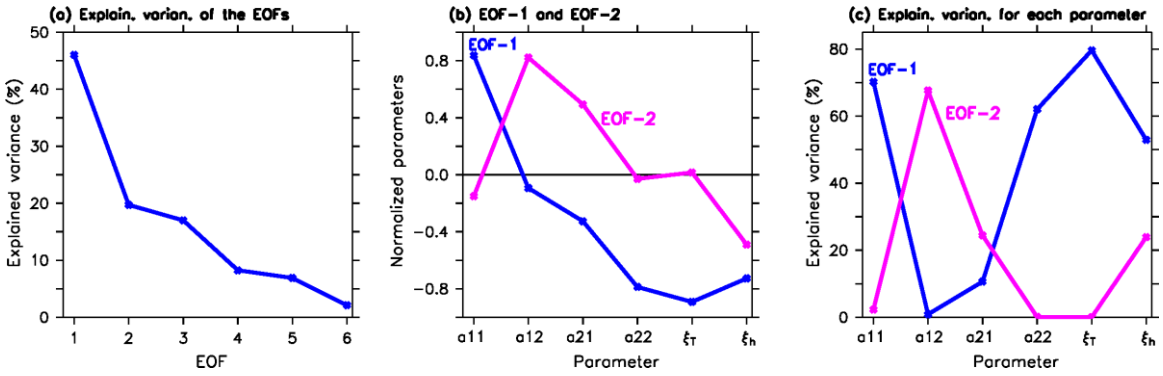

Figure A6 Same as Figure 3 but for the CMIP5 model selection of *Kim et al.* [2014].

Label number	Model
1	ACCESA1-0
2	ACCESA1-3
3	CCSM4
4	CNRM-CM5
5	CSIRO-Mk3-6-0
6	FGOALS-g2
7	GFDL-ESM2G
8	GFDL-ESM2M
9	GISS-E2-H
10	GISS-E2-R
11	HadCM3
12	HadGEM2-CC
13	HadGEM2-ES
14	IPSL-CM5A-LR
15	IPSL-CM5A-MR
16	MIROC5
17	MPI-ESM-LR
18	MRI-CGCM3
19	NorESM1-M

Table A8 List of the CMIP5 models from the selection of *Kim et al.* [2014].

	$\mathbf{a_{11}}$	$\mathbf{a_{12}}$	$\mathbf{a_{21}}$	$\mathbf{a_{22}}$	ξ_T	ξ_h
$\mathbf{a_{11}}$		-0.22	-0.11	**-0.59**	**-0.73**	-0.42
$\mathbf{a_{12}}$			0.08	0.12	-0.02	-0.17
$\mathbf{a_{21}}$				0.13	0.42	-0.02
$\mathbf{a_{22}}$					**0.51**	**0.54**
ξ_T						**0.59**

Table A9 Same as Table 1 but for the CMIP5 model selection of *Kim et al.* [2014].

RMS error	$\mathbf{a_{11}}$	$\mathbf{a_{12}}$	$\mathbf{a_{21}}$	$\mathbf{a_{22}}$	ξ_T	ξ_h
Single parameter variation	1.40	1.01	0.96	0.90	0.92	0.83
All parameter variation (EOF-1)	1.07	-	-	0.85	0.89	0.80

Table A10 Same as Table A4 but for the CMIP5 model selection of *Kim et al.* [2014].

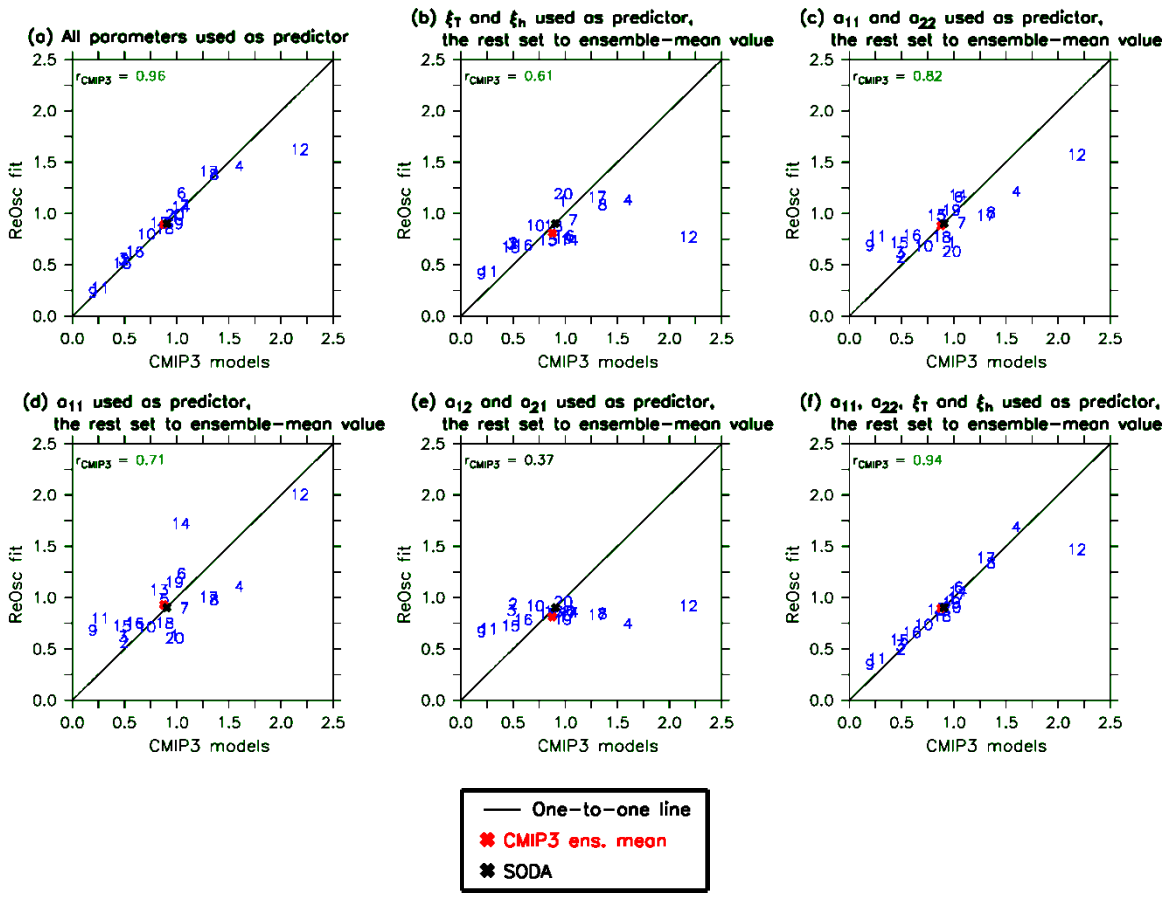

Figure A7 Same as Figure 1 but for the CMIP3 models. Note the different axis scales.

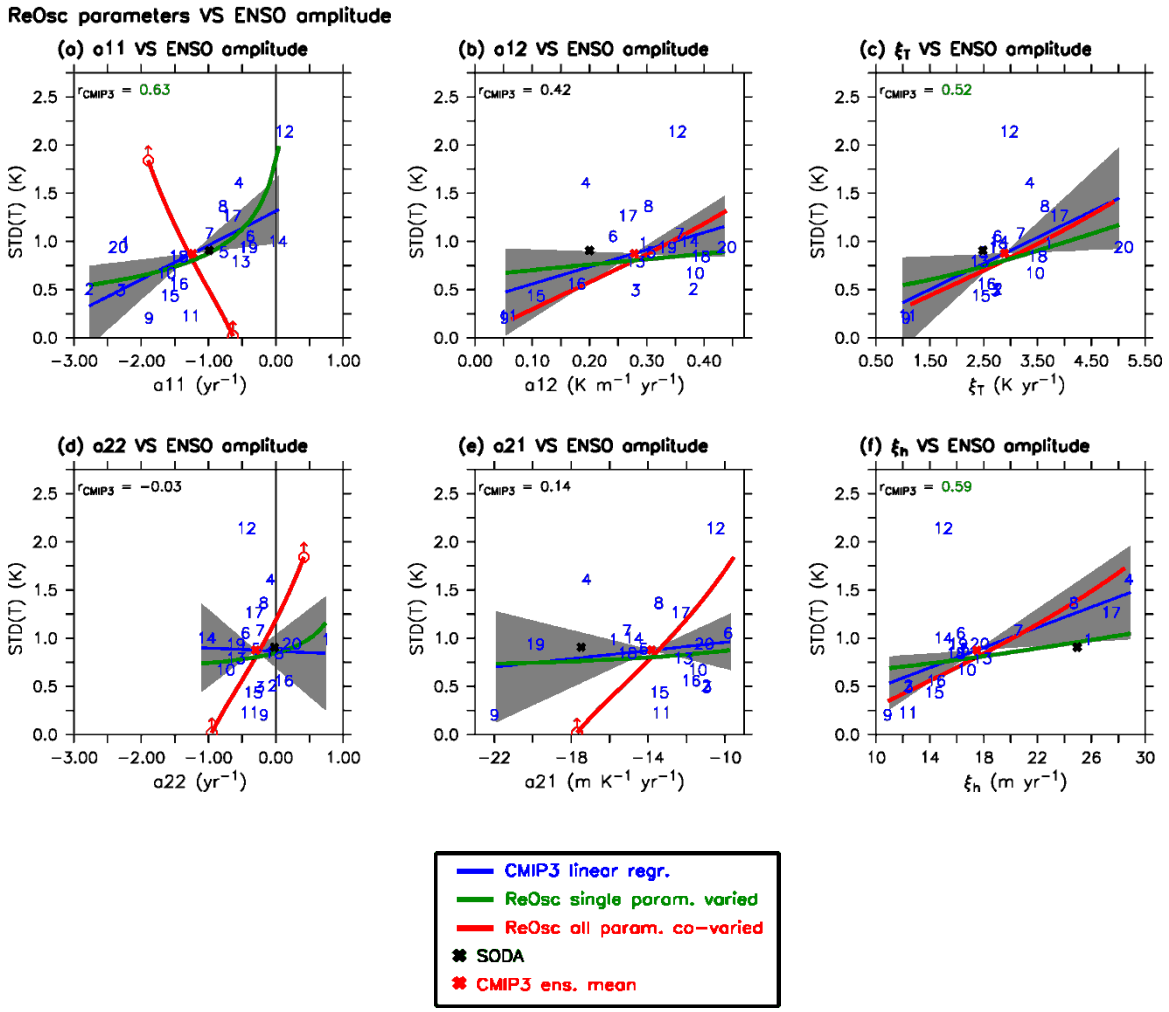

Figure A8 Same as Figure 2 but for the CMIP3 models. Note the very different axis scales.

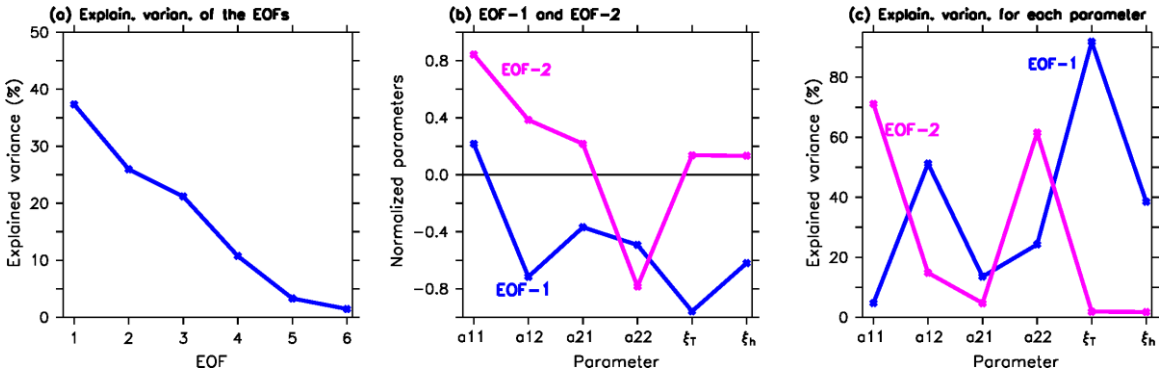

Figure A9 Same as Figure 3 but for the CMIP3 models.

Label number	Model
1	bccr_bcm2_0
2	cccma_cgcm3_1
3	cccma_cgcm3_1_t63
4	cnrm_cm3
5	csiro_mk3_0
6	csiro_mk3_5
7	gfdl_cm2_0
8	gfdl_cm2_1
9	giss_aom
10	giss_model_e_h
11	giss_model_e_r
12	iap_fgoalA1_0_g
13	ingv_echam4
14	ipsl_cm4
15	miroc3_2_hires
16	miroc3_2_medres
17	mpi_echam5
18	mri_cgcm2_3_2a
19	ncar_ccsm3_0
20	ncar_pcm1

Table A11 List of the CMIP3 models.

	$\mathbf{a_{11}}$	$\mathbf{a_{12}}$	$\mathbf{a_{21}}$	$\mathbf{a_{22}}$	ξ_T	ξ_h
$\mathbf{a_{11}}$		0.01	-0.09	**-0.60**	-0.10	0.25
$\mathbf{a_{12}}$				-0.03	**0.72**	0.16
$\mathbf{a_{21}}$				-0.06	0.31	-0.08
$\mathbf{a_{22}}$					0.33	0.33
ξ_T						**0.60**

Table A12 Same as Table 1 but for the CMIP3 models.

RMS error	$\mathbf{a_{11}}$	$\mathbf{a_{12}}$	$\mathbf{a_{21}}$	$\mathbf{a_{22}}$	ξ_T	ξ_h
Single parameter variation	1.48	1.96	2.04	2.08	1.83	1.83
All parameter variation (EOF-1)	-	1.96	-	-	1.78	1.77

Table A13 Same as Table A4 but for the CMIP3 model.

5 Summary and Outlook

5.1 Summary

This thesis investigated the simulation of equatorial Pacific variability in coupled general circulation models with a focus on the eastern equatorial Pacific (EEP) sea surface temperature (SST) annual cycle (AC) and on the interannual El Niño/Southern Oscillation (ENSO).

In chapter 2, the simulation of the EEP SST AC was investigated in an ensemble of Kiel Climate Model (KCM) integrations at different atmospheric resolutions and the results were compared to a subset of models from the Coupled Model Intercomparison Project (CMIP) phase 5. The KCM configuration at coarse atmospheric resolution features similar biases as those found in the CMIP5 models. These biases are reflected in a wrong timing of the equatorial cold tongues' onset and termination of up to 3 months. Further, the magnitude of the seasonal warming in boreal spring is underestimated compared to observations. The mechanisms in driving the SST biases in the KCM are largely consistent with those found in CMIP5. An incorrect simulation of equatorial zonal winds in boreal spring and fall was identified as a major cause of the SST biases. The origin of the zonal wind biases is linked to a wrong representation of precipitation patterns. Another driving mechanism of the SST biases, especially in boreal summer, originates in a wrong representation of cloud cover which induces shortwave radiation biases at the surface. A large part of the zonal wind and cloud cover biases are inherent to the atmospheric model components as shown by means of uncoupled atmosphere model integrations forced by observed SSTs. Furthermore, it was shown that enhancing atmospheric resolution in the KCM leads to a significant improvement of the simulation of the EEP SST AC by alleviating zonal wind and cloud cover biases. This is linked to a reduction of precipitation biases as a result of improved meridional and vertical momentum transport. Further contribution to an improved simulation of surface winds comes from an enhanced representation of orography at higher atmospheric resolution.

In chapter 3, the simulation of seasonal ENSO phase locking was investigated in a perturbed atmospheric physics ensemble of KCM integrations and compared to a set of CMIP5 models. Despite a large spread of the individual KCM integrations, the KCM ensemble-mean features a realistic timing of the seasonal ENSO phase locking but underestimates the strength of the seasonal variation by 50% compared to observations, which is linked to an excessive simulation of the equatorial cold tongue. A similar relationship is found for the CMIP5 models. The effect of the equatorial cold bias is to reduce the magnitude of coupled feedbacks that produce ENSO variability, in particular the Ekman feedback, thermocline feedback and thermodynamic damping as shown by

employing a Bjerknes Stability (BJ) index analysis. To a limited extent, the equatorial cold SST bias and the seasonal phase locking in the KCM can be controlled by perturbing atmospheric physics via local changes in boundary layer cloud cover.

In chapter 4, the model diversity of ENSO amplitudes in CMIP5 was investigated in the framework of the linear recharge oscillator model (ReOsc model). The ENSO amplitudes in the CMIP5 models and as determined from reanalysis data are well represented by the ReOsc model. It was shown that a large fraction of ENSO-amplitude diversity in CMIP5 originates from stochastic forcing (34%) and second largest contribution from the growth rates of the ReOsc model. The stochastic forcing and the growth rates together explain more than 80% of the variance. Another important source of ENSO-amplitude diversity was identified to originate from competing effects in the dynamics. The effect of changes in the growth rate of SST anomalies (SSTa) on ENSO amplitude is largely offset by that of the growth rate of equatorial heat content anomalies and by the stochastic forcing of SSTa. The results provide an explanation why the growth rate of SSTa must not necessarily correlate with ENSO amplitude in a multi-model ensemble.

This thesis stresses the importance of the atmospheric model component in driving equatorial Pacific coupled model biases. Results from the KCM imply that coupled model biases can be significantly alleviated by only applying changes in the atmospheric component while keeping the ocean model configuration fixed. In particular, it was shown that simulation benefits can be achieved by enhancing atmospheric resolution, horizontally and vertically, and by varying selected coefficients in atmospheric cloud parameterizations. This is in agreement with other studies pointing out the importance of atmospheric processes in determining equatorial Pacific variability (Frauen and Dommenget 2010; Bayr et al. 2017; Dommenget and Yu. 2017; Ferrett et al. 2017) and in acting as a major source for ENSO simulation diversity (Schneider 2002; Guilyardi et al. 2004; Kim et al. 2008; Sun et al. 2009; Lloyd et al. 2011).

The results from chapter 3 show that a climate model can be highly sensitive to choices of coefficients in selected atmospheric parameterizations. This has large potential to introduce uncertainties in climate model simulations of any kind. These results emphasize the importance of an extensive testing of climate models to sensitivities in this regard prior to an application.

A cautionary note must be made in terms of the limited availability of observed ocean data. In this thesis, the analysis was largely restricted to reanalysis data, which potentially exhibits similar characteristics as the climate models. However, the data reliability for the equatorial Pacific is continuously improving due to measurement efforts such as the TAO/TRITON, ship campaigns and satellite observations.

5.2 Outlook

The results in chapter 2 of this thesis have shown that enhancing atmospheric resolution reduces eastern equatorial Pacific model biases in the KCM. Further investigation is required to assess whether similar improvements can be achieved for the simulation of ENSO variability. Furthermore, in chapter 3 it was shown that improvements in the simulation of seasonal ENSO phase locking and the mean state can be achieved by changes in coefficients in atmospheric parameterizations in the KCM. Additional work is required to investigate whether this approach can have a beneficial effect on the simulation of the EEP SST AC.

In chapter 3 it was mentioned that the sensitive effects to perturbed atmospheric physics in the KCM can be highly model-dependent. Therefore, additional investigation to further test this sensitivity in other climate models would be of benefit.

Yet limited is the understanding of the origin of the equatorial cold SST bias, which commonly is present across many climate models and is known to degrade the skill in simulating ENSO (Latif et al. 2001; AchutaRao and Sperber 2006; Guilyardi 2006; Wittenberg et al. 2006; Misra et al. 2008; Ham and Kug 2012). It is argued that the equatorial cold SST bias originates from the coupling of ocean atmosphere (Li and Xie 2014), however further investigation is needed to better assess the role of the atmospheric or the oceanic model component. The results presented in chapter 3 of this thesis highlight the role of atmospheric heat fluxes in influencing equatorial SST.

The work provided in this thesis motivates to perform additional research on the role of the oceanic model components' configuration in influencing equatorial Pacific variability. The sensitivity to changes in oceanic resolution and in coefficients in oceanic parameterizations is of interest. Sasaki et al. (2013) investigate the relationship of parameterized ocean mixing induced by small vertical scales on the mean state in an ocean general circulation model, finding that it can significantly affect the simulation of equatorial SST. This motivates to conduct a similar approach with the KCM and the Flexible Ocean and Climate Infrastructure (under development at GEOMAR).

Not entirely understood are the processes governing the stochastic forcing that was highlighted in chapter 4. It is suggested that the stochastic forcing is largely determined by atmospheric noise. The importance of stochastic forcing for ENSO simulations in climate models, as shown in chapter 4, motivates for additional investigation.

Also unknown is the origin of the cross-relations of the ReOsc model parameters that were found to be present among climate models as shown in chapter 4. These cross-relations present an important source for ENSO-amplitude diversity in climate models and are potentially related to the identified compensations between ENSO atmospheric feedbacks (Lloyd et al. 2009; Bellenger et al. 2014;

Bayr et al. 2017). This potential connection requires further investigation to provide additional insight on the origin of the cross-relations and the associated competing processes.

The results on the controls of ENSO-amplitude diversity in climate models that were presented in chapter 4 motivate for additional investigation on the diversity of other ENSO characteristics. For example, ENSO skewness also exhibits large spread among climate models. The potential importance of stochastic forcing in this regard can be assessed.

Another interesting aspect for future research is to better understand the impact of equatorial Pacific mean-state and variability biases in climate models on a realistic simulation of equatorial Pacific teleconnections and on climate predictability. An example is a realistic simulation of the Indian summer monsoon under the exposure of an incorrect simulation of seasonal ENSO phase locking. The set of KCM perturbed physics experiments, introduced in chapter 3, provides a basis for investigation due to its large variety in the simulation of equatorial Pacific mean-state and variability.

Bibliography

AchutaRao, K. M. and Sperber, K. R. (2006). ENSO Simulation in Coupled Ocean-Atmosphere Models: Are the Current Models Better? Climate Dynamics, Vol. 27, 1–15, DOI: 10.1007/s00382-006-0119-7

Alexander, M. A., Blade, I., Newman, M., Lanzante, J. R., Lau, N.-C., and Scott J. D. (2002). The atmospheric bridge: The influence of ENSO teleconnections on air–sea interaction over the global oceans. Journal of Climate, 15, 2205–2231

An S.-I., Heo E. S., Kim S. T. (2017). Feedback process responsible for intermodel diversity of ENSO variability. Geophysical Research Letters, 44:4272–4279. doi: 10.1002/2017GL073203

Barsugli, J. J., and Sardeshmukh, P. D. (2002). Global atmospheric sensitivity to tropical SST anomalies throughout the Indo-Pacific basin. Journal of Climate, 15, 3427–3442

Bayr, T., Latif, M., Dommenget, D, Wengel, C., Harlaß, J., and Park, W. (2017). Mean-state dependence of ENSO atmospheric feedbacks in climate models. Climate Dynamics, doi: 10.1007/s00382-017-3799-2

Bellenger, H., Guilyardi, E., Leloup, J., Lengaigne, M., and Vialard, J. (2014). ENSO representation in climate models: From CMIP3 to CMIP5. Climate Dynamics 42:1999–2018. doi: 10.1007/s00382-013-1783-z

Bjerknes, J. (1969). Atmospheric teleconnections from the equatorial Pacific 1. Monthly Weather Review, 97:163–172. doi: 10.1175/1520-0493(1969)097<0163:ATFTEP>2.3.CO;2

Diaz, H. F., and Markgraf, V. (Editors) (2000). El Niño and the Southern Oscillation: Multiscale Variability and Its Impacts on Natural Ecosystems and Society. Cambridge University Press, 496 pp.

Dommenget, D., and Yu, Y. (2016). The seasonally changing cloud feedbacks contribution to the ENSO seasonal phase-locking. Climate Dynamics, 47:1–12. doi: 10.1007/s00382-016-3034-6

Ferrett, S., and Collins, M. (2016). ENSO feedbacks and their relationships with the mean state in a flux adjusted ensemble. Climate Dynamics 1–20. doi: 10.1007/s00382-016-3270-9

Frauen, C., Dommenget, D., (2010). El Niño and la Niña amplitude asymmetry caused by atmospheric feedbacks. Geophysical Research Letters, 37:1–6. doi: 10.1029/2010GL044444

Guilyardi, E., Gualdi, S., Slingo, J., Navarra, A., Delecluse, P,. Cole, J., Madec, G., Roberts, M., Latif, M., and Terray, L. (2004). Representing El Niño in coupled ocean–atmosphere GCMS: the dominant role of the atmospheric component. Journal of Climate, 17:4623–4629. doi:10.1175/JCLI-3260.1

Guilyardi, E. (2006). El Niño-mean state-seasonal cycle interactions in a multi-model ensemble. Climate Dynamics, 26:329–348. doi: 10.1007/s00382-005-0084-6

Guilyardi, E., Wittenberg, A., Fedorov, A., Collins, M., Wang, C., Capotondi, A., van Oldenborgh, G. J., and Stockdale, T. (2009). Understanding El Niño in Ocean–Atmosphere General Circulation Models: Progress and Challenges. Bulletin of the American Meteorological Society, 90:325–340. doi: 10.1175/2008BAMS2387.1

Ham, Y. G., and Kug, J. S. (2014). ENSO phase-locking to the boreal winter in CMIP3 and CMIP5 models. Climate Dynamics, 43:305–318. doi: 10.1007/s00382-014-2064-1

Ham, Y. G., Kug, J. S., Kim, D., Kim, Y.-H., and Kim, D.-H. (2012). What controls phase-locking of ENSO to boreal winter in coupled GCMs? Climate Dynamics, 40:1551–1568. doi: 10.1007/s00382-012-1420-2

Hsu, H.-H., and Moura, A. D. (2001). Workshop on the impacts of the 1997–99 ENSO. Bulletin of the American Meteorological Society, 82, 305–312

Jin, E. K., and Kinter, J. L. (2009). Characteristics of tropical Pacific SST predictability in coupled GCM forecasts using the NCEP CFS. Climate Dynamics, 32:675–691. doi: 10.1007/s00382-008-0418-2

Jin, F.-F. (1997). An Equatorial Ocean Recharge Paradigm for ENSO . Part I : Conceptual Model Pacific. Journal of the Atmospheric Sciences, 54:811–829. doi: 10.1175/1520-0469(1997)054<0811:AEORPF>2.0.CO;2

Kim, D., Kug, J.-S., Kang, I.-S., Jin, F.-F., Wittenberg, A. T. (2008). Tropical Pacific impacts of convective momentum transport in the SNU coupled GCM. Climate Dynanmics, 31:213–226. doi:10.1007/s00382-007-0348-4

Kim, S. T., Cai, W., Jin, F.-F., and Yu, J.-Y. (2014). ENSO stability in coupled climate models and its association with mean state. Climate Dynamics, 42:3313–3321. doi: 10.1007/s00382-013-1833-6

Latif, M., Sperber, K., Arblaster, J., Braconnot, P., Chen, D., Colman, A., Cubasch, U., Cooper, C., Delecluse, P., Dewitt, D., Fairhead, L., Flato, G., Hogan, T., Ji, M., Kimoto, M., Kitoh, A., Knutson, T., Le Treut, H., Li, T., Manabe, S., Marti, O., Mechoso, C., Meehl, G., Power, S., Roeckner, E., Sirven, J., Terray, L., Vintzileos, A., Voss, R., Wang, B., Washington, W., Yoshikawa, I., Yu, J., and Zebiak, S. (2001). ENSIP: the El Niño simulation intercomparison project. Climate Dynamics, 18:255–276. doi: 10.1007/s003820100174

Levitus, S., Boyer, T. P., Conkright, M. E., O' Brien, T., Antonov, J., Stephens, C., Stathoplos, L., Johnson, D., and Gelfeld, R. (1998). NOAA Atlas NESDIS 18, World Ocean Database 1998: VOLUME 1: INTRODUCTION, U.S. Gov. Printing Office, Wash., D.C., 346pp.

Li, G., and Xie, S.-P. (2014). Tropical Biases in CMIP5 Multimodel Ensemble: The Excessive Equatorial Pacific cold tongue and Double ITCZ Problems. Journal of Climate, 27, 1765–1780, doi:10.1175/JCLI- D-13-00337.1

Liu, Z. (2002). A simple model study of ENSO suppression by external periodic forcing. Journal of Climate, 15:1088–1098. doi: 10.1175/1520-0442(2002)015<1088:ASMSOE>2.0.CO;2

Lloyd, J., Guilyardi, E., Weller, H., and Slingo, J. (2009). The role of atmosphere feedbacks during ENSO in the CMIP3 models. Atmospheric Science Letters, 10:170–176. doi: 10.1002/asl.227

Lloyd, J., Guilyardi, E., Weller, H., Slingo, J. (2011). The role of atmosphere feedbacks during ENSO in the CMIP3 models. Part II: using AMIP runs to understand the heat flux feedback mechanisms. Climate Dynanmics, 37:1271–1292. doi:10.1175/JCLI-D-11-00178.1

McGregor, S., Timmermann, A., Schneider, N., Stuecker, M., and England, M. H. (2012). The Effect of the South Pacific Convergence Zone on the Termination of El Niño Events and the Meridional Asymmetry of ENSO. Journal of Climate, 25:5566–5586. doi: 10.1175/JCLI-D-11-00332.1

McPhaden, M. J. (1999). The child prodigy of 1997-1998, *Nature*, *398*(15 April), 559–562

Misra, V., Marx, L., Brunke, M., and Zeng, X. (2008). The equatorial Pacific cold tongue bias in a coupled climate model, Journal of Climate, 21, 5852–5869, doi:10.1175/2008JCLI2205.1

Neelin, J. D., Jin, F.-F., and Syu, H. H. (2000). Variations in ENSO phase locking. Journal of Climate, 13:2570–2590. doi: 10.1175/1520-0442(2000)013<2570:VIEPL>2.0.CO;2

Rashid, H., and Hirst, A. C. (2015). Investigating the mechanisms of seasonal ENSO phase locking bias in the ACCESS coupled model. Climate Dynamics. doi: 10.1007/s00382-015-2633-y

Rayner, N. A., Parker, D. E., Horton, E. B., Folland, C. K., Alexander, L. V., Rowell, D. P., Kent, E. C., and Kaplan, A. (2003). Global analyses of sea surface temperature, sea ice, and night marine air temperature since the late Nineteenth Century. Journal of Geophysical Research, 108:4407. doi: 10.1029/2002JD002670

Reynolds R. W., Rayner, N. A., Smith, T. M., Stokes, D. C., and Wang, W. (2002). An improved in situ and satellite SST analysis for climate. Journal of Climate, 15:1609–1625. doi: 10.1175/1520-0442(2002)015<1609:AIISAS>2.0.CO;2

Rossow W. B., and Schiffer R. A. (1999). Advances in Understanding Clouds from ISCCP. Bulletin of the American Meteorological Society, 80:2261–2287. doi: 10.1175/1520-0477(1999)080<2261:AIUCFI>2.0.CO;2

Sasaki, W., Richards, K. J., and Luo, J.-J. (2013). Impact of vertical mixing induced by small vertical scale structures above and within the equatorial thermocline on the tropical Pacific in a CGCM. Climate Dynamics, 41:443–453. doi: 10.1007/s00382-012-1593-8

Schneider, E. K. (2002). Understanding differences between the equatorial Pacific as simulated by two coupled GCMs. Journal of Climate, 15:449–469. doi:10.1175/1520-0442(2002)015<0449:UDBTEP>2.0.CO;2

Siedler, G., Griffies, S. M., Gould, J., and Church, J. A. (2013). Ocean circulation and climate: A 21st century perspective. International Geophysics Series.

Song, Z. Y., Liu, H. L., Wang, C. Z., Zhang, L. P., and Qiao, F. L. (2014). Evaluation of the eastern equatorial Pacific SST seasonal cycle in CMIP5 models. Ocean Science, 10:837–843. doi: 10.5194/os-10-837-2014

Sun, D. Z., Yu, Y., Zhang, T. (2009). Tropical water vapor and cloud feedbacks in climate models: a further assessment using coupled simulations. J Clim 22:1287–1304. doi:10.1175/2008JCLI2267.1

Tziperman, E., Cane, M. A., Zebiak, S. E., Xue, Y., and Blumenthal, B. (1998). Locking of El Niño's Peak Time to the End of the Calendar Year in the Delayed Oscillator Picture of ENSO. Journal of Climate, 11:2191–2199. doi: 10.1175/1520-0442(1998)011<2191:LOENOS>2.0.CO;2

Webster, P. J., Magaña V. O., Palmer, T. N., Shukla, J., Tomas, R. A., Yanai, M., and Yasunari, T., (1998) Monsoons: Processes, predictability, and the prospects for prediction. Journal of Geophysical Research Ocean 103:14451–14510. doi: 10.1029/97JC02719

Wentz, F. J., Scott, J., Hoffman, R., Leidner, M., Atlas, R., and Ardizzone, J. (2015) Remote Sensing Systems Cross-Calibrated Multi-Platform (CCMP) 6-hourly ocean vector wind analysis product on 0.25 deg grid, Version 2.0. Remote Sensing Systems, Santa Rosa, CA. Available online at www.remss.com/measurements/ccmp. Accessed Feb 2016.

Wittenberg, A. T., Rosati, A., Lau, N. C., and Ploshay, J. J. (2006). GFDL's CM2 global coupled climate models. Part III: Tropical Pacific climate and ENSO. Journal of Climate, 19, 698–722

Wittenberg, A. T. (2009). Are historical records sufficient to constrain ENSO simulations? Geophysical Research Letters, 36:L12702. doi: 10.1029/2009GL038710

Xie, S.-P. (2005). The shape of continents, air-sea interaction, and the rising branch of the Hadley circulation. The Hadley Circulation: Present, Past and Future, 121–152. doi: 10.1007/978-1-4020-2944-8_5

Xie, S.-P., and Arkin, P. A. (1997). Global precipitation: a 17-year monthly analysis based on gauge observations, satellite estimates, and numerical model outputs. Bulletin of the American Meteorological Society, 78:2539–2558. doi:10.1175/1520-0477(1997)078<2539:GPAYMA>2.0.CO;2

Zheng, W., and Yu, Y. (2007). ENSO phase-locking in an ocean-atmosphere coupled model FGCM-1.0. Advances in Atmospheric Sciences, 24:833–844. doi: 10.1007/s00376-007-0833-z

Own Publications

Bayr, T., Latif, M., Dommenget, D, **Wengel, C**., Harlaß, J., and Park, W. (2017). Mean-state dependence of ENSO atmospheric feedbacks in climate models. Climate Dynamics, doi: 10.1007/s00382-017-3799-2

Khon, V. C., Schneider, B., Latif, M., Park, W., **Wengel, C**. (2017) Evolution of Eastern Equatorial Pacific Seasonal and Interannual Variability during the Holocene and Eemian from Model Simulations. Geophysical Research Letters, in revision.

Wengel, C., Latif, M., Park, W., Harlaß, J., and Bayr, T. (2017). Eastern Equatorial Pacific Sea Surface Temperature Annual Cycle in the Kiel Climate Model: Simulation Benefits from Enhancing Atmospheric Resolution. Climate Dynamics, in revision.

Wengel, C., Latif, M., Park, W., Harlaß, J., and Bayr, T. (2018). Seasonal ENSO phase locking in the Kiel Climate Model: The importance of the equatorial cold sea surface temperature bias. Climate Dynamics, 50: 901. https://doi.org/10.1007/s00382-017-3648-3

Wengel, C., Dommenget, D., Latif, M., Bayr, T., and Vijayeta, A. (2018). What controls ENSO-amplitude diversity in climate models? Geophysical Research Letters, 45, 1989–1996. https://doi.org/10.1002/2017GL076849

Acknowledgments

I would like to thank Mojib Latif for giving me the opportunity to do my doctorate. I appreciate the steep learning curve I felt due to his expertise and the freedom to follow up my own ideas.

I also want to thank Wonsun Park for his very helpful co-supervision and Dietmar Dommenget for the opportunity to do a research stay at Monash University in Melbourne. Further thanks to Peter Brandt and Sascha Flögel for being members of my ISOS committee.

I would like to thank Joke Lübbecke for being the second examiner of my thesis. Thanks also to Christian Berndt and Arne Biastoch who will be part of the committee during my disputation.

Many thanks go to Tobias Bayr who I intensively worked together with; it was very motivating and helpful to continuously exchange our current results and ideas. Further thanks to Jan Harlaß for a nice office time and the support concering the work with the Kiel Climate Model. I also want to thank Annika Reintges and Zhaoyang Song for their great help and the fruitful discussions throughout the time.

Thanks to all colleagues from the department, particularly to Tania Chiarini and Silke Gesinn for their very efficient and helpful assistance.

I also want to thank the ISOS for presenting a great support during these years and, especially, for creating the opportunity to do a research stay in Australia.

Finally, I would like to thank Rike for her great help and support during these three years and my parents for always supporting my decisions.

Declaration

I hereby declare that this work is my own work apart from my supervisors' guidance and acknowledged assistance. This thesis has not been submitted for a degree to any other examining body. This thesis was prepared in accordance with the Rules of Good Scientific Practice of the German Research Foundation.

Kiel, March 2018, _____

Christian Wengel